ISSN 0914-9244
CODEN JSTEEW

Journal of Photopolymer Science and Technology

Volume 34 Number 3

2021

JOURNAL OF PHOTOPOLYMER SCIENCE AND TECHNOLOGY
Home Page http://www.spst-photopolymer.org
https://www.jstage.jst.go.jp/browse/photopolymer

Journal of Photopolymer Science and Technology publishes papers on the scientific progress and the technical development of photopolymers.

The Editorial Office
Assoc. Prof. Hiroyuki MAYAMA
Department of Chemistry, Asahikawa Medical University, 2-1-1-1 Midorigaoka-Higashi, Asahikawa, Hokkaido 078-8510, Japan.
FAX: +81-166-68-2782, e-mail: mayama@asahikawa-med.ac.jp

Information for Contributors

Submit Manuscripts to the SPST Homepage (Journal --> Submission of Papers --> Editorial Manager). Submission is a representation that the manuscript has not been published previously elsewhere. The manuscript should be accompanied by a statement transferring copyright from the authors (or their employers-whoever holds the copyright) to the Society of Photopolymer Science and Technology. A suitable form for copyright transfer is available from the SPST Homepage. This written transfer of copyright, which previously was assumed to be implicit in the act of submitting a manuscript, is necessary under the Japan copyright law. Further information may be obtained from the "Manual for Manuscript Writing" at the SPST Homepage.

Proofs and All Correspondence: Concerning papers in the process of publication should be addressed to the Editorial Office.

Manuscript Preparation: All the papers submitted are reproduced electronically as they were. For this reason, the manuscripts should be prepared according to the Manual for Manuscript Writings shown at the SPST Homepage.

Subscription Price (Airmail Postage included):
¥12,000 (in Japan), US$ 150.00 (for Foreign)

Subscriptions, renewals, and address changes should be addressed to the Editorial Office. For the address changes, please send both old and new addresses and, if possible, include a mailing label from the wrapper of recent issue. Requests from subscribers for missing journal issues will be honored without charge only if received within six months of the issue's actual date of publication; otherwise, the issue may be purchased at the single-copy price.

Publication Charge (Reprint Order): To support a part of the cost of publication of journal pages, the author's institution is requested to pay a page charge of ¥3,000 per page (with a one-page minimum) and an article charge of ¥12,000 per article. The page charge (if honored) entitles the author to 50 free reprints. For Errata the minimum page charge is ¥3,000, with no articles charge and no free reprints.

The cover designed by M. Tsuda and M. Morishita

JOURNAL OF PHOTOPOLYMER SCIENCE AND TECHNOLOGY

Volume 34 Number 3

2021

Published by

THE SOCIETY OF PHOTOPOLYMER SCIENCE AND TECHNOLOGY

THE SOCIETY OF PHOTOPOLYMER SCIENCE AND TECHNOLOGY (SPST)
http://www.spst-photopolymer.org

Office of the Administration
c/o Prof. Takashi KARATSU
Department of Applied Chemistry and Biotechnology,
Chiba University
1-33 Yayoicho, Inage-ku,
Chiba 263-8522, Japan
Phone: +81-43-290-3366
Fax +81-43-290-3401
e-mail:office@spst-photopolymer.org

THE SPST REPRESENTATIVES 2021

Communication

Journal of Photopolymer Science and Technology
Volume 34, Number 3 (2021) 219−224 ©2021SPST

Synthesis of Photo-degradable Polyphthalaldehyde Macromonomer and Adhesive Property Changes of its Copolymer with Butyl Acrylate on UV-irradiation

Hirokazu Hayashi[1*], Hideki Tachi[2], and Kanji Suyama[3]**

[1] Research Division of Applied Material Chemistry,
Izumi Center, Osaka Research Institute of Industrial Science and Technology (ORIST),
[2] Research Division of Polymer Functional Materials,
Izumi Center, Osaka Research Institute of Industrial Science and Technology (ORIST),
7-1 Ayumino-2, Izumi, Osaka 594-1157, Japan,
[3] Faculty of Liberal Arts and Sciences, Osaka Prefecture University,
1-1 Gakuencho, Nakaku, Sakai, Osaka 599-8531, Japan
**hayashi@tri-osaka.jp*
***suyama@las.osakafu-u.ac.jp*

We prepared a new polyphthalaldehyde (PPA) macromonomer by introducing a polymerizable methacryloyl group at the terminal of PPA main-chain. Resulting macromonomer was copolymerized with butyl acrylate to obtain pressure-sensitive adhesives (PSAs). We also compared the behavior of the copolymers with those of polymer blends of poly(butyl acrylate) and linear PPA polymers to clarify the role of polymerization. Higher peel strengths were observed for copolymers than those of corresponding polymer blends. As an increase in irradiation time, the strength generally decreased, although once increased for the copolymer films at the early stage. These results suggest that the introduction and the depolymerization of PPA side-chains caused drastic changes in adhesive properties.

Keywords: Polyphthalaldehyde, Photo-degradation, Macromonomer, Peel strength, Pressure-sensitive adhesive

1. Introduction

Polyphthalaldehydes (PPAs) are known as self-immolative polymers that can be end-to-end depolymerized (unzipping) [1,2]. Recently, PPAs attract much attention again as a candidate for stimuli-responsible polymers for many applications [3-5].

We have synthesized PPAs with oxime ether terminals, and their photoreactions were investigated [6]. On UV-irradiation both in solution and film state, the depolymerization of the PPAs was confirmed by NMR, UV, and IR spectral measurements. Furthermore, the results of the nanoindentation measurement indicated that the films became elastic on irradiation. Among them, a PPA with 1-acetonaphthone oxime and acetyl terminal (1NaPPA) showed a good depolymerizable behavior.

In this study, we have prepared a new PPA macromonomer 1NaPPAMA by introducing a polymerizable methacryloyl group at the terminal of PPA main-chain. Also, resulting macromonomer was copolymerized with butyl acrylate (BA) to obtain pressure-sensitive adhesives (PSAs) as shown in Scheme 1.

The performance of PSAs such as tack, peel resistance, and share resistance generally depends on the viscoelastic properties caused by the balance of storage and loss moduli [7-11]. These properties are provided by soft and hard molecular structures in the PSAs. The latter enables cohesive interaction between polymer chains in the PSA matrixes [12] and have been often introduced in the form of fillers [13-15], side-chains [16-18], and

Received April 12, 2021
Accepted April 24, 2021

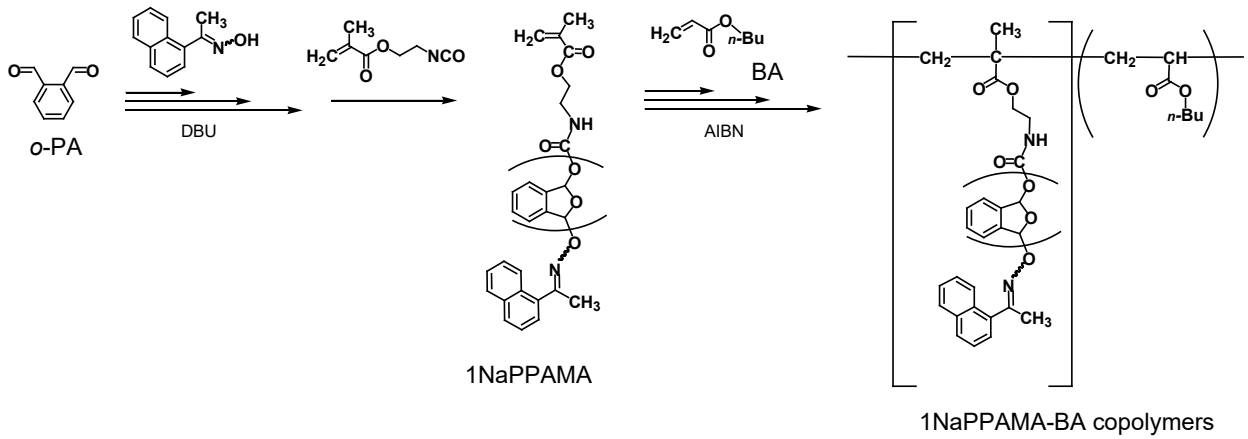

Scheme 1. Syntheses of 1NaPPAMA and its copolymers with BA.

physically or chemically crosslinking points [19-22].

Because our copolymers 1NaPPAMA-BA involve less flexible and photo-degradable PPA chains, remarkable changes of mechanical property in PSAs are expected. These characteristics are advantageous from the viewpoint of stimuli-sensitive PSAs [23-28]. Although we have already proposed PSAs composed of oxime-ester based photolabile crosslinkers [29], quite different mechanism and behavior are anticipated. We also compared the behavior of the copolymers with those of polymer blends of PBA and linear PPA polymers such as 1NaPPA to clarify the role of polymerization.

2. Experimental

2.1. General

IR and UV spectra were recorded on Jasco FT-IR4200, and Shimadzu UV1600PC spectrometers, respectively. NMR spectra were measured by JEOL JNM-ECX400 and Bruker BioSpin Ascend 400 spectrometers.

Number (M_n) and weight (M_w) average molecular weights of polymers were obtained by size exclusion chromatography (SEC) with a Tosoh 8020 liquid chromatography system (Tokyo, Japan) composed of two TSKgel GMH_{XL} columns, and a ViscoTech TDA-302 (RI, DP, RALS, LALS) detector with THF eluent and polystyrene standards at 40 °C.

Commercially available reagents were used as received unless otherwise noted. BA, *o*-dichlorobenzene (DCB), tetrahydrofuran (THF), and *N,N*-dimethylformamide (DMF) were subjected to activated alumina columns before use. 1-Acetonaphthone oxime and 1NaPPA were obtained as described previously [6].

2.2. Preparation of 1NaPPAMA

In a flask, 4.8 g (35.8 mmol) of *o*-phthalaldehyde (*o*-PA) (SP grade for fluorometry, Nacalai, Kyoto, Japan) and 10 mL of CH_2Cl_2 (dehydrated grade, Nacalai) was added under argon, and the flask was cooled to –80 °C in an aluminum block cryostat PSL-2500 A (EYELA, Tokyo, Japan). In other vial, 82.4 mg (0.54 mmol) of 1,8-diazabicyclo[5.4.0]undec-7-ene (DBU) and 102 mg (0.56 mmol) of 1-acetonaphthone oxime were dissolved in 3 mL of CH_2Cl_2. Then, 2.5 mL of the solution was taken out with a syringe and added to the flask dropwise over 20 s, and the mixture was kept stirring at –80 °C for 20 min.

The polymerization was terminated by dropping 1 mL of CH_2Cl_2 solution containing 72 μL (0.51 mmol) of 2-methacryloyloxyethyl isocyanate (MOI, Showa Denko) over 20 s. After stirring at –80 °C for 10 min, the flask was taken out from the cryostat bath and stirred for 20 min at room temperature. Then, 5 mL of methanol was added to the flask and removed the solvent under reduced pressure to obtain 6.13 g of a white solid. The solid was reprecipitated 5 times from methanol after dissolving in $CHCl_3$ to afford 3.69 g (Conv. 77 %) of 1NaPPAMA as colorless powder.

2.3. Preparation of copolymers of 1NaPPAMA and BA

1NaPPAMA, BA, and 2,2'-azobisisobutyronitrile were dissolved in a solvent and bubbled with N_2 gas. The mixture was heated at 60 ºC until the bubbles raised slowly. Obtained copolymers were reprecipitated 5 times from methanol after dissolving in $CHCl_3$.

Table 1. Polymerization conditions and characterization of 1NaPPAMA and BA copolymers.

Polymer	In feed (mol %)		In polymer (mol %)[a]			R. T. (h)[b]	Conv. (%)[c]	M_n[d] (kDa)	M_w[d] (kDa)
	1NaPPAMA	BA	1NaPPAMA	BA	*o*-PA : BA				
1NaPPAMA$_{0.61}$-BA	0.15	99.85	0.61	99.39	0.57 : 1	5.5	36	312	559
1NaPPAMA$_{0.21}$-BA	0.050	99.95	0.21	99.79	0.20 : 1	3.7	66	391	1,480
1NaPPAMA$_{0.05}$-BA	0.016	99.98	0.05	99.95	0.05 : 1	6.0	34	266	781
PBA[e]	0	100	0	100	0 : 1	0.8	50	227	787

a) Estimated by ^{1}H NMR area ratio. b) Reaction time at 60 °C in DCB. c) After reprecipitation. d) From SEC. e) BA homopolymer.

2.4. Peel strength measurement

Polymers were dissolved in toluene (15 wt%), coated on 50 μm PET films with an applicator (200 μm gap), and dried overnight in reduced pressure at room temperature. The thickness of the coated films was estimated to be 30 μm. The films were cut into 10 mm × 80 mm pieces, overlapped with another 2 mm PET plate, and pressed by a roller with 2 kgf. After leaving for 20 min, the films were irradiated with a Hamamatsu Photonics LC5 Hg-Xe lamp (Shizuoka, Japan) through of the PET plate. The light intensity was measured by an Orc UV-M03 illuminometer (Tokyo, Japan) and found to be 150 mW/cm^2 at 365 nm. 180° Peel strength was evaluated using an Instron 5582 Materials Testing System with 100 N loadcell at 300 mm/min. For all samples, 3 runs were carried out.

3. Results and discussion

3.1. Synthesis and characteristics of macromonomer 1NaPPAMA

1NaPPAMA was prepared by anionic polymerization of *o*-PA using 1-acetonaphthone oxime as initiator and DBU as a catalyst as described in our previous study [6], except the terminating reagent. In the present study, the polymerization was terminated with MOI which has both isocyanato and methacryloyl groups. Purified polymer was obtained by repeated reprecipitation.

In ^{1}H NMR spectrum of resulting polymer, small peak at 2.4 ppm assignable to CH_3 unit in oxime moiety is observed along with broad bands (6.4-7.6 ppm) due to aromatic and CH groups in main-chains. Also, small peaks at 1.9, 4.3, 5.6, and 6.1 ppm due to CH_3, CH_2, and CH_2=C groups in MOI moiety appeared. In addition, the UV spectrum of obtained polymer solution has a shoulder around 290 nm due to naphthyl unit. These results clearly show the presence of both naphthyl and methacryloyl terminals.

From SEC, M_n and M_w values were 12.8 and 23.5 kDa, respectively. From M_n value, the repeating units of *o*-PA in 1NaPPAMA are estimated to be 93.

3.2. Preparation of 1NaPPAMA and BA copolymers

In order to obtain polymers for PSAs, 1NaPPAMA was copolymerized with BA in free-radical mode. In preliminary experiments, we used THF, DMF, and DCB as a solvent. Because DCB afforded the highest yield, we used DCB as a polymerization solvent in further experiments.

The polymerization condition and characteristics of the copolymer with different ratio of 1NaPPAMA and BA are summarized in Table 1. After purification, ^{1}H NMR spectra showed that both 1NaPPAMA and BA units were successfully incorporated in the copolymers. Based on that 1NaPPAMA contains 93 units of *o*-PA, the ratios of *o*-PA to BA in copolymers are calculated as shown in Table 1. It is estimated that one polymer chain of 1NaPPAMA$_{0.61}$-BA, 1NaPPAMA$_{0.21}$-BA, and 1NaPPAMA$_{0.05}$-BA have 15, 6.4, and 1.0 PPA side-chains, respectively.

3.3. Comparison of copolymers and polymer blends in peel strength

Films of 1NaPPAMA-BA copolymers were prepared for peel strength measurement. Although films of 1NaPPAMA$_{0.05}$-BA were clear, 1NaPPAMA$_{0.21}$-BA and 1NaPPAMA$_{0.61}$-BA gave cloudy and opaque films, respectively.

Peel strengths of 1NaPPAMA-BA copolymers are plotted as a function of irradiation time in Fig. 1. Before irradiation, both 1NaPPAMA$_{0.21}$-BA and 1NaPPAMA$_{0.05}$-BA films showed much higher peel strength compared to PBA, probably due to PPA side-chains which aggregate to form hard segments. In case of 1NaPPAMA$_{0.61}$-BA, the initial peel

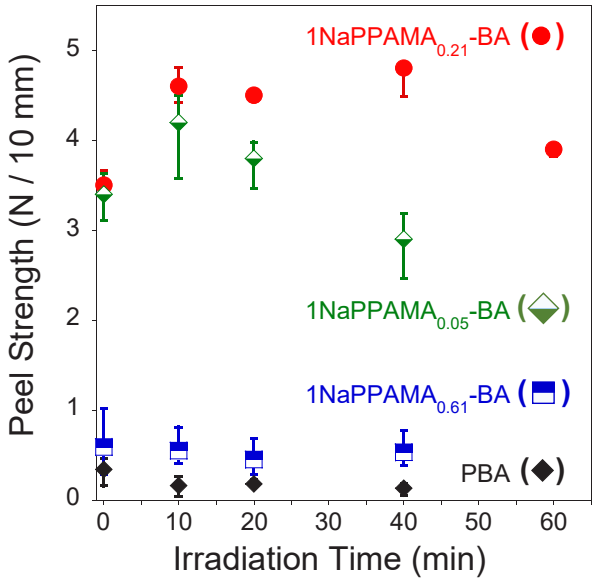

Fig. 1. Peel strength changes of 1NaPPAMA-BA copolymer films on irradiation. Symbols in error bars indicate the averaged values of 3 runs.

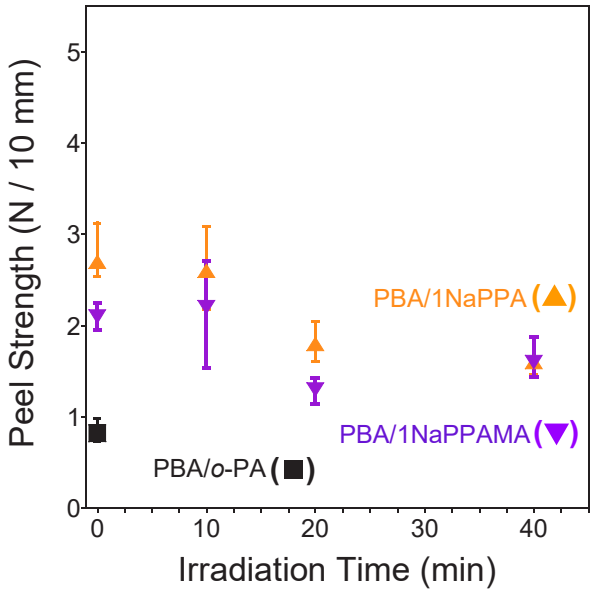

Fig. 3. Peel strength changes of polymer blend films on irradiation. BA unit : *o*-PA unit = 1 : 0.2 (mol/mol). Symbols in error bars indicate the averaged values of 3 runs.

strength was 0.6 N as low as PBA, suggesting that too much PPA fraction caused the copolymer harder as a PSA.

On irradiation of 1NaPPAMA$_{0.21}$-BA, peel strengths increased from 3.5 to 4.5 N, and the strength decreased on irradiation for 60 min. Similar trend is observed for 1NaPPAMA$_{0.05}$-BA, where the peel strength once increased on 10 min irradiation and then decreased. Considering that the photo-induced depolymerization of 1NaPPA films proceeded on irradiation for 15 min or above [6], it is expected that photo-degradation of PPA chains in copolymers also proceeds with similar irradiation time. Thus, the increase in peel strength for both copolymers will correspond to the depolymerization of PPA side-chains, although the reason is unknown at present.

Longer time irradiation caused the decrease in peel strength for both copolymers, which would be due to the disappearance of hard PPA segments as shown in Fig. 2. The degradation of BA main-chains might contribute the decrease, because the slight decrease is often observed for PBA in the previous [29] and present study.

Films of 1NaPPAMA$_{0.61}$-BA did not show the increase in the peel strength. This result suggests that too much PPA side-chains in 1NaPPAMA$_{0.61}$-BA made the matrix glassy to detect the changes of peel strength.

In order to clarify the effect of covalent bonding of PPA chains and BA chains, we investigated the peel strengths of PSAs composed of PBA/1NaPPA and PBA/1NaPPAMA polymer blends with the same ratio of BA to *o*-PA units as

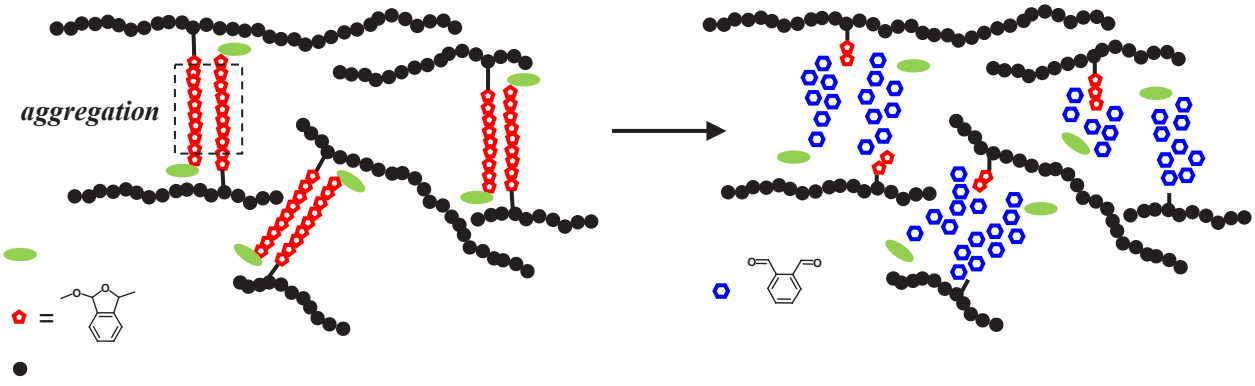

Fig. 2. Schematic illustration of photo-degradation of 1NaPPAMA-BA copolymers.

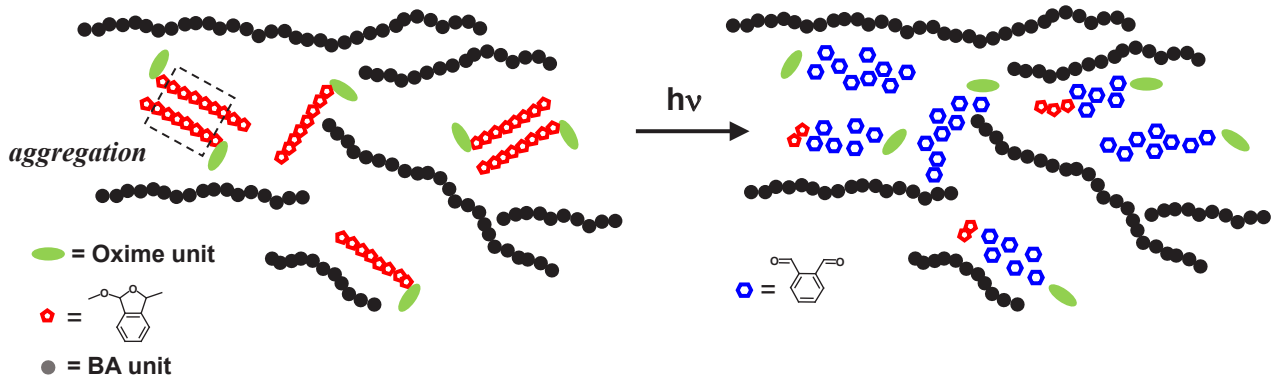

Fig. 4. Schematic illustration of photo-degradation of polymer blends.

that in 1NaPPAMA$_{0.21}$-BA. Figure 3 shows the changes of peel strength of the polymer blends. The initial peel strengths of PBA/*o*-PA, PBA/1NaPPA, and PBA/1NaPPAMA were 0.8, 2.1, and 2.6 N, respectively, located between those of 1NaPPAMA$_{0.21}$-BA and PBA. It was considered that these results were caused by the increase of hard segment in PSA matrixes.

On irradiation, the peel strengths for both PSAs gradually decreased with an increase in irradiation time and got closer to the value of PBA/*o*-PA, 0.8 N. This trend was different from those of 1NaPPAMA$_{0.21}$-BA and 1NaPPAMA$_{0.05}$-BA films as illustrated in Fig. 4.

Failure modes of the PSAs are consistent with this assumption. For copolymers 1NaPPAMA$_{0.21}$-BA, interfacial mode was preferential, although 1NaPPAMA$_{0.05}$-BA and blended polymers detached with cohesive mode. These behaviors did not change before and after irradiation for all coated films.

In conclusion, we have prepared a macromonomer 1NaPPAMA and its copolymers with BA, and investigated the peel strength changes on irradiation to evaluate their pressure-sensitive adhesive properties. Higher peel strengths were observed for copolymers than those of corresponding polymer blends. As an increase in irradiation time, the strength generally decreased, although once increased for 1NaPPAMA$_{0.21}$-BA and 1NaPPAMA$_{0.05}$-BA copolymer films at the early stage. These results suggest that the introduction and the depolymerization of PPA side-chains caused drastic changes in adhesive properties.

Acknowledgements

This work was supported by Ogasawara Foundation. The authors also thank to Dr. Akiko Nakahashi of ORIST for SEC analysis.

References

1. H. Ito and C. G. Willson, *Polym. Eng. Sci*., **23** (1983) 1012.
2. F. Wang and C. E. Diesendruck, *Macromol. Rapid Commun.*, **39** (2018) 1700519.
3. R. E. Yardley, A. R. Kenaree, and E. R. Gillies, *Macromolecules*, **52** (2019) 6342.
4. J. P. Lutz, O. Davydovich, M. D. Hannigan, J. S. Moore, P. M. Zimmerman, and A. J. McNeil, *J. Am. Chem. Soc*., **141** (2019) 14544.
5. V. Eriksson, M. A. Trojer, S. Vavra. M. Hulander, and L. Nordstierna, *J. Colloid Interface Sci.*, 579 (2020) 645.
6. H. Hayashi, H. Tachi, and K. Suyama, *J. Photopolym. Sci. Technol*., **33** (2020) 269.
7. E. P. Chang, *J. Adhes.*, **34** (1991) 189.
8. I. Benedek, "Development and Manufacture of Pressure-Sensitive Products", Marcel Dekker, New York (1998).
9. I. Benedek and M. M. Feldstein Ed., "Fundamentals of Pressure Sensitivity", CRC Press, Boca Raton, Florida (2008).
10. M. M. Feldstein, E. E. Dormidontova, and A. R. Khokhlov, *Prog. Polym. Sci*., **42** (2015) 79.
11. S. Mapari, S. Mestry, and S. T. Mhaske, *Polym. Bull*., (2020) DOI: 10.1007/s00289-020-03305-1.
12. R. Li, J. A. T. Loontjens, and Z. Shan, *Eur. Polym. J.*, **112** (2019) 423.
13. V. G.-Pacios, Y. Iwata, M. Colera, and J. M. M.-Martínez, *Int. J. Adhes. Adhes.*, **31** (2011) 787.
14. M. K. Shamsabadi and M. R. Moghbeli, *Int. J. Adhes. Adhes.*, **78** (2017) 155.
15. Z. Dastjerdi, E. D. Cranston, and M. A. Dubé,

Int. J. Adhes. Adhes., **81** (2018) 36.
16. S. Yamaguchi, S. Tabuchi, S. Kawahara, and H. Murakami, *Chem. Lett.*, **45** (2016) 463.
17. S. Yamaguchi, R. Nakanishi, M. Nanchi, S. Kawahara, and H. Murakami, *Chem. Lett.*, **47** (2018) 344.
18. Y. Wang, F. Weng, J. Li, L. Lai, W. Yu, S. J. Severtson, and W.-J. Wang, *ACS Omega*, **3** (2018) 6945.
19. C. Fang and Z. Lin, *Int. J. Adhes. Adhes.*, **61** (2015) 1.
20. C. Fang, Y. Jing, Y. Zong, and Z. Lin, *J. Adhes. Sci. Technol*., **31** (2017) 858.
21. Y. Wang, K. Jia, C. Xiang, J. Yang, X. Yao, and Z. Suo, *ACS Appl. Mater. Interfaces*, **11** (2019) 40749.
22. E. S. Kim, D. B. Song, K. H. Choi, J. H. Lee, D. H. Suh, and W. J. Choi, *J. Polym. Sci.*, **58** (2020) 3358.
23. R. Vendamme, N. Schüwer, and W. Eevers, *J. Appl. Polym. Sci*., **131** (2014) 40669.
24. Q. Chen, Q. Yang, P. Gao, B. Chi, J. Nie, and Y. He, *Ind. Eng. Chem. Res.*, **58** (2019) 2970.
25. P. Hao, T. Zhao, L. Wang, S. Liu, E. Tang, and X. Xu, *Prog. Org. Coat.*, **137** (2019) 105281.
26. M. Koike, M. Aizawa, N. Akamatsu, A. Shishido, Y. Matsuzawa, and T. Yamamoto, *Bull. Chem. Soc. Jpn.*, **93** (2020) 1588.
27. G.-S. Shim, J.-S. Kim, J.-H. Back, S.-W. Jang, J.-W. Park, H.-J. Kim, J.-S. Choi, and J.-S. Yeom, *Int. J. Adhes. Adhes.*, **96** (2020) 102445.
28. P. Bednarczyk, K. Mozelewska, and Z. Czech, *Int. J. Adhes. Adhes.*, **102** (2020) 102652.
29. K. Suyama and H. Tachi, *J. Photopolym. Sci. Technol.*, **28** (2015) 45.

Communication

Journal of Photopolymer Science and Technology
Volume 34, Number 3 (2021) 225−230 ©2021SPST

Fabrication of Diffractive Waveplates by Scanning Wave Photopolymerization with Digital Light Processor

Hirona Nakamura[1,2], Yoshiaki Kobayashi[1,2], Megumi Ota[1], Miho Aizawa[3], Shoichi Kubo[1,2], and Atsushi Shishido[1,2*]

[1] Laboratory for Chemistry and Life Science, Institute of Innovative Research, Tokyo Institute of Technology, Yokohama 226-8503, Japan
[2] Department of Chemical Science and Engineering, School of Materials and Chemical Technology, Tokyo Institute of Technology, Meguro, Tokyo 152-8552, Japan
[3] Research Institute for Sustainable Chemistry, National Institute of Advanced Industrial Science and Technology, Tsukuba, Ibaraki 305-8565, Japan
**ashishid@res.titech.ac.jp*

Liquid-crystalline materials with precise molecular orientation patterns have attracted much attention due to their potential application to diffractive waveplates by utilizing their optical anisotropy. However, even by the most sophisticated photoalignment processes, the control of large-area molecular orientation patterns remains a challenge due to the need of a fine spatial control of polarization state of incident light or light interference. Recently, we have developed a photoalignment method based on a novel concept of scanning wave photopolymerization (SWaP) that enables us to control arbitrary two-dimensional orientation patterns without polarized light. Here, we demonstrate the fabrication of LC polymer films with a cycloidal molecular orientation over a large area by SWaP with a digital light processor, and investigate their unique optical property of the resultant film as a cycloidal diffractive waveplate. SWaP could be an excellent method to provide a new pathway for designing high-performance optical devices.

Keywords: Photopolymerization, Molecular orientation, Liquid crystal

1. Introduction

Manipulation of polarization, intensity, and shape of a laser beam is key for functionalizing various optical devices. So far, large and complex optical components are required to fabricate optical systems to manipulate laser beams. Diffractive waveplates (DWs) with both functions of diffraction and polarization conversion are promising to replace such complicated optical systems. DWs are thin films composed of liquid-crystalline (LC) materials [1]. Since the diffraction behavior of DWs is governed by the birefringence of aligned LCs with patterned molecular orientation, fine and precise control of molecular orientation is essential to achieve desired optical performance. As the simplest example of such an optical modulation, one-dimensionally aligned LCs can rotate the polarization direction of a linearly polarized incident beam as a half-wave plate when the retardation matches half wavelength of the incident light. Furthermore, two-dimensional (2D) control of molecular patterns allows us to develop optical elements having various functions [2–4]. In particular, the LC films with cycloidal molecular pattern act as cycloidal diffractive waveplates (CDWs), which selectively diffract the circularly polarized incident light depending on its cycloidal pattern [5–7]. Due to these properties, CDWs have the potential to open windows for applications, i.e. next-generation projection displays.

The CDWs are generally fabricated by the polarization holographic technique based on photoalignment processes. In this technique, the interference of two coherent writing beams with orthogonal polarizations induces highly precise complex 2D orientation patterns [8–11]. However,

Received March 31, 2021
Accepted April 25, 2021

there remain fundamental challenges in the existing methods including low processability, necessity of polarized laser beams, and difficulty of large-area patterning. In photoalignment methods, inducing molecular orientation requires axis selective photoresponsive dye molecules [12–15]. In addition to the need of specific molecules, the irradiation area to generate polarization patterns in the holographic technique based on interfering beams is limited to the size of a few millimeters [16]. Thus, the conventional method takes much time to generate cycloidal molecular orientation patterns over a large area owing to the necessity of the extremely precise control of the polarization direction.

Recently, we have developed a single-step and dye-free photoalignment process based on a novel concept of scanning wave photopolymerization (SWaP), which enables to easily induce macroscopic and complicated molecular orientation without polarized light [17–23]. Spatiotemporal photopolymerization generates chemical potential gradient between irradiated and unirradiated regions, resulting in a molecular diffusion. The diffusion triggers molecular flow that allows one to align molecules along the flow direction. Thus, SWaP can induce a large-area and complicated orientation pattern in a single step without dyes nor polarized light. We have successfully controlled 2D molecular orientation and fabricated CDWs with a size of 4.4 mm × 2.5 mm by SWaP in the previous work [24]. In this paper, we demonstrate that the fabrication of LC films with cycloidal molecular orientation with a size of 10 mm × 5.6 mm is achieved. Furthermore, we investigate the optical properties of the obtained CDWs.

2. Experimental

Figure 1 shows chemical structures of the materials used in this study. The photopolymerizable monomer, 4′-[6-(acryloyloxy)hexyloxy]-4-cyanobiphenyl (A6CB), was employed as previously reported [15]. The crosslinker, 1,6-bis(methacryloyloxy)hexane (HDDMA), was purchased from Tokyo Chemical Industry Co., Ltd., Tokyo, Japan. The product was washed with a 5-wt% aqueous sodium hydroxide solution, dried over anhydrous magnesium sulfate, and then obtained by filtration. The photoinitiator, Irgacure 651, was purchased from Tokyo Chemical Industry Co., Ltd., Tokyo, Japan, and used without further purification.

The glass cell was prepared by adhering

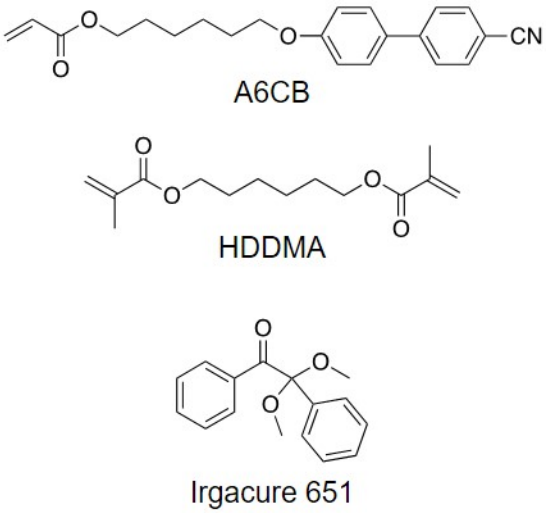

Fig. 1. Chemical structures used in this study.

ultrasonically cleaned two glass substrates (25 mm × 15 mm) with glue including 2-μm-thick silica spacers (Thermo Scientific, 9000 series). The thickness of the obtained cell was approximately 3 μm according to the evaluation by UV-vis spectroscopy. The photopolymerizable mixture of A6CB, HDDMA, and Irgacure 651 with a molar

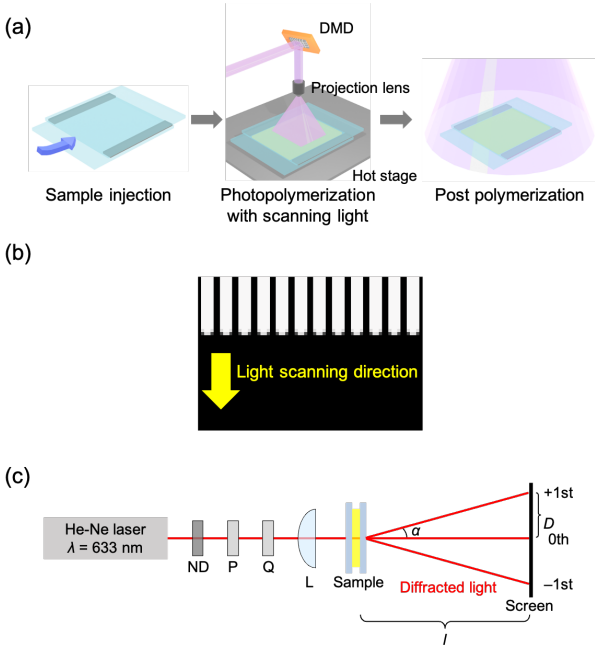

Fig. 2. (a) Schematic illustrations of the fabrication of a polymer film by SWaP with a digital light processor (DLP). (b) The UV pattern with the periodically arranged rod-shape (width of each rod: 20.9 μm). The size of the whole area irradiated by UV light was 10 mm × 5.6 mm. The yellow arrow shows the light scanning direction. (c) Schematic illustration of the optical setup to evaluate the diffraction property of the resultant film. ND: Neutral density filter; P: Polarizer; Q: Quarter-wave plate; L: Plano-convex lens (f = 150 mm); S: Sample.

ratio of 97:3:1. The mixture was injected into the glass cell at its isotropic temperature (150 °C), and then cooled down to photopolymerization temperature (100 °C), at which the resultant polymer exhibits a nematic phase. Photopolymerization was conducted with UV-DLP (digital light processor, MiLSS irradiator, ASKA COMPANY, MLS-DIR-LC65365) composed of a UV light source (λ_{max}, 369 nm) equipped with a digital micromirror device (DMD; number of pixels, 1920 × 1080; size of each pixel, 7.56 μm) (Fig. 2a). The size of the irradiated area was 10 mm × 5.6 mm according to the measurements by a beam profiler (OPHIR-SPIRICON, SP620). The glass cell was irradiated with the UV light by scanning the periodic rod-shape patterns with a rod width of 20.9 μm (Fig. 2b). The light intensity was optimized to be 10 mW/cm^2. Finally, the film was irradiated with UV light (λ_{max}, 365 nm; light intensity, 5 mW/cm^2) to fix the induced molecular orientation.

The diffraction property of the resultant film was measured with the optical setup as shown in Fig. 2c. A right- or left-circularly polarized beam was obtained from a He-Ne laser (λ = 633 nm) by adjusting the angles of the quarter-wave plate and polarizer. Evaluating diffraction angle of the beam, we calculated the lattice period (Λ) from the following equations:

$$\alpha = \arctan\left(\frac{D}{l}\right) \quad (1)$$

$$\Lambda = \frac{m\lambda}{\sin\alpha} \quad (2)$$

where α denotes the diffraction angle, D the distance between the 0th and 1st order diffracted beams that appeared on the screen, l the distance between the sample and the screen, m the diffraction order, λ a wavelength of incident light. To quantitatively evaluate the diffraction behavior of cycloidal orientation patterns in the film, we calculated the diffraction efficiency (η) by the following equation:

$$\eta = \frac{I_n}{I} \times 100 \quad (3)$$

where I and I_n are defined as the intensity of the incident beam and n-th order diffracted beam passing through the film, respectively. The light intensity was measured with an optical power meter.

3. Results and discussion

The sample mixture was irradiated with various patterns by scanning UV light to induce uniform cycloidal molecular orientation by SWaP. We employed four types of UV patterns (Λ = 26.1, 31.3, 36.6, 41.8 μm) with unirradiated widths of 5.2 μm, 10.4 μm, 15.7 μm and 20.9 μm, respectively, keeping the irradiated rod-shaped area with a width of 20.9 μm. By using these designed UV patterns, the films ($Cyc_{26.1}$, $Cyc_{31.3}$, $Cyc_{36.6}$, $Cyc_{41.8}$) were fabricated by SWaP with the light scanning rate of 15 μm/s. The polarized optical microscope (POM) images of the obtained films showed different textures depending on the periodicity of UV patterns (Fig. 3). The $Cyc_{31.3}$ and $Cyc_{36.6}$ films clearly showed a grating structure, and each periodicity was consistent with that of the designed optical patterns (Fig. 3b,c). The grating vector was perpendicular to the light scanning direction. On the other hand, the POM images of $Cyc_{26.1}$ and $Cyc_{41.8}$ films showed obscure grating structure (Fig. 3a,d). The POM observation with a tint plate (R = 530 nm) was carried out to evaluate the molecular orientation in the grating structures of $Cyc_{31.3}$ and $Cyc_{36.6}$ films. The additive and subtractive colors periodically appeared. The ratio of additive-colored area to

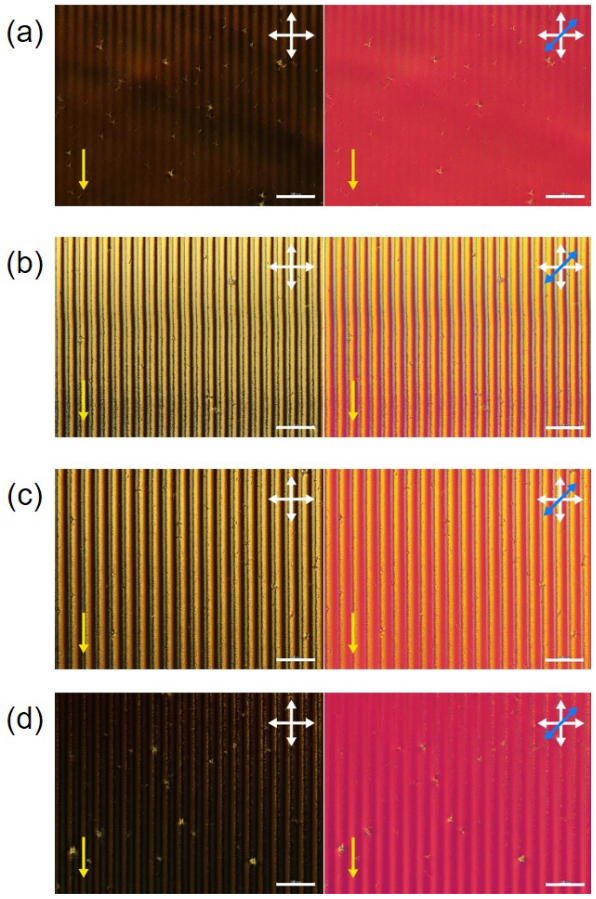

Fig. 3. Polarized optical micrographs of $Cyc_{26.1}$ (a), $Cyc_{31.3}$ (b), $Cyc_{36.6}$ (c), $Cyc_{41.8}$ (d). The left and right columns show the images observed with and without a tint plate, respectively. Scale bars, 100 μm.

subtractive-colored area in the patterns in $Cyc_{31.3}$ and $Cyc_{36.6}$ films resulted in 0.79 and 0.67, respectively. The ratio should be 1 if the cycloidal molecular orientation is perfectly symmetric to the irradiated rod-shape patterns. The $Cyc_{31.3}$ film showed a larger value, indicating that the unirradiated area width of 10.4 μm is more suitable to induce cycloidal orientation, probably due to the appropriate arc in the rod-shape pattern.

Effect of the scanning rate in SWaP on the cycloidal molecular orientation was examined to achieve high-performance CDWs. The sample was irradiated with the rod-shape pattern of $\Lambda = 31.3$ μm at scanning rates of 5, 10, 15, and 20 μm/s. The retardation of the obtained films was determined by POM equipped with both an interference filter (λ = 546 nm) and a Berek compensator. The retardation depended on the scanning rate, and showed the maximum value of 429 nm at a scanning rate of 15 μm/s as shown in Fig. 4. The scanning rate which has a relationship with exposure energy in SWaP affects a molecular flow. Thus, this result suggests that the most appropriate flow to direct precise cycloidal molecular orientation is induced under this condition.

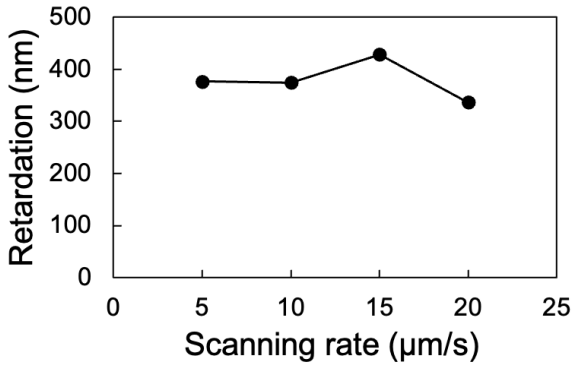

Fig. 4. Retardation of the $Cyc_{31.3}$ films as a function of scanning rate.

To evaluate the optical property of the induced cycloidal molecular orientation under optimized photopolymerization conditions, we investigated diffraction behavior of the He-Ne laser beam from the film. For this measurement, we prepared a film with a retardation of 340 nm, which is similar to the half wavelength of the He-Ne laser beam (λ = 633 nm). The film diffracted circularly polarized incident light in different directions depending on its handedness; the right- and left-circularly polarized light was diffracted on the +1st and –1st orders, respectively (Fig. 5). On the other hand, the linearly polarized incident light was diffracted in both directions. The lattice period calculated from

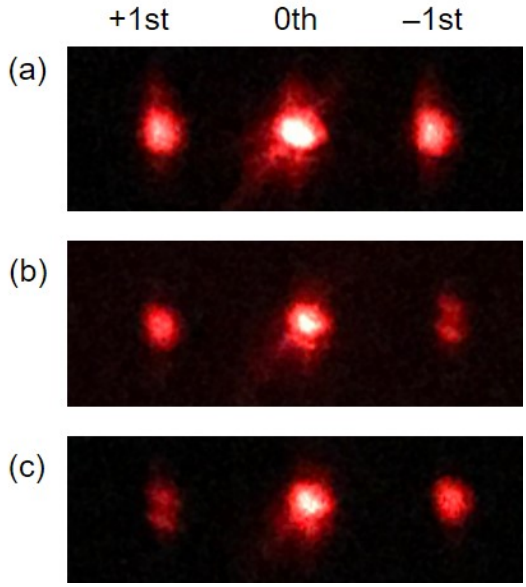

Fig. 5. Photographs of the diffraction pattern of the linearly (a), right-circularly (b), and left-circularly (c) polarized incident light passing through the obtained film on a screen.

Table 1. Diffraction efficiency of the $Cyc_{31.3}$ film.

	Diffraction efficiency (%)		
	+1st	0th	–1st
Linearly polarized light	9.8	53.6	11.0
Right-circularly polarized light	15.0	52.4	5.5
Left-circularly polarized light	4.7	55.1	14.9

the diffraction angle was 31.9 μm, which corresponds to the periodic cycloidal molecular orientation pattern (Λ = 31.3 μm). Diffraction efficiency of the $Cyc_{31.3}$ film with the retardation of 340 nm is summarized in Table 1. When the right-circularly polarized light was normally incident on the film, the +1st order diffraction showed the higher diffraction efficiency of 15.0% compared to the –1st order diffraction. The left-circularly polarized incident beam showered the opposite tendency; +1st and –1st order diffraction efficiencies were 4.7% and 14.9%, respectively.

The selective diffraction behavior of circularly polarized light implies that the fabricated LC polymer films function as a CDW. A conventional half-wave plate has orthogonal fast and slow axes to cause the retardation of incident light. In the case of the film with cycloidal molecular orientation, the fast and slow axes gradually rotate according to the molecular orientation. As a result, the light passing through the film has the spatial distribution of the phase of inverted circular polarization, leading to the selective +1st and –1st order diffraction depending on the handedness of the incident light

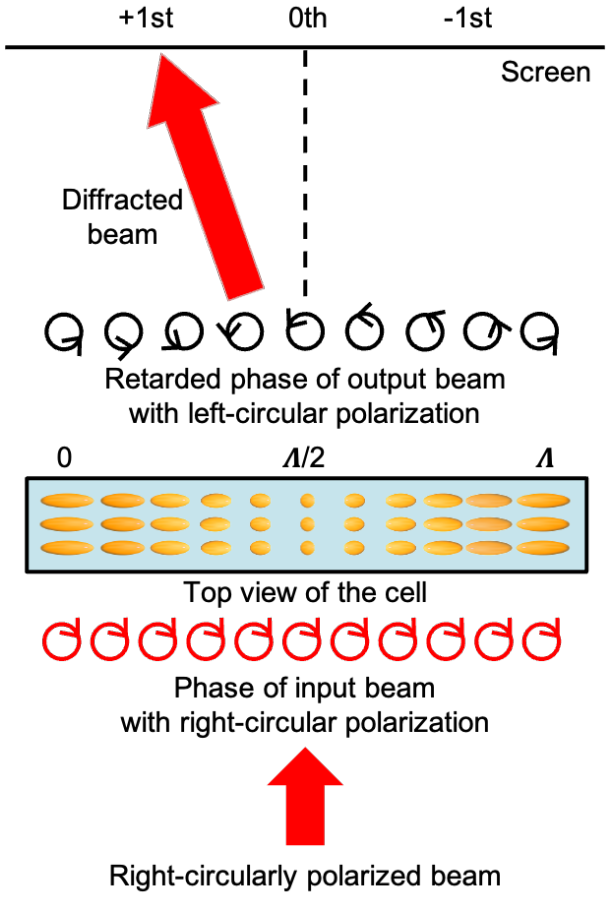

Fig. 6. Schematic illustration of the selective diffraction behavior of a right-circularly polarized beam incident on the film. Yellow ellipsoids represent the mesogenic units in the top view of the cell. Symbols indicate the polarization direction of each detected beam. Λ: grating period.

(Fig. 6). Considering linearly polarized light as integration of right- and left-circularly polarized light, both +1st and –1st order diffraction occurred equally.

4. Conclusion

In summary, we fabricated LC polymer films by SWaP under various light irradiation conditions and successfully obtained optically transparent films with the highly symmetric cycloidal molecular orientation over a large area. We optimized SWaP conditions; the uniform cycloidal molecular orientation was precisely prepared by irradiating the rod-shape patterns with a width of 20.9 μm and a distance of 10.4 μm at a scanning rate of 15 μm/s. The CDW fabricated by SWaP exhibited circular-polarization selective diffraction behavior, and right- and left-circularly polarized light was diffracted in different directions. We believe that SWaP provides a sophisticated way to fabricate next-generation photonic devices.

Acknowledgements

This work was supported by a Grant-in Aid for Scientific Research on Innovative Areas “Molecular Engine” (JSPS KAKENHI Grant Number JP18H05422). This work was supported by JST CREST Grant Number JPMJCR18I4, Japan. This work was performed under the Cooperative Research Program of “Network Joint Research Center for Materials and Devices”. This work was performed under the Research Program of “Dynamic Alliance for Open Innovation Bridging Human, Environment and Materials” in “Network Joint Research Center for Materials and Devices”.

References

1. S. R. Nersisyan, N. V. Tabiryan, D. M. Steeves, and B. R. Kimball, *Opt. Photon. News*, **21** (2010) 40.
2. G. P. Crawford, J. N. Eakin, M. D. Radcliffe, A. Callan-Jones, and R. A. Pelcovits, *J. Appl. Phys.*, **98** (2005) 123102.
3. J. Kim, Y. Li, M. N. Miskiewicz, C. Oh, M. W. Kudenov, and M. J. Escuti, *Optica*, **2** (2015) 958.
4. S. V. Serak, D. E. Roberts, J.-Y. Hwang, S. R. Nersisyan, N. V. Tabiryan, T. J. Bunning, D. M. Steeves, and B. R. Kimball, *J. Opt. Soc. Am. B*, **34** (2017) B56.
5. H. Sarkissian, S. V. Serak, N. V. Tabiryan, L. B. Glebov, V. Rotar, and B. Y. Zeldovich, *Opt. Lett.*, **31** (2006) 2248.
6. C. Provenzano, P. Pagliusi, and G. Cipparrone, *Appl. Phys. Lett.*, **89** (2006) 121105.
7. H. Ono, A. Emoto, F. Takahashi, N. Kawatsuki, and T. Hasegawa, *J. Appl. Phys.*, **94** (2003) 1298.
8. T. Todorov, L. Nikolova, and N. Tomova, *Appl. Opt.*, **23** (1984) 4309.
9. L. Nikolova and P. S. Ramanujam, “Polarization Holography”, Cambridge University Press, (2009).
10. A. Shishido, *Polym. J.*, **42** (2010) 525.
11. T. Seki, *J. Mater. Chem. C*, **4** (2016) 7895.
12. V. G. Chigrinov, V. M. Kozenkov, and H.-S. Kwok, “Photoalignment of Liquid Crystalline Materials: Physics and Applications”, John Wiley & Sons, Inc., (2008).
13. O. Yaroshchuk and Y. Reznikov, *J. Mater. Chem.*, **22** (2012) 286.
14. T. Seki, S. Nagano, and M. Hara, Polymer, **54** (2013) 6053.
15. A. Priimagi, C. J. Barrett, and A. Shishido, *J. Mater. Chem. C*, **2** (2014) 7155.
16. M. Häckel, L. Kador, D. Kropp, and H.-W.

Schmidt, *Adv. Mater.*, **19** (2007) 227.
17. K. Hisano, Y. Kurata, M. Aizawa, M. Ishizu, T. Sasaki, and A. Shishido, *Appl. Phys. Express*, **9** (2016) 072601.
18. K. Hisano, M. Aizawa, M. Ishizu, Y. Kurata, W. Nakano, N. Akamatsu, C. J. Barrett, and A. Shishido, *Sci. Adv.*, **3** (2017) e1701610.
19. M. Aizawa, K. Hisano, M. Ishizu, N. Akamatsu, C. J. Barrett, and A. Shishido, *Polym. J.*, **50** (2018) 753.
20. M. Ishizu, M. Aizawa, N. Akamatsu, K. Hisano, S. Fujikawa, C. J. Barrett, and A. Shishido, *Appl. Phys. Express*, **12** (2019) 041004.
21. M. Aizawa, M. Ota, K. Hisano, N. Akamatsu, T. Sasaki, C. J. Barrett, and A. Shishido, *J. Opt. Soc. Am. B*, **36** (2019) D47.
22. S. Hashimoto, M. Aizawa, N. Akamatsu, T. Sasaki, and A. Shishido, *Liq. Cryst.*, **46** (2019) 1995.
23. Y. Kobayashi, R. Taguchi, N. Akamatsu, and A. Shishido, *J. Photopolym. Sci. Technol.*, **33** (2020) 291.
24. K. Hisano, M. Ota, M. Aizawa, N. Akamatsu, C. J. Barrett, and A. Shishido, *J. Opt. Soc. Am. B*, **36** (2019) D112.

Journal of Photopolymer Science and Technology
Volume 34, Number 3 (2021) 231−236 ©2021SPST

Control of Radical Polymerization and Cationic Polymerization in Photocurable Resin for 3D Printers

Kotaro Kobayashi[1], Hirohumi Takamatsu[1], Tatsuo Taniguchi[1], Hiroaki Okamoto[2 *], and Takashi Karatsu[1,3 **]

[1] Department of Applied Chemistry and Biotechnology, Graduate School of Engineering, Chiba University, 1-33 Yayoi-cho, Inage-ku, Chiba-shi, Chiba 263-8522, Japan
[2] Okamoto Chemical Industry Co., Ltd., 2-6-4 Chuo, Warabi-shi, Saitama 335-0004, Japan
[3] Molecular Chirality Research Center, Chiba University, 1-33 Yayoi-cho, Inage-ku, Chiba-shi, Chiba 263-8522, Japan
** okamoto@okachemi.com, **karatsu@faculty.chiba-u.jp*

Stereolithography 3D printers mainly use acrylic or epoxy monomers, or a mixture of these monomers. High-definition and smooth modeling is possible; however, the product is vulnerable to impact. These products are generally photopolymerized by irradiation with light of a single wavelength to obtain a cured product. In this study, radical polymerization and cationic polymerization were polymerized stepwise using initiators with different absorption wavelengths for acrylic and epoxy monomers, and stepwise irradiation with the corresponding light. The impact resistance was compared between a product cured by irradiation with only a single wavelength and the cured product obtained by stepwise irradiation.

Keywords: 3D printer, Stereolithography, Acrylic monomer, Epoxy monomer, Interpenetrating polymer network

1. Introduction

The three-dimensional (3D) printer (additive manufacturing; AM) produces a 3D object by stacking 2D layers based on data designed by computer aided design (CAD). Stereolithography (SLA) is one modeling method for 3D printers, in which a photocurable resin is irradiated with light to cure the resin and form a 3D object. High-definition solids can be created with high modeling speed, although these solids are vulnerable to impact [1-4]. Acrylic or epoxy monomers are used in SLA as resin components. Acrylic monomers make the model hard and have a fast reaction rate; however, the model is vulnerable to impact [5,6]. On the other

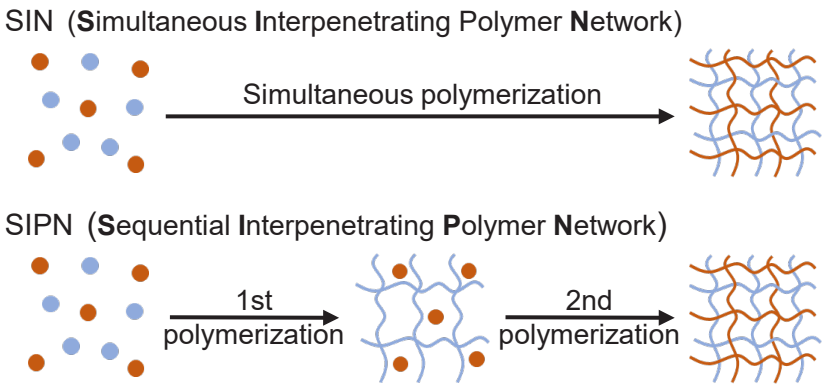

Fig. 1. Typical methods used to produce IPNs.

Received March 31, 2021
Accepted April 25, 2021

hand, epoxy monomers have a slow reaction rate, but the resultant model is flexible and strong against impact [2,7]. A mixture of these monomers is also frequently used [8-11]; an interpenetrating polymer network (IPN) can be formed by mixing these monomers, which compensates for the mutual disadvantages of reaction rate and impact resistance [12-16]. Typical methods to produce IPN are SIN and SIPN (Fig. 1) [15,16]. In SLA, the resin is generally cured only at a single wavelength of light, and an IPN is formed by SIN during curing of the resin.

In this work, radical polymerization and cationic polymerization were controlled using initiators and the irradiation wavelength with an aim of forming an IPN by SIPN. Initiators with different absorption wavelengths for radical polymerization and cationic polymerization were used to stepwise form an IPN by SIPN at the corresponding wavelengths. The impact resistance of a cured product obtained by irradiation with only a single wavelength and the cured product obtained in this study were compared.

2. Experimental

Dipentaerythritol hexaacrylate (**DPHA**; Daicel-Allnex Ltd.) and triethyleneglycol dimethacrylate (**TEGDM**; Kyoeisha Chemical Co., Ltd.) were used as the acrylic monomers. Sorbitol polyglycidylether (**SR-SEP**; Sakamoto Yakuhin Kogyo Co., Ltd.) was used as the epoxy monomer. 3-Ethyl-3-hydroxymethyl oxetane (**ETERNACOLL EHO**; Ube Industries, Ltd.) was used as the curing accelerator for the epoxy monomer. The photo-radical initiator 1-hydroxycycrohexyl phenyl ketone (**HCPK**; IGM Resins) and the photocationic initiator diphenyl [4-(phenylthio)phenyl]sulfonium hexafluorophosphate (**CPI-100P**, 50 wt% propylene carbonate solution, San-Apro Ltd.) were used as initiators that are cured under irradiation at 365 nm [17,18]. All reagents were used as-received. 1-Phenyl-1,2-propanedione (**PPD**; Tokyo Chemical Industry Co., Ltd.) was also used as-received as a photoradical initiator that is cured under irradiation at 405 nm [19].

As a radical polymerization monomer system, DPHA and TEGDM were mixed in a ratio of 96:4 (w/w), and this mixture was used as the radical polymerization monomer. As a cationic polymerization monomer system, SR-SEP and oxetane were mixed at a ratio of 7:4 (w/w), and this mixture was used as the cationic polymerization monomer. A 1:1 (w/w) mixture of the radical polymerization monomer and the cationic polymerization monomer was used as the monomer solution [20].

For simultaneous polymerization, the radical and cationic polymerization monomers were cured at the same wavelength of 365 nm. HCPK, which has an absorption at 365 nm (26.5 M^{-1} cm^{-1}), was used as the radical initiator, and CPI-100P, which also exhibits absorption at 365 nm (89.8 M^{-1} cm^{-1}), was used as the cationic initiator. Stepwise polymerization of the radical and cationic polymerization monomers was conducted at different wavelengths of 405 nm and 365 nm. PPD, which has an absorption at 405 nm, was used as the radical initiator (33.5 M^{-1} cm^{-1}), and CPI-100P with absorption at 365 nm was used as the cationic initiator. In both methods, the radical initiator was mixed with the radical polymerization monomer at a ratio of 0.4 wt%, and the cationic initiator was mixed with the cationic polymerization monomer at ratios of 0.5, 1.0, 1.5, and 2.0 wt%. After stirring the monomer solution and various initiators at room temperature for 2 h under dark conditions, 700 μL of the mixed solution was placed in a silicon mold by a micropipette and irradiated with light.

For the simultaneous light irradiation procedure, a 365 nm LED lamp (ZUV-C30H, Omron) was used for 3 min light irradiation (initial curing), and then a 365 nm UV lamp (High Power UV Light, Nailio; 36 W) was used for 30 min light irradiation (complete curing) to produce a cured product. Two patterns of light irradiation for the stepwise polymerization procedure were compared: pattern I with irradiation by light at 365 nm (Omron LED) for 3 min for initial curing, followed by irradiation by light at 405 nm from a LED lamp (EL-3D-086, Elegoo; 25 W) for 8 min, and irradiation at 365 nm (Omron LED) for 7 min. The latter two steps were repeated once more, so that the sample was irradiated for a total of 33 min. On the other hand, in pattern II, the 405 nm LED lamp was first used for 3 min (initial curing), after which the 365 nm lamp (Omron LED) was used for 8 min, and the 405 nm LED lamp was again used for 7 min. The latter two steps were repeated once more, so that and the sample was irradiated for a total of 33 min. For both procedures, a cured product was obtained by light irradiation for 33 min, which included initial curing and complete curing.

As an evaluation method, impact resistance tests were conducted with a drill bit (61.4 g, 0.13 cm tip diameter) dropped onto the cured product. The impact resistance was evaluated from the drop height at which the cured product was cracked. The same sample was continuously used until it cracked.

The structure of the cured product was also observed using scanning electron microscopy (SEM; JEOL, JEOL-6510) and the conversion rate of the radical polymerization monomer was measured using Fourier transform infrared spectroscopy (FT-IR; JASCO, FT/IR-4100).

3. Results and discussion

3.1. Impact resistance

The resin was successfully cured in all irradiation patterns to obtain an elliptical columnar cured product. The size of the cured product was 3 cm on the major axis, 2 cm on the minor axis, and 0.2 cm thick.

Figure 2 shows the impact resistance when the resin was cured using only light at 365 nm. When the cationic initiator concentration was 1.0 wt%, the drop height to cracking was 80 cm (36.2 J/cm^2), which was the highest result in this pattern. The impact resistance decreased as the cationic initiator concentration increased. Figure 3 shows the impact resistance when both radical and cationic polymerization were conducted stepwise using light at 405 nm and 365 nm. In pattern I, with the first irradiation at 365 nm, the drop height to cracking was the highest at 55 cm (24.9 J/cm^2) when the cationic initiator concentration was 1.0 wt%. The impact resistance decreased as the cationic initiator concentration increased, as in the case of simultaneous polymerization using only light at 365 nm. However, in pattern II, with the first irradiation at 405 nm, the impact resistance improved as the cationic initiator concentration increased. The highest impact resistance was achieved when the cationic initiator concentration was 2.0 wt%; the drop height to cracking was 125 cm (56.6 J/cm^2). In pattern II, the impact resistance was significantly improved.

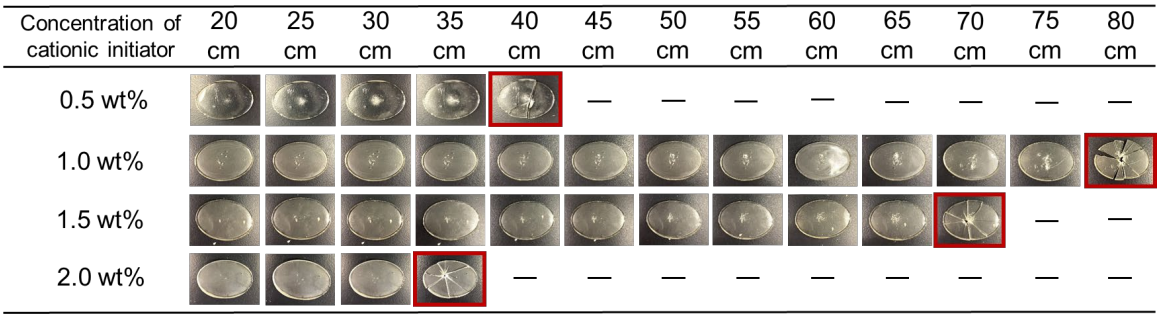

Fig. 2. Impact resistance for simultaneous polymerization.

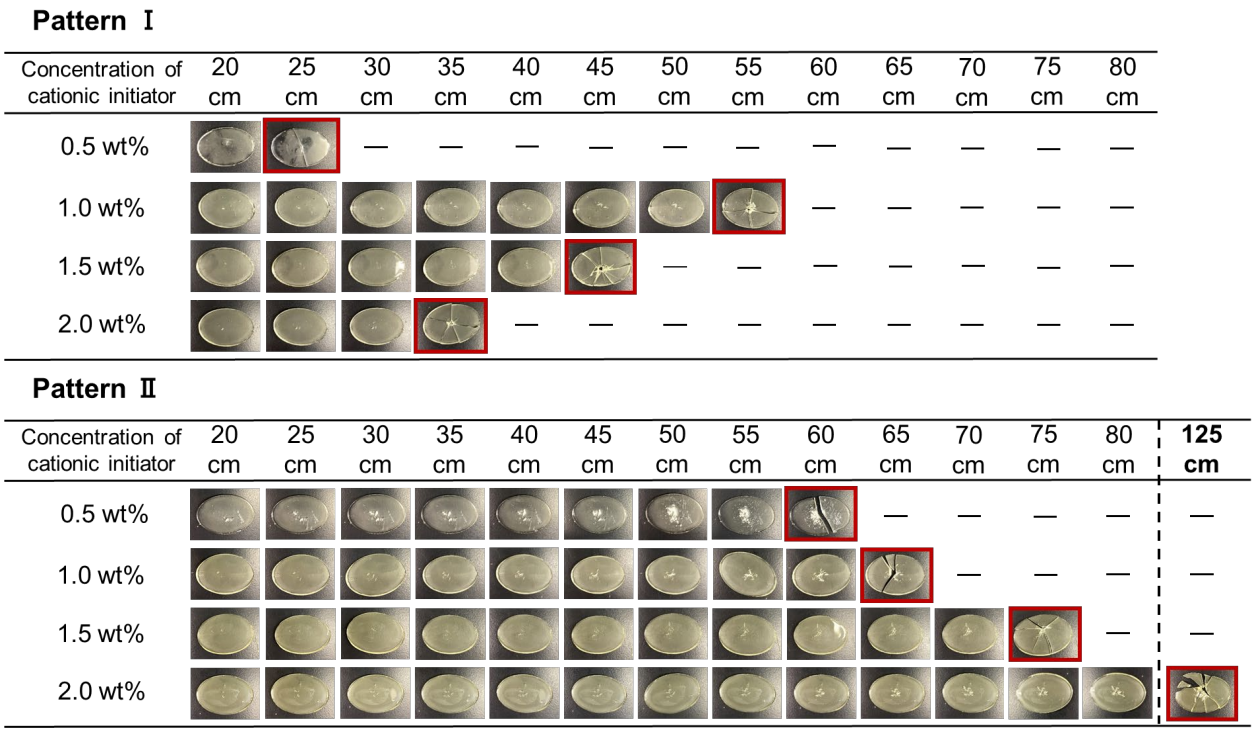

Fig. 3. Impact resistance for stepwise polymerization.

3.2. Structural observation using SEM

The cured product fragments were impregnated with a 10% sodium hydroxide aqueous solution for 7 days, so that the acrylic part was hydrolyzed by alkaline etching, and the structure was then observed using SEM. Figure 4 shows SEM images of each cured product. Even when radical polymerization and cationic polymerization were performed simultaneously or when the polymerization was stepwise, the cured products with excellent impact resistance had a surface with fine unevenness. In particular, for stepwise polymerization, pattern I with first irradiation at 365 nm resulted in a flat structure, whereas pattern II with first irradiation at 405 nm resulted in complicated and fine unevenness. For pattern II, the impact resistance improved as the cationic initiator concentration increased, which resulted in a finer and more complicated structure. Figure 5a shows an

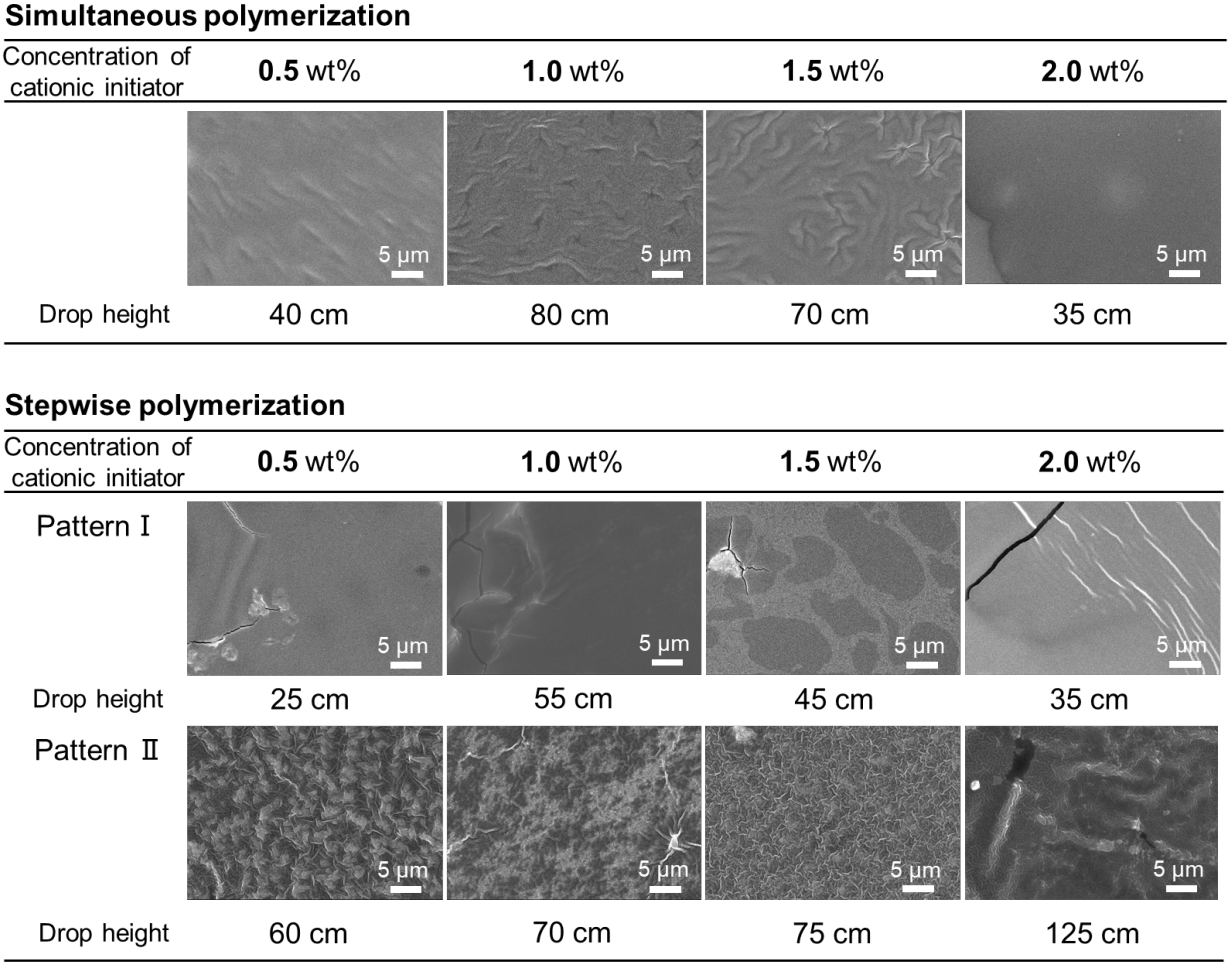

Fig. 4. SEM images of cured products.

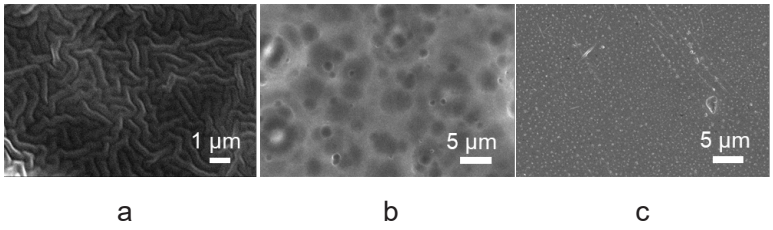

Fig. 5. SEM images for the products of (a) stepwise polymerization (pattern II, 2.0 wt% cationic initiator), (b) only the radical polymerization monomer, and (c) only the cationic polymerization monomer.

enlargement of the product formed with pattern II and a cationic initiator concentration of 2.0 wt%, which had the best impact resistance. The surface of this product has finer and more complicated unevenness. In addition, the structures of the resins that were stepwise cured with only the radical polymerization monomer and with only the cationic polymerization monomer had no fine unevenness (Figs. 5b and c), which suggests that the fine unevenness appears only when both of the monomers are mixed.

3.3. Monomer conversion

The conversion rate for the radical polymerization-based monomer was calculated from the FT-IR peak ratio at 1635 cm^{-1} before and after light irradiation. The conversion rate for the cationic polymerization monomer was not calculated because the peak of the epoxy group is 911 cm^{-1} in the fingerprint region. In this study, the conversion rate for the radical polymerization monomer for each irradiation pattern was measured for those samples with cationic initiator concentrations of 1.0 wt% and 2.0 wt%.

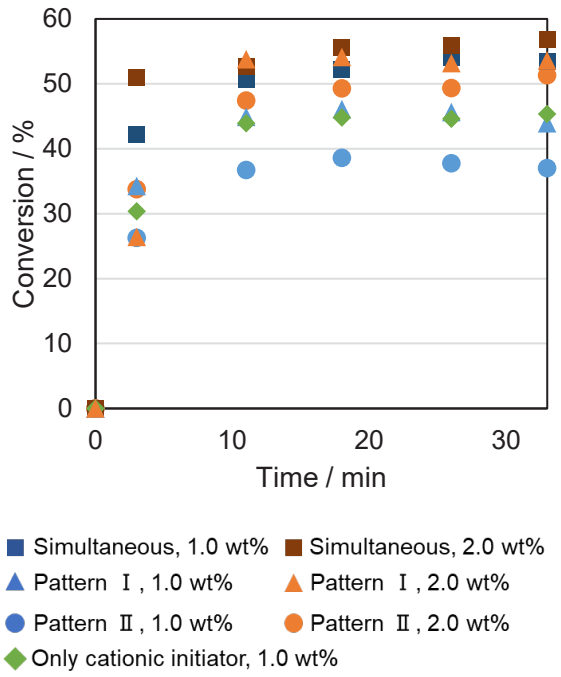

Fig. 6. Conversion rate for radical polymerization monomer.

Figure 6 shows the conversion rate for the radical polymerization monomer in each resin. The conversion rate did not change significantly after the first stage of complete curing (after the first 11 min). Therefore, we focused on this 11 min period. In this study, the cationic initiator concentration and the light irradiation pattern were changed, which are considered to cause a difference in the reactivity of the radical polymerization and cationic polymerization monomers.

When radical polymerization and cationic polymerization are performed stepwise, the reaction time for the cationic polymerization monomer for the first 11 min in pattern I is only 3 min during the initial curing. After irradiation for 3 min, only radical polymerization proceeds during irradiation at 405 nm for 8 min. Therefore, the radical polymerization monomer with a high reaction rate forms a polymer network before the cationic polymerization monomer (the epoxy monomer) with a low reaction rate. As a result, it is considered that the unreacted cationic polymerization monomer remains in the polymer network, and the impact resistance is decreased. On the other hand, in pattern II is where irradiation is conducted first at 405 nm, and then at 365 nm, during which the cationic polymerization monomer reacts for 8 min during the first 11 min; therefore, it is considered that the polymer network of the radical polymerization polymer was not completely formed by the initial curing at 405 nm, and each monomer reacted in the form of SIPN, which is the sequential introduction of the IPN. As a result, the impact resistance of the pattern II product was improved. In addition, the pattern II product had a structure with fine and complicated unevenness, as observed using SEM; therefore, it is considered that the product was generated by the complex entanglement of the polymer chains of both the radical and cationic polymerization monomers.

The reactivity of each monomer also changes depending on the concentration of the cationic initiator. In the simultaneous polymerization of the radical and cationic polymerization monomers, the impact resistance was the best when the cationic initiator concentration was 1.0 wt%, and the impact resistance decreased as the cationic initiator concentration increased. From Fig. 6, the conversion rate for the radical polymerization monomer during simultaneous polymerization was higher at the end of the initial curing when the cationic initiator concentration was 2.0 wt% than when it was 1.0 wt%. In addition, there was little change in the conversion rate after that. As the concentration of the cationic initiator increased, the initiation point of cationic polymerization increased and more cationic polymerization monomers react. However, radical polymerization proceeds due to

radicals generated during the cation formation process. From Fig. 6, radical polymerization proceeds, even with only the cationic initiator. Photochemical initiation of **CPI-100P** generates both radical and cationic species, therefore, when there is large amount of cationic initiator, radical polymerization also proceeds rapidly due to radicals generated from the cationic initiator. Vice versa, it is well known that radical initiator induces cationic polymerization under certain condition [21], however, we have no direct data such process might proceed. As a result, a network of the radical polymerization polymer is formed before the cationic polymerization monomer reacts, and the unreacted cationic polymerization monomer remains. Therefore, the impact resistance decreased when the cationic initiator concentration was 2.0 wt%. When the cationic initiator concentration was 1.0 wt%, the progress of radical polymerization and cationic polymerization was well-balanced and it is considered that the impact resistance was improved through the formation of the IPN by SIN.

In stepwise pattern I polymerization, when the concentration of the cationic initiator was high, radical polymerization proceeded by radicals generated from the cationic initiator during the initial curing at 365 nm, as in the case of simultaneous polymerization. Therefore, it did not form an IPN and had a flat structure, which was inferior in terms of impact resistance. In pattern II, the higher cationic initiator concentration resulted in more cationic polymerization initiation points, and it is considered that more cationic polymerization monomers and cationic initiator remained in the incomplete network formed by the initial curing, which reacted to form the IPN, which significantly improved the impact resistance.

4. Conclusion

A cured product with excellent impact resistance was produced by control of radical polymerization and cationic polymerization through the use of initiators and specific irradiation wavelengths. The impact resistance, structure, and monomer conversion rate changed depending on the light irradiation pattern and the concentration of the cationic initiator. The results suggested that the polymer chains are entwined more closely in the IPN formed by SIPN than in that formed by SIN, so that the impact resistance was improved.

Acknowledgements

This work was partly supported by the Strategic Priority Research Promotion Program (Chiral Materials Science) at Chiba University, and by the Five-star Alliance Research Program within NJRC Materials & Devices.

References

1. B. C. Gross, J. L. Erkal, S. Y. Lockwood, C. Chen, and D. M. Spence, *Anal. Chem.*, **86** (2014) 3240.
2. A. Bagheri and J. Jin, *ACS Appl. Polym. Mater.,* **1** (2019) 593
3. X. Wang, M. Jiang, Z. Zhou, J. Gou, and D. Hui, *Composites Part B,* **110** (2017) 442.
4. G. Postiglione, G Natale, G. Griffini, M. Levi, and S. Turri, *Polym. Compos.*, **38** (2017) 1662.
5. S. C. Ligon-Auer, M. Schwentenwein, C. Gorsche, J. Stampfl, and R. Liska, *Polym. Chem.*, **7** (2016) 257.
6. J. W. Kim, L. U. Kim, C. K. Kim, B. H. Cho, and O. Y. Kim, *Biomacromolecules*, **7** (2006) 154.
7. S. C. Ligon, R. Liska, J. Stampfl, M. Gurr, and R. Mülhaupt, *Chem. Rev.*, **117** (2017) 10212.
8. N. Ogane, E. Nakamoto, C. Homma, and Y. Daicho, Japan Patent JP2015-89932A.
9. E. Nakamoto, N. Ogane, and C. Homma, Japan Patent JP2014-234473A.
10. C. Decker, T. Nguyen Thi Viet, D. Decker, and E. Weber-Koehl, *Polymer*, **42** (2001) 5531.
11. P. Xiao, F. Dumur, M. Frigoli, M. Tehfe, B. Graff, J. P. Fouassier, D. Gigmes, and J. Lalevee, *Polym. Chem*., **4** (2013) 5440.
12. G. Griffini, M. Invernizzi, M. Levi, G. Natale, G. Postiglione, and, S. Turri, *Polymer*, **91** (2016) 174.
13. R. Yu, X. Yang, Y. Zhang, X. Zhao, X. Wu, T. Zhao, Y. Zhao, and W. Huang, *ACS Appl. Mater. Interfaces*, **9** (2017) 1820.
14. M. Invernizzi, G. Natale, M. Levi, S. Turri, and G. Griffini, *Materials*, **9** (2016) 583.
15. S. Tsunoda, *Sen'i Gakkaishi*, **48** (1992) 464 (in Japanese)
16. L. H. Sperling, *Adv. Chem.*, **239** (1991) 3.
17. F. Jasinski, P. B. Zetterlund, A. M. Braun, and A. Chemtob, *Prog. Polym. Sci.*, **84** (2018) 47.
18. J. V. Crivello and J. H. W. Lam, *J. Polym., Polym. Chem. Ed.,* **17** (1979) 977.
19. W. D. Cook and F. Chen, *J. Polym. Sci. Part A: Polym. Chem.*, **49** (2011) 5030.
20. H. Okamoto and M. Nakatsuka, Japan Patent JP2016-196597A.
21. M. A. Tasdelen, J. Lalevee, and Y. Yagci, *Polym. Chem.*, **11** (2020) 1111.

Journal of Photopolymer Science and Technology
Volume 34, Number 3 (2021) 237−249 ©2021SPST

Effect of Acrylic and Epoxy Hybrid Crosslinker on the Mechanical Strength of Photocurable Resin for 3D Printing

Miharu Ito[1], Hirofumi Takamatsu[1], Tatsuo Taniguchi[1], Hiroaki Okamoto[3*], and Takashi Karatsu[1,2 **]

[1] Department of Applied Chemistry and Biotechnology, Graduate School of Engineering, Chiba University, 1-33 Yayoi-cho, Inage-ku, Chiba 263-8522, Japan
[2] Okamoto Chemical Industry Co., Ltd., 2-6-4 Chuo, Warabi-shi, 335-0004, Japan
[3] Molecular Chirality Research Center, Chiba University, 1-33 Yayoi-cho, Inage-ku, Chiba, 263-8522, Japan
**okamoto@okachemi.com, **karatsu@faculty.chiba-u.jp*

In the acrylic and epoxy monomers copolymerization system, a hybrid crosslinking agent (CLA) with an acrylic group and an epoxy group at both ends of one molecule was added to a resin and cured photochemically. The hybrid CLA formed a crosslinked network between acrylic and epoxy polymer chains. The effect of this hybrid CLA on the mechanical strength of the resin was investigated. The results indicated that excellent impact resistance, acrylic monomer conversion rate, and heat resistance were obtained by the addition of a certain amount of the hybrid CLA to the resin. Furthermore, changes to the structure of the central skeleton of the hybrid CLA resulted in changes to the mechanical properties of the cured resin. When the internal structure of the cured resin with the hybrid CLA was observed using scanning electron microscopy, the structural texture indicated the formation of an interpenetrating polymer network (IPN)-like structure. This IPN structure could have a role in the improvement of the mechanical strength of the cured polymer.
Keywords: 3D printer, Stereolithography, Acrylic and Epoxy monomer, Hybrid crosslinker, Interpenetrating polymer network

1. Introduction

A 3D printer (additive manufacturing technology) is a machine that creates a 3D model by stacking 2D layers one-by-one based on 3D CAD design data. In recent years, 3D printers have not only been applied to the production of architectural models and trial production of 3D products, but also to the medical field [1] and the production of shoe soles with a grid-like skeleton, which was difficult with conventional manufacturing methods [2]. The price of 3D printers has fallen and modeling methods have become easier, so that home 3D printers have become widespread.

Stereolithography (SLA), a 3D printer modeling method, was developed in the late 1970s [3] and is the oldest 3D modeling method. SLA is typically used for businesses in rapid prototyping to evaluate shape.

The SLA modeling method is as follows (Fig. 1). A large container is filled with a photocurable resin solution, which is then scanned with a UV laser based on the 3D data. Only the surface of the laser irradiated portion is cured. By repeating laser irradiation while lowering the container platform, a 3D laminated object can be obtained. Only one layer (micrometer scale) is cured at a time and is very thin; therefore, it is possible to form high-definition and smooth surfaces [4]. By taking advantage of this feature, SLA is applied to photoresists [5] and dental materials [6]. Research on shape memory [7] and self-healing [8] materials is also in progress. The reaction of the monomer is not completed by only photocuring with a 3D printer; therefore, a post-curing process is required. In recent years, there have been reports of photocuring using different wavelengths in the post-curing process [9] and reports of post-curing by thermosetting [10]. However, thermosetting has a disadvantage in that

Received April 2, 2021
Accepted April 17, 2021

the strength of the modeled solid is relatively low, and the product eventually becomes hardened and brittle under natural light [11].

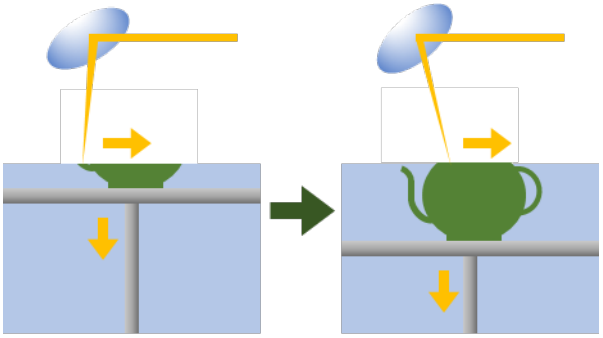

Fig. 1. Stereolithography apparatus (SLA).

One typical SLA method uses photocurable resin consisting of both radical polymerization and cationic polymerization materials (Fig. 2) [12,13]. A (meth)acrylic compound is commonly used for radical polymerization. While the polymerization rate is high and a hard solid can be obtained, the polymerization is inhibited by oxygen [14,15], and a solid that is vulnerable to impact can be obtained. Epoxy compounds are used for cationic polymerization, where although the polymerization rate is slower than that of radical polymerization, a flexible and impact-resistant solid can be obtained. 3-Membered ring oxiranes and 4-membered ring oxetane compounds are used for cationic polymerization. The oxirane ring compound has a relatively fast initiation reaction; however, it has a slow growth reaction and a small molecular weight of the polymerized polymer. In contrast, although the oxetane ring compound has a slow initiation reaction, pK_b, which indicates the strength of attack on the active terminal, is 3.1, and the growth reaction is rapid, which produces a polymer with a high molecular weight [16,17].

A 3D object formed by combining these materials compensates for the shortcomings of each, and a 3D object that has a high reaction speed, is hard, and has a certain degree of impact resistance is formed. However, the reaction progresses further due to natural light, which causes self-destruction, and the mechanical strength is still insufficient. Therefore, a solid modeled using SLA or material jetting is currently difficult to apply to the manufacture of final products [11].

A compound having an acrylic group and an epoxy group at both ends of one molecule is called a hybrid CLA. It was reported in recent years that a photocured solid prepared using glycidyl methacrylate (**GMA**) with a methacrylic group and an epoxy group as a hybrid CLA has excellent impact resistance as compared with a conventional solid [9]. The reason why a tougher resin could be produced is that the acrylic and epoxy polymers are intricately entwined in the resin; however, when a hybrid CLA is added, each polymer chain is chemically bonded. This is because a resin with a stronger connection is formed with adopts an interpenetrating polymer network (IPN) structure. Therefore, it is important to maintain a good mixing balance of the reaction components, i.e., the ratio of the radical polymerizable monomer, the cationic polymerizable monomer, and CLA to realize a tougher model.

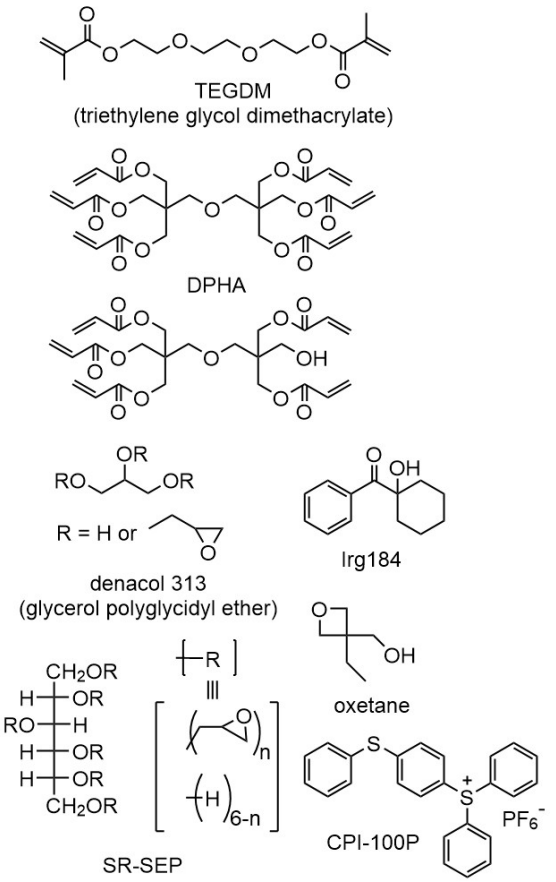

Fig. 2. Materials used for SLA.

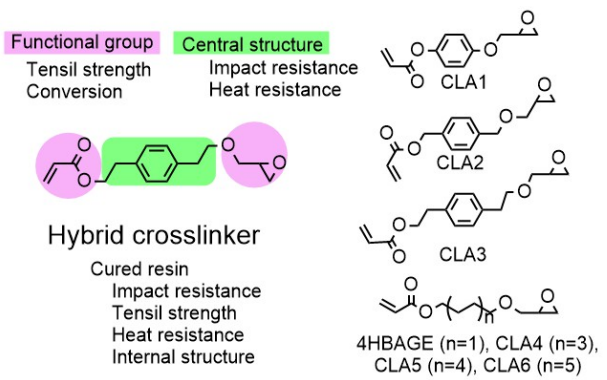

Fig. 3. Aim of this research and structure of the hybrid CLAs used.

In this study, two-step photocuring was performed using the same wavelength of 365 nm, i.e., no irradiation with different wavelengths or an increase in the number of thermosetting procedures. The purpose here was to develop a SLA material with the most suitable mixing ratio of acrylic and epoxy monomers for modeling. Commercially available 4-hydroxybutyl acrylate glycidyl ether (**4HBAGE**) was used as the hybrid CLA, where a butyl group was used as the central skeleton that connects the acrylic and epoxy groups to impart more flexibility than **GMA**. In addition, **CLA1**, **CLA2**, and **CLA3**, which have aromatic rings in the central skeleton, were used to impart rigidity within the molecule. **CLA4**, **CLA5**, and **CLA6** with extended alkyl chains in the central skeleton of **4HBAGE** were also used. The synthesized hybrid CLA was added to the resin and photocured, and the effects on the physical properties and mechanical strength were investigated (Fig. 3).

2. Experimental

2.1. Apparatus

Following apparatuses were used in this research, ^{1}H NMR; Bruker, DPX-300 (300 MHz) or AVANCE-III-400M (400 MHz), UV-LED light source; OMRON, ZUV-C30H (365 nm) and NAILIO, High power UV light (365 nm), FT-IR; JASCO, FT/IR-4100, SEM; JEOL, JEOL-6510, and TGA; SHIMADZU, DTG-60A equipped with FC-60A.

2.2. Reagents

Usual reagents were purchased from Kanto Chemical Co. Inc., TCI Co, Ltd., or MilliporeSigma Corp. Following special chemicals were obtained from the supplier written in a parenthesese, dipentaerythritol hexacrylate (**DPHA**, Daicel-allnex Ltd.), triethyleneglycol dimethacrylate (**TEGDM**, Light ester 3EG, Kyoeisha Chemical Co., Ltd.), d-glucitol, reaction products with epichlorohydrin (**SR-SEP**, Osaka Organic Chemical Ind. Ltd.), glycerol polyglycidyl ether (**Denacol 313**, Nagase ChemteX Corp.), 2-hydroxymethyl-2-ethyl-1-epoxy-propane (oxetane) (ETERNACOLL EHO, Ube Industries, Ltd.), 1-hydroxycycrohexyl phenyl ketone (**Irgacure 184**, IGM Resins), diphenyl[4-(phenylthio)-phenyl]sulfonium hexafluorophosphate (**CPI-100P**, San-Apro Ltd.), 4-hydroxybutyl acrylate glycidyl ether (**4HBAGE**, Mitsubishi Chemical Corp.).

2.3. Syntheses

For the preparation of crosslinkers, the corresponding α,ω-diol was allowed to react stepwise with 2-chloromethyloxirane and acryloyl chloride (Table 1).

2.3.1. 4-(Oxiran-2-ylmethoxy)phenol [18] (**OXOL1**)

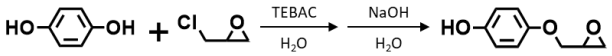

In a typical run, 1,4-dihydroxybenzene 16.53 g (0.15 mol), 2-chloromethyloxirane 13.89 g (0.15 mol) and benzyltriethylammonium chloride 1.71 g (0.0075 mol) were placed in a three-necked round flask. 20 mL of H_2O was then added and the flask was purged with nitrogen, and then held at 90 °C for 5 h while starring. 44 mL of 15 wt% NaOH aqueous solution was added to the mixture and vigorously stirred for 30 min. The reaction mixture was extracted with $CHCl_3$ and washed with brine and water, followed by drying with anhydrous sodium sulfate. The product was isolated by silica gel column chromatography (AcOEt:hexane = 2:1) to give a yellowish liquid (3.49 g, 14% yield).

OXOL1: ^{1}H NMR ($CDCl_3$, 300 MHz), δ ppm : 8.99 (s, 1H), 6.73 (d, J = 44.21 Hz, 4H), 4.19 (dd, J_1 = 11.26 Hz , J_2 = 2.66 Hz, 1H), 3.70 (dd , J_1 = 8.52 Hz , J_2 = 13.20 Hz, 1H), 3.31−3.25 (m, 1H), 2.82 (dd, J_1 = 4.73 Hz, J_2 = 4.73 Hz, 1H), 2.67 (dd, J_1 = 2.67 Hz , J_2 = 5.16 Hz, 1H).

2.3.2. 4-(Oxiran-2-ylmethoxy)phenyl acrylate [19] (**CLA1**)

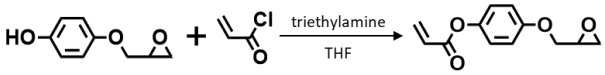

3.39 g of 4-(oxiran-2-ylmethoxy)phenol (20.4 mmol), 4.13 g of triethylamine (40.8 mmol), and 20 mL of tetrahydrofuran (THF) as a solvent were placed in a 50 mL three-necked round flask. The flask was purged with nitrogen and held at -40 °C. A solution of 1.85 g of acryloyl chloride (20.4 mmol) in 10 mL of THF was added to this solution over 20 min and then stirred for 2 h. The reaction mixture was extracted with AcOEt and washed with brine and water, and then dried with anhydrous sodium sulfate. The product was isolated by silica gel column chromatography (AcOEt:hexane = 1:2) to give a yellowish liquid (1.72 g, 39% yield).

CLA1: ^{1}H NMR ($CDCl_3$, 300 MHz): δ ppm : 7.05 (d, J = 6.46 Hz, 2H), 6.93 (d, J = 9.88 Hz, 2H), 6.60 (dd, J_1 = 17.29 Hz , J_2 = 1.16 Hz, 1H), 6.31 (dd, J_1 = 17.23 Hz, J_2 = 10.33 Hz, 1H), 6.01 (dd, J_1 = 10.38 Hz, J_2 = 1.29 Hz, 1H), 4.23 (dd , J_1 = 10.98 Hz , J_2 =

3.06 Hz, 1H), 3.94 (dd, J_1 = 11.02 Hz, J_2 = 5.72 Hz, 1H), 3.38−3.34 (m, 1H), 2.92 (dd, J_1 = 4.51 Hz, J_2 = 4.51 Hz, 1H), 2.77 (dd, J_1 = 4.89 Hz, J_2 = 2.64 Hz, 1H).

2.3.3. ^{1}H NMR data for other OXOLs and CLAs

(4-((Oxiran-2-ylmethoxy)methyl)phenyl)methanol (**OXOL2**)**:** ^{1}H NMR ($CDCl_3$, 300 MHz), δ ppm : 7.29 (dd, J = 8.97 Hz, 4H), 5.18 (dd, J = 5.60 Hz, 4H), 4.49 (dd, J = 5.62 Hz), 3.73 (dd, J_1 = 2.64 Hz, J_2 = 11.43 Hz, 1H), 3.27 (dd, J_1 = 6.42 Hz, J_2 = 11.46 Hz, 1H), 3.11−3.16 (m, 1H), 2.73 (dd, J = 2.73 Hz, 1H), 2.55 (dd, J_1 = 2.67 Hz , J_2 = 5.10 Hz, 1H).

4-(Oxiran-2-ylmethoxy)benzyl acrylate (**CLA2**) [19]: ^{1}H NMR ($CDCl_3$, 300 MHz): δppm : 7.36 (dd, J_1 = 8.38 Hz, J_2 = 13.17 Hz, 4H), 6.37 (dd, J_1 = 1.73 Hz, J_2 = 17.23 Hz, 1H), 6.23 (dd, J_1 = 10.11 Hz, J_2 = 17.28 Hz, 1H), 5.98 (dd, J_1 = 1.75 Hz, J_2 = 10.09 Hz, 1H), 5.18 (s, 1H), 4.52 (s, 1H), 3.75 (dd, J_1 = 2.56 Hz, J_2 = 11.42 Hz, 1H), 3.28 (dd, J_1 = 6.41 Hz , J_2 = 11.42 Hz, 1H), 3.12−3.17 (m, 1H), 2.73 (dd, J = 4.68 Hz , 1H), 2.55 (dd, J_1 = 2.70 Hz , J_2 = 5.10 Hz, 1H).

2-(4-(2-(Oxiran-2-ylmethoxy) ethyl)phenyl)ethanol (**OXOL3**) [18]: ^{1}H NMR ($CDCl_3$, 400 MHz), δ ppm : 6.85 (t, J = 9.43 Hz, 4H), 4.00−4.13 (m, 4H), 3.80−3.96 (m, 5H), 3.49 (dd, J_1 = 5.88 Hz, J_2 = 11.70 Hz, 1H), 3.17−3.22 (m, 1H), 2.81 (dd, J_1 = 4.21 Hz, J_2 = 4.87 Hz, 1H), 2.64 (dd, J_1 = 2.72 Hz, J_2 = 5.03 Hz, 1H).

4-(2-(Oxiran-2-ylmethoxy)ethyl)phenethyl acrylate (**CLA3**): ^{1}H NMR ($CDCl_3$, 400 MHz): δppm : 6.85 (s, 1H), 6.45 (dd, J_1 = 1.53 Hz, J_2 = 17.37 Hz, 1H), 6.17 (dd, J_1 = 10.25 Hz, J_2 = 17.29 Hz, 1H), 5.86 (dd, J_1 = 1.50 Hz, J_2 = 10.50 Hz, 1H), 4.49 (dd, J = 4.72 Hz, 2H), 4.17 (dd, J = 4.72 Hz, 2H), 4.09 (dd, J = 4.85 Hz, 2H), 3.79−3.92 (m, 3H), 3.49 (dd, J_1 = 5.97 Hz, J_2 = 11.67 Hz, 1H), 3.17−3.22 (m, 1H), 2.81 (dd, J = 4.63 Hz, 2H), 2.64 (dd, J_1 = 2.74 Hz, J_2 = 5.00 Hz, 1H).

8-(Oxiran-2-ylmethoxy)octanol (**OXOL4**) [13]: ^{1}H NMR ($CDCl_3$, 400 MHz), δppm : 3.69−3.74 (dd, J_1 = 11.8 Hz, J_2 = 3.11 Hz, 1H), 3.62−3.66 (t, J = 6.59 Hz, 2H), 3.42−3.56 (m, 2H), 3.35−3.41 (dd, J_1 = 11.6 Hz, J_2 = 5.93 Hz, 1H), 3.13−3.18 (m, 1H), 2.79−2.82 (dd, J_1 = 5.14 Hz, J_2 = 3.01 Hz, 1H), 2.60−2.62 (dd, J_1 = 5.02 Hz, J_2 = 4.08 Hz, 1H), 1.32, 1.52−1.61 (m, 12H).

8-(Oxiran-2-ylmethoxy)octyl acrylate (**CLA4**) [14]: ^{1}H NMR ($CDCl_3$, 400 MHz), δ ppm : 6.37−6.42 (dd, J_1 = 17.38 Hz, J_2 = 1.51 Hz, 1H), 6.09−6.16 (dd, J_1 = 17.57 Hz, J_2 = 10.42 Hz, 1H), 5.80−5.83 (dd, J_1 = 10.48 Hz, J_2 = 1.57 Hz, 1H), 4.13−4.16 (t, J = 6.71 Hz, 2H), 3.69−3.73 (dd, J_1 = 11.48 Hz, J_2 = 3.14 Hz, 1H), 3.43−3.54 (m, 2H), 3.36−3.40 (dd, J_1 = 11.54 Hz, J_2 = 5.84 Hz, 1H), 3.13−3.17 (m, 1H), 2.79−2.81 (dd, J_1 = 5.14 Hz, J_2 = 4.14 Hz, 1H), 2.60−2.62 (dd, J_1 = 5.08 Hz, J_2 = 2.64 Hz, 1H), 1.34, 1.55−1.70 (m, 12H).

10-(Oxiran-2-ylmethoxy)decanol (**OXOL5**) [13]: ^{1}H NMR ($CDCl_3$, 400 MHz), δppm : 3.69−3.73 (dd, J_1 = 11.48 Hz, J_2 = 3.14 Hz, 1H), 3.62−3.66 (dd, J_1 = 13.49 Hz, J_2 = 6.71 Hz, 2H), 3.43−3.53 (m, 2H), 3.33−3.40 (dd, J_1 = 11.54 Hz, J_2 = 5.84 Hz, 1H), 3.13−3.17 (m, 1H), 2.79−2.81 (dd, J_1 = 5.14 Hz, J_2 = 4.14 Hz, 1H), 2.60−2.62 (dd, J_1 = 5.08 Hz, J_2 = 2.64 Hz, 1H), 1.29, 1.53−1.63 (m, 16H).

10-(Oxiran-2-ylmethoxy)decyl acrylate (**CLA5**) [14]: ^{1}H NMR ($CDCl_3$, 400 MHz), δ ppm : 6.37−6.42 (dd, J_1 = 17.40 Hz, J_2 = 1.51 Hz, 1H), 6.09−6.15 (dd, J_1 = 17.62 Hz, J_2 = 10.42 Hz, 1H), 5.79−5.82 (dd, J_1 = 10.48 Hz, J_2 = 1.57 Hz, 1H), 4.13−4.16 (t, J = 6.71 Hz, 2H), 3.68−3.72 (dd, J_1 = 11.48 Hz, J_2 = 3.14 Hz, 1H), 3.43−3.54 (m, 2H), 3.36−3.40 (dd, J_1 = 11.54 Hz, J_2 = 5.84 Hz, 1H), 3.12−3.16 (m, 1H), 2.78−2.81 (dd, J_1 = 5.14 Hz, J_2 = 4.14 Hz, 1H), 2.60−2.61 (dd, J_1 = 5.08 Hz, J_2 = 2.64 Hz, 1H), 1.29, 1.55−1.70 (m, 16H).

12-(Oxiran-2-ylmethoxy)dodecanol (**OXOL6**)[13]: ^{1}H NMR ($CDCl_3$, 400 MHz), δppm : 3.69−3.72 (dd, J_1 = 11.54 Hz, J_2 = 3.07 Hz, 1H), 3.62−3.65 (t, J = 7.97 Hz, 2H), 3.43−3.54 (m, 2H), 3.36−3.40 (dd, J_1 = 11.54 Hz, J_2 = 5.83 Hz, 1H), 3.13−3.17 (m, 1H), 2.79−2.81 (dd, J_1 = 5.08 Hz, J_2 = 4.20 Hz, 1H), 2.60−2.62 (dd, J_1 = 4.96 Hz, J_2 = 2.70 Hz, 1H), 1.27, 1.53−1.65 (m, 20H).

12-(Oxiran-2-ylmethoxy)dodecyl acrylate (**CLA6**) [14]: ^{1}H NMR ($CDCl_3$, 400 MHz), δ ppm : 6.37−6.42 (dd, J_1 = 17.32 Hz, J_2 = 1.51 Hz, 1H), 6.09−6.15 (dd, J_1 = 17.57 Hz, J_2 = 10.48 Hz, 1H), 5.80−5.83 (dd, J_1 = 10.35 Hz, J_2 = 1.51 Hz, 1H), 4.13−4.17 (t, J = 6.71 Hz, 2H), 3.69−3.73 (dd, J_1 = 11.42 Hz, J_2 = 3.14 Hz, 1H), 3.43−3.54 (m, 2H), 3.36−3.40 (dd, J_1 = 11.61 Hz, J_2 = 5.84 Hz, 1H), 3.13−3.17 (m, 1H), 2.79−2.81 (dd, J_1 = 5.21 Hz, J_2 = 4.20 Hz, 1H), 2.60−2.62 (dd, J_1 = 5.14 Hz, J_2 = 2.70 Hz, 1H), 1.27, 1.55−1.70 (m, 20H).

2.4. Tuning of monomer viscosity

DPHA and **TEGDM** as radical polymerization monomers were mixed in ratios of 100:0, 9:1, 7:1, 5.53:1, 4.5:1, and 0:100. The mixture was sucked up with a 5 mL measuring pipette, and the time until the scale of the measuring pipette fell naturally from 4.5 to 4.0 mL was measured (Fig. 4). Viscosity measurements were also conducted on **SR-SEP** and **Denacol 313**, which were used as cationic

Table 1. Materials stoichiometry and yield of the crosslinker syntheses.

Reactant of the first step reaction[a)]		Product (yield / %)	Reactant of the second step reaction[b)]		Final product (yield / %)
DOL1 (16.53 g, 150 mmol)	OX (13.9 g, 150 mmol)	OXOL1 3.49 g (14 %)	OXOL1 (3.39 g, 20 mmol)	AC (1.85 g, 20 mmol)	CLA1 1.72 g (39 %)
DOL2 (6.89 g, 50 mmol)	OX (4.62 g, 50 mmol)	OXOL1 1.65 g (17 %)	OXOL1 (1.64 g, 8.5 mmol)	AC (1.53 g, 17 mmol)	CLA2 0.40 g (19 %)
DOL3 (41.5 g, 250 mmol)	OX (23.1 g, 250 mmol)	OXOL1 2.22 g (4 %)	OXOL1 (4.11 g, 19mmol)	AC (3.35 g, 37 mmol)	CLA3 1.21 g (23 %)
DOL4-6	OX	OXOL4-6		AC	
DOL4 n=3 (7.31 g, 50 mmol)	(4.70 g, 51 mmol)	OXOL4 1.75 g (17 %)	(1.70 g, 8.4 mmol)	(1.63 g, 18 mmol)	CLA4 0.65 g (30 %)
DOL5 n=4 (43.57 g, 250 mmol)	(34.70 g, 375 mmol)	OXOL5 14.95 g (26 %)	(14.9 g, 65 mmol)	(11.7 g, 129 mmol)	CLA5 4.80 g (26 %)
DOL6 n=5 (10.1 g, 50 mmol)	(6.94 g, 75 mmol)	OXOL6 1.548 g (12 %)	(1.60 g, 6.2 mmol)	(1.25 g, 14 mmol)	CLA6 0.68 g (35 %)

a) Base; NaOH, solvent; H_2O, phase transfer catalyst, TEBAC for DOL1 and TBAB for others. b) Base; TEA, solvent; THF. TEBAC: benzyltrimethylammonium chloride, TBAB: tetrabutylammonium bromide, TEA: triethylamine.

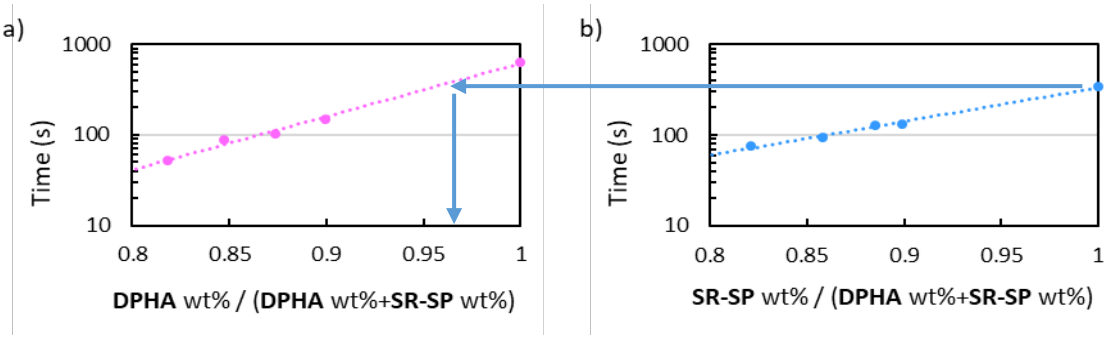

Fig. 4. Logarithm plot of the time required for level in the pipette to drop as a function of the material ratio.

polymerization monomers. The monomer ratio to be used in future experiments was determined so that the viscosity of the radical polymerization monomer and the cationic polymerization monomer were the same; hereafter, these materials with the determined monomer ratio are referred to as acrylic monomer and epoxy monomer, respectively.

2.5. Tuning component ratio

The contents of acrylic monomer, epoxy monomer, and other additives were determined by impact resistance test using prepared samples. A certain amount of initiator and oxetane were mixed. After stirring for 2 h under dark conditions, 3 g, ca. 700 μL of the mixture was placed in a silicon mold (oval shape, long and short axis, thickness = 30 × 20 × 2 mm) and photocured for 3 min with an Omron LED lamp, and then additionally photo-cured for 30 min with a Nailio LED lamp [19].

2.6. Impact resistance test

For the impact resistance test, a metal weight was freely dropped from a certain height onto the photocured resin, and the physical state of the resin was observed. In addition, the impact energy (E) imparted to the resin by a drill bit was calculated. The impact given by the drill bit was dependent on the weight of the drill bit, the area of the tip, and the

height that the drill bit falls, which was calculated with the following formula:

E: Impact energy [J/cm^2] = mgh/S, (1)

where,

m: Weight of drill bit [kg], (0.0614 kg),

g: Gravitational acceleration [9.8 m/s^2],

h: Height the drill bit falls [m],

S: Area of the drill bit tip [cm^2].

The weight and tip area of the drill bit were kept constant, and only the height from which the drill bit was allowed to fall naturally was changed. As an example calculation, drop heights of 20 and 25 cm are expected to give impact energies of 9.0 and 11.3 J/cm^2, respectively.

2.7. Observation of cured resin surface and interior

A cured resin test piece was prepared and was crushed with a metal weight. The crushed surface was observed using scanning electron microscopy (SEM). The crushed piece was immersed in 10% NaOH aqueous solution for 5.5 days, and then washed with pure water. After air-drying for 7 days, the sample surface was observed using SEM.

2.8. Monomer conversion rate measurement

4HBAGE and **CLA2** were used as hybrid CLAs. The monomer mixture, hybrid CLA, oxetane, and each polymerization initiator were mixed for 2 h under light. The mixture was sandwiched between KBr plates, exposed to UV light for a certain period of time, and then measured using FT-IR spectroscopy.

3. Results and discussion

3.1. Viscosity of the resins

In photochemical curing systems, matching of the viscosity between the radical and cationic polymerization systems is very important to prevent segregation. For the acrylic and epoxy monomers, multifunctional and higher viscosity agents (**DPHA**, **SR-SEP**) are diluted with a reagent having a lower viscosity (**TEGDM** and **Denacol 313**, respectively). Figure 4 shows the logarithm of the time required for the sample level in the pipette to drop as a function of the material ratio. The time required was proportional to the viscosity.

For both **DPHA** and **SR-SEP**, the material has higher viscosity due to a larger number of polymerization functional groups per molecule, so that the resultant resin has a high polymerization rate and is difficult to bend. **SR-SEP** has lower viscosity than **DPHA**; therefore, DPHA was diluted with **TEGDM** to set the viscosities of the acrylic and epoxy polymerization monomers to be the same. Hereafter, DPHA was used with **TEGDM** (**DPHA**:**TEGDM** = 96.1:3.9).

3.2. Determination of acryl and epoxy monomer ratios

The ratio of acrylic to epoxy monomer was changed by 10% from 10:0 to 0:10, and 11 samples were mixed. The mixture was placed in a silicon mold and photocured for 3 min with an Omron LED lamp, and then photocured for 30 min with a Nailio LED lamp [20]. A metal weight was then freely dropped from a certain height onto the photocured resin, and the condition of the resin was observed. The materials with the determined monomer ratio are hereafter referred to as the monomer mixture.

Figure 5 shows the evaluation results for the photocured resins with each monomer ratio. The upper panels show the state of the resin after curing, the middle panels show the state when the drill bit is given an impact of 9.0 J/cm^2, and the lower panels show the state when the drill bit is dropped with an impact of 11.3 J/cm^2. The resins with any monomer mixing ratio were cured after light irradiation, and were colorless and transparent. When the drill bit was dropped, the samples with a high content of acrylic polymerized monomers (10:0, 9:1, 8:2, and 7:3) were cracked by an impact of 9.0 J/cm^2, and that with a 6:4 ratio was cracked by an impact of 11.3 J/cm^2. Those samples containing more than half of the epoxy polymerization-based monomer did not crack, even when an impact of 11.3 J/cm^2 was applied.

It was thus confirmed that the acrylic polymerization-based monomer is more vulnerable to impact than the epoxy polymerization-based monomer. Further experiments examined resistance to impacts of 9.0 J/cm^2, and the resin with a ratio of acrylic to epoxy monomers of 6:4 that was destroyed by an impact of 11.3 J/cm^2 was used as a reference for comparison.

3.3. Tuning of the amount of hybrid CLA additive

In the first step in tuning of the amount of hybrid CLA additive, **4HBAGE** was used. According to section 3.2, samples (total weight: 3 g) were prepared in the presence of **4HBAGE** (0, 0.06, 0.12, 0.24, 0.48 g, respectively). After photocuring, the resins were subjected to impact tests with a drill bit dropped from heights of 20 and 25 cm.

Figure 6 shows photograph taken before and after the impact tests. The upper panels show the colorless transparent cured resins, the middle panels

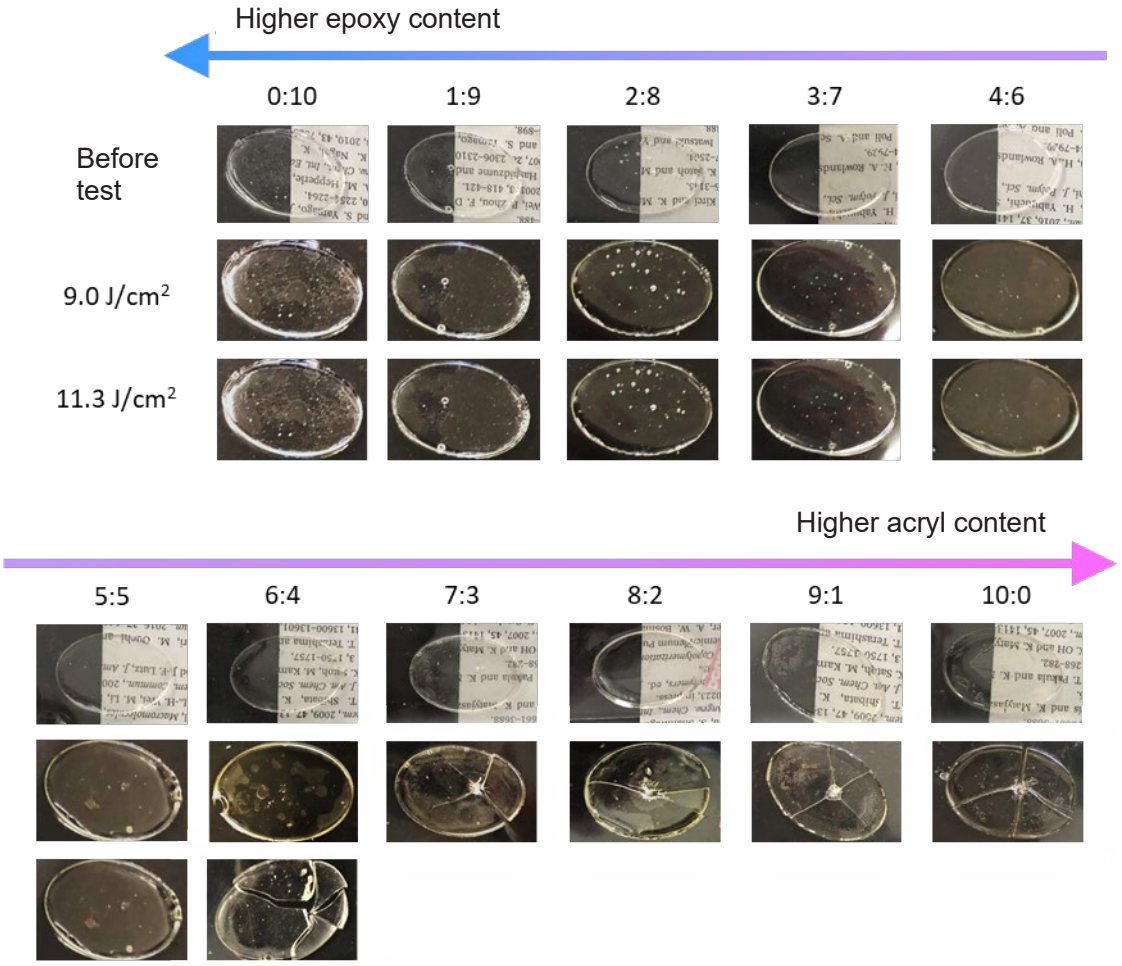

Fig. 5. Effect of acryl/epoxy ratios (weight ratio, total weight: 3 g) on the impact strength. Other additives: oxetane/**Irg184**/**CPI-100P**=0.5g/0.005g/0.01g.

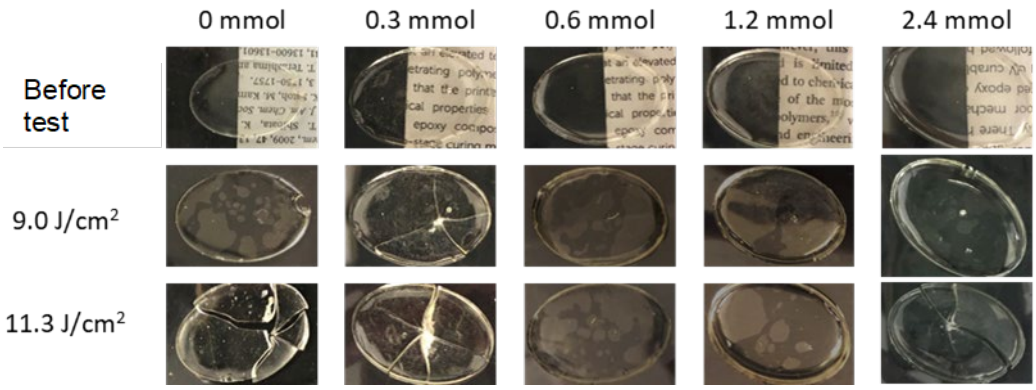

Fig. 6. Tuning of the amount of **4HBAGE** added. (weights of **4HBAGE** were 0, 0.06, 0.12, 0.24, 0.48g, respectively, total weight: 3 g. Other additives: oxetane/**Irg184**/**CPI-100P**=0.5g/0.005g/0.01g).

show the states after drill bit impact at 9.0 J/cm^2, and the lower panels show the states after an impact of 11.3 J/cm^2. The specimen without the hybrid CLA was cracked by an impact of 11.3 J/cm^2. The test piece to which 0.3 mmol of the hybrid CLA was added was destroyed when an impact of 9.0 J/cm^2 was applied, and the impact resistance was lower than that without the hybrid CLA. The test piece to which 0.6 mmol and 1.2 mmol of the hybrid CLA were added had no cracks, even after an impact of 11.3 J/cm^2. The test piece to which 2.4 mmol of the hybrid CLA was added was destroyed by an impact of 11.3 J/cm^2.

If the amount of the hybrid CLA added was too

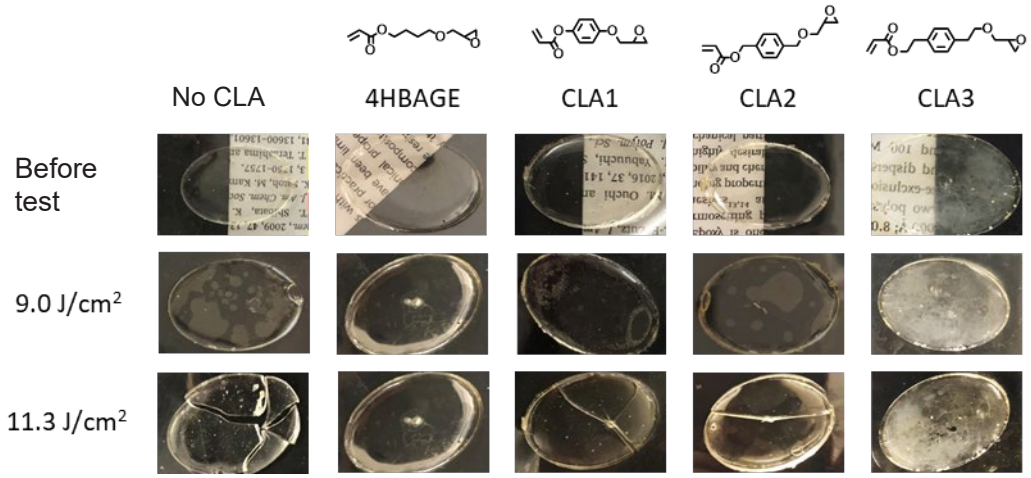

Fig. 7. Impact tests for **4HBAGE**, **CLA1**, **CLA2**, and **CLA3** containing samples.

Table 2. Contents of resins for impact test.

Hybrid CLA	Hybrid CLA / g	Monomeric mixture[a] / g	Other additives
none	0	3.0	b
4HBAGE	0.12	2.88	b
CLA1	0.13	2.87	b
CLA2	0.15	2.85	b
CLA3	0.17	2.83	b
CLA4	0.15	2.85	b
CLA5	0.17	2.83	b
CLA6	0.19	2.81	b

a: acrylic monomer 60 wt% (**DPHA**:**TEGDM** = 96.1:3.9 wt%) and epoxy monomer 40 wt% (**SR-SEP**). b: oxetane/**Irg184**/**CPI-100P**=0.5 g/0.005 g/0.01 g.

small, then the connection between polymer chains was insufficient, and thus, the impact resistance was lower. If the amount of the hybrid CLA additive is reduced, then the cross-linking density between the acrylic and epoxy monomers is also reduced. As a result, it is considered that the impact resistance was inferior to that of the test piece without the addition of the hybrid CLA. It is also considered that if the amount of the hybrid CLA added is too large, the proportion of polyfunctional monomer with many polymerization points is less, and the monomer becomes brittle and thus vulnerable to impact. Further addition of hybrid CLA improved the impact resistance of the resin because a network of polymer chains was formed by the connection of acrylic and epoxy polymerization functional groups in addition to a network of similar polymers [9]. Based these results, the resin with 0.6 mmol of the hybrid CLA added to produce a total of 3 g of monomer mixture was used for further evaluation.

3.4. Impact resistance test for hybrid CLAs

Other hybrid CLAs were examined using a method similar to that described in section 3.3. The contents of each sample prepared are summarized in Table 2.

Figure 7 shows the results of impact resistance tests for the photocured resins with various hybrid CLAs (**4HBAGE**, **CLA1**, **CLA2**, **CLA3**). No matter which hybrid CLA was added, it was successfully photocured. None of the samples broke, even when an impact of 9.0 J/cm^2 was applied. When an impact of 11.3 J/cm^2 was applied, the resin without the hybrid CLA broke into several pieces, while the resins with **CLA1** and **CLA2** only broke into a couple of fragments. In addition, those resins with the **4HBAGE** and **CLA3** hybrid CLAs were not destroyed at an impact of 11.3 J/cm^2. Therefore, reinforcement was observed with these hybrid CLAs.

The difference in the impact resistance due to the difference in the structure of the hybrid CLA was investigated. The structure of **4HBAGE** at the center of the compound is a highly flexible alkyl chain, so that the photocured resin was also resistant to impact. The addition of **CLA1**, for which the central skeleton is not an alkyl chain, but a rigid aromatic ring, resulted in a resin with reduced impact resistance compared to the addition of **4HBAGE**. From the rigid aromatic ring, **CLA2** and **CLA3** with extended alkyl chains are considered to have improved the impact resistance due to flexibility of the resultant polymer compared to **CLA1** [21]. In particular, the **CLA3** structure contains an alkyl chain, similar to **4HBAGE**, and also an aromatic ring, so that both flexibility and rigidity are increased and impact dents after testing are less noticeable.

Figure 8 shows the results of impact tests for

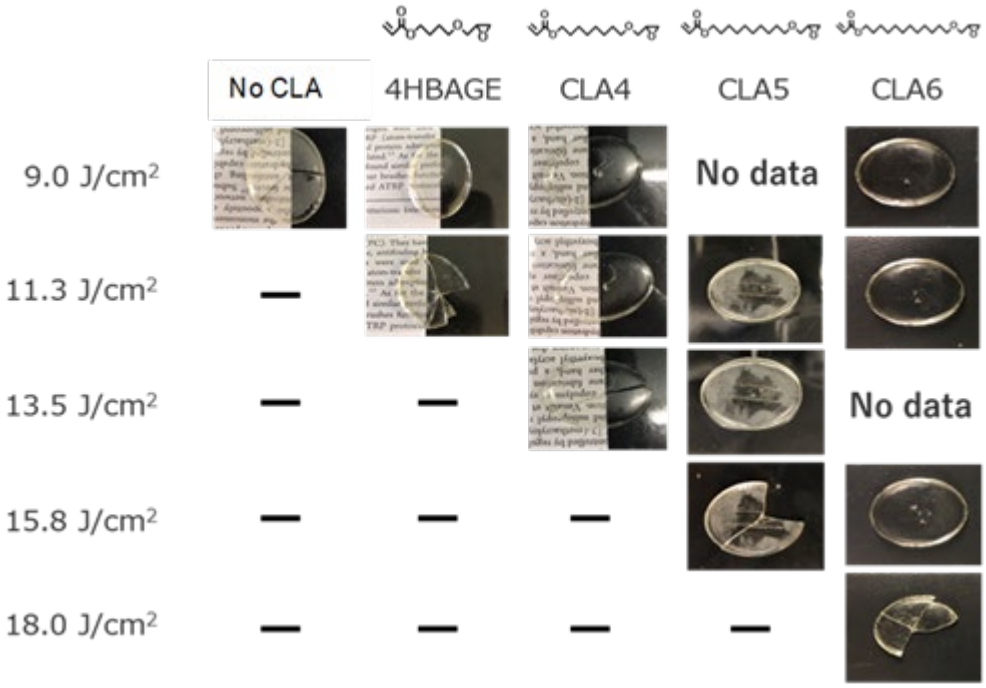

Fig. 8. Impact tests for the samples containing **4HBAGE**, **CLA4**, **CLA5**, and **CLA6**.

photocured resins with hybrid CLAs (**CLA4**, **CLA5**, and **CLA6**), in which the alkyl chain of the central skeleton of **4HBAGE** was extended. The resin without the hybrid CLA cracked with an impact energy of 9.0 J/cm^2; however, with the introduction of a longer alkyl chain, **CLA6** did not crack even under an impact of 15.8 J/cm^2. The impact resistance was also improved by extending the alkyl chain of the central skeleton of the hybrid CLA.

3.5. Monomer conversion rate

Using the sample without the hybrid CLA, FT-IR spectra were compared for the sample exposed to UV-light for 0 s and 1800 s. The absorbance peak at 1637 cm^{-1} [18] derived from the C=C bond of the acrylic group decreased with the irradiation time, without a change in peak shape, when exposed to UV-light. On the other hand, the peak at 916 cm^{-1} [18] due to the ether moiety (C-O-C) of the epoxy group did not show a clear decrease, so that the monomer conversion rate for cationic polymerization could not be determined.

The conversion rate for the acrylic group (C=C) is discussed next (Fig. 9). The sample without the hybrid CLA (0 wt%) had the most prominent peak, although the C=C peak did not decrease until ca. 200 s after the first UV irradiation. This is considered to be due to the effects of oxygen inhibition. The test pieces used for the impact resistance test were also prepared in the atmosphere; therefore, the measurement results are considered to

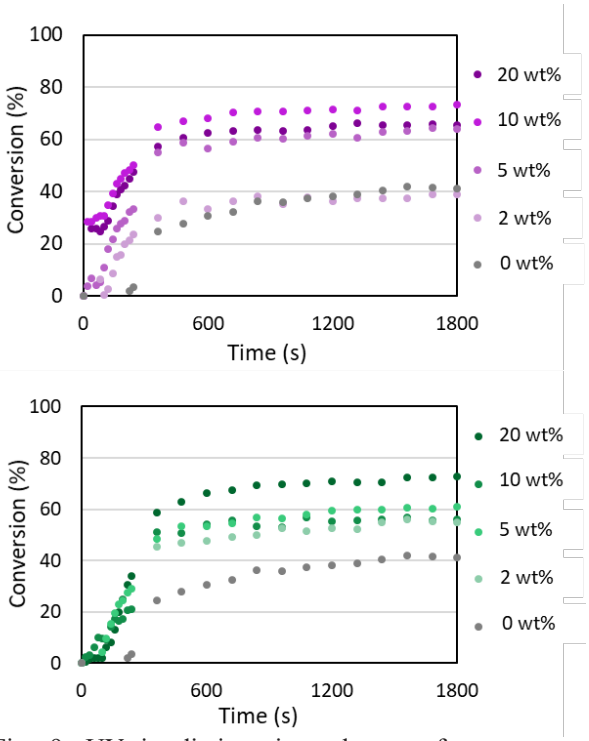

Fig. 9. UV irradiation time change of monomer conversion rate with respect to the amount of CLA added when a: **4HBAGE** and b: **CLA2** are used as the hybrid CLA.

be applicable to an actual curing system. The conversion rate increased logarithmically in both samples with **4HBAGE** and **CLA2** as hybrid CLAs, and the decrease in unsaturated bonds peaked 500 s after the start of UV irradiation. The final monomer

conversion rate improved with increasing concentration of the hybrid CLA. This is due to the number of polymerization functional groups. The main material for radical polymerization, **DPHA**, has 5 to 6 functional groups, and the main material for cationic polymerization, **SR-SEP**, has 3 to 6 functional groups. With a large number of functional groups per molecule, the number of functional groups left unreacted during polymerization increased [20]; however, it is considered that the polymerization rate was improved by an increase in the amount of hybrid CLA, which has a small number of functional groups.

3.6. Heat resistance characteristics

The resin from a test piece was scraped off with a cutter and TG measurements were performed in the range of 100 to 600 °C at a ramp rate of 5 °C/min.

TG profiles were measured for samples without a hybrid CLA, and with **4HBAGE**, **CLA2**, and **CLA3** additives. Weight loss occurred from approximately 180 to 550 °C. It is presumed that the first weight loss from around 180 °C is due to decomposition and/or evaporation of the epoxy polymerization monomer, and the weight loss from around 380 °C is due to the acrylic polymerization monomer relation.

In the sample without the hybrid CLA, a gentle peak stage appeared at ca. 380 °C, although this peak stage was smoother with a CLA in the order of **4HBAGE** > **CLA2** > **CLA3**. When a hybrid CLA was added, the separation of each peak was not very clear. Therefore, the acrylic polymer chain and the epoxy-derived polymer chain become entangled, and each component is polymerized in a properly mixed state [19]. It is thus considered that the polymer chains are bonded to each other to form a network with CLA addition, so that peak separation becomes more unclear.

The temperatures at 5% and 10% weight loss ($T_{5\%}$ and $T_{10\%}$) for each sample are shown in Table 3. The lowest to the highest temperature was in the order of no hybrid CLA < **4HBAGE** < **CLA2** < **CLA3**. There was a difference of ca. 30 °C between the sample without the hybrid CLA and that with **CLA3**. It is considered that the heat resistance was improved with a hybrid CLA having an aromatic ring [22].

Similar TG measurements were performed with the **CLA4**, **CLA5**, and **CLA6** additives. Samples were prepared with a different batch to those in Table 4, and samples without CLA and with **4HBAGE** were also examined again. For all samples, there was no significant difference in the temperature at which weight loss began and the behavior of weight loss thereafter. $T_{5\%}$ and $T_{10\%}$ for each sample are shown in Table 4. No change was observed in these values with the presence or absence of the hybrid CLA and the change in the alkyl chain length of the central skeleton of the hybrid CLA. This result indicates the difference in $T_{5\%}$ and $T_{10\%}$ is not due to the molecular weight of the hybrid CLAs.

Table 3. Temperature at 5% and 10% weight loss determined by TGA measurement.

	$T_{5\%}$ / °C	$T_{10\%}$ / °C
No CLA	215.8	243.0
4HBAGE	223.3	256.6
CLA2	227.2	265.3
CLA3	242.1	271.3

Table 4. Temperature at 5% and 10% weight loss determined by TGA measurement.

	$T_{5\%}$ / °C	$T_{10\%}$ / °C
No CLA	208.8	236.3
4HBAGE	197.3	226.6
CLA4	206.4	232.7
CLA5	205.0	233.3
CLA6	211.6	230.3

3.7. Surface/internal structure of cured resin

The surfaces of the photocured resin samples were observed using SEM. The sample without the hybrid CLA had many irregularities such as agglomerates on the surface, whereas the samples containing the hybrid CLAs had smooth surfaces and almost no agglomerates. It is considered that when the hybrid CLA is added, the photocured polymer is uniformly entangled and the surface becomes smooth.

Figure 10 shows the internal structures of the photocured resins observed using SEM after alkaline etching. From the upper images (low magnification), a small amount of unevenness appears almost uniformly throughout the area. In the sample without the hybrid CLA, fine appears almost uniformly throughout the area. In the sample without the hybrid CLA, fine irregularities are visible only on the surface. However, when the hybrid CLA was added, the irregularities of etched

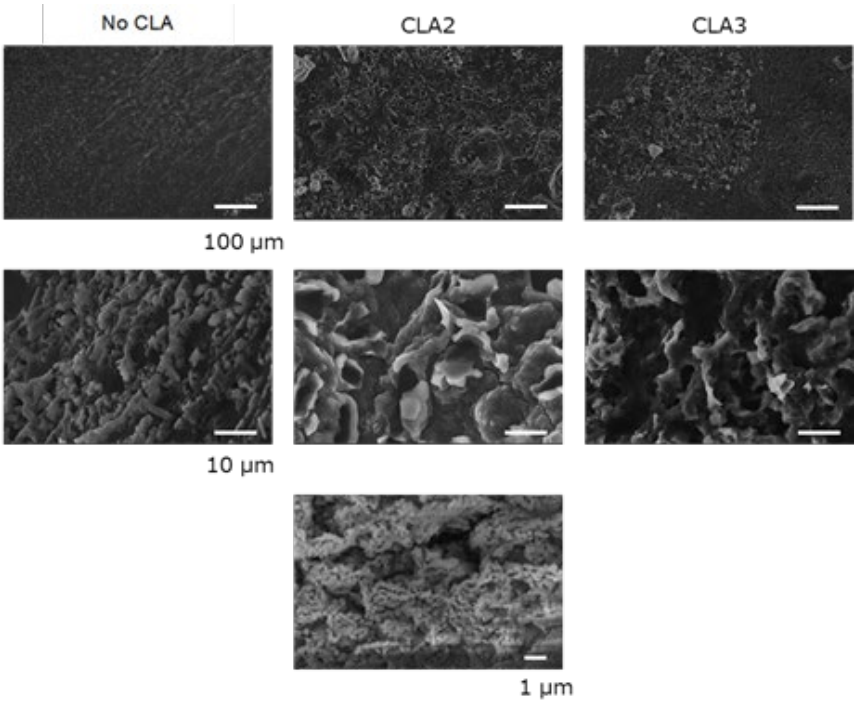

Fig. 10. SEM images of the internal structure of the samples without CLA, and with the **CLA2** and **CLA3** additives.

surface became large, and it was observed that the samples were widely intricated structures in the depth direction. This is considered to be because the polymer chains are intricately intertwined in the depth direction. Looking in more detail, the sample with **CLA2** had many small irregularities of less than 1 μm on the uneven surface. This is a typical internal structure of a mutual IPN; resins with IPN structures have excellent strength [23,24]. Therefore, in the resins using the **CAL2** and **CAL3** hybrid CLAs in this study, the IPN structure is formed in the photocured product, which improved the impact resistance of the product.

Figure 11 compares the internal structures of the samples using **CLA4** to **CLA6** with extended alkyl chain structures. The lower images are enlargements of the upper images, and comparing each image, the internal structure of the resin without the hybrid CLA has more gaps and the structure is more sparse than those with hybrid CLAs. However, structures with the hybrid CLA additives have only small gaps and the structures are dense. In addition, when the

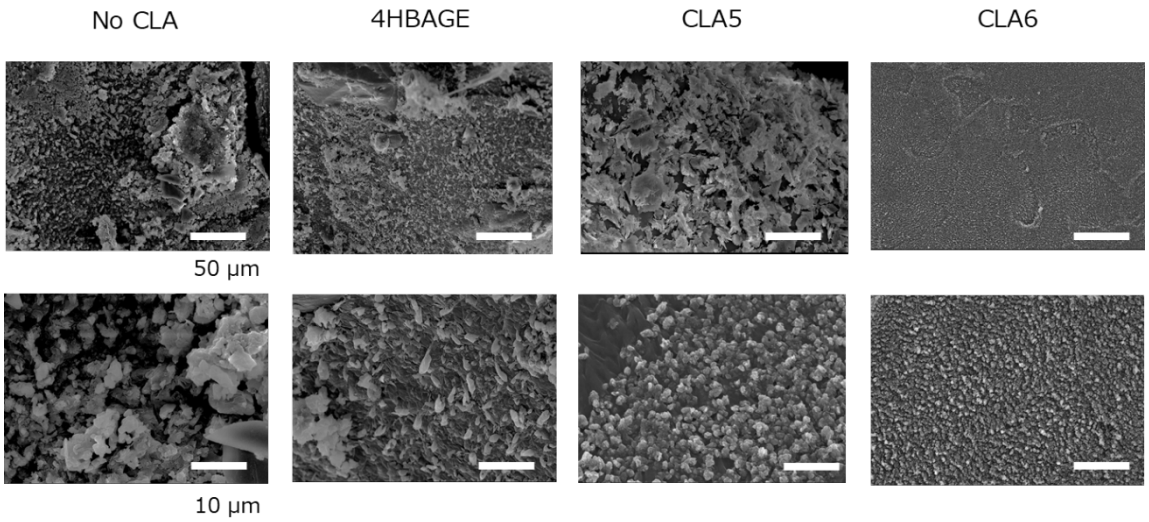

Fig. 11. SEM images of the internal structures of the samples (without CLA, and with **4HBAGE**, **CLA5**, and **CLA6**).

alkyl chain length of the central skeleton of the hybrid CLA was increased, the size of the aggregates became uniform and smaller, which resulted in a denser structure.

Considering the relationship between the change in the internal structure of the resin and the improvement in the impact resistance due to the introduction of these hybrid CLAs, acrylic monomers are characterized by a faster reaction rate than epoxy monomers. Therefore, even if radical and cationic polymerization start at the same time, the acrylic monomer preferentially reacts faster. When the hybrid CLA is not introduced, the cross-linking density increases due to the large amount of the **DPHA** acrylic polyfunctional monomer. As a result, large aggregates as shown in Fig. 11, are formed over the entire area. It is probable that the network was fixed with a large amount of unreacted epoxy remaining, which results in a non-uniform structure that would lead to fragility. On the other hand, the hybrid CLA has a structure with only one radical polymerization site, so that the cross-linking density also decreases due to the relative decrease in the number of polymerization functional groups. It is considered that this reduces the size of the agglomerates and slows the gelation process, which reduces the proportion of unreacted monomers, so that a dense structure is formed.

The improvement in the impact resistance of the resin by extending the alkyl chain length of the central skeleton is described. For the reason of the reaction rate, it is conceivable that the acrylic sites first react preferentially, even with the addition of a hybrid CLA. The motility of the alkyl chains that include the remaining unreacted epoxy polymerization site increases as its length is extended. As a result, the reactivity of the epoxy increases, and many agglomerates due to the epoxy are formed, so that a structure with uniformly dispersed small agglomerates can be observed, as shown in the image of **CLA6** in Fig. 11 and the mechanical strength is thus also improved.

The improvement in the impact resistance of the resin by extending the alkyl chain length of the central skeleton is described. For the reason of the reaction rate, it is conceivable that the acrylic sites first react preferentially, even with the addition of a hybrid CLA. The motility of the alkyl chains that include the remaining unreacted epoxy polymerization site increases as its length is extended. As a result, the reactivity of the epoxy increases, and many agglomerates due to the epoxy are formed, so that a structure with uniformly dispersed small agglomerates can be observed, as shown in the image of **CLA6** in Fig. 10, and the mechanical strength is thus also improved.

4. Conclusion

The addition of hybrid CLA resulted in better impact resistance than for the case without hybrid CLA addition. When the amount of the hybrid CLA additive is small, the bonds between the polymer chains are insufficient and the impact resistance is not significantly improved. If the amount of CLA added is larger than that of the resin with excellent impact resistance, then the proportion of the monomer with a large number of polymerization functionality decreases, and the number of crosslinks in the entire resin decreases, so that the impact resistance decreases. The impact resistance was improved in all cases where a hybrid CLA was used; therefore, the presence of the hybrid CLA affects the mechanical strength, regardless of the structure of the central part of the hybrid CLA. In addition, a longer alkyl chain in the central part resulted in better impact resistance, so that the fluidity in the resin was improved and the ability to absorb impact energy was increased. Therefore, the central part structure of the hybrid CLA is also a factor that affects the mechanical strength, and also improves the heat resistance.

The conversion rate for the polymerization functional groups of the acrylic monomers increased with the amount of hybrid CLA added. This is because a reduction in the number of polymerization functional groups per molecule causes a reduction of unreacted polymerization functional groups being incorporated into the polymer chain, which induces an excellent conversion rate. When the surface and internal structure of the resin were observed, the micro to sub-nano size structures were different, depending on the presence or absence of the hybrid CLA. An internal structure that appears to be a mutual IPN was obtained, which had a clear effect on improvement of the impact resistance.

Acknowledgements

Authors thank Mr. Hiroyuki Naito (RICOH Co. Ltd.) for his advices and help of evaluation of cured polymers. This work was partly supported by the Strategic Priority Research Promotion Program (Chiral Materials Science) at Chiba University and the Five-star Alliance Research Program within NJRC Materials & Devices. The authors also acknowledge the Center for Analytical

Instrumentation for ^{1}H NMR.

References

1. B. A. E. Lehner, D. T. Schmieden, and A. S. Meyer, *ACS Synth. Biol.*, **6** (2017) 1124.
2. J. P. Rolland, K. Chen, J. Poelma, J. Goodrich, R. Pinschmidt, and J. M. DeSimone, Japan Patent JP 2017-524566.
3. C. W. Hull, U.S. Patent, 4,575,330.
4. S. C. Ligon, R. Liska, J. Stampfl, M. Gurr, and R. Mülhaupt, *Chem. Rev.*, **117** (2017) 10212.
5. A. E. Zweber, M. Wagner, J. DeYoung, and R. G. Carbonell, *Langmuir*, **25** (2009) 6176.
6. A. Gonzalez-Bonet, G. Kaufman, Y. Yang, C. Wong, A. Jackson, G. Huyang, R. Bowen, and J. Sun, *Biomacromolecules,* **16** (2015) 3381.
7. X. Kuang, K. Chen, C. K. Dunn, J. Wu, V. C. F. Li, and H. J. Qi, *ACS Appl. Mater. Interfaces*, **10** (2018) 7381.
8. J. Liu, J. Cao, Z. Zhou, R. Liu, Y. Yuan, and X. Liu, *ACS Omega*, **3** (2018) 11128.
9. S. Lantean, I. Roppolo, M. Sangermano, C. F. Pirri, and A. Chiappone, *Inventions*, **3** (2018) 29.
10. Q. Shi, K. Yu, X. Kuang, X. Mu, C. K. Dinn, M. L. Dunn, T. Wang, and H. J. Qi, *Mater. Horiz.*, **4** (2017) 598.
11. T. Watanabe, *Bull. Jpn. Soc. Prosthetics Orthotics*, **32** (3), (2016) 148 (in Japanese).
12. N. Okane and E. Nakamoto, Japan Patent JP 2015-89932.
13. N. Okane and E. Nakamoto, Japan Patent JP 2014-234473.
14. J. Lacombe and C. Soulie-Ziakovic, *Polym. Chem*., **8** (2017) 1129.
15. H. S. Kim and A. J. Crosby, *Adv. Mater.*, **23** (2011) 4188.
16. Z. Chen and D. Webster, *J. Polym. Sci.: Part A: Polym. Chem*., **44** (2006) 4435.
17. H. Sasaki and A. Yuriyama, *Network Polymer*, **34** (3) (2010) 151 (in Japanese).
18. M. Fache, B. Boutevin, and S. Caillol, *Green. Chem.,* **18** (2016) 712.
19. J. H. Kim, E.-S. Park, J. H. Shim, M.-N. Kim, W.-S. Moon, K.-H. Chung, and J.-S. Yoon, *J. Agric. Food Chem.*, **52** (2004) 7480.
20. H. Okamoto and M. Nakatsuka, Japan Patent JP 2016-196597.
21. I. Ogura, *Network Polymer*, **31** (2010) 113 (in Japanese).
22. N. Okane and E. Nakamoto, Japan Patent JP 2016-188308.
23. G. Griffini, M. Invernizzi, M. Levi, G. Natale, G. Postiglione, and S. Turri, *Polymer*, **91** (2016) 174.
24. R. Yu, X. Yang, Y. Zhang, X. Zhao, X. Wu, T. Zhao, Y. Zhao, and W. Huang, *ACS Appl. Mater. Interfaces*, **9** (2017) 1820.

Communication

Journal of Photopolymer Science and Technology
Volume 34, Number 3 (2021) 251−254 ©2021SPST

Synthesis and Characterization of High Refractive Index Polythiocyanurates

Songyan Shi, Yoshihisa Onodera, Tadashi Tsukamono, Yuji Shibasaki, and Yoshiyuki Oishi*

Department of Chemistry, Graduate School of Engineering, Iwate University, 4-3-5 Ueda, Morioka, Iwate 020-8551, Japan
**yoshiyu@iwate-u.ac.jp*

The polythiocyanurates with high molecular weights were successfully prepared by the phase-transfer catalyzed polycondensation of triazinedithiol with activated dibromides. These polymers were soluble in tetrahydrofuran (THF) and *N*-methyl-2-pyrrolidone (NMP), and readily afforded colorless and transparent cast films. The films of polythiocyanurates exhibited good thermal stabilities such as thermal decomposition temperatures of 320 ˚C in air. A relatively high glass transition temperatures of the polymers were in the range of 112-143 ˚C. The optical transmittance of the films was as high as 80% at 400 nm. The films exhibited high refractive index of 1.73 at d line, which is attributed to the triazine rings and sulfur atoms, and Abbe's number of around 18. Furthermore, the films showed the low birefringence of 0.0007-0.0022 at d-line. The obtained polymers are promising candidates for thermoplastic optical lens application.

Keywords: Polythiocyanurate, Triazinedithiol, High refractive index, Low birefringence, Thermoplasticity

1. Introduction

A high refractive index, low birefringence and good thermal solubility, and high optical transparency are the basic concerns in designing optical polymers for high performance components for advanced display devices, various lenses, and optical waveguides [1,2]. The advantages of polymers are their good proccessability, good impact resistance and lightweight compared to inorganic glasses.

Refractive indices of polymers can be expressed using the Lorentz-Lorenz equation (1) [3,4]. The equation which defines the relationship between the refractive and individual parameters depending on polymer structure is quite useful for designing high refractive index polymers.

$$\frac{n^2-1}{n^2+2} = \frac{4\pi}{3}\frac{\rho N_A}{M_W}\alpha = \frac{[R]}{V_0} \qquad (1)$$

where n is the refractive index, ρ is the density, N_A is the Avogadro number, M_W is the molecular weight, α is the linear molecular polarizability, $[R]$ is the molar refraction, and V_0 is the molecular volume of the polymer repeating unit. According to the equation, the introduction of substituents with a high molar refraction and a small molar volume efficiently increases the refractive index of the polymers. Sulfur is the most commonly used atom for increasing the refractive index because of its high atomic polarizability and ability to be introduced into polymers. Various sulfur-containing polymers exhibiting high refractive index values have been synthesized and characterized for the optical applications [1,2].

Recently, in the image pickup optical system of a camera, thermoplastic lenses have been used instead of optical inorganic glasses. Several thermoplastic lenses with a high refractive index, a low birefringence have been reported such as polyesters with phenylfluorene moieties. These polymers exhibited relatively high refractive indices of 1.6 and small birefringence. Considering their use in thermoplastic lenses, their refractive indices over 1.7 are required. As well as the sulfur atom, heteroaromatic rings such as triazine [5] and pyrimidine [6] are promising components with high

Received January 13, 2021
Accepted January 19, 2021

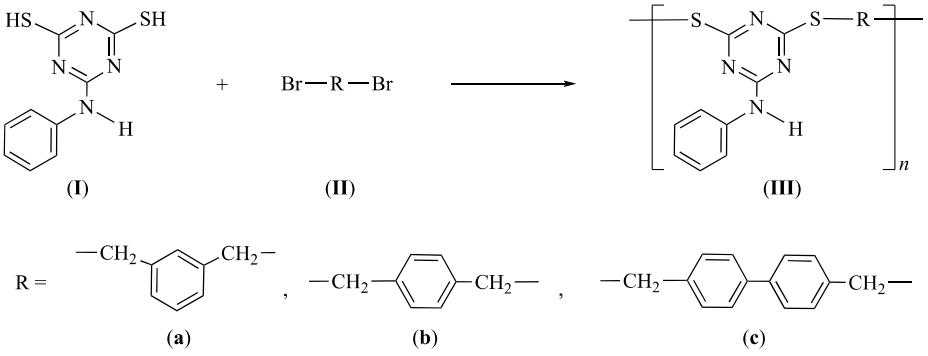

Scheme 1. Synthesis of polythiocyanurates.

refractive index due to the higher polarity of the rings, the replacement of benzene units to heteroaromatic rings might be effective for the enhancement of the refractive index.

We now report the synthesis and characterization of polythiocyanurates (**III**) containing sulfur atoms and triazine units prepared by the polycondensation of triazinedithiol (**I**) and activated dibromides (**II**). The polythiocyanurates exhibited excellent optical transparency as high as 80% over the wavelength of 400 nm, and furthermore afforded high refractive indices of 1.73 and low birefringence values as well as good thermal stability.

2. Experimental

2.1. Materials

2-Anilino-1,3,5-triazine-4,6-dithiol (**I**) supplied by Sankyo Kasei Co. was purified by recrystallization from *N,N*-dimethylformamide (DMF) and washed with diethyl ether. α,α'-Dibromo-*p*-xylene, α,α'-dibromo-*m*-xylene and 4,4'-bis(bromomethyl)biphenyl were used as received. Cetyltrimethylammonium bromide (CTMAB) was obtained commercially and used without further purification. Nitrobenzene was purified by distillation under reduced pressure after drying with calcium hydride.

2.2. Synthesis of polymer (**IIIb**)

In a flask, 0.5907 g (2.50 mmol) of 2-anilino-1,3,5-triazine-4,6-dithiol (**I**) dissolved in 5.1 mL of 1 M aqueous sodium hydroxide. To the solution was added 0.365 g (1.0 mmol: 40 mol%) of CTMAB. Then, to the stirred mixture was quickly added a solution of 0.6599 g (2.5 mmol) of α,α'-dibromo-*p*-xylene (**IIb**) in 5 mL of dry nitrobenzene. The two-phase mixture was vigorously stirred at 70 °C for 24 h under nitrogen. The reaction mixture formed an emulsion as the polymerization proceeded. The mixture was poured into 300 mL of methanol. The precipitated polymer was collected by filtration and dried at 80 °C under vacuum. The yield of the polymer was 0.677 g (80%) and the inherent viscosity was 0.93 dL/g, measured at a concentration of 0.5 g/dL in NMP at 30 °C.

IR (film): 2963-2923 (CH_2), 1556 (C=N), 1510 cm^{-1} (C=C).

^{1}H NMR (DMSO-d_6, ppm): δ 4.28 (s, 4H, CH_2), 6.97-7.55 (m, 9H, Ar-H), 10.18 (s, 1H, NH).

2.3. Measurement

FT-IR spectra were recorded on a JASCO FT/IR-4200. NMR spectroscopy was performed on a Bruker AC-400P spectrometer. The molecular weights were determined using a Tosoh HLC-8220 gel permeation chromatograph with polystyrene gel column (TSK-GEL α-M) at 40 °C and eluted with NMP containing 0.01 mol/L LiBr. Thermogravimetric analysis (TG) was performed on a Hitachi TG/DTA7220 at a heating rate of 10 °C/min. Differential scanning calorimetry (DSC) was performed on a Hitachi DSC7000 at a heating rate of 20 °C/min. The UV-vis spectra were recorded

Table 1. Synthesis of polythiocyanurates[a].

Polymer	Temp. (°C)	Solvent (mL)	Yield (%)	η_{inh}[b] (dL/g)	M_n[c]/10^4	M_w/M_n
IIIa	70	5	76	0.82	5.5	2.4
IIIb	70	5	80	0.93	6.2	1.9
IIIc	r. t.	8	81	0.71	5.2	2.8

a) Polymerization was carried out with each monomer (2.5 mmol) in the presence of CTMAB (40 mol%) in nitrobenzene and 1 M aqueous sodium hydroxide (5.1 mL) for 24 h. b) Measured at a concentration of 0.5 g/dL in NMP at 30 °C. c) Determined by GPC on the basis of polystyrene calibration in NMP containing 0.01 mol/L LiBr.

on a Shimadzu UV-1800. The in-plane (n_{TE}) and out-of-plane (n_{TM}) refractive indices of polymer films were carried out using a Metricon Prism Coupler Model 2010/M.

3. Results and discussion

The phase-transfer catalyzed polycondensation has been preferably used for the synthesis of the polysulfides using dithiols or sodium sulfide as a nucleophilic monomer [7-9]. We had adopted this polymerization method to the synthesis of 1,3,5-triazine-containing polysulfides [5,10] by the polycondensation of triazinedithiols with α,α'-dibromoxylene or 1,10-dibromodecane in the nitrobenzene-aqueous alkaline solution system in the presence of a phase-transfer catalyst. The synthesis of polythiocyanurates (**III**) from 6-anilino-1,3,5-triazine-2,4-dithiol (**I**) and activated dibromides (**II**) was investigated by the two-phase polycondensation (Scheme 1). Polycondensation was carried out in a nitrobenzene-aqueous NaOH solution in the presence of cetyltrimethylammonium bromide (CTMAB, 40 mol%) at r.t. or 70 °C for 24 h. The results are summarized in Table 1.

Three types of colorless polymers (**IIIa-IIIc**) with high inherent viscosities (η_{inh}) of 0.7-0.9 dL/g and number average molecular weight (M_n) of 52,000-62,000 were successfully obtained. The chemical structure of the polymer was characterized by ^{1}H NMR and FT-IR spectroscopies.

The solubilities of polymers (**III**) are summarized in Table 2. All polymers were soluble in common organic solvents such as THF, DMF, *N,N*-dimethylacetamide (DMAc) and NMP, probably

Table 2. Solubility[a] of polythiocyanurates.

Polymer	NMP	DMAc	DMF	THF	$CHCl_3$
IIIa	+	+	+	+	-
IIIb	+	+	+	+	-
IIIc	+	+	+	+	-

a) Solubility: +, soluble at room temp.; -, insoluble.

Table 3. Thermal properties of polythiocyanurates.

Polymer	T_g[a] (°C)	T_5[b] (°C)		T_{10}[c] (°C)	
		in air	in N_2	in air	in N_2
IIIa	112	319	336	328	343
IIIb	126	320	338	327	347
IIIc	143	316	338	327	345

a) By DSC at a heating rate of 20 °C/min. b) 5% weight loss temperature by TG at a heating rate of 10 °C/min. c) 10% weight loss temperature.

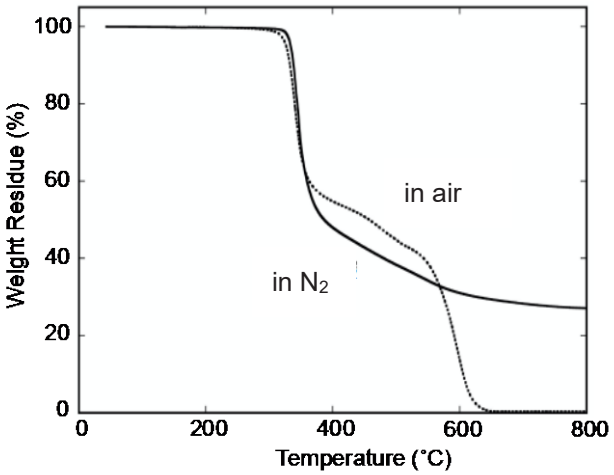

Fig. 1. TG curves of polymer (**IIIb**).

Table 4. Optical properties of polythiocyanurates.

Polymer	d[a] (μm)	λ_{cutoff}[b] (nm)	Mode[c]	n_F[d]	n_d[d]	n_C[d]	n_{dav}[e]	ν_d[f]
IIIa	33	338	TE	1.7549	1.7329	1.7215	1.7327	21.9
			TM	1.7539	1.7322	1.7215		22.6
			(Δn[g])	0.0010	0.0007	0.0000)		
IIIb	25	336	TE	1.7543	1.7319	1.7205	1.7316	21.7
			TM	1.7530	1.7311	1.7194		21.7
			(Δn[g])	0.0013	0.0008	0.0011)		
IIIc	24	336	TE	1.7720	1.7397	1.7275	1.7389	16.6
			TM	1.7695	1.7375	1.7252		16.6
			(Δn[g])	0.0025	0.0022	0.0023)		

a) Film thickness. b) Cutoff wavelength. c) TE: in-plane mode, TM: out-of-plane mode. d) Refractive index by a prism coupler: F-line, 486 nm; d-line, 589 nm; C-line, 656 nm. e) Average refractive index at d-line: $n_{dav} = [(2n_{dTE}^2 + n_{dTM}^2)/3]^{1/2}$. f) Abbe's number: $\nu_d = (n_d - 1)/(n_F - n_C)$. g) Birefringence: $\Delta n = n_{TE} - n_{TM}$.

due to the existence of methylene units in the polymer backbone structure.

The thermal decomposition temperature and glass transition temperature (T_g) are quite important considering the thermal process for optical device fabrication. The thermal properties of polymers were investigated by TG and DSC measurements. The results are summarized in Fig. 1 and Table 3. Polymers (**III**) showed good thermal stability, a 5% weight loss temperature (T_5) around 320 °C under air atmosphere. The T_g values of polymers (**IIIa**-**IIIc**) were in the range of 112-143 °C. Thermoplastic lenses are required to have a relatively high T_g over 100 °C and high thermal decomposition temperature because injection molding is generally carried out around 100 °C higher than the T_gs of the polymers to increase their fluidity in the molten state. Thus, the T_g of thermoplastic polymers processable by injection molding would be suitable at around 120-150 °C. Polymer (**IIIc**) possessed the highest T_g due to the introduction of the rigid biphenylene units. *m*-Linkages and methylene units contributed to lower T_g of polymer (**IIIa**).

The optical properties of the polymer (**III**) films with the thickness of 24-33 μm are shown in Fig. 2 and Table 4. The cutoff wavelengths (λ_{cutoff}) of the polymer (**III**) films were in the range of 336-338 nm, and the transmittance was as high as 80% at around 400 nm. The refractive indices (n_d) of the polymer (**III**) films were measured at d-line by a prism coupler. All the films exhibited high n_d values around 1.73, resulting from the sulfur atoms and the triazine rings with a high molar refraction. The in-plane (n_{TE}) and out-of-plane (n_{TM}) refractive indices of the polymer (**IIIc**) film were 1.739 and 1.737 at d line, respectively by a prism coupler. The low birefringence (Δn) value of 0.002 observed for polymer (**IIIc**) was relatively higher than those of polymers (**IIIa**, **IIIb**) because of rigid biphenyl units. The calculated Abbe numbers for polymers (**III**) were in the range of 16-22.

4. Conclusion

A series of polythiocynurates with high molecular weights were successfully prepared by the phase-transfer catalyzed polycondensation.

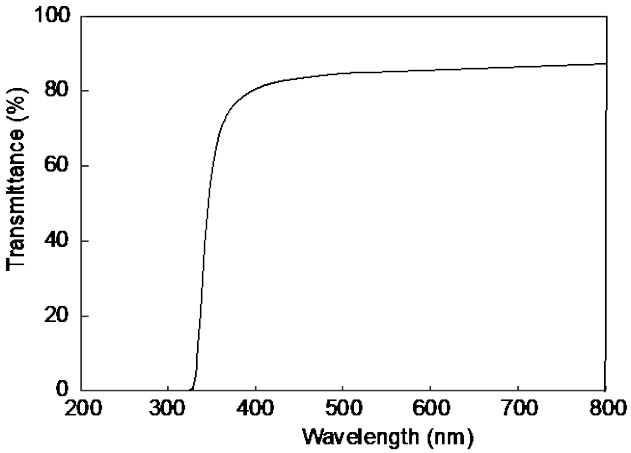

Fig. 2. UV-vis spectrum of polymer (**IIIb**) thin film.

The polythiocyanurates had a high potential as an optical material exhibiting a high refractive index of 1.73, high transparency, low birefringence, relatively high glass transition temperatures of 126-143 °C, and excellent thermal stability. Therefore, the polythiocyanurate is a promising candidate for thermoplastic optical lens application.

References

1. H. Higashihara and M. Ueda, *Macromolecules*, **48** (2015) 1915.
2. E. K. Macdonald and M. P. Shaver, *Polym. Int.*, **64** (2015) 6.
3. H. A. Lorentz, *Ann. Phys.*, **9** (1880) 641.
4. L. V. Lorenz, *Ann. Phys.*, **11** (1880) 70.
5. J. J. Kim, Y. Oishi, H. Hirahara, and K. Mori, *Kobunshi Ronbunshu*, **56** (1999) 159.
6. K. Nakabayashi, T. Imai, M. C. Fu, S. Ando, T. Higashihara, and M. Ueda, *J. Mater. Chem. C.*, **3** (2015) 7081.
7. Y. Imai, A. Kato, M. Li, and M. Ueda, *J. Polym. Sci., Polym. Lett. Ed.*, **17** (1979) 579.
8. M. Ueda, Y. Oishi, N. Sakai, and Y. Imai, *Macromolecules*, **15** (1982) 248.
9. M. Ueda, R. Takasawa, and Y. Imai, *Makromol. Chem., Rapid Commun.*, **3** (1983) 905.
10. Y. Oishi, J. J. Kim, M. Nakamura, H. Hirahara, and K. Mori, *Macromol. Rapid Commun.*, **20** (1999) 294.

Journal of Photopolymer Science and Technology
Volume 34, Number 3 (2021) 255−258 ©2021SPST

Preparation and Applications of a Polysilane-allyl Methacrylate Copolymer

Fumiya Kato[1], Yukihito Matsuura[1]*, Masanobu Ohikita,[2] and Tomoharu Tachikawa[2]

[1]Department of Chemical Engineering, Nara National College of Technology
Yatacho 22, Yamato-koriyama, Nara 639-1080, Japan
[2]Frontier Materials Laboratories, Osaka, Gas Chemicals Co., Ltd.
5-11-61, Torishima, Konohana-ku, Osaka 554-0051, Japan
**matsuura@chem.nara-k.ac.jp*

Copolymers of polysilane and allyl methacrylate were prepared using the polysilane as a photoradical initiator. The polysilane block and allyl group were retained even after photopolymerization. The σ-conjugation of polysilane block in the copolymer allowed it to exhibit light absorption in the ultraviolet region. Subsequently, an ene-thiol reaction between the copolymer and mercapto-containing molecule was carried out by photocuring a thin film of the mixture. The photoreaction formed –CH–CH_2–S– bonding between the organic component and a silica component that was formed by photolysis of the polysilane block in the copolymer. Therefore, the polysilane-allyl methacrylate copolymer successfully provided a silicon-rich organic–inorganic hybrid material.

Keywords: Polysilane, Allyl methacrylate, Photo-polymerization, ene-thiol reaction

1. Introduction

Polysilane exhibits electron delocalization on the Si–Si main chain. These electronic states are known as σ-conjugation owing to their characteristics resembling π-conjugation in organic molecules [1]. In addition, polysilane has good electrical conductivity and light absorption in the ultraviolet region [2], which allows its application to photopolymers [3]. However, its gradual degradation in air limits its industrial applications. To develop the functionality of polysilane, polysilane-methacrylate block copolymers were synthesized using a masked disilene precursor [4]. Polysilane with a sulfide tripod terminus was synthesized to make use of the selective chemisorption of this terminus on a gold surface [5]. Our research group developed photopolymerization of methacrylate to prepare polysilane-methacrylate copolymers using the polysilane itself as a photoradical initiator to retain the polysilane block [6, 7]. In particular, we prepared a copolymer bearing an alkoxy group, which could be used to produce a polysilane–inorganic hybrid material through a sol-gel reaction with metal alkoxide [8]. However, the alkoxy group is significantly unstable for long-term storage.

To improve the weak point of alkoxyl group for the sol-gel reaction, the ene-thiol reaction has

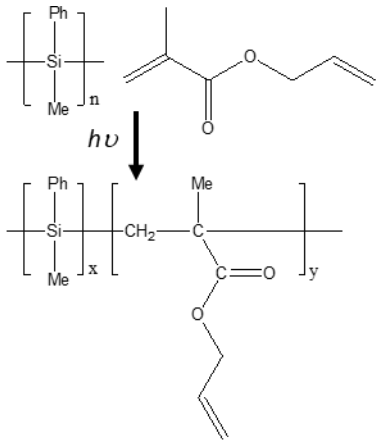

Fig. 1. Photo-polymerization of polysilane-allyMA copolymer.

Received January 22, 2021
Accepted March 16, 2021

been applied for the fabrication of organic–inorganic hybrid materials for hard coat and negative-type resists [9, 10]. The reaction system is superior in durability, low shrinkability, flexibility, and adhesion. Therefore, replacement of sol-gel reaction with the ene-thiol reaction will allow improvements in the preparation methods and properties of polysilane–inorganic hybrid materials. Furthermore, a polysilane-containing thin film can provide a silica component through photocuring to prepare a silicon-rich organic–inorganic hybrid material, which could be used for hard coats and low dielectric materials, among others [11]. Therefore, in this study, we have prepared a copolymer of polysilane and allyl methacrylate (allylMA) using the polysilane itself as a photoradical initiator (Fig.1). Furthermore, photocuring was used to react the allyl group in the copolymer with a mercapto-containing molecule via an ene-thiol reaction to obtain a new type of organic–silica hybrid material (Fig. 2).

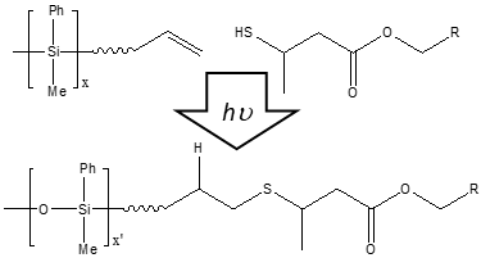

Fig. 2. Photo-reaction of polysilane-ally MA copolymer and mercapto-containing compound to fabricate an organic-silica hybrid film.

2. Experimental

2.1 Materials

Poly(methylphenylsilane) (PMPS) was used for the photoreaction with allylMA. PMPS (product OGSOL SI-10-10) was supplied by Osaka Gas Chemicals Co., Ltd. [12]. The crude sample was reprecipitated in hexane, filtered, and dried under vacuum overnight. AllylMA was purchased from Aldrich and used after ^{1}H-NMR analysis. Photopolymerization of methacrylate with PMPS was performed using PMPS itself as a photoradical initiator. The typical photoreaction procedure was as follows: PMPS (~ 0.5 g) and allylMA (~ 0.5 g) were dissolved in toluene (5 mL), where the molar ratio of methylphenylsilane (MPS) unit in PMPS to allylMA was determined to be approximately equimolar. The mixture was sufficiently degassed using a freeze–thaw method. After sealing the Pyrex glass tube under N_2 gas, the tube was irradiated with UV light (SEN LIGHTS CORPORATION, high-pressure Hg lamp, 10 mW cm^{-2}) for 20 min. The reaction mixture was reprecipitated in hexane (300 mL) to obtain a white insoluble product. The hexane containing the insoluble product was filtered through a glass filter (pore size: 20–30 μm), and the residue was dried under vacuum overnight.

Ene-thiol reactions were performed using mercapto-containing molecules, which were purchased from Showa Denko K. K. The molecules were 1,4-bis(3-mercaptobutylyloxy)butane, trimethyrolepropane tris(3-mercaptobutylate), pentaerythritol tetrakis(3-mercaptobutylate), and 1,3,5-tris(3-mercaptobutylyloxyethylene)-1,3,5-triazyl. The PMPS-allylMA copolymer and mercapto-containing molecule were dissolved in THF, and the resulting solution was spin-coated on a silicon wafer. The resulting thin film was photocured under UV light and then heated to 80 °C.

2.2 Measurements

The molecular weight was measured using a Shodex GPC-101 system against a polystyrene standard and in THF as the solvent. The ratio (x/y) of the number of MPS units to the number of allylMA units was determined by ^{1}H-NMR using a JEOL JNM-ECX400 spectrometer with deuterated chloroform as the solvent. Spectroscopic measurements were recorded using a Shimadzu UV-3600 spectrophotometer, a Shimadzu IR Affinity-ATR system equipped with a zinc selenide crystal, and a Tokyo Instruments micro-Raman spectroscopy Nanofinder 30 A with 532 nm green laser. X-ray photoelectron spectroscopy (XPS) was performed using an Ulvac Phi ESCA 3057 with an X-ray tube at MgKα energy. Differential scanning calorimetry (DSC) measurements were recorded using a Seiko Instrument DSC-X5400 apparatus at a heating/cooling rate of 10 °C min^{-1} in a temperature range of −70 to 230 °C. Molecular orbital calculations were performed using the GAMESS program with an approximation of B3LYP/6-31 G** [13].

3. Results and discussion

The product of photoreaction of PMPS and allylMA was a white powder that was soluble in toluene, THF, and chloroform. The FT-IR spectra suggested a chemical structure originating from allylMA and PMPS. For example, a peak at 1728 cm^{-1} indicated the presence of a carbonyl group of allylMA. In addition, a peak at 1470 cm^{-1} was assigned to the bending vibration of methylene in the allylMA unit of the product. The chemical shift in ^{1}H-NMR spectrum showed that the methacryl group of allylMA reacted completely to form a single C–C bond. The details of the ^{1}H-NMR are presented in reference [14]. A single peak observed in the GPC chromatogram confirmed the presence of only a single component in the copolymer. The reason that the allyl group was retained even after photopolymerization was a contribution to the frontier orbitals of allylMA, where the LUMO consisted of the atomic orbitals on only the methacryl group, while the HOMO had the atomic orbitals on the methacryl and allyl groups. Therefore, the HOMO accelerated the photoradical polymerization of the methacryl group with a silyl radical derived from the photolysis of polysilane.

Table 1 lists the molecular weight, content ratio *x/y*, and UV absorption wavelength of the products. The molecular weight decreased as the photoreaction time increased, while the molecular weights of the photopolymerization products were greater than that of PMPS. Increasing photoreaction time reduced the ratio of *x/y*. The changes in the molecular weight and *x/y* with increasing photoreaction time suggested that the number of MPS units decreased as the photoreaction time increased, while the number of allylMA units in the product saturated, as in our previous report [15]. As shown in Table 1, UV absorption in the range of 320–330 nm of products of 1–3 suggested the presence of a PMPS block that exhibited σ-conjugated characteristics even after photopolymerization. In addition, the wavelength of UV absorption became shorter as the photoreaction time increased. This suggests that the σ-conjugation area in the products of 1–3 tends to decrease as the number of MPS units is reduced. These results were in accordance with the ^{1}H-NMR results, as summarized in Table 1. Furthermore, the products exhibited glass transition at 34 °C, which resulted from the allylMA block. From the above results, it was considered that PMPS was successfully connected to allylMA to form the PMPS-allylMA copolymer.

Table 1. Results of photo-polymerization of PMPS and allylMA.

Products	UV-irradiation Time [min]	^{1}H-NMR x/y[1)]	GPC		λ_{max}[2)] [nm]
			Mn	Mw/Mn	
PMPS[3)]	0	-	5100	3.2	331.4
1	10	257	7800	2.4	329.0
2	20	8	7000	2.9	327.5
3	30	3	6100	3.6	323.5

[1)] Ratio of [MePhSi]/[AllylMA].

[2)] Wavelength of UV-Vis absorption spectra.

[3)] PMPS as a starting material.

Subsequently, the copolymer was applied in an ene-thiol reaction with mercapto-containing molecules by photocuring a thin film of the mixture. We used the aforementioned four species of mercapto-containing molecules and observed very similar characteristics among the photocured thin films. Hereinafter, we will describe a result of the ene-thiol reaction using pentaerythritol tetrakis(3-mercaptobutylate). The FT-IR results indicated that the allyl groups of the copolymer reacted completely, because the peaks at 1429 cm^{-1} assigned to C=C and 1585 cm^{-1} assigned to R–CH=CH_2 were not observed after photocuring. In addition, as shown in Figure 3, the Raman spectrum of the thin film after photocuring exhibited a peak at 720 cm^{-1}, which suggested that a C–S bond was formed by the ene-thiol reaction between the allyl moiety of the copolymer and thiol moiety of the mercapto-containing molecule. Although the thin film formed by photocuring was slightly sticky because of the unreacted thiol, as confirmed by the presence of a Raman peak at 2553 cm^{-1}, this could be resolved by optimizing the preparation conditions for the ene-thiol reaction. Furthermore, the XPS results confirmed the formation of a

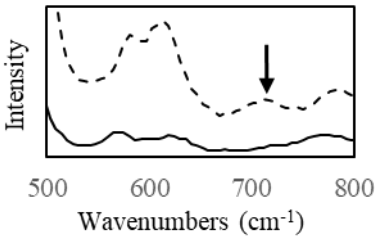

Fig. 3. Raman spectrum of a thin film prepared from photo-reaction of polysilane-allylMA copolymer and pentaerythritol tetrakis(3-mercaptobutylate). The solid and dotted lines indicate the Raman spectra of the copolymer and the ene-thiol product.

silica component, as shown in Figure 4. The copolymer exhibited a peak at 101.8 eV, which was assigned to Si–Si bonding, whereas the peak at 104.4 eV of the ene-thiol reaction product suggested the formation of Si–O bonds. The thermal properties determined by DSC showed no remarkable change in heat flow up to 200 °C. This result indicates that the film exhibits heat resistance at a sufficient degree for application in hard coat and photoresist.

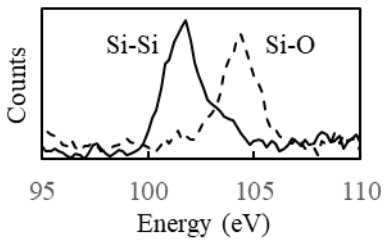

Fig. 4. XPS Si2p peaks of PMPS-allylMA copolymer and the product of ene-thiol reaction with pentaerythritol tetrakis(3-mercaptobutylate). The solid and dotted lines indicate the XPS spectra of the copolymer and the ene-thiol product, respectively.

4. Conclusion

Photopolymerization of polysilane and allyl methacrylate was carried out using the polysilane itself as a photoradical initiator. By adjusting UV light, a polysilane-allyl methacrylate copolymer was prepared, retaining the polysilane block and allyl group. The copolymers exhibited σ-conjugation between polysilane blocks that enabled light absorption in the ultraviolet region. Furthermore, a thin film of a mixture of the copolymer and mercapto-containing molecule allowed the production of an organic–inorganic hybrid thin film. The ene-thiol reaction resulted in strong –CH–CH_2–S– bonding between the organic component and silica component that was derived from the photolysis of the polysilane block in the copolymer. The results show that through photocuring, the polysilane-allyl methacrylate copolymer can provide a silicon-rich organic–inorganic hybrid material for applications such as a hard coat and low dielectric materials. Furthermore, if other species of methacrylate are inserted in the polysilane-methacrylate copolymers, new functionality can be added to the hybrid materials in the future.

Acknowledgement

The authors wish to thank Dr. Kimihiro Matsukawa (Kyoto Institute of Technology) for advice on experiment and useful discussion. This work was supported by JSPS KAKENHI Grant Number 19K05638.

References

1. R. D. Miller and J. Michl, *Chem. Rev.*, **89** (1989) 1359.
2. K. Takeda, H. Teramae, and N. Matsumoto, *J. Am. Chem. Soc.*, **108** (1986) 8186.
3. S. Seki, Y. Kunimi, Y. Sakurai, S. Tsuji, K. Maeda, and S. Tagawa, *J. Photopolym. Sci. Tech.*, **13** (2000) 395.
4. T. Sanji, K. Takase, and H. Sakurai, *J. Am. Chem. Soc.*, **123** (2001) 12690.
5. K. Furukawa, K. Ebata, H. Nakashima, Y. Kashimura, and K. Torimitsu, *Macromolecules*, **36** (2003) 9.
6. K. Matsukawa and Y. Matsuura, *Mater. Res. Soc. Symp. Proc.*, Vol. 847 (2005) EE10.1.1.
7. K. Matsukawa, S. Fukui, N. Higashi, M. Niwa, and H. Inoue, *Chem. Lett.*, **28** (1999) 1073.
8. Y. Matsuura, K. Matsukawa, and H. Inoue, *Chem. Lett.*, **30** (2001) 244.
9. K. Matsukawa, T. Fukuda, S. Watase, and H. Goda, *J. Photopolym. Sci. Tech.*, **23** (2010) 115.
10. K. M. Schreck, D. Leung, and C. N. Bowman, *Macromolecules*, **44** (2011) 7520.
11. T. Hamada, T. Nagase, M. Watanabe, S. Watase, H. Naito, and K. Matsukawa, *J. Photopolym. Sci. Tech.*, **21** (2008) 319.
12. H. Murase, M. Sugimoto, H. Nishimura, and K. Yamada, *Mater. Sci. Appl.*, **6** (2015)576.
13. M. W. Schmidt, K. K. Baldridge, J. A. Boatz, S. T. Elbert, M. S. Gordon, J. H. Jensen, S. Koseki, N. Matsunaga, K. A. Nguyen, S. Su, T. L. Windus, M. Dupuis, and J. A. Montgomery, *J. Comput. Chem.*, **14** (1993) 1347.
14. Results of photoreaction of PMPS and allylMA as follows: ^{1}H-NMR ($CDCl_3$, 400 MHz, δ) –0.7–0.8 (-SiMe 3H), 0.9–1.2 (-C(Me)-$\underline{CH_2}$ 2H), 1.6–2.1 (-C-Me in methacrylate 3H), 4.5 (-O-$\underline{CH_2}$ 2H), 5.2–5.4 (CH_2= of allyl 1H), 5.8–6.0 (CH_2= of allyl 1H), 6.5–7.8 (-Si-Ph 5H).
15. Y. Matsuura, T. Sakatani, Y. Kado, Y. Takahashi, Y. Muramoto, S. Fukunishi, and S. Minami, *Euro. Polym. J.*, **108** (2018) 219.

Communication

Journal of Photopolymer Science and Technology
Volume 34, Number 3 (2021) 259−262 ©2021SPST

Novel Effective Photoinitiators for the Production of Dental Fillings

Monika Topa[1*], and Joanna Ortyl[1,2*]

[1] Faculty of Chemical Engineering and Technology, Cracow University of Technology, Warszawska 24, 31-155 Cracow, Poland
[2] Photo HiTech Ltd., Bobrzyńskiego 14, 30-348 Cracow, Poland
**monika.topa@doktorant.pk.edu.pl*
**jortyl@pk.edu.pl*

Photopolymerization is an environmentally-friendly, non-destructive, safe and solvent-free method. Moreover it guarantees low energy consumption. Therefore the photopolymerization is used in many scientific disciplines, including dentistry for production photocurable dental materials. In this work, the new photoinitiating systems based on camphoroquinone (CQ) and iodonium salts with tosyl anion for initiation of photopolymerization of the acrylates monomers bisphenol A - glycidyl methacrylate (BisGMA) and triethyleneglycol dimethacrylate (TEGDMA) was studied. As a reference, camphorquinone (CQ) and ethyl 4-(dimethylamino)benzoate (EDB) photoinitiating system was used.
Keywords: Photopolymerization, Photoinitiators, Iodonium salts, Camphoroquinone, Dental Fillings

1. Introduction

Photopolymerization is popularity because it is an environmentally friendly and non-destructive method for production of different materials for various industries.

The photopolymerization process is so widespread because it has a number of significant advantages. The primary advantage of the photopolymerization over other methods used for preparation of polymer coatings or composites is its speed. Photo-curable compositions are transformed from a liquid state into a fully cross-linked solid within seconds. The photopolymerization ensures no emission of any volatile solvents to atmosphere. Moreover, photopolymerization is carried out at room temperature, without the use of solvents and with low energy consumption [1-5].

Therefore the photopolymerization is used in many scientific disciplines, e.g. in coatings industry for preparation of coating materials; for automotive and furniture industries, in polygraphic industry for making color imprints on different materials or even in medicine for preparation of polymeric hydrogels. Moreover, the photopolymerization nowadays is used mostly in stomatology for production of new generation photocurable dental materials [6-7].

Most popular materials designated for obtaining dental composites through photopolymerization are (meth)acrylatemonomers (RCB – resin based composites) characterized by high reactivity which form an organic matrix. Usually, organic matrixes based on cross-linking dimethacrylates like 2,2-bis[4-(2-hydroxy-3-methacryloxypropoxy)phenyl]propane (Bis-GMA), ethoxylated Bis-GMA (EBPDMA),1,6-bis-[2-methacryloyloxyethoxycarbonylamino]-2,4,4-trimethylhexane (UDMA), dodecanedioldimethacrylate (D3MA) or triethyleneglycoldimethacrylate (TEGDMA) are used. BisGMA is very popular for the production of photocurable dental composites. Due to the presence of the aromatic structure of Bisphenol A in the core of the molecule, it ensures low volatility of the composition and a high modulus of cured composite [8-13].

On the other hand, the commonly used photoinitiating system for the radical photopolymerization process for dental application is the system based on camphorquinone / aromatic amine. In the step of generating radicals in the

Received April 1, 2021
Accepted May 4, 2021

photolysis process, amine interacted with the excited camphorquinone molecule. This process involves the transfer of the electron from the amine to the ketone, followed by abstraction of the proton. The radicals initiating the polymerization process are mainly radicals formed from amines (Figure 1).

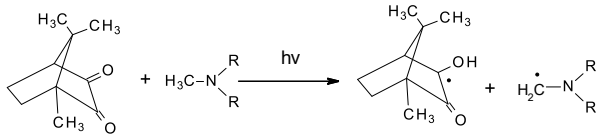

Fig.1. Photolysis of camphorquinone and amine.

The basic problem of this system is the fact that too high concentration of camphorquinone in photocurable dental composites may generate a yellow color. Such discoloration can influence the aesthetics and quality of the final product. In addition, amines are a cytotoxic and genotoxic factor. Therefore, effective photoinitiators for photocurable dental composites without these compounds are needed to be developed [10-9].

In this work, completely new, safe initiating systems based on camphorochinone and a tosyl salt with different substituents have been presented. This system was compared with the standard camphorquinone / amine system. A mixture of BisGMA / TEGDMA monomers in a weight ratio of 7: 3 as the organic matrix was used. It is the most popular organic matrix used to obtain light-cured dental composites. Dental composites conversion rates were studied using real time-FT-IR.

2. Experimental

2.1. Materials

Bisphenol A-glycidyl methacrylate (BisGMA from Sigma Aldrich) and triethylene glycol dimethacrylate (TEGDMA from Sigma Aldrich) (Figure 2) in the 7:3 weight ratio were applied as a model monomers for free-radical photopolymerization for dental application. Camphorquinone (CQ from Sigma Aldrich) and various tosyl salts (Table 1) were used as new initiation systems for photopolymerization processes. The molar ratio of CQ to the tosyl salt was 2: 1 which corresponds to: 0.5 wt. % CQ and about 1 wt. tosyl salt. Camphorquinone (CQ from Sigma Aldrich) and ethyl 4- (dimethylamino) benzoate (EDB from Sigma Aldrich) was used as reference in a molar ratio of 2: 1, which corresponds to 0.5 wt.%. CQ and 0.3% EDB.

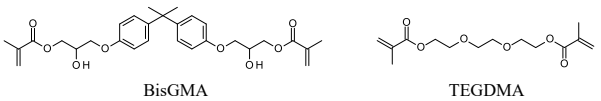

BisGMA TEGDMA

Fig.2. Structures of the monomers.

Table 1. Acronyms, color after curing, and calculated conversion for initiating systems.

Acronym	Colour	Substituent	Conversion [%]
CQ		-	7,0
CQ/EDB		-	75,5
CQ/07-128		**-H**	71,4
CQ/07-129		**-NO_2**	74,6
CQ/07-130		**-CN**	72,3
CQ/07-131		**-$SO2CH_3$**	69,9
CQ/07-133		**dibenzofuran**	68,1
CQ/07-134		**naphthalene**	72,0
CQ/07-027		**anthracene**	71,6

2.2. Methods and apparatus

To determine the conversion rate of monomers, the real time-FT-IR method was used. The equipment was composed of the Thermo Scientific i10 NicoletTM spectrometer with an appropriate horizontal adapter adapted for real time measurements of photopolymerization processes of samples with a thickness of 1.4 mm. As the light source for photopolymerization measurements different diodes (from Thorlabs Inc.) was used. The light was emitted by the UV-LED diode to the sample with a liquid fiber optic cable (from Torlabs Inc.) with a diameter of 5 mm and a length of 1.2 meters was delivered [16]. Measurements were recorded in the OMNIC program.

The photocurable formulations were deposited on a PP films under air. The progress of photopolymerization process was monitored by observing the disappearance of the band at wave number equal approximately 6165 cm^{-1} (Figure 3). The UV-LED diode was started 10 seconds after the start of spectral registration.

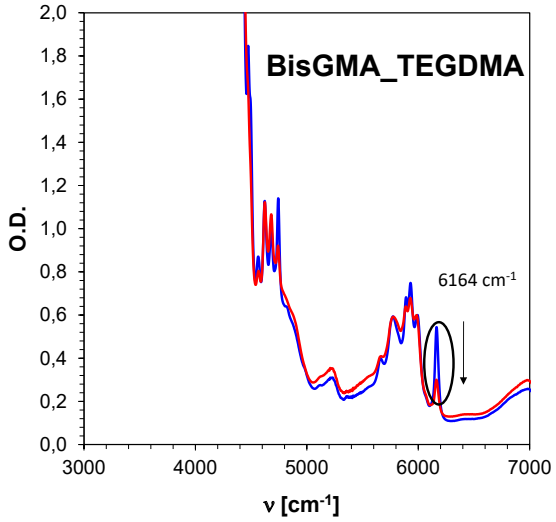

Fig. 3. Near IR spectra recorded before and after polymerization for CQ/EDB in a molar ratio of 1:3 photoinitiating system and BisGMA and TEGDMA monomers followed at 6165 cm^{-1}.

Because the decrease of absorption of the peak area is directly proportional to the number of polymerized groups, the degree of conversion of the function group was calculated by measuring the peak area at each time of the reaction by using equation (1):

$$C_{FT-IR}\ [\%] = \left(1 - \frac{A_{After}}{A_{Before}}\right) * 100\ \% \quad (1)$$

where A_{Before} is an area of the absorbance peak characteristic for used monomer and type of photopolymerization before polymerization process and A_{After} is an area of the same absorbance peak, but after polymerization process.

3. Results and discussion

The photopolymerization process was carried out for only 100 seconds. The compositions were irradiated by a LED with maximum emission at a wavelength of 455 nm (18 mW / cm^2). The samples were 1.4mm thick, so they are applied in dental offices by dentists. Figure 4 shows the dependence of the conversion on time. Camphorquinone alone is not effective in initiating photopolymerization processes of BisGMA / TEGDMA monomers in a weight ratio of 7:3. Nevertheless, the initiation systems consist of camphorquinone and tosyl salts significantly improve the conversion rates obtained. The conversion for all initiation systems is comparable and ranges from 68,1% for the initiating system composed of compound 07-133 (having the benzofuran substituent), to as much as 74,6% for the initiating system composed of caphoroquinone and compound 07-129 (having the -NO_2 substituent) (Table 1).

Moreover, the conversion and speed of the photopolymerization process are comparable to those of the CQ and aromatic amine EDB reference initiator system. The color of the obtained dental composites was also analyzed. then it was shown that only the yellowing of the composite is visible for the initiating system composed of the caphoroquinone and the tosyl salt having the nitro substituent (Table 1).

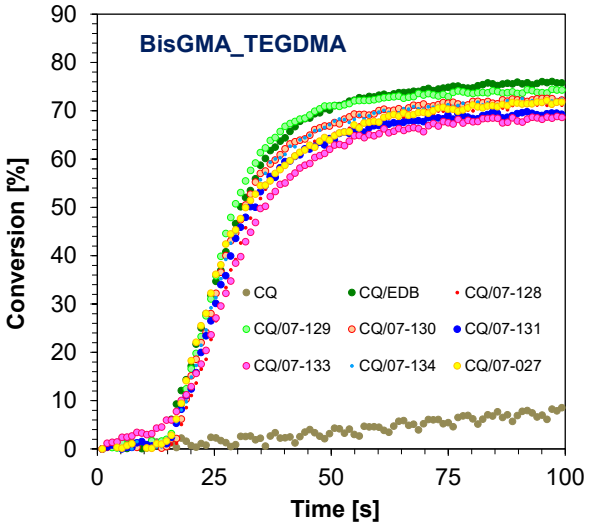

Fig. 4. Polymerization profiles (methacrylate function conversion) for BisGMA/TEGDMA in a weight ratio of 7:3 and initiating system based on CQ and different iodonium salts with tosyl anion.

4. Conclusion

The above communication presents alternative initiating systems based on caforoquinone and tosyl salt in a 2: 1 molar ratio to initiate photopolymerization processes of acrylate monomers used in the production of dental fillings. These systems are comparable to the standard camphorquinone and aromatic amine initiator EDB. As a result, cyto and genotic amine were eliminated from the initiating system, which is extremely beneficial in the production of new generation dental composites.

Acknowledgement

This work was financed by the Polish Ministry of Science and Higher Education from budget funds

for science in the years 2018–2022 as a research project no. 0052/DIA/2018/47 under the "Diamond Grant" program.

References

1. C. Dietlin, S. Schweizer, P. Xiao, J. Zhang, F. Morlet-Savary, B. Graff, J.P. Fouassier, and J. Lalevée, *Polym. Chem*., 6(21) (2015) 3895–3912.
2. W. Funke, *Prog. Org. Coat.*, 6 (1980), 110.
3.M. Kaur, and A. K. Srivastava, J. Macromol. *Sci. Polymer Rev.*, 42(4) (2002) 481–512.
4. M. Layani, X. Wang and S. Magdassi, *Adv. Mater*, (2018), 1706344.
5. I. V. Khudyakov, J.C. Legg, M. B. Purvis, and B. J. Overton, *Ind. Eng. Chem. Res.*, 38(9) (1999) 3353–3359.
6. E. Andrzejewska, *Prog. Polym. Sci.*, 26(4) (2001) 605–665.
7. S. C. Ligon, B. Husár, H. Wutzel, R. Holman R. and R. Liska, *Chem. Rev.*, 114(1) (2013) 557–589.
8. H.Y. Marghalani, H.Y. Handbook of Bioceramics and Biocomposites. Berlin/Heidelberg, Germany: 1st ed.; Springer, 2014; ISBN 9783319092300.
9.A.A. Zandinejad, M. Atai, And A Pahlevan, *Dent. Mater.*, 22 (2006) 382–387.
10.N.B. Cramer, Ch.L. Couch, K. M. Schreck, J. E.Boulden, R.Wydra, J.W. Stansbury and Ch. N. Bowman, *Dent. Mater.*, 26(8) (2010) 799-806.
11. J. Ge, M. Trujillo and J. Stansbury, *Dent. Mater.*, 21(12) (2005) 1163-1169.
12. M. Topa and J. Ortyl, *Materials*, 13 (2020), 4093.
13. B. Pratap, R.K. Gupta, B. Bhardwaj and M. Nag, *Japanese Dental Science Review*, 55(1) (2019) 126–138.
14. R. Srivastava, Wolska, J. Walkowiak-Kulikowska, H. Koroniak and Y. Sun, *Europ. Polym. J.,* 90, (2017) 334–343.
15. J. W. Stansbury, *Journal of Esthetic and Restorative Dentistry*, 12(6) (2000) 300–308.
16. M. Topa, F. Petko, M. Galek, K. Machowski, M. Pilch, P. Szymaszek and J. Ortyl, *Polymers* 11 (2019) 1756.

Journal of Photopolymer Science and Technology
Volume 34, Number 3 (2021) 263−269 ©2021SPST

Top Thermal Annealing of 2D/3D Lead Halide Perovskites: Anisotropic Photoconductivity and Vertical Gradient of Dimensionality

Rei Shimono[1], Ryosuke Nishikubo[1], Fumitaka Ishiwari,[1,2] and Akinori Saeki[1,3*]

[1] Department of Applied Chemistry, Graduate School of Engineering, Osaka University, 2-1 Yamadaoka, Suita, Osaka 567-0871, Japan
[2] Frontier Research Base for Global Young Researchers, Graduate School of Engineering, Osaka University, Suita 565-0871, Japan
[3] Innovative Catalysis Science Division, Institute for Open and Transdisciplinary Research Initiatives (ICS-OTRI), Osaka University, 2-1 Yamadaoka, Suita, Osaka 565-0871, Japan., Japan
**saeki@chem.eng.osaka-u.ac.jp*

Triggered by the notable evolution of organic-inorganic metal halide perovskite solar cells (PSCs) with three-dimensional (3D) ABX_3 (A: organic/inorganic cation, B: metal cation, X: halogen anion) structures, Ruddlesden-Popper two-dimensional (2D) pseudo perovskites given by $A_{n+1}B_nX_{3n+1}$ (n = 1, 2, …) are also becoming a material of interest, as they exhibit improved stability against moisture and oxygen. Controlling the crystallographic orientation of these 2D layers plays a key role in the power conversion efficiency (PCE) of PSCs and their environmental tolerance. Here, we report the effect of top thermal annealing (TTA) on the PSC photoconductivity and performance, where TTA is a process that exposes heat from the top side (rather than the bottom (substrate) side in normal annealing) to form the perovskite layer after anti-solvent treatment. The anisotropic photoconductivity in the in-plane and out-of-plane directions was evaluated, which suggested a vertical gradient of 2D/3D phases with a 3D-rich component on the surface.

Keywords: Perovskite solar cell, Ruddlesden-Popper phase, 2D and 3D structures, Anisotropy, Photoconductivity

1. Introduction

The outstanding nature of organic-inorganic metal halide perovskites has made these materials most suitable for optoelectronic applications such as perovskite solar cells (PSCs)[1–7] and light-emitting diodes.[8–10] The highly efficient perovskite material used in these devices is composed of an ABX_3 type three-dimensional (3D) structure, where A is an organic cation (such as methylammonium, MA; formamidinium, FA), an inorganic cation (such as cesium, Cs), or a mixture of both; B is a lead (Pb) cation; and X is a halogen anion (Cl, Br, I, or a mixture). The power conversion efficiency (PCE) of PSCs almost reaches that of crystalline silicon solar cells,[11] and their applicability in the roll-to-roll solution process and fabrication on a flexible substrate are other notable advantages of PSCs over conventional inorganic solar cells. However, the use of toxic Pb, albeit in small amounts, as well as insufficient long-term stability against environmental conditions (moisture, oxygen, hot/cold) are critical issues for commercialization.[12]

Along these lines, the composition of Ruddlesden-Popper two-dimensional (2D) perovskites described as $R_2A_{n-1}B_nX_{3n+1}$ (n = 1, 2, …), form an immensely important part of PSC[13–15] because the insulating layer introduced by R, bulky organic cations such as *n*-butylammonium cation (BA)[16–19] and 2-phenyl-ethylammonium cation (PEA),[20,21] can prevent the intrusion of oxygen and moisture, thus improving the environmental stability compared to traditional 3D perovskites. By

Received March 14, 2021
Accepted April 28, 2021

sacrificing enhanced stability, 2D perovskites have greater exciton binding energy owing to the formation of quantum wells,[22] resulting in anisotropic charge transport paths.[23,24] These situations lead to a strict requirement on the orientation and gradient of the 2D/3D component to achieve balanced PCE and improved stability of the PSC.

Considering a semiconducting 2D sheet structure composed of octahedral $[PbI_6]^{4-}$, a vertical crystallographic alignment is preferred for efficient charge separation in the out-of-plane (OOP) direction with respect to the electrodes. To implement the vertical orientation, many efforts have been made to explore bulky R cations and develop new solution processes (e.g., solvent, additive, and annealing). Organic cations such as BA, PEA, guanidium (GA), *para*-fluorinated PEA (FPEA),[25,26] and 3-phenyl-2-propenammonium (PPA)[27] have been incorporated in the R spacer cation, which leads to improvements in PCE (~14%), stability, and vertical orientation. Regarding the solution process approach, a hot-casting technique that uses a hot substrate for spin-coating was reported to induce the preferred OOP orientation in the 2D perovskites $BA_2MA_2Pb_3I_{10}$ (n = 3) and $BA_2MA_3Pb_4I_{13}$ (n = 4).[28] Addition of ammonium chloride (NH_4Cl) to the precursor solution can also improve OOP crystal alignment during film formation due to its high volatility and specific adsorption of NH_4Cl to the (202) crystal plane of BA-based 2D perovskites, and the fast deprotonation of NH_4^+ in the presence of H_2O can further facilitate the vertical orientaion.[29] The importance of crystallization control during solvent evaporation has been demonstrated by pre-crystallization annealing, which was carried out by thermal annealing in the presence of dimethylacetamide solvent after a short spin-coating time (20 s).[30] Owing to nucleation from the air-liquid interface, this process induces a vertical orientation in $BA_2MA_3Pb_4I_{13}$ 2D perovskites. This is in sharp contrast to the random orientation obtained after a typical spin-coating time (60 s), which results in nucleation from the mesoporous TiO_2 scaffold or the bulk material due to solvent evaporation and spin-induced convection.[30] These studies suggest that the evaporation of solvent/additive is key for the controlled preparation of 2D perovskites with the preferred OOP orientation.

In this work, we examined another method of thermal annealing, top thermal annealing (TTA), which exposes heat from the top side, rather than from the bottom (substrate) side as in the normal thermal annealing (NTA) process. The n = 3 2D perovskites $R_2A_2Pb_3I_{10}$ with R = BA, PEA, or FPEA and A = MA or FA were prepared from a dimethyl sulfoxide (DMSO) solution and chlorobenzene (CB) was used for poor anti-solvent treatment. After spin-coating, TTA or NTA were applied to the films, where TTA was expected to facilitate crystallization from the top side and improve the vertical orientation. As shown in Fig. 1, TTA was performed by flipping the substrate and keeping it on a heater with a 1 cm-height glass spacer. The orientation of the 2D perovskites was evaluated by 2-dimensional grazing-incidence X-ray diffraction (2D-GIXRD). The anisotropic photoconductivities in the OOP and in-plane (IP) directions were measured by flash-photolysis time-resolved microwave conductivity (TRMC).[31–35] We discuss the conjunction of PSC outputs and stability with the orientation and gradient of 2D/3D perovskites.

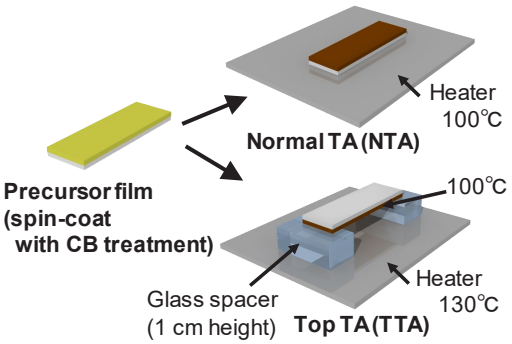

Fig. 1. Schematic of normal thermal annealing (NTA) on a heater and top thermal annealing (TTA).

2. Experimental

Following the reported procedure,[36] the electron transport materials compact TiO_2 ($cTiO_2$) and mesoporous TiO_2 ($mpTiO_2$) were deposited on a cleaned and etched fluorine-doped tin oxide (FTO) on a glass substrate. A DMSO (Wako-Fujifilm) solution of PEAI (Sigma-Aldrich,: SA), MAI (Tokyo Chemical Inc.,: TCI), and PbI_2 (TCI) in a 2 : 2 : 3 ratio (concentration: 1.3 M based on PbI_2) was prepared in a N_2-filled glovebox. Subsequently, a precursor layer was formed by spin-coating the solution at 4,000 rpm. At the end of the spin-coating, CB (SA, anhydrous, 99.8%) was added immediately. In the NTA process, the resulting film was annealed at 100 °C for 20 min, affording a 300 nm-thick perovskite layer. In the TTA process, the film was annealed at 100 °C for 6 min (optimized time) from the top side. Note that this temperature is measured

at the substrate position (heater temperature set to 130 °C). After TTA, the substrate was annealed in the NTA setup at 100 °C for 20 min for complete conversion to a 2D/3D perovskite. The other 2D (FPEA/MA, BA/MA, and PEA/FA) and 3D ($MAPbI_3$, MA:PbI_2=1:1) perovskites were prepared in the same manner with the PEA/MA 2D perovskite. The chemicals were purchased from SA for FPEAI and TCI for BAI and FAI. A 50 nm-thick hole transport material (HTM) of SpiroOMeTAD (Borun New Material Technology Ltd.) in CB (78.2 mg mL^{-1}) was deposited by spin-coating with LiTFSI (52 mol%; SA) and CoTFSI (5.4 mol%; FK209, SA) relative to SpiroOMeTAD dissolved in acetonitrile (SA, anhydrous, 99.8%) and TBP (2.9 vol%; SA, 98%) relative to the solution volume. Subsequently, a 100 nm-thick stripe-shaped gold electrode was thermally deposited in a vacuum chamber.

Current-voltage curves were measured using a source-meter unit (ADCMT Corp., 6241A) under AM 1.5 G solar illumination at 100 mW cm^{-2} (1 sun, monitored by a calibrated standard cell, Bunko Keiki BS-520BK) from a 300 W solar simulator (SAN-EI Corp., XES-301S). The size of the active area was defined by a black metal mask with a square hole (2 × 2 mm^2).

For the TRMC measurements, perovskite, $mpTiO_2$, HTM, and their composite layers were prepared in the same manner as the solar cells on a quartz plate. The sample was set in a resonant cavity and probed by continuous microwaves at ca. 9.1 GHz. The excitation laser from an optical parametric oscillator (Continuum Inc., Panther) seeded by the third harmonic generation of a Nd:YAG laser (Continuum Inc., Surelite II, 5–8 ns pulse duration, 10 Hz) was set at 500 nm at I_0 = 6.4 × 10^{14} photons cm^{-2} $pulse^{-1}$. The photoconductivity transient $\Delta\sigma$ was converted to the product of the quantum efficiency (φ) and the sum of charge carrier mobilities, $\Sigma\mu$ (= $\mu_h + \mu_e$) by $\varphi\Sigma\mu = \Delta\sigma\,(eI_0F_{light})^{-1}$, where e and F_{Light} are the unit charge of a single electron and a correction factor, respectively. All the experiments were conducted at 25 °C in air.

Steady-state photoabsorption spectroscopy was performed using a Jasco V-730 UV-Vis spectrophotometer. Atomic force microscopy (AFM) was performed using a Bruker Innova. X-ray diffraction (XRD) measurements in reflection geometry were performed using a Rigaku MiniFlex-600 instrument (Cu K_α radiation: λ = 1.54 Å). 2D-GIXRD was conducted at the BL46XU beamline of SPring-8, Japan Synchrotron Radiation Research Institute using 12.39 keV (λ = 1.00 Å) X-rays.

3. Results and discussion

Fig. 2a shows schematics of 2D perovskites, and the photoabsorption spectra of 2D and 3D perovskites of R = PEA, A = MA, B = Pb, and X = I. Although the nominal precursor composition was $PEA_2MA_2Pb_3I_{10}$ (n = 3), a wide distribution of n = 1 (PEA_2PbI_4), 2 ($PEA_2MAPb_2I_7$), 3 ($PEA_2MA_2Pb_3I_{10}$), 4 ($PEA_2MA_3Pb_4I_{13}$), and ∞ (3D, $MAPbI_3$) are observed with distinct excitonic peaks. The photoabsorption spectra of the 2D/3D perovskite films prepared by TTA and NTA were mostly identical, indicating that these thermal annealing processes did not change the composition of the n-layered 2D perovskites.

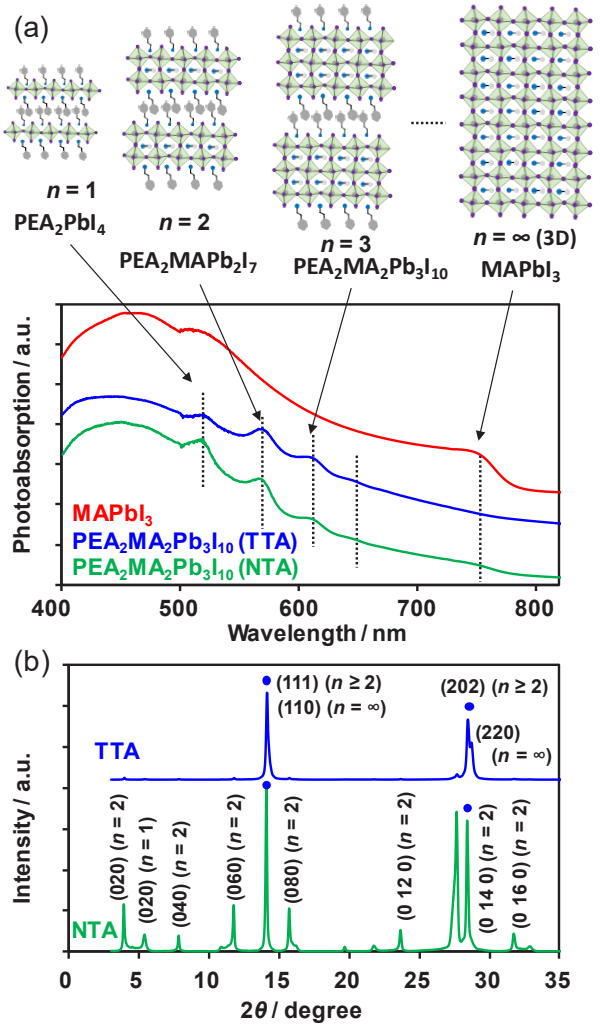

Fig. 2. (a) Upper panel: schematic of 2D and 3D perovskites. Lower panel: photoabsorption spectra of $MAPbI_3$ (3D, red), and $PEA_2MA_2Pb_3I_{10}$ prepared by TTA (blue) and NTA (green). (b) XRD profiles of $PEA_2MA_2Pb_3I_{10}$ prepared by TTA (blue) and NTA (green).

In contrast, the XRD patterns of 2D perovskites prepared by TTA and NTA exhibited a distinct difference at a small diffraction angle ($2\theta < 13°$) (Fig. 2b). The peaks in the 2θ region attributed to 2D perovskites[37] were clearly observed for the NTA film; however, they almost completely disappeared for the TTA film. This suggests either a dramatic change in the crystallographic orientation or the disappearance of 2D perovskites from the surface, which is sensitive to XRD measurements in reflection geometry.

To provide a more detailed insight into the orientation, 2D-GIXRD experiments were performed, as shown in Fig. 3a. The diffraction profiles of the NTA and TTA films in the OOP direction (Fig. 3b) were similar to those from XRD (Fig. 2b). An alternation of crystallographic orientation was, however, not observed, but the intensities of the 2D perovskite diffraction were decreased in both the OOP and IP directions. This result indicated that 3D perovskites preferentially formed on the surface (liquid-air interface side), whereas the 2D perovskite components were likely pushed into the bulk or to the bottom side (less sensitive to XRD and 2D-GIXRD), leading to a vertical gradient of 3D (top) and 2D (bulk and bottom) perovskites. Thus, orientation control of 2D layers could not be achieved. AFM images of NTA and TTA films showed small-sized grains (34.4±17.3 nm and 25.1±10.8 nm, respectively, Fig. 3c), which was more than one order smaller than that of high efficient 3D perovskite and one of the reasons for the low PCE (vide infra).

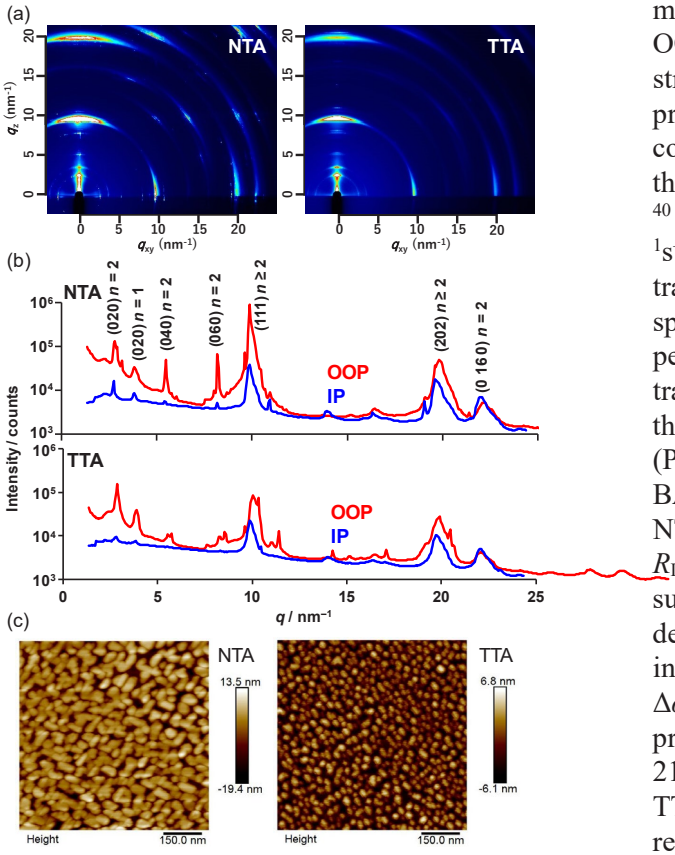

Fig. 3. (a) 2D-GIXRD images of $PEA_2MA_2Pb_3I_{10}$ on a quartz substrate prepared by NTA (left) and TTA (right). (b) OOP (red) and IP (blue) profiles of NTA (upper panel) and TTA (lower panel) samples. (c) AFM images of NTA (left) and TTA (right) $PEA_2MA_2Pb_3I_{10}$.

The anisotropic charge carrier mobilities were evaluated using a TRMC technique, which allows for a contactless measurement of the photoconductivity ($\Delta\sigma$) along the parallel (IP) or perpendicular (OOP) direction by simply changing the optics and sample geometry of an identical film. Because φ (quantum efficiency of charge carrier generation) is basically the same between IP and OOP setups, the ratio of the IP and OOP TRMC signal maxima is regarded as the anisotropy of $\Sigma\mu$ (the sum of charge carrier mobilities) (Figs. 4a–4d). As shown in Figs. 4e and 4f, the ratio of IP and OOP mobilities ($R_{IP/OOP}$) found for $MAPbI_3$ is as large as 140, which indicates a higher charge carrier mobility in the IP direction [(110) plane] than in the OOP direction, despite the relatively isotropic 3D structure ($MAPbI_3$: tetragonal phase), and the presence of multiple grain boundaries. This is consistent with a charge carrier diffusion length in the range of few to tens of μm in the IP direction[38–40] and high charge carrier mobility (> ~1–10 $cm^2V^{-1}s^{-1}$) as measured by Hall effect,[41] a field-effect transistor,[42] TRMC,[43,44] and terahertz spectroscopy.[45,46] The defect-tolerant nature of 3D perovskites is responsible for the efficient charge transport even at the grain boundary.[47,48] In contrast, the $R_{IP/OOP}$ values of 2D perovskites ($PEA_2MA_2Pb_3I_{10}$, $FPEA_2MA_2Pb_3I_{10}$, $BA_2MA_2Pb_3I_{10}$, and $PEA_2FA_2Pb_3I_{10}$) prepared by NTA were decreased to 14–43. The small value of $R_{IP/OOP}$ corresponds to the vertical charge transport suitable for solar cell applications; however, the decreased $R_{IP/OOP}$ is caused by a significant decrease in $\Delta\sigma$ in the IP direction rather than an increase in $\Delta\sigma$ in the OOP direction. The 2D perovskites prepared by TTA showed similar $R_{IP/OOP}$ values of 21–29. $FPEA_2MA_2Pb_3I_{10}$ showed a lower $R_{IP/OOP}$ for TTA (20) than NTA (36), while its OOP $\Delta\sigma$ remained mostly unchanged. Therefore, the TTA process was found to improve the anisotropy in one case (R = PEA and A = MA) but decreased its photoconductivity values.

To examine the vertical gradient of the 3D-rich

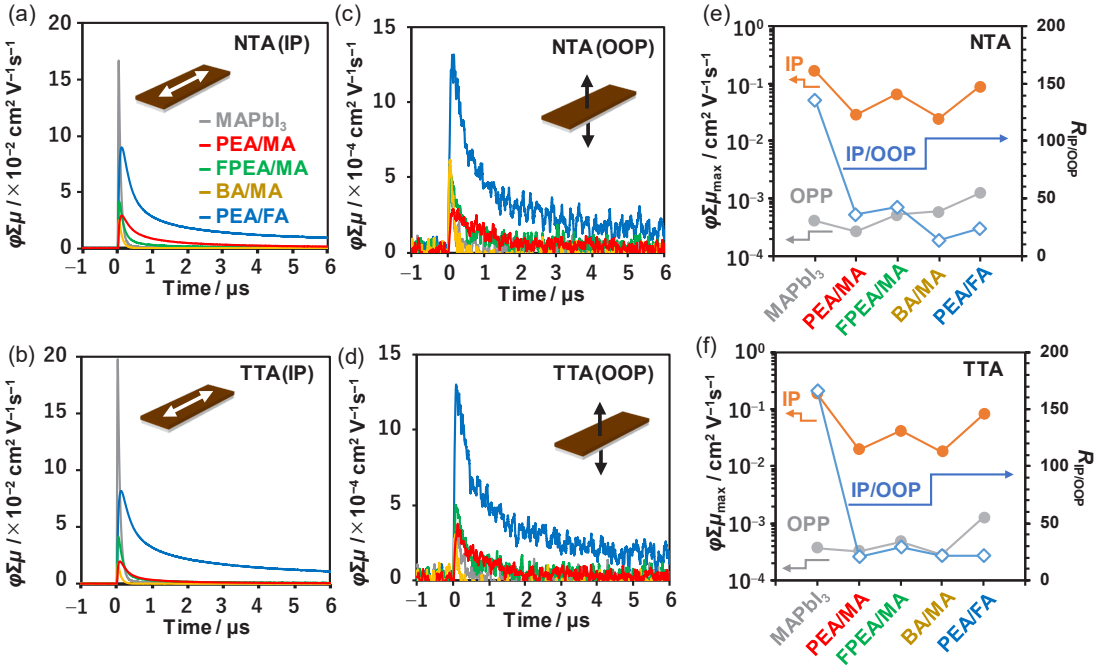

Fig. 4. (a–d) TRMC transients (λ_{ex} = 500 nm) of $MAPbI_3$, $PEA_2MA_2Pb_3I_{10}$, F-$PEA_2MA_2Pb_3I_{10}$, $BA_2MA_2Pb_3I_{10}$, and $PEA_2FA_2Pb_3I_{10}$ observed for NTA (a) and TTA (b) in the IP direction, and NTA (c) and TTA (d) in the OOP direction. The arrow on the schematic film represents the direction of the electric field of microwave probe. (e, f) Plots of the $\varphi\Sigma\mu_{max}$ of NTA (e) and TTA (f) films in the IP (orange) and OOP (gray) direction, with $R_{IP/OOP}$ is plotted on the right axis.

surface and 2D in the bulk, as suggested in the 2D-GIXRD analyses, the $R_{IP/OOP}$ values obtained from TRMC measurements on the back (bottom) and front (top) sides of $PEA_2MA_2Pb_3I_{10}$ were compared. As shown in Fig. 5a, the NTA film did not change for back ($R_{IP/OOP}$ = 24.8) and front ($R_{IP/OOP}$ = 23.4) illumination, whereas the TTA film exhibited an increase in $R_{IP/OOP}$ from 23.7 (back) to 40.5 (front) (Fig. 5b). This result is consistent with the 3D-rich surface (Fig. 5c), because the 3D perovskite shows a high $R_{IP/OOP}$ of over 100. This is also consistent with the increased photoluminescence in the high-energy region (~500–600 nm) and the decreased terahertz signal with light irradiation from the back surface.[49]

Based on these characterizations, we evaluated the standard PSC device FTO/$cTiO_2$/$mpTiO_2$/$PEA_2MA_2Pb_3I_{10}$/SpiroOMeTAD(doped)/Au processed by TTA or NTA. The maximum PCE values of TTA and NTA were 2.20% and 2.67% (average over 6 devices: 1.44 ± 0.59% and 2.22 ± 0.34%, respectively), the difference being mainly due to the short-circuit current density (J_{SC}) (6.92 vs. 7.95 mA cm^{-2}) rather than the open-circuit voltage (V_{OC}) (0.78 vs. 0.81 V) and the fill factor (FF) (0.44 vs. 0.43), as seen from the current density-voltage curves in Fig. 5d. The hysteresis factors [(forward PCE–reserve PCE)(forward PCE)$^{-1}$] of NTA and

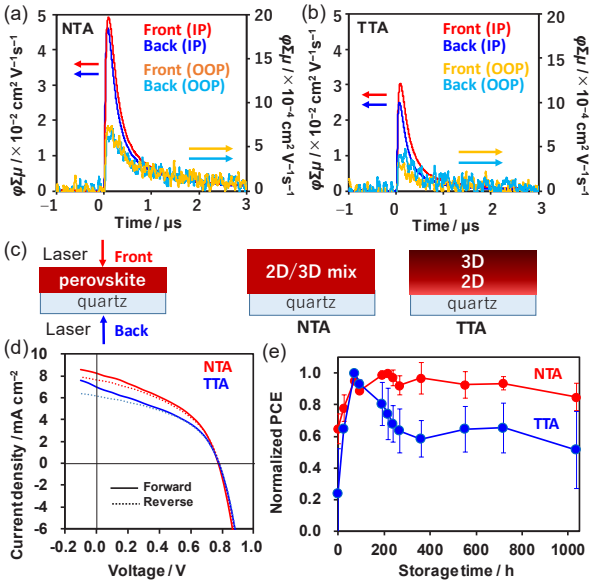

Fig. 5. TRMC transients (λ_{ex} = 500 nm) of $PEA_2MA_2Pb_3I_{10}$ prepared by (a) NTA and (b) TTA. Laser illumination side (front or back) and microwave probe electric field direction (IP or OOP) were changed. (c) Schematics of the front/back illumination and vertical gradient of 3D/2D perovskite for NTA and TTA. (d) Current density-voltage curves of best-performing $PEA_2MA_2Pb_3I_{10}$ PSC prepared by NTA and TTA. (e) Normalized PCE after storage in air (averaged over 6 devices).

TTA were insignificant (0.02 and 0.04, respectively), although a mismatch of J_{SC} for in the forward and reverse scans was observed. The stability tests of these devices were performed for up to 1000 h of storage in air under ambient conditions (Fig. 5e). The PCE reached a maximum at ~20 h, tentatively assigned to oxidation of SpiroOMeTAD in air, and then gradually decreased. The degradation of PCE is mainly owing to the J_{SC} for NTA devices, while the change in both J_{SC} and V_{OC} largely contribute to the PCE of TTA devices. The relative PCE decreased to 51% for TTA and 85% for NTA after 1000 h. The device stability is therefore consistent with the preferential location of 3D perovskite on the surface of the TTA film rather than on the NTA film, as suggested by 2D-GIXRD and TRMC evaluations.

4. Conclusion

We investigated the impact of the TTA (top thermal annealing) process on the orientation, gradient, and anisotropic charge carrier mobility of 2D Ruddlesden-Popper $R_2A_2Pb_3I_{10}$ (n = 3) perovskites. TTA was found to induce a vertical gradient with the 3D phase-rich surface, which led to an unfavorable effect on the P CE and stability of the PSC device. The anisotropy ($R_{IP/OOP}$) of charge carrier mobilities was decreased in the 2D perovskite (R = PEA and A = MA), which is suitable for vertical charge transport but concomitant with a decrease in the OOP photoconductivity. Although TTA has been unsuccessful so far, its combination with additive/solvent may provide an alternative option for 2D perovskite processing, and the findings in this study are useful for further consideration.

Acknowledgment

This work was supported by the Japan Society for the Promotion of Science (JSPS) with the KAKENHI Grant-in-Aid for Scientific Research (A) (Grant No. JP16H02285 and JP20H00398) and Transformative Research Areas (A) "Dynamic Exciton" (Grant No.JP20H05836), Japan Science and Technology Agency (JST) Advanced Low Carbon Technology Research and Development Program (ALCA) (Grant No. JPMJAL1603), and Asahi Glass Foundation. R. N. acknowledges the financial support of a JSPS scholarship (No. 201820108). 2D-GIXRD experiments at SPring-8 were conducted for proposals No. 2020A1742 and 2020A1875.

References

1. W. Chen, X. Li, Y. Li, and Y. Li, *Energy Environ. Sci.*, **13** (2020) 1971.
2. J. Y. Kim, J.-W. Lee, H. S. Jung, H. Shin, and N.-G. Park, *Chem. Rev.* **120** (2020) 7867.
3. A. K. Jena, A. Kulkarni, and T. Miyasaka, *Chem. Rev.*, **119** (2019) 3036.
4. L. Mao, C. C. Stoumpos, and M. G. Kanatzidis, *J. Am. Chem. Soc.*, **141** (2019) 1171.
5. J. S. Manser, J. A. Christians, and P. V. Kamat, *Chem. Rev.*, **116** (2016)12956.
6. W. Zhang, G. E. Eperon, and H. J. Snaith, *Nat. Energy*, **1** (2016) 16048.
7. P. Gao, M. Grätzel, and M. K. Nazeeruddin, *Energy Environ. Sci.*, **7** (2014) 2448.
8. Z. Wei and J. Xing. *J. Phys. Chem. Lett.*, **10** (2019) 3035.
9. P. Docampo and T. Bein, *Acc. Chem. Res.*, **49** (2016) 339.
10. S. A. Veldhuis, P. P. Boix, N. Yantara, M. Li, T. C. Sum, N. Mathews, and S. G. Mhaisalkar, *Adv. Mater.*, **28**, (2016) 6804.
11. M. A Green, E. D. Dunlop, J. Hohl-Ebinger, M. Yoshita, N. Kopidakis, A. W. Y. Ho-Baillie, *Prog. Photovoltaics*, **28** (2020) 3.
12. S. Attique, N. Ali, S. Ali, R. Khatoon, N. Li, A. Khesro, S. Rauf, S. Yang, and H. Wu, *Adv. Sci.*, **7** (2020) 201903143.
13. A. O. El-Ballouli, O. M. Bakr, and O. F. Mohammed, *J. Phys. Chem. Lett.*, **11** (2020) 5705.
14. L. Mao, C. C. Stoumpos, and M. G. Kanatzidis *J. Am. Chem. Soc.*, **141** (2019) 1171.
15. A. S. R. Bati, M. Batmunkh, and J. G. Shapter, *Adv. Energy Mater.*, **10** (2019) 1902253.
16. J.-C. Blancon, H. Tsai, W. Nie, C. C. Stoumpos, L. Pedesseau, C. Katan, M. Kepenekian, C. M. M. Soe, K. Appavoo, M. Y. Sfeir, S. Tretiak, P. M. Ajayan, M. G. Kanatzidis, J. Even, J. J. Crochet, and A. D. Mohite, *Science*, **355** (2017), 1288.
17. X. Zhang, X. Ren, B. Liu, R. Munir, X. Zhu, D. Yang, J. Li, Y. Liu, D.-M. Smilgies, R. Li, Z. Yang, T. Niu, X. Wang, A. Amassian, K. Zhao, and S. F. Liu, *Energy Environ. Sci.*, **10** (2017) 2095.
18. N. R. Venkatesan, J. G. Labram, and M. L. Chabinyc, *ACS Energy Lett.*, **3** (2018) 380.
19. M. Long, T. Zhang, D. Chen, M. Qin, Z. Chen, L. Gong, X. Lu, F. Xie, W. Xie, J. Chen, and J. Xu, *ACS Energy Lett.*, **4** (2019) 1025.
20. X. Zhang, G. Wu, W. Fu, M. Qin, W. Yang, J. Yan, Z. Zhang, X. Lu, and H. Chen, *Adv. Energy Mater.*, **8** (2018) 1702498.
21. S. Chen, N. Shen, L. Zhang, W. Kong, L. Zhang, C. Cheng, and B. Xu, *J. Mater. Chem. A*, **7** (2019) 9542.
22. F. Thouin, D. A. Valverde-Chávez, C. Quarti, D. Cortecchia, I. Bargigia, D. Beljonne, A. Petrozza,

C. Silva, and A. R. S. Kandada, *Nat. Mater.*, **18** (2019) 349.
23. Y. Lin, Y. Fang, J. Zhao, Y. Shao, S. J. Stuard, M. M. Nahid, H. Ade, Q. Wang, J. E. Shield, N. Zhou, A. M. Moran, J. Huang, *Nat. Commun.*, **10** (2019) 1008.
24. Y. Zhang, M. Sun, N. Zhou, B. Huang, and H. Zhou, *J. Phys. Chem. Lett.*, **11** (2020) 7610.
25. F. Zhang, D. H. Kim, H. Lu, J.-S. Park, B. W. Larson, J. Hu, L. Gao, C. Xiao, O. G. Reid, X. Chen, Q. Zhao, P. F. Ndione, J. J. Berry, W. You, A. Walsh, M. C. Beard, and K. Zhu, *J. Am. Chem. Soc.*, **141** (2019) 5972.
26. J. Hu, I. W. H. Oswald, S. J. Stuard, M. M. Nahid, N. Zhou, O. F. Williams, Z. Guo, L. Yan, H. Hu, Z. Chen, X. Xiao, Y. Lin, Z. Yang, J. Huang, A. M. Moran, H. Ade, J. R. Neilson, and W. You, *Nat. Commun.*, **10** (2019) 1276.
27. J. Xi, I. Spanopoulos, K. Bang, J. Xu, H. Dong, Y. Yang, C. D. Malliakas, J. M. Hoffman, M. G. Kanatzidis, and Z. Wu, *J. Am. Chem. Soc.*, **142** (2020) 19705.
28. H. Tsai, W. Nie, J.-C. Blancon, C. C. Stoumpos, R. Asadpour, B. Harutyunyan, A. J. Neukirch, R. Verduzco, J. J. Crochet, S. Tretiak, L. Pedesseau, J. Even, M. A. Alam, G. Gupta, J. Lou, P. M. Ajayan, M. J. Bedzyk, M. G. Kanatzidis, and A. D. Mohite, *Nature*, **536** (2016) 312.
29. Y. Yang, C. Liu, A. Mahata, M. Li, C. Roldán-Carmona, Y. Ding, Z. Arain, W. Xu, Y. Yang, P. A. Schouwink, A. Züttel, F. De Angelis, S. Dai, and M. K. Nazeeruddin, *Energy Environ. Sci.*, **13** (2020) 3093.
30. A. Z. Chen, M. Shiu, J. H. Ma, M. R. Alpert, D. Zhang, B. J. Foley, D.-M. Smilgies, S.-H. Lee, and J. J. Choi, *Nat. Commun.*, **9** (2018) 1336.
31. A. Saeki, *Polym. J.*, **52** (2020) 1307.
32. R. Nishikubo and A. Saeki, *J. Photopolym. Sci. Techol.*, **32** (2019) 735.
33. K. Yamada and A. Saeki, *J. Photopolym. Sci. Technol.* **31** (2018) 157.
34. M. J. Hong, L. Zhu, C. Chen, L. Tang, Y.-H. Lin, W. Li, R. Johnson, S. Chattopadhyay, H. J. Snaith, C. Fang, and J. G. Labram, *J. Am. Chem. Soc.*, **142** (2020) 19799.
35. E. M. Hutter, J.-J. Hofman, M. L. Petrus, M. Moes, R. D. Abellón, P. Docampo, and T. J. Savenije, *Adv. Energy Mater.*, **7** (2017) 1602349.
36. N. Ishida, A. Wakamiya, and A. Saeki, *ACS Photonics* **3** (2016) 1678.
37. W. Peng, J. Yin, K.-T. Ho, O. Ouellette, M. De Bastiani, B. Murali, O. El Tall, C. Shen, X. Miao, J. Pan, E. Alarousu, J.-H. He, B. S. Ooi, O. F. Mohammed, E. Sargent, and O. M. Bakr, *Nano Lett.*, **17** (2017) 4759.
38. G. Xing, N. Mathews, S. Sun, S. S. Lim, Y. M. Lam, M. Grätzel, S. Mhaisalkar, and T. C. Sum, *Science* **342** (2013) 344.
39. V. Gonzalez-Pedro, E. J. Juarez-Perez, W.-S. Arsyad, E. M. Barea, F. Fabregat-Santiago, I. Mora-Sero, and J. Bisquert, *Nano Lett.*, **14** (2014) 888.
40. Q. Dong, Y. Fang, Y. Shao, P. Mulligan, J. Qiu, L. Cao, J. Huang, *Science*, **347** (2015) 967.
41. Y. Chen, H. T. Yi, X.Wu, R. Haroldson, Y. N. Gartstein, Y. I. Rodionov, K. S. Tikhonov, A. Zakhidov, X.-Y. Zhu, and V. Podzorov, *Nat. Commun.*, **7** (2016) 12253.
42. N. Cho, F. Li, B. Turedi, L. Sinatra, S. P. Sarmah, M. R. Parida, M. I. Saidaminov, B. Murali, V. M. Burlakov, A. Goriely, O. F. Mohammed, T. Wu, and O. M. Bakr, *Nat. Commun.*, **7** (2016) 13407.
43. C. S. Ponseca, Jr., T. J. Savenije, M. Abdellah, K. Zheng, A. Yartsev, T. Pascher, T. Harlang, P. Chabera, T. Pullerits, A. Stepanov, J.-P. Wolf, and V. Sundström, *J. Am. Chem. Soc.*, **136** (2014) 5189.
44. H. Oga, A. Saeki, Y. Ogomi, S. Hayase, and S. Seki, *J. Am. Chem. Soc.*, **136** (2014) 13818.
45. C. Wehrenfennig, G. E. Eperon, M. B. Johnston, H. J. Snaith, and L. M. Herz, *Adv. Mater.*, **26** (2014) 1584.
46. H. Zhang, E. Debroye, J. A. Steele, M. B. J. Roeffaers, J. Hofkens, H. I. Wang, and M. Bonn, *ACS Energy Lett.*, **6** (2021) 568.
47. A. Walsh; D. O. Scanlon, S. Chen, X. Gong, and S.-H. Wei, *Angew. Chem., Int. Ed.*, **54** (2015) 1791–1794.
48. R. E. Brandt, J. R. Poindexter, P. Gorai, R. C. Kurchin, R. L. Z. Hoye, L. Nienhaus, M. W. B. Wilson, J. A. Polizzotti, R. Sereika; R. Žaltauskas, L. C. Lee, J. L. MacManus-Driscoll, M. Bawendi, V. Stevanović, and T. Buonassisi, *Chem. Mater.*, **29** (2017) 4667−4674.
49. R. L. Milot, R. J. Sutton, G. E. Eperon, A. A. Haghighirad, J. M. Hardigree, L. Miranda, H. J. Snaith, M. B. Johnston, L. M. Herz, *Nano Lett.* **16** (2016) 7001–7007.

Journal of Photopolymer Science and Technology
Volume 34, Number 3 (2021) 271−278 ©2021SPST

Photoinduced Charge Carrier Dynamics of Metal Chalcogenide Semiconductor Quantum Dot Sensitized TiO_2 Film for Photovoltaic Application

Safna Ravindi Padmaperuma[1], Maning Liu[1], Ryosuke Nakamura[2], and Yasuhiro Tachibana[1,2*]

[1] School of Engineering, RMIT University, Bundoora, VIC 3083, Australia
[2] Project Research Center for Fundamental Sciences, Faculty of Science, Osaka University, 1-1 Machikaneyama, Toyonaka, Osaka 560-0043, Japan
**yasuhiro.tachibana@rmit.edu.au; y.tachibana@uic.osaka-u.ac.jp*

Semiconductor quantum dot (QD) sensitization is one of the most attractive structures to employ QDs for photovoltaic application. The function of QD sensitized solar cells (QDSSC) is controlled by the interfacial charge transfer dynamics. Here we employ transient absorption spectroscopy (TAS) to assess charge transfer dynamics at CdS QD/TiO_2 interface, and correlate their dynamics with their solar cell performance. An electron injection occurs from CdS QD conduction band to TiO_2 on ultrafast time scales, and the time constant decreases from ~10 ps to 1 ps, as the QD size decreases from 4 nm to 1.6 nm. Also, the charge recombination lifetime at the QD/TiO_2 interface increases, as the QD size increases. An absorbed photon to current conversion efficiency (APCE) of the QDSSC increases, as the QD size increases. Therefore, we conclude that the APCE of the CdS QDSSC is controlled by the interfacial charge recombination dynamics competing with dynamics of the hole transfer from the QD valence band to the reduced electrolyte. The optimum CdS QD size is close to or larger than 4 nm, as long as the light harvesting efficiency of the CdS QD sensitized film is sufficiently high.

Keywords: Electron injection, Charge recombination, CdS quantum dot sensitized TiO_2, Solar cells, Quantum dot size, Photocurrent generation efficiency

1. Introduction

Semiconductor quantum dot (QD) is one of the most attractive photoactive nanomaterials to be applied to optoelectronic devices such as light emitting diodes, lasers, optical sensors and solar cells.[1-7] For photovoltaics application, QDs are generally employed as a light absorber owing to their band gap tunability with their size, excellent photostability and their relatively high extinction coefficient.[8-12] Once ODs are assembled to form a QD solid film, it can also be employed as a charge transporting layer.

To design efficient QD based devices, it is extremely important to control charge carrier transfer dynamics at a QD/charge transport layer interface. To function as a solar cell, such an interface is designed to induce fast interfacial charge separation following light absorption by the QDs and subsequently to retard interfacial charge recombination (ICR), while the dissociated charge carriers are transported away from the interface. QD sensitization is the most suitable structure to understand a mechanism of their interfacial charge transfer dynamics and to identify an underlying key parameter to control and optimize the charge separation and recombination dynamics.

Metal chalcogenide QD sensitized solar cells (QDSSCs) have widely been developed over the last decade. A solar energy conversion efficiency of 5.4% was achieved by Kamat and coworkers by doping optically active transition metal ion (Mn^{2+}) into CdS QDs to suppress interfacial charge recombination.[13] This metal ion (Mn^{2+}) creates mid band gap states where the light generated electrons are trapped, but screened to prevent recombination with the generated holes in the QDs

Received April 17, 2021
Accepted April 30, 2021

or reaction with the oxidized species in the electrolyte.[13, 14] Intensive studies have been conducted to develop highly efficient QDSSCs with a solar energy conversion efficiency of 12%[15], and recently, a significant improvement has been made with an efficiency of 15.3% by introducing a novel secondary deposition method resulting in $MgCl_2$ solution treated Zn-Cu-In-S-Se QD sensitized TiO_2 electrodes.[16]

The function of the QDSSC is initiated by an electron injection (EI) from a QD to the conduction band (CB) of n-type nanocrystalline metal oxide such as TiO_2, following light absorption by the QD.[17] Upon light excitation, i.e. when the absorbed photon energy exceeds the band gap energy of the QD, an electron-hole pair (exciton state) is formed inside the QD, and then the EI reaction occurs from the QD CB to the TiO_2 CB, before the electron-hole recombination occurs inside the QD. The injected electrons are readily transported inside TiO_2 (n-type semiconductor) and collected by the FTO before recombined with the generated holes inside the QD or the oxidized electrolyte. Also before the ICR, the generated holes inside the QD are reduced by the electrolyte, and transported to the counter electrode.[18]

Extensive studies have been performed to investigate interfacial charge transfer processes, in particular EI[19, 20] and ICR[21] between a QD and TiO_2 using transient absorption spectroscopy (TAS). The dynamics results confirm that the EI occurs on ultrafast time scales (typically on sub-picosecond to 100 ps),[20, 22-25] while ICR occurs on nanosecond to microsecond time scale.[23, 26, 27] However, despite these ample kinetic results and investigation to control the interfacial charge transfer reactions, no study has so far been conducted to correlate the interfacial charge transfer dynamics with the solar cell performance. Therefore, no study was reported to design interfacial structures to optimize QD size and solar cell performance.

In this paper, we employ CdS QD sensitized TiO_2 films to investigate photo-induced charge transfer dynamics at the CdS QD/TiO_2 interface, and to assemble and characterize a CdS QDSSC. The resultant dynamics will be correlated with the solar cell performance to identify an underlying key parameter to control a solar cell performance. The most suitable CdS QD size will be proposed to design an optimal solar cell structure.

2. Experimental

2.1. Materials

TiO_2 paste (Solaronix SA, Ti-Nanoxide HT/SP) was purchased from Solaronix SA, Switzerland. Sulfur powder (99.98%), lithium perchlorate ($LiClO_4$) (99.99%), $Na_2S{\cdot}9H_2O$ (≥98%), $Cd(ClO_4)_2{\cdot}xH_2O$, were purchased from Sigma-Aldrich, Australia, and ethanol (99.5%) was from ChemSupply, Australia, Al_2O_3 powder (Aeroxide Alu C, particle diameter: approximately 13 nm) was provided by Evonik Degussa GmbH, Australia. All chemicals were used without further purification.

2.2. Preparation of CdS QD attached nanoporous metal oxide films

A fluorine doped tin oxide (FTO) glass plate (15 × 25 mm^2, 9 - 11 Ω/sq., Asahi Glass, type-U) was sonicated for 15 min in acetone. A transparent TiO_2 nanocrystalline film (printed area: 0.25 cm^2, film thickness: 6 μm) was prepared by screen-printing the TiO_2 paste (Solaronix SA, Ti-Nanoxide HT/SP) on the FTO substrate. Al_2O_3 nanocrystalline films (thickness: 3.0 μm) were prepared by the same screen printer, but with a different printing mask, using a home-made Al_2O_3 paste, following the previously reported method.[26, 28] A CdS QD attached nanocrystalline film was prepared by using the "successive ionic layer adsorption and reaction" (SILAR) technique.[17, 29] One cycle was completed by dipping the film in 0.1 M $Cd(ClO_4)_2$ aqueous solution for 1 min, followed by rinsing in water and drying, and then dipping the film in 0.1 M Na_2S aqueous solution for 1 min, followed by rinsing in water and drying. This sequential coating was repeated 5~25 cycles for the TiO_2 film (CdS-5~25/TiO_2) and 18 cycles for the Al_2O_3 film (CdS/Al_2O_3).

2.3. Solar cell fabrication

The sandwich cell was fabricated by binding a polysulfide electrolyte in a PET spacer (thickness 25 μm) with the QD sensitized TiO_2 electrode and the Pt counter electrode.[17, 29] The polysulfide electrolyte was prepared by dissolving 3 M S, 2 M $Na_2S{\cdot}9H_2O$, and 0.1 M $LiClO_4$ in an ethanol/water mixture at a ratio of 1:4, and purged with N_2 gas. All the steps involved in the solar cell fabrication were conducted under ambient conditions. The QDs in the solar cell are stable at least for several hours under the light irradiation in the laboratory.

2.4. Characterization of CdS QD sensitized films

Absorption spectra were measured by a UV/Vis absorption spectrometer (JASCO, V-670).

Morphology of the CdS QD sensitized film was observed by FE-SEM (Hitachi, S-5200).

2.5. Photovoltaic measurements

Performance of the solar cell was assessed by observing incident photon-to-current conversion efficiency (IPCE) spectra under the light irradiation with an irradiation aperture area of 4.8 × 4.8 mm^2 using a photomask.[17, 29] The IPCE spectra were obtained by a monochromatic light source (Bunko-Keiki, SM-100) and a source meter (Keithley Instruments Inc.: 2400). A 0.5 cm^2 silicon photodiode was used to calibrate the monochromatic light intensity.

2.6. Transient absorption spectroscopy (TAS)

Femtosecond TAS measurements were conducted by an amplified mode-locked Ti:sapphire laser system operating at 1 kHz.[22] Pump pulses at 400 nm (3.1 eV) were generated by frequency doubling fundamental pulses in BBO crystal, while the femtosecond supercontinuum generated in a sapphire plate was used as broadband probe pulses. The spot sizes at sample position were 200 and 100 μm in diameter for pump and probe pulses, respectively. The pump pulse energy was adjusted to 40 nJ/pulse, which corresponds to about 100 $\mu J/cm^2$ per pulse. The polarization of the pump pulse was set at the magic angle (54.7°) with respect to the probe pulse. The probe pulse after the sample was dispersed onto a diode array detector with a spectrometer. The output signals were digitized and collected at the repetition rate of the laser system (1 kHz). The pump beam was modulated at 500 Hz by a mechanical chopper, frequency locked to the laser pulse train. The group velocity dispersion (GVD) of the broadband probe pulse was estimated from the measurement of the cross-phase modulation in 1.0 mm quartz glass, and then, the data were corrected for GVD. The full width at half-maximum of the cross-correlation traces between the pump and probe pulses was 0.15 ps.

Sub-microsecond to millisecond transient absorption studies were conducted by a home-built transient absorption spectrometer with a Nd/YAG laser (Spectra Physics, QuantaRay GCR-11) pumped dye laser (Usho Optical Systems, DL100, ~10 ns pulse duration) as a pump pulse source, a 100 W tungsten lamp as a probe light source, a photodiode-based detection system (Costronics Electronics), and a TDS-2022 Tektronix oscilloscope.[26] All transient data were collected by confirming identical excitation homogeneity and density of absorbed photons for all samples. An excitation wavelength was selected to 425, 480, 500, 515, and 520 nm for CdS-5, -10, -15, -20, and -25/TiO_2, respectively. The CdS/Al_2O_3 film was excited at 480 nm. The measurements were conducted with low pulse excitation energy densities (120~150 $\mu J/cm^2$), corresponding to about 2 absorbed photons per TiO_2 nanoparticle, with a repetition rate of 1 Hz at 25 ºC. This excitation energy adjustment was confirmed by setting ~2 mΔOD at 800 nm for the TiO_2 film sensitized by (tetrabutylammonium)$_2$cis-(2,2′-bipyridyl-4-COOH,4′-COO-)$_2$(NCS)$_2$-ruthenium (II), N719 (Solaronix), for each excitation wavelength.[30, 31] No change in the steady state absorption spectra before and after the transient experiments was observed, suggesting that the samples are stable during the optical experiments.

3. Results and discussion

3.1. Influence of CdS coating cycles on QD sizes

Fig. 1 shows absorption spectra of CdS QD sensitized TiO_2 films at different coating cycles. A shift of the absorption onset to a longer wavelength was observed with the increase of the coating cycle, indicative of "quantum size effect", suggesting that the QD size increases with the increase of the coating cycle. An absorbance also linearly increases with the number of the coating cycles, suggesting that the amount of CdS inside the TiO_2 nanoporous structure increases almost linearly with the number of the coating cycle.

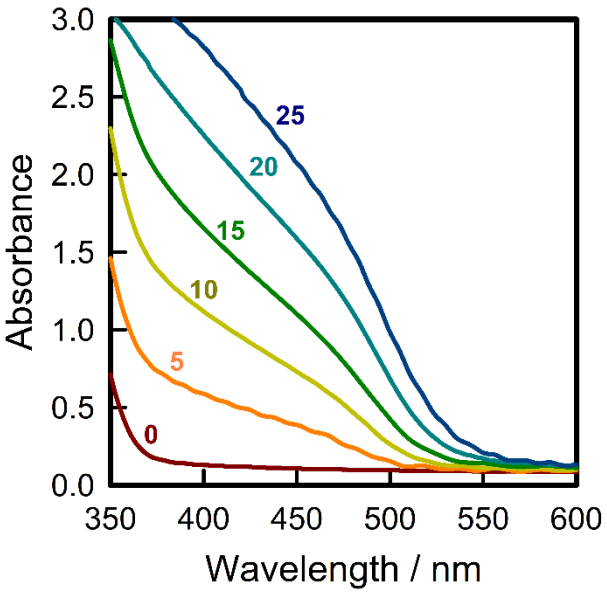

Fig. 1. Absorption spectra of CdS QD sensitized TiO_2 films. The number in the figure indicates a coating cycle of the SILAR method to prepare in-situ CdS QDs inside the TiO_2 nanoporous structure.

Table 1. CdS QD size and electron transfer dynamics.

Coating cycle	QD diameter / nm	QD surface coverage	EI time constant / ps	EI yield / %	ICR half lifetimes / μs	APCE at 400 nm / %
5	1.6	0.97	1.2	96	0.5	38
10	3.0	0.20	3.2	90	4	65
15	4.0	0.22	9.5	80	25	75
20	4.1	0.30			40	74
25	4.2	0.38	8.2	81	50	82

Fig. 2 shows FE-SEM images of a TiO_2 nanocrystalline film and a CdS QD sensitized TiO_2 film with 5 CdS coating cycles. The comparison clearly indicates the formation of CdS QDs on the TiO_2 surface (Fig. 2b). Although the QD can be recognized in the figure, it is not easy to estimate the average QD size formed on the TiO_2 surface. We therefore estimated average QD size in each film with XRD measurements.[26] The QD size was estimated by fitting the line widths ((111), (220) and (311) faces) of the CdS XRD spectra with Gaussian function, using the Debye-Scherrer formula. The results are summarized in Table 1. The results indicate that the CdS crystal size increases to about 4 nm with the number of coating cycles up to 15 cycles, and does not increase further with the extended coating cycles.[26]

Based on the reported relationship of the extinction coefficient with the CdS QD size,[12] using the absorption data shown in Fig. 1 and the average QD size summarized in Table 1, we estimated the coverage of the QDs on the TiO_2 nanoporous surface, assuming that the TiO_2 film is formed with close packing of the TiO_2 nanoparticles with the diameter of 20 nm, and all TiO_2 surface area is available for QDs to be occupied. The results are summarized in Table 1. In all films, less than 1 mono-particle layer of CdS QDs is formed on the TiO_2 nanoporous film.

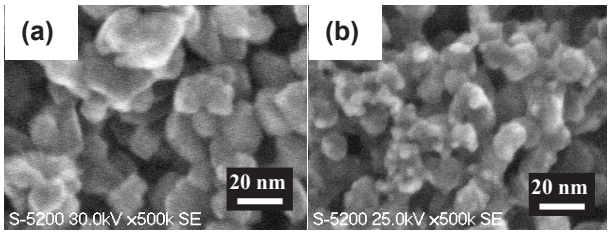

Fig. 2. FE-SEM images of an unsensitized TiO_2 film (a) and the CdS QD (5 coatings) sensitized TiO_2 film (b).

3.2 Photo-induced charge transfer dynamics

We conducted TAS measurements for CdS sensitized TiO_2 films with the coating cycles ranging from 5 to 25 cycles, to observe influence of the coating cycles on interfacial charge transfer dynamics.

Fig. 3 shows transient absorption spectra of CdS QD sensitized TiO_2 films, observed at 0.2 and 100 ps, and 2 μs after the excitation. The spectrum of CdS QD attached Al_2O_3 film, observed at 2 μs after the excitation is included in Fig. 3c. The CdS/Al_2O_3 was used as a reference sample, as Al_2O_3 doesn't thermodynamically accept an electron from the CdS QD CB. A weak positive absorption difference was observed for CdS QD attached Al_2O_3 film, attributed to the tail of the exciton states of CdS QDs. In contrast, a clear positive absorption difference with the maximum at 600-650 nm was observed at

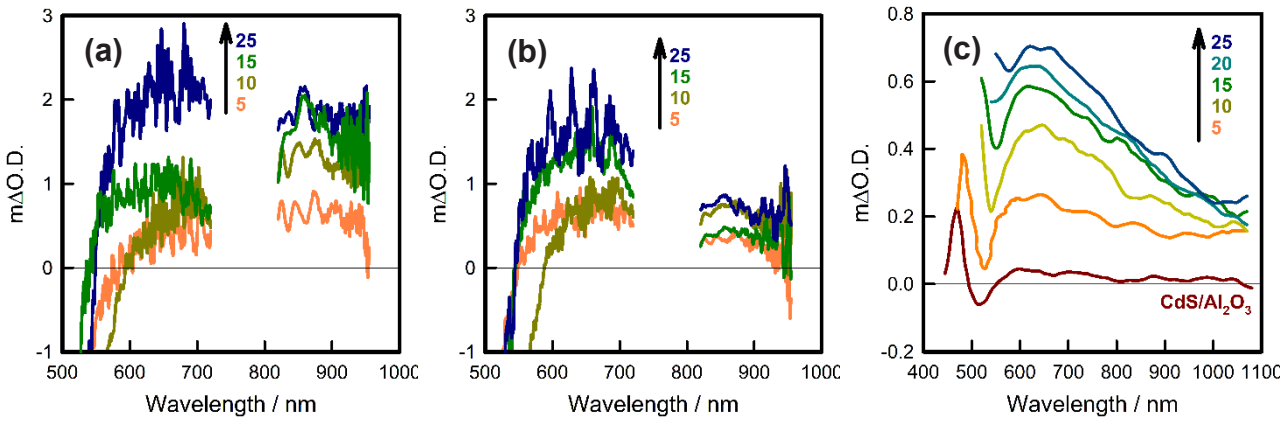

Fig. 3. Transient absorption spectra of CdS QD sensitized TiO_2 films, observed at 0.2 ps (a), 100 ps (b) and 2 μs (c) after the excitation. The number indicates a coating cycle to prepare CdS QDs. Transient absorption spectrum of CdS QD attached Al_2O_3 is also shown as a reference in Fig. 2c.

100 ps and 2 μs after the excitation for the CdS/TiO_2 films. This positive broad absorption is assigned to absorption by trapped holes or S^- radical states in CdS QDs,[26] thereby indicating a charge separated state (an electron in TiO_2 and a hole in CdS QD). The larger absorption difference was observed in the wavelength range of 800~950 nm, compared to the range of 550~720 nm in Fig. 3a, indicating that the charge separation at the CdS/TiO_2 interface occurs after 0.2 ps, but prior to 100 ps.

Fig. 4 shows ultrafast EI dynamics from the CB of CdS QD to that of the TiO_2, monitored at 650 nm, for the CdS QD sensitized films with different coating cycles ranging from 5 to 25 cycles. Note that such dynamics was not observed for the CdS/Al_2O_3 films.[22] The EI time constant was evaluated by fitting all decay data with a global analysis, and the fitted result was summarized in Table 1. The results indicate that the EI occurs on <10 ps, but is faster with the smaller QD size. These observations are reasonable, since the thermodynamic driving force for the EI reaction, i.e. Gibbs free energy difference between the QD CB edge and the TiO_2 CB edge becomes larger, and the electronic coupling between the CdS QD CB edge and the TiO_2 CB edge also becomes larger with the decrease of the QD size.

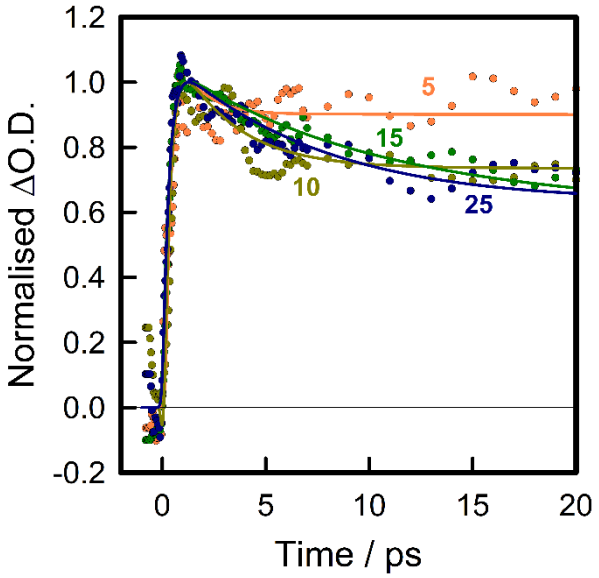

Fig. 4. Transient absorption profiles of CdS QD sensitized TiO_2 films, monitored at 650 nm after 400 nm excitation. A solid line shows the result of fitting with a single exponential function following a global analysis. The number indicates a coating cycle to prepare CdS QDs.

The EI yield was calculated using Equation 1 by comparing the electron injection rate with the rate of the electron trapping in CdS QDs, assuming that the trapped electrons are not injected into TiO_2.

$$EI\ yield = \frac{\frac{1}{\tau_{EI}}}{\frac{1}{\tau_{EI}} + \frac{1}{\tau_{Trap}}} \quad (1)$$

where τ_{EI} is the EI time constant, and τ_{Trap} is the time constant of an electron trapped in the CdS QD. The results are shown in Table 1. The yield decreases with the increase of the coating cycle or the QD size, but the yield exceeds 80% at any QD size.

Fig. 5 shows transient decay dynamics measured at 650 nm for CdS QD/TiO_2 films ranging from 5 to 25 coating cycles. These multi-exponential kinetics indicate the ICR between the electron in TiO_2 and the hole in CdS QD. Since the identical number of photons is absorbed by CdS QDs for any film with different coating cycles upon the excitation, the difference in the decay dynamics must originate from the difference of the CdS QD size.

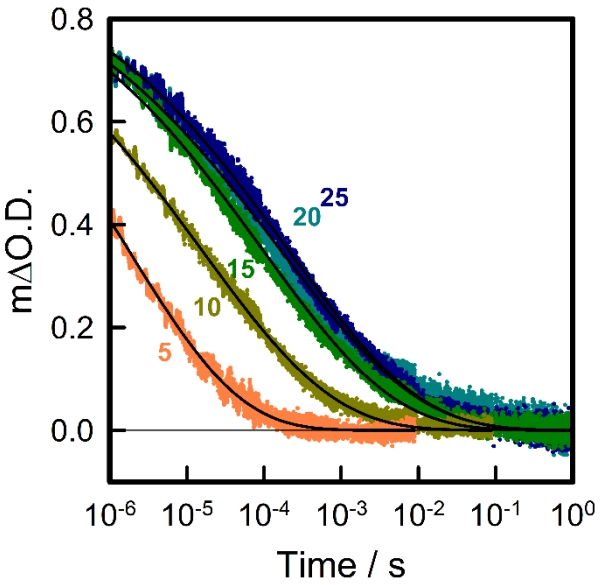

Fig. 5. Transient absorption decays of CdS QD sensitized TiO_2 films, monitored at 650 nm. A solid line shows the results of fitting with a stretched exponential function. The number indicates a coating cycle to prepare CdS QDs.

These decays were analyzed by fitting them with a stretched exponential function ($\Delta OD(t) = \Delta OD_0\ e^{-(t/\tau)^{\alpha}}$) and the half lifetimes (time taken for 50% of charge separated states to recombine) are included in Table 1. It is clear that the ICR occurs on nanosecond to microsecond time scales. The ICR was retarded by increasing the number of the coating cycles. These observations are reasonable, since the electronic coupling between the CdS QD valence band edge and TiO_2 CB edge becomes larger with the decrease of the CdS QD size (from 1.6 nm to 4 nm). Note that influence of the hole mobility between the CdS QDs on the ICR rate is

negligible, as all films show less than 1 mono-particle layer coverage of CdS QDs on the TiO_2 surface.

3.3. Correlation of charge transfer dynamics with photocurrent generation efficiency

To investigate the influence of the coating cycle on the solar cell performance, we have fabricated a solar cell with CdS QD/TiO_2 films ranging from 5 to 25 coating cycles, Pt counter electrode and a polysulfide electrolyte (see Experimental for the details of the cell fabrication), and measured photocurrent generation under monochromatic light irradiation.

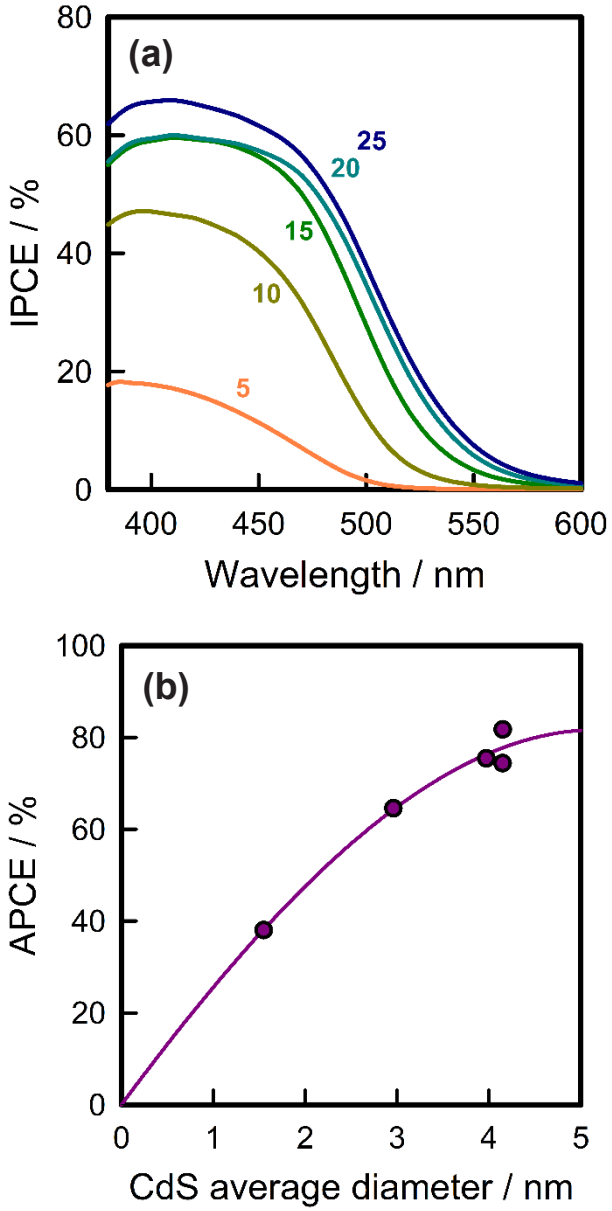

Fig. 6. (a) IPCE spectra of CdS QDSSCs. The number indicates a coating cycle to prepare CdS QDs. (b) APCE at 400 nm as a function of CdS QD size. A solid line shows a guide for the eyes.

Fig. 6a shows their IPCE spectra. The IPCE increases with the number of the CdS coating cycles owing to increase of light harvesting efficiency (LHE). The highest IPCE of 65% at 400 nm was achieved with 25 coating cycles. Moreover, with the number of the coating cycles the IPCE onset shifted to longer wavelengths. This may be due to the band gap decrease resulting from QD size increase (quantum size effect), in agreement with the absorption onset shift to a longer wavelength, shown in Fig. 1.

Fig. 6b shows the absorbed photon to current conversion efficiency (APCE) at 400nm as a function of CdS QD size. The APCE was calculated with IPCE and LHE at the specified wavelength. The LHE of the cell was determined from the absorbance at the specified wavelength using Equation 2.

$$LHE\ (\lambda)\ = 1 - 10^{-Absorbance\ (\lambda)} \qquad (2)$$

The APE was then calculated with Equation 3, and the results are summarized in Table 1.

$$APCE\ (\lambda) = IPCE(\lambda)/LHE(\lambda) \qquad (3)$$

The APCE value clearly increases with the increase of the QD size, however it reaches the maximum as the QD size increases to about 4 nm.

In Fig. 4 and Table 1, the EI completes in <10 ps, and the EI efficiency is greater than 80% at any QD size. These results suggest that the APCE is not limited by the EI process. In contrast, the ICR is retarded with the QD size increase (Fig. 5), and this retardation appears to influence the APCE value. Thus, it is reasonable to consider that the hole transfer from the QD valence band to the reduced electrolyte (S^{2-}) competes with the ICR reaction at the CdS QD/TiO_2 interface, thereby determining the APCE.

From the current study, we have identified that controlling the ICR rate at the CdS QD/TiO_2 interface is the underlying key parameter to maximize the photocurrent generation, i.e. short circuit photocurrent density, J_{SC}. Since the CB edge of the bulk CdS is more negative by at least 200 mV than the TiO_2 CB edge,[26] the efficient EI is expected at the bulk CdS/TiO_2. The optimum CdS QD size is therefore close to or larger than 4 nm, as long as the LHE of the CdS QD sensitized film is sufficiently high.

4. Conclusion

We have employed transient absorption spectroscopy (TAS) to measure charge transfer reactions of CdS sensitized TiO_2 films prepared by the SILAR method. We have investigated the influence of the coating cycles on electron injection (EI) rate, EI yield, interfacial charge recombination (ICR) rate, IPCE and APCE. The EI rate increased with the decreased QD size while the ICR was retarded with the increase of the CdS QD size. The APCE is mainly influenced by the ICR rate which competes with the transfer of the hole in CdS QD to the electrolyte. These observations suggest that the ICR process at the CdS QD/TiO_2 interface is the most important factor determining the CdS QDSSC performance. Therefore, the optimum CdS QD size is close to or larger than 4 nm, as long as the LHE of the CdS QD sensitized film is sufficiently high.

Acknowledgement

This work was partly supported by JSPS KAKENHI Grants (JP16K05885) and (JP19H02813) and the Collaborative Research Program of Institute for Chemical Research, Kyoto University (grant number 2021-78), Japan. We also acknowledge supports from ARC DP fund (DP180103815), ARC LIEF fund (LE200100051) and ARC LIEF fund (LE170100235), Australia, and Project Research Center for Fundamental Sciences, Faculty of Science at Osaka University.

References

1. H. Zhang, Q. Su, and S. Chen, *Nat. Commun.,* **11** (2020) 2826.
2. T. Kim, K.-H. Kim, S. Kim, S.-M. Choi, H. Jang, H.-K. Seo, H. Lee, D.-Y. Chung, and E. Jang, *Nature,* **586** (2020) 385.
3. J. Roh, Y.-S. Park, J. Lim, and V. I. Klimov, *Nat. Commun.,* **11** (2020) 271.
4. J. Lim, Y.-S. Park, and V. I. Klimov, *Nat. Mater.,* **17** (2018) 42.
5. K.-S. Cho, C.-W. Baik, H. Jeong, S. Hwang, K.-S. Cho, K. Heo, C.-W. Baik, S. Hwang, K. Heo, Y. Choi Jun, H. Jeong, and Y. Lee Sang, *Nat. Commun.,* **8** (2017) 840.
6. J. Du, R. Singh, I. Fedin, A. S. Fuhr, and V. I. Klimov, *Nat. Energy,* **5** (2020) 409.
7. M.-J. Choi, F. P. Garcia de Arquer, A. H. Proppe, A. Seifitokaldani, J. Choi, J. Kim, S.-W. Baek, M. Liu, B. Sun, M. Biondi, B. Scheffel, G. Walters, D.-H. Nam, J. W. Jo, O. Ouellette, O. Voznyy, S. Hoogland, S. O. Kelley, Y. S. Jung, and E. H. Sargent, *Nat. Commun.,* **11** (2020) 103.
8. P. V. Kamat, *J. Phys. Chem. C,* **112** (2008) 18737.
9. S. Rühle, M. Shalom, and A. Zaban, *Chem. Phys. Chem.,* **11** (2010) 2290.
10. L. Cademartiri, E. Montanari, G. Calestani, A. Migliori, A. Guagliardi, and G. A. Ozin, *J. Am. Chem. Soc.,* **128** (2006) 10337.
11. I. Mora-Seró, S. Giménez, T. Moehl, F. Fabregat-Santiago, T. Lana-Villareal, R. Gómez, and J. Bisquert, *Nanotechnology,* **19** (2008) 424007.
12. W. W. Yu, L. Qu, W. Guo, and X. Peng, *Chem. Mater.,* **15** (2003) 2854.
13. P. K. Santra and P. V. Kamat, *J. Am. Chem. Soc.,* **134** (2012) 2508.
14. K. Zhao, Z. Pan, and X. Zhong, *J. Phys. Chem. Lett.,* **7** (2016) 406.
15. A. Sahu, A. Garg, and A. Dixit, *Solar Energy,* **203** (2020) 210.
16. H. Song, Y. Lin, Z. Zhang, H. Rao, W. Wang, Y. Fang, Z. Pan, and X. Zhong, *J. Am. Chem. Soc.,* **143** (2021) 4790.
17. R. M. Evangelista, S. Makuta, S. Yonezu, J. Andrews, and Y. Tachibana, *ACS Appl. Mater. Interfaces,* **8** (2016) 13957.
18. H. K. Jun, Careem, and A. K. Arof, *Renew. Sus. Energy Rev.,* **22** (2013) 148.
19. I. Robel, V. Subramanian, M. Kuno, and P. V. Kamat, *J. Am. Chem. Soc.,* **128** (2006) 2385.
20. J. L. Blackburn, R. J. Ellingson, O. I. Mićić, and A. J. Nozik, *J. Phys. Chem. B,* **107** (2003) 102.
21. H. J. Lee, J.-H. Yum, H. C. Leventis, S. M. Zakeeruddin, S. A. Haque, P. Chen, S. I. Seok, M. Grätzel, and M. K. Nazeeruddin, *J. Phys. Chem. C,* **112** (2008) 11600.
22. R. Nakamura, S. Makuta, and Y. Tachibana, *J. Phys. Chem. C,* **119** (2015) 20357.
23. J.-W. Lee, S. Makuta, S. Sukarasep, J. Bo, T. Suzuki, T. Nakayama, H. Suematsu, K. Niihara, and Y. Tachibana, *J. Photopolym. Sci. Technol.,* **29** (2016) 357.
24. K. Gopidas, M. Bohorquez, and P. V. Kamat, *J. Phys. Chem.,* **94** (1990) 6435.
25. J. E. Evans, K. W. Springer, and J. Z. Zhang, *J. Chem. Phys.,* **101** (1994) 6222.
26. Y. Tachibana, K. Umekita, Y. Otsuka, and S. Kuwabata, *J. Phys. Chem. C,* **113** (2009) 6852.
27. R. S. Dibbell and D. F. Watson, *J. Phys. Chem. C,* **113** (2009) 3139.
28. S. Makuta, M. Liu, M. Endo, H. Nishimura, A. Wakamiya, and Y. Tachibana, *Chem. Commun.,* **52** (2016) 673.
29. Y. Tachibana, H. Y. Akiyama, Y. Ohtsuka, T. Torimoto, and S. Kuwabata, *Chem. Lett.,* **36**

(2007) 88.
30. M. Liu, M. Endo, A. Shimazaki, A. Wakamiya, and Y. Tachibana, *ACS Appl. Energy Mater.,* **1** (2018) 3722.
31. M. Liu, S. Makuta, S. Tsuda, S. Russo, S. Seki, J. Terao, and Y. Tachibana, *J. Phys. Chem. C,* **121** (2017) 25672.

Journal of Photopolymer Science and Technology
Volume 34, Number 3 (2021) 279−284 ©2021SPST

Effect of 2-propanol Immersing on Organohalide Perovskite Layer in Perovskite Solar Cells Fabricated by Two-step Method

Daiki Okawa, Yoshiyuki Seike, and Tatsuo Mori *

Department of Electrical and Electronics Engineering, Graduate School of Engineering, Aichi Institute of Technology,
1247 Yachigusa, Yakusa-cho, Toyota, Aichi 470-0392, Japan
**t2mori@aitech.ac.jp*

In the 2-step method of $CH_3NH_3PbI_3$, the $CH_3NH_3PbI_3$ layer is converted using methylammonium iodide (MAI) after coating a PbI_2 layer. Although the use of dimethyl sulfoxide (DMSO) is reported to enhance the crystal quality of perovskite layer, we could not achieve the similar result. We studied the relationship between the layer properties of PbI_2 and the DMSO content in solvent. In addition, we checked the layer properties of perovskite layer and the photovoltaic performance of the cells with the above perovskite active layers. We found the immerse process of PbI_2 in 2-propanol influences the reconstruction of PbI_2 morphology and the diffusion process of MAI depends on the PbI_2 morphology.
Keywords: Organic perovskite, Solar cell, 2-step method, Immersion treatment, XRD, IR spectroscopy

1. Introduction

12 years passed over since Miyasaka group used a perovskite material as an absorbance dye of dye-sensitized solar cell in 2009[1]. The power conversion efficiency (PCE) of a whole solid perovskite solar cell approached to 11%[2]. The PCE of perovskite solar cell is reported to be beyond 25% in 2020[3]. This PCE is almost comparable to that of mono-crystal silicon solar cell. The fabrication methods of perovskite solar cells are categorized by a dry process, vacuum-deposition [4,5] and a wet process. The stable and high quality perovskite layer can be fabricated by the vacuum-deposition. However, the use of vacuum equipment have a disadvantage for a low-cost manufacture and massive production. Therefore, the production of perovskite solar cells will carry out by a wet process. In a wet (solution) fabrication process of perovskite layer, two main methods are well-known: 1-step method [6,7] and 2-step method[8]. In 1-step method, the solution including all materials is applied in one coating. On the other hand, in 2-step method, the post material (i.e. methylammonium iodide (MAI)) is applied in second coating after applying one material (i.e. PbI_2) in first coating. Finally the precursor layer is converted to perovskite (i.e. $CH_3NH_3PbI_3$).

The formation process of crystal is classified by the formation of crystal nuclei and the growth of crystal. In the 1-step method, both processes are thought to occur at a time in the converted process. When the formation of crystal nuclei and the growth of crystal progress at a time, it is possible to form small crystals because each crystal growth is blocked each other. Therefore, some post treatments are often used in the 1-step method. One is the solvent engineering (another name, anti-solvent) method[9] and the other is the solvent annealing method[10]. On the other hand, if the formation of crystal is optimally controlled in the 2-step method, the formation of crystal nuclei will occur at the surface of the pre-coated layer and the crystal will grow gradually to the direction of thickness. Therefore, a high quality perovskite layer can be fabricated by the ideal 2-step method. It is important to study the formation process of perovskite layer in detail. We reported the fabrication processes of perovskite layer in the previous papers, i.e., air

Received April 2, 2021
Accepted April 30, 2021

flow[11,12], solvent anneal[13,14], and electron extraction layer[15-17].

Wu et.al. reported that the PbI_2 layer fabricated from dimethyl sulfoxide (DMSO) solution is amorphous[18]. Other paper also reported the similar result[19-21]. The high-quality perovskite layer without a resultant PbI_2 layer can be converted from the amorphous PbI_2 layer. Although we attempted the perovskite layer using DMSO solvent in the 2-step method, unfortunately our perovskite layers were not always converted perfectly. In this paper, we report the effect of DMSO solvent to the fabrication of PbI_2 and perovskite layers.

2. Experimental

2.1. Materials and fabrication

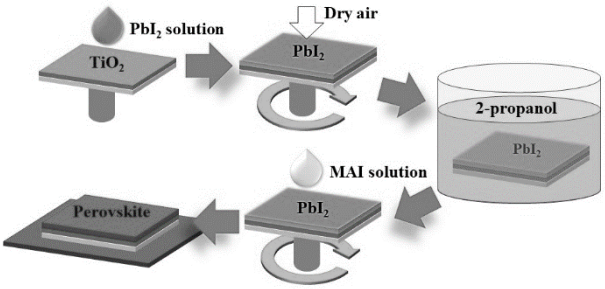

Fig. 1. Schematic of the 2-step method for the fabrication of $CH_3NH_3PbI_3$ layer.

Fluorine-doped tin oxide (FTO) substrates were cleaned by water, organic solvents and tetramethylammonium hydroxide. 30 nm-thick TiO_2 compact layer was fabricated as an electron extraction layer on FTO electrodes. PbI_2 layers were spin-coated from the mixture solution of DMSO and DMF. The PbI_2 of 461 mg was dissolved in the mixture solvent of 1 mL. The composition of the mixture solvents were DMSO 0, 25, 50, 75, and 100 vol%. The spin-coated PbI_2 layers were immersed in 2-propanol for 5 minutes to obtain a shiny black surface under air atmosphere. The spin-coat condition was 4,000 rpm, 30 s with the air-flow procedure. Detailed air-flow experimental procedure is described in the previous paper[11-13]. The PbI_2 layers were converted to perovskite layer by dipping in MAI solution for 30 seconds. MAI 30mg was dissolved in 2-propanol of 3mL. The perovskite ($CH_3NH_3PbI_3$) layers were annealed at 100 °C, 10 minutes on a hotplate.

In the fabrication of PV cells, 100 nm-thick spiro-MeOTAD layer was fabricated on perovskite layer as a hole extraction layer. 50 nm-thick Au was vacuum-deposited as a top electrode. The structure of our devices were FTO/TiO_2/ $CH_3NH_3PbI_3$/spiro-MeOTAD/Au.

2.2. Measurements

Specimen thickness were measured with a thickness tester (Kosaka Laboratory, Surfcorder, ET200). X-ray diffraction (XRD) patterns were recorded in the 2θ range of 5-60°using an X-ray diffractometer (Rigaku RINT2500/PC) with Cu Kα radiation (40kV, 100mA). The infrared spectroscopic spectra were measured using the IR Prestige 21 (Shimadzu). Current-voltage (J-V) characteristics were measured using a digital source meter (Agilent B2901A). A 150 W xenon lamp (Bunkoukeiki, Otento-SUN3 Xe-150) was used as the solar simulator of the AM 1.5 G condition (100 mW/cm^2)

3. Results and discussion

Fig. 2 shows the thickness of PbI_2 immersed in 2-propernol and the $CH_3NH_3PbI_3$ layers converted from the PbI_2 layers. The thickness of PbI_2 layers decreases with increasing DMSO content. Since the unit cell of $CH_3NH_3PbI_3$ is larger than the unit cell of PbI_2, the thickness of $CH_3NH_3PbI_3$ layer is thicker than the thickness of original PbI_2 layer. Of course, the thickness of converted $CH_3NH_3PbI_3$ layer depends on that of original PbI_2 layer.

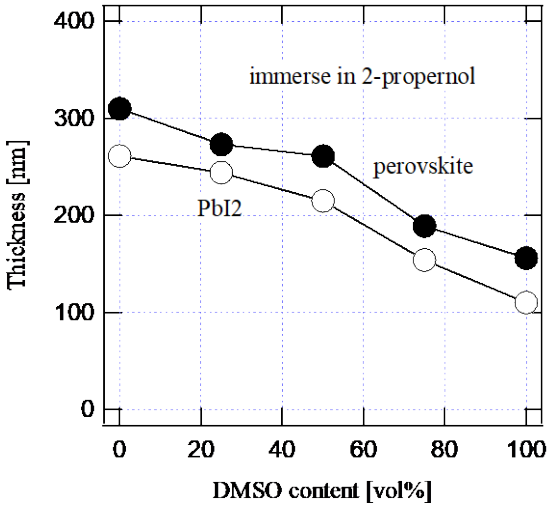

Fig. 2. The thickness of PbI_2 layers immersed in 2-propernol and converted $CH_3NH_3PbI_3$ layers.

Figs. 3 (a) and 3(b) show the XRD patterns of PbI_2 and perovskite layers depending on DMSO content in solvent. The peaks of $2\theta = 12.6°$ and 13.8° are due to the peak of PbI_2(001) and $CH_3NH_3PbI_3$(110), respectively. The peaks of PbI_2(001) and perovskite(110) are observed in XRD patterns in Fig. 3 (b). In most perovskite specimens, the resultant PbI_2 layer exists. The addition of DMSO does not diminish the crystallinity of PbI_2 but enhances the crystallinity. For example, the thickness of PbI_2 layer

fabricated from DMSO 50 vol%-solvent is twice or more thicker than that of PbI_2 layer fabricated from DMSO 100vol%-solvent, but the peak intensity of PbI_2(001) of the former is a half or less lower than that of the latter. The PbI_2 layer fabricated from only DMF solvent is low-crystalline. This result is inconsistent with the previous reports[19-21]. The boiling point of DMF, 153℃ is lower than that of DMSO, 189℃. When the drying rate is fast, the crystallinity is poorer because of the inhibition of crystal growth. Therefore, if PbI_2-DMSO complex are not formed, we speculate the crystallinity of PbI_2 layers fabricated by DMSO solution ought to be higher than that of PbI_2 layers fabricated by DMF solution. The crystallinity of PbI_2 layers fabricated by DMF solution strongly depends on the fabrication atmosphere (temperature, DMF gas concentration, etc.).

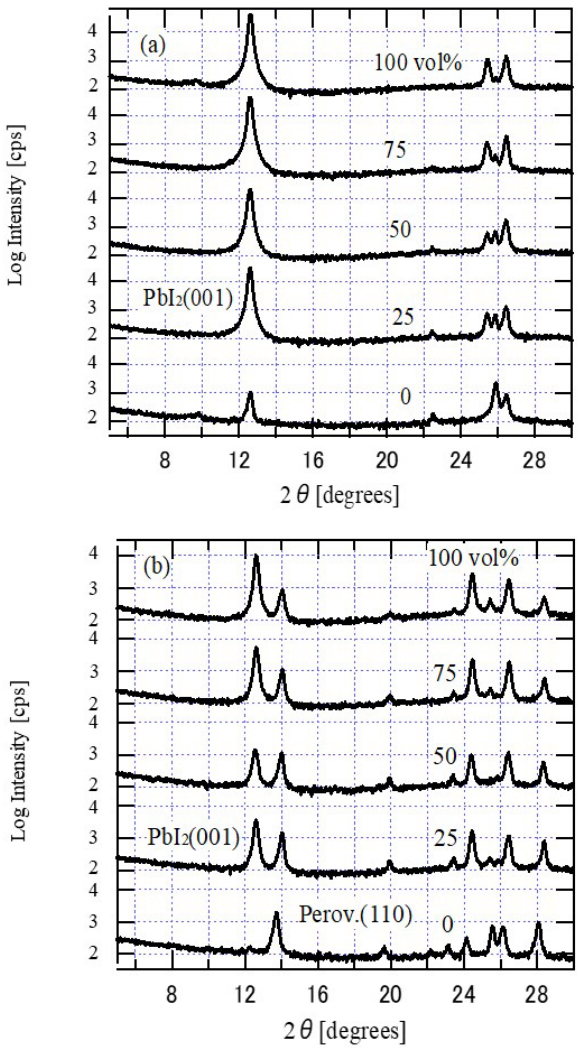

Fig. 3. The XRD pattern of PbI_2 layers fabricated using the solvents with DMSO content of 0, 25, 50, 75, and 100 vol% (a) and perovskite layers converted from the above PbI_2 (b).

Fig. 4 shows the absorption spectra of perovskite layers which are converted from PbI_2 layers fabricated using the solvents with different DMSO contents. As DMSO content increases, the absorbance of the perovskite layer decreases because of the decrease in thickness. The absorbance of perovskite layer is proportional to the thickness.

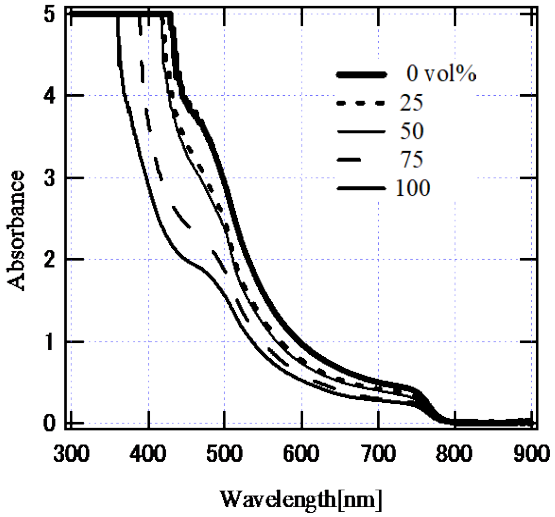

Fig. 4. Absorption spectra of perovskite layers converted using PbI_2 layers fabricated with different DMSO contents in solvent.

Fig. 5 shows the photocurrent curves of the perovskite solar cells fabricated using PbI_2 layers converted with different DMSO contents in solvent. Table 1 shows the PV parameters of perovskite solar cells in Fig. 5. As DMSO content increases, the short-circuit current density (J_{SC}), open circuit voltage (V_{OC}), and fill factor (FF) decrease. Consequently the PCE of the DMSO 0vol%-specimen is the maximum. The slight decrease of J_{SC} is caused by the decrease in optical absorption, i.e. the decrease in the thickness of perovskite layer. However, the ratios of thickness and of absorption (@700 nm) for 0 vol% per 100 vol% perovskite layer are 0.50 and 0.57, respectively. The ratio of PbI_2(001) peak in XRD for 0 vol% per 100 vol% perovskite layer is 0.44. The difference of J_{SC} between 0 vol% and 100 vol% specimens cannot be quantitatively explained by the amount of light absorption. In spite of small light absorption, the fact that the 100 vol% specimen shows the comparable J_{SC} to the 0 vol% specimen may suggest the formation of high-quality perovskite layer. On the other hand, the decreases in V_{OC} and FF suggest a poor device performance.

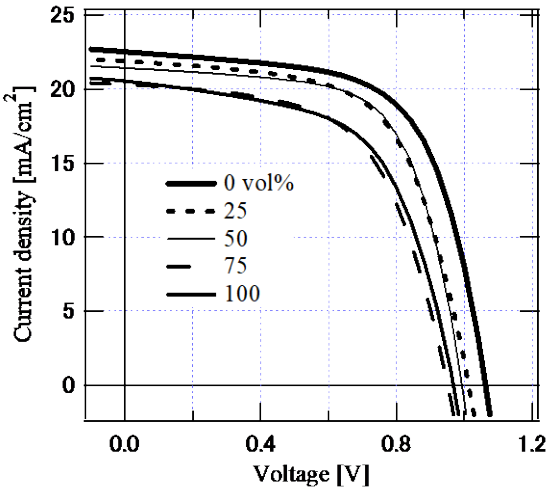

Fig. 5. Photocurrent curves of the perovskite solar cells fabricated using PbI_2 layers converted with different DMSO contents in solvent.

Table 1. Summary of PV parameters of cells in Fig. 5.

DMSO[vol%]	0	25	50	75	100
J_{SC} [mA/cm^2]	22.4	21.8	21.4	20.3	20.5
V_{OC} [V]	1.05	1.00	0.976	0.930	0.949
FF	0.585	0.583	0.614	0.552	0.551
PCE[%]	13.8	12.7	12.8	10.5	10.7

We measured some EQE spectra of 0 vol%(DMF) and 100 vol%(DMSO) specimens. However, the Jsc calculated from IPCE spectra are 24.7 and 18.2 mA/cm^2, respectively. Since the former thickness of perovskite layer is twice thicker than the latter thickness, the crystalline quality of perovskite layer in the 100 vol%(DMSO) specimen may be higher than that of perovskite layer in the 0 vol%(DMF) specimen.

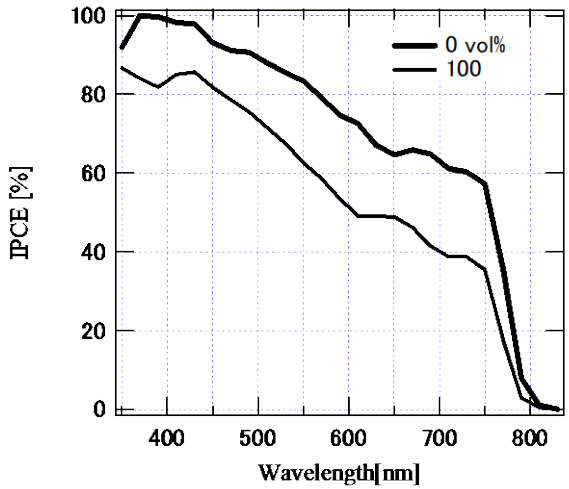

Fig. 6. IPCE spectra of the perovskite solar cells fabricated using PbI_2 layers with 0 vol%(DMF) and 100 vol%(DMSO).

The PbI_2 layer fabricated using only DMF is low-crystalline in our result. The device performance of the 0 vol% specimen is the best of five specimens. As reported in the previous papers[18-21], when the perovskite layer converted from the low-crystalline PbI_2 is used, the device performance is improved.

We compared our fabrication process with the previous fabrication processes. In our process, the immersion treatment in 2-propanol is carried out after spin-coating PbI_2 layers. Therefore, the effect of immersion treatment on the PbI_2 layer was estimated by IR spectroscopy.

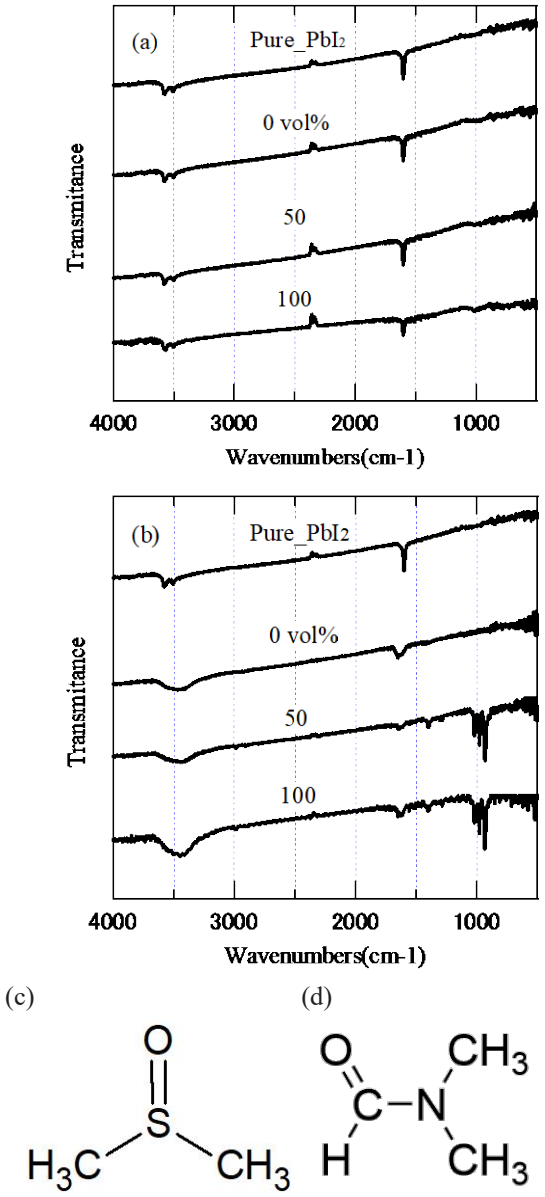

Fig. 7. The IR spectra of the fine PbI_2 layers fabricated (a) with and (b) without the immersion treatment in 2-propanol: the chemical structures of DMSO (c) and DMF (d); DMSO contents of 0, 50, 100 vol%.

Figs. 7 (a) and (b) show the IR spectra of the fine PbI_2 layer fabricated with and without the immersion treatment in 2-propanol. The absorption of 1,000 cm^{-1} is due to the stretching vibration of S = O. The absorption of the stretching vibration of C - N is around 1,200 cm^{-1}.

The IR spectra of all immersed PbI_2 pellets are same and either absorption is not observed in Fig. 7 (a). It is thought that any resultant solvent is little included in the immersed PbI_2 layers. On the other hand, the absorption of SO is observed in the IR spectra of non-immersed PbI_2 pellets of 50 and 100 vol% in Fig. 7 (b). However, the absorption of CN is not observed in the IR spectra of non-immersed PbI_2 pellet of 0 vol%.

This result suggests that the DMSO molecules remain in the PbI_2 layers fabricated from DMSO solvents but the DMSO molecules are removed by the immersion treatment in 2-propanol.

Fig. 8 shows the IR spectra of PbI_2 layers fabricated with different immersion times. When the immersing time is 0 min (non-immersion), the absorption of DMSO is observed at 1,000 cm^{-1}. However, the absorption of S = O disappears after 5 min immersion. Residual DMSO molecules in the PbI_2 layer are removed by 2-propanol immersion for 5 minutes. In addition, PbI_2 crystals are reconstructed when the DMSO molecules are removed. Consequently, the crystallinity of PbI_2 will be improved by 2-propanol immersion treatment.

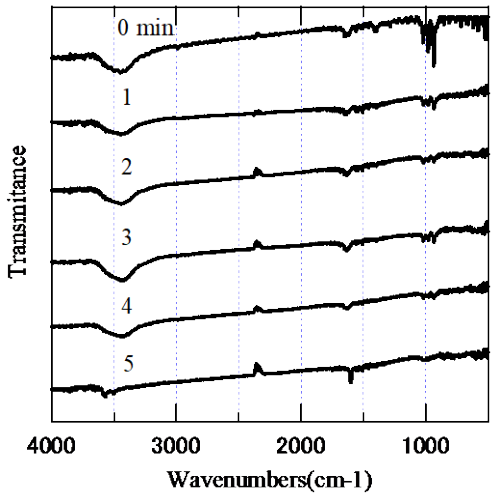

Fig. 8. The IR spectra of the PbI_2 layer fabricated from 100 vol% DMSO solvent by changing an immersion time.

Figs. 9 (a) and (b) show the XRD patterns of non-immersed PbI_2 layers fabricated from different DMSO solvents and the perovskite layers converted the above PbI_2 layers. The peaks of $2\theta = 9.7°$, 12.6° and 13.8° are due to the peak of $PbI_2(DMSO)x$, $PbI_2(001)$ and $CH_3NH_3PbI_3(110)$, respectively. The peaks of $PbI_2(001)$ and perovskite(110) are observed in XRD patterns in Fig. 9 (b). When DMSO is included in the solvent for PbI_2, DMSO molecules form the complex with PbI_2 as reported in the previous paper[19]. Since these complexes inhibit the smooth crystal growth of PbI_2. Consequently, PbI_2 layers fabricated from DMSO solvents are low-crystalline.

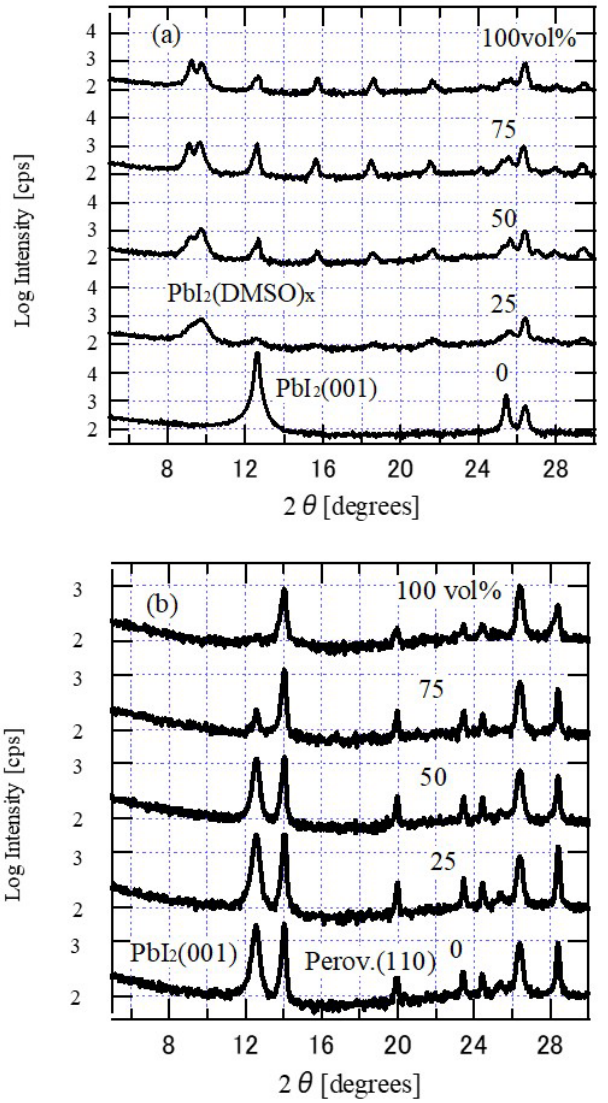

Fig. 9. The XRD patterns of (a) non-immersed PbI_2 layers fabricated and (b) perovskite layers fabricated using the above PbI_2 layers.

PbI_2 are converted from the surface contacted with MAI. When the diffusion rate of MAI in PbI_2 layer is slower than the conversion rate of $CH_3NH_3PbI_3$, the supply of MAI from the contacted surface will be suppressed by the compact $CH_3NH_3PbI_3$ thin layer because the unit cell of $CH_3NH_3PbI_3$ is larger than the unit cell of PbI_2. MAI will be not supplied in the PbI_2 region separated from the surface.

Consequently, the resultant PbI_2 layer occur in $CH_3NH_3PbI_3$ layer. When the low-crystalline PbI_2 layer is formed, MAI can be rapidly supplied to the deep PbI_2 region through free volumes. Therefore, it is thought that there are little the resultant PbI_2 layers in the low-crystalline PbI_2 layer. How we check the device performance.

4. Conclusion

We fabricated PbI_2 layers fabricated from different DMSO contents in solvent and the $CH_3NH_3PbI_3$ layer converted from the above PbI_2 layers. First we did not obtain the similar results in the previous papers but found to be caused by the immersion treatment in 2-propanol. Although the addition of DMSO in solvent produced the complex PbI_2(DMSO)x, DMSO molecules were removed by the immersion of PbI_2 in 2-propanol for 5 min. The addition of DMSO enhanced low-crystalline. The low-crystalline PbI_2 layer is effective for the rapid conversion to $CH_3NH_3PbI_3$ layer without a resultant PbI_2 layer.

Acknowledgements

This research is partially obtained by the AIT Special Grant “Development of Hybrid-Power Science & Technology for Green-Energy”, and the AIT special grant for Education and Research.

References

1. A. Kojima, K. Teshima, Y. Shirai, and T. Miyasaka, *J. Am. Chem. Soc.*, **131** (2009) 6050.
2. M. M. Lee, J. Teuscher, T. Miyasaka, T. N. Murakami, and H. J. Snaith, *Science*, **338** (2012) 643.
3. NREL, URL https://www.nrel.gov/pv/ device-performance.html.
4. M. Liu, M. B. Johnston, and H. J. Snaith, *Nature*, **501** (2013) 395.
5. S.-Y. Hsiao, H.-L. Lin, W.-H. Lee, W.-L. Tsai, K.-M. Chiang, W.-Y. Liao, C.-Z, Ren-Wu, C.-Y. Chen, and H.-W. Lin, *Adv. Mater.*, **28** (2016) 7013.
6. H.-S. Kim, C.-R. Lee, J.-H. Im, L.-B. Lee, T. Moehl, A. Marchioro, S.-J. Moon, R. Humphry-Baker, J.-H. Yum, J. E. Moser, M. Grätzel, and N.-G. Park, *Sci. Rep.*, **2** (2012) 1.
7. L. Etgar, P. Gao, Z. Xue, Q. Peng, A. K. Chandiran, B. Liu, Md. K. Nazeeruddin, and M. Grätzel, *J. Am. Chem. Soc.*, **134** (2012) 17396.
8. J.-H. Im,I.-H. Jang, N. Pellet, M. Grätzel, and N.-G. Park, *Nature Nanotechnol.*, **9** (2014) 927.
9. N. J. Jeon, J. H. Noh, W. S. Yang, Y. C. Kim, S. Ryu, J. Seo, and S. I. Seok, *Nature Mater.*, **13** (2014) 897.
10. Z. Xiao, Q. Dong, C. Bi, Y. Shao, Y. Yuan, and J. Huang, *Adv. Mater.*, **26** (2014) 65.
11. B. Lei, V. O. Eze, and T. Mori, *Jpn J. Appl. Phys.*, **54** (2015) 100305.
12. V. O. Eze, B. Lei, and T. Mori, *Jpn J. Appl. Phys.*, **55** (2016) 02BF08.
13. T. Mori, H. Okada, V. O. Eze, and Y. Seike, *J. Photopolym. Sci. Technol.*, **33** (2020) 399.
14. V. O. Eze, Y. Seike, and T. Mori, *ACS Appl. Mater. Interfaces*, **12**, **41** (2020) 46837.
15. B. Lei, V. O. Eze, and T. Mori, *J. Nanosci. and Nanotechnol.*, **16** (2016) 3176.
16. V. O. Eze, Y. Seike, and T. Mori, *Org. Electron.*, **46** (2017) 253.
17. X. Li, Y. Liu, V. O. Eze, T. Mori, Z. Huang, K. P. Homewood, Y. Gao, and B. Lei, *Solar Ener. Mater. Solar Cells*, **196** (2019) 157.
18. Y. Wu, A. Islam, X. Yang, C. Qin, J. Liu, K. Zhang, W. Peng, and L. Han, *Energy & Environ. Sci.*, **7** (2014) 2934.
19. W. Li, J. Fan, J. Li, Y. Mai, and L. Wang, *J. Am. Chem. Soc*, **137** (2015) 10399.
20. D.-H. Ma, W.-J. Zhang, Z.-Y. Jiang, D.-Y. Song, L. Zhang, and W. Yu, *J. Phys. Chem. C*, **121** (2017) 22607.
21. C.-Y. Long, N. Wang, K.-Q. Huang, H.-Y. Li, B. Liu, and J.-L. Yang, *Chinese Phys. B*, **29** (2020) 048801.

Journal of Photopolymer Science and Technology
Volume 34, Number 3 (2021) 285−290 ©2021SPST

Synthesis, Properties, and Photovoltaic Characteristics of Arch- and S-shaped Naphthobisthiadiazole-based Acceptors

Seihou Jinnai and Yutaka Ie*

The Institute of Scientific and Industrial Research, Osaka University,
8-1 Mihogaoka, Ibaraki, Osaka 567-0047, Japan.
**yutakaie@sanken.osaka-u.ac.jp*

Fine-tuning physical properties by structural modification is important for developing organic semiconducting materials. In this work, we designed and synthesized new electron-accepting compounds containing naphtho[1,2-*c*:7,8-*c*′]bis([1,2,5]thiadiazole (vNTz) or naphtho[1,2-*c*:5,6-*c*′]bis[1,2,5]thiadiazole (NTz) groups as electron-accepting units; these units are structural isomers. The vNTz-based compounds have an arch-shaped molecular backbone with C_{2v} symmetry, whereas the NTz-based compound forms an S-shaped molecular backbone with C_{2h} symmetry. Property measurements showed unique behavior originating from the vNTz core. An organic solar cell comprising the vNTz-based compound and poly(3-hexylthiopehene) showed a power conversion efficiency of 2.06%. This result demonstrates the potential of vNTz as an electron-accepting unit in organic semiconducting materials.

Keywords: Organic solar cells, Nonfullerene acceptors, Organic semiconducting materials, π-Conjugated molecules, Naphthobisthiadiazole, Surface free energies

1. Introduction

π-Conjugated compounds have been intensively developed as semiconducting materials for organic solar cells (OSCs).[1,2] The active layer of OSCs consists of donor and acceptor materials, which form a bulk-heterojunction structure.[3] Low band-gap polymers have been extensively utilized as donor materials to acquire broad absorption.[4] However, poly(3-hexylthiophene) (P3HT) is still considered one of the most promising practical donors.[5] Among the various acceptor materials, nonfullerene acceptors (NFAs), which comprise planar π-conjugated backbones and electron-accepting units, have attracted significant attention due to their tunable electronic properties, synthetic accessibilities, and structural diversities.[6,7] Several C_{2v}-symmetric (arch-shaped) NFAs, such as ZY-4Cl[8] and Y6[9], have reportedly shown photovoltaic characteristics due to their high carrier mobilities and crystallinities, as well as the optimal phase separations of their blend films.[10-12] However, investigations into the influence of structural symmetry on acceptor performance are limited.

Recently, we have developed electron-accepting π-conjugated materials including a C_{2h} symmetric naphtho[1,2-*c*:5,6-*c*′]bis[1,2,5]thiadiazole (NTz) unit,[13] and found that NTz derivatives are promising constituents for NFAs.[14-16] The corresponding structural C_{2v} isomer of NTz, naphtho[1,2-*c*:7,8-*c*′]bis([1,2,5]thiadiazole (vNTz), was first synthesized by Mataka *et al.* in 1991.[17] However, acceptor materials comprising extend π-conjugated systems bearing vNTz units have not yet been investigated in detail.[18] In this contribution, we combined a vNTz unit with 3-ethylrhodanine [19] as a representative terminal

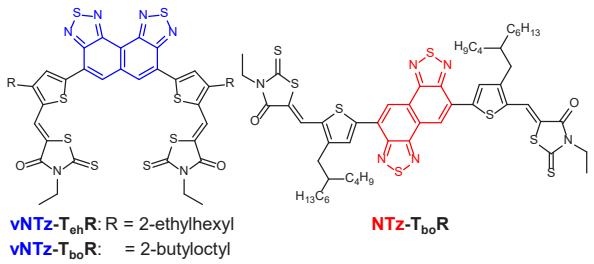

Fig. 1. Chemical structures of target molecules.

Received March 31, 2021
Accepted April 25, 2021

unit to investigate the properties and OSC characteristics of the resultant electron-accepting materials. Specifically, we synthesized the π-conjugated compounds **vNTz-T$_{bo}$R** and **vNTz-T$_{eh}$R** that feature C_{2v} symmetry (Fig. 1). For comparison, **NTz-T$_{eh}$R**, bearing C_{2h} symmetry, was also synthesized.

2. Experimental

Cyclic voltammetry (CV) was carried out on a BAS CV-620C. UV-vis spectra were recorded on a Shimadzu UV-3600 spectrophotometer. Fluorescence spectra were recorded using a Fluoromax-4 spectrometer in the photo-counting mode equipped with a Hamamatsu R928P photomultiplier. Photoelectron yield spectroscopy (PYS) was performed by Bunkoukeiki BIP-KV202GD. The surface structures of the active layers were observed by atomic force microscopy (AFM) using Shimadzu, SPM9600.

OSCs were prepared with a structure of ITO/ZnO/active layer/MoO_3/Ag.[20] ITO-coated glass substrates were first cleaned by ultrasonication in acetone, water, and 2-propanol, respectively. The substrates were then activated by ozone treatment for 1 h. ZnO layer was spin-coated using the solution of zinc acetate dihydrate at 3000 rpm. and baked at 200 °C for 30 min in air. Subsequently, the active layer was then formed by spin-coating on the ITO/ZnO electrode using 10 mg mL^{-1} solutions including P3HT and acceptor at a weight ratio of 1:1 in chloroform, followed by thermal annealing at 130 °C for 10 min. in a glove box. MoO_3 and Ag electrodes were evaporated on the top of active layer through a shadow mask to define the active area of the devices (0.09 cm^2) under a vacuum of 10^{-5} Pa to a thickness of 10, 100 nm. After sealing the device from the air, the photovoltaic characteristics were measured in air under simulated AM 1.5G solar irradiation (100 mW cm^{-2}) (SAN-EI ELECTRIC, XES-301S) by using a KEITHLEY 2400 source meter. The external quantum efficiency (EQE) spectra were measured by using a Soma Optics Ltd. S-9240.

The contact angles of film surface were measured by a NiCK LSE-ME1 using distilled water and glycerol. SFEs were estimated based on the theory established by Kaelble and Uy.[21]

3. Results and discussion

3.1. Synthesis

We began our study with the syntheses of **vNTz-T$_{bo}$R** and **NTz-T$_{bo}$R** (Scheme 1), which have 2-butyloctyl moieties as solubilizing groups. The dibromo compound **vNTz-Br** [17] was cross-coupled via Migita–Kosugi–Stille reactions to obtain **1**. Compound **1** was then formylated by the Vilsmeier-Haack reaction in dichloroethane (DCE)[22] followed by condensation reactions with 3-ethylrhodanine to give the target compound **vNTz-T$_{bo}$R**. The **NTz-T$_{bo}$R** compound was synthesized in the same manner. Since **vNTz-T$_{bo}$R** is relatively soluble, we also synthesized **vNTz-T$_{eh}$R** bearing a 2-ethylhexyl group.

The solubilities of the synthesized compounds against chloroform, chlorobenzene, and *o*-dichlorobenzene (as representative solvents) in OSCs are summarized in Table 1. Compared to **NTz-T$_{bo}$R**, **vNTz-T$_{bo}$R** showed higher solubilities. This result is consistent with the reported phenomenon that acceptors with C_{2v} symmetry provide improved solubilities.[12]

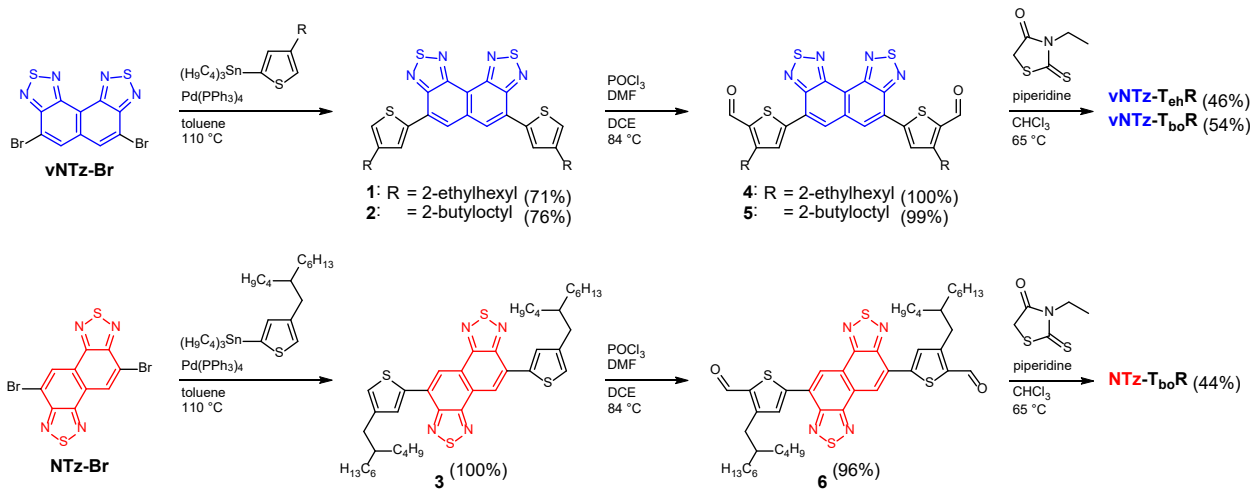

Scheme 1. Synthesis of target compounds.

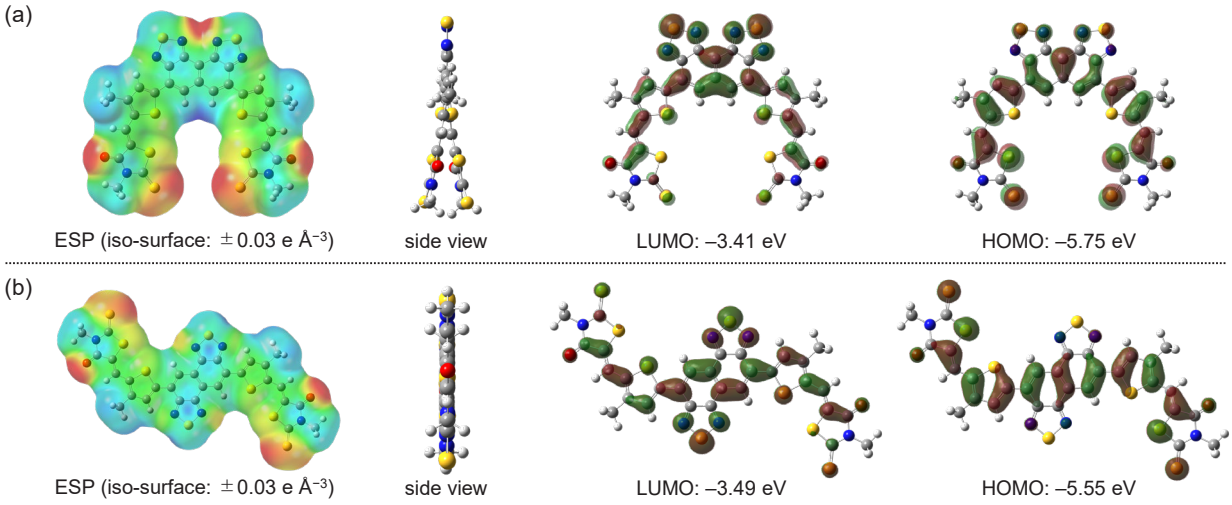

Fig. 2 Electrostatic potential map, structures, the LUMO, and the HOMO of model compounds for (a) vNTz-T_{eh}R and vNTz-T_{bo}R, and for (b) NTz-T_{bo}R. Calculations were carried out using DFT at the B3LYP/6-31G(d,p) level.

Table 1. Solubilities of compounds.

compound	solubilities / mg mL^{-1}		
	chloroform	chlorobenzene	*o*-dichlorobenzene
vNTz-T_{eh}R	38	2.2	2.3
vNTz-T_{bo}R	> 50	> 50	> 50
NTz-T_{bo}R	7	1.0	1.2

3.2. Computational Results

Theoretical investigations were performed by density functional theory (DFT) calculations at the B3LYP/6-31G(d,p) level. For these calculations, we replaced alkyl groups with methyl groups. The optimized structure of **vNTz-T_{bo}R** has lower energy of 1.5~41.6 kJ mol^{-1}, compared to the 10 possible conformers. As shown in Fig. 2, electrostatic potential maps of the optimized structures indicate that electron-rich sites were mainly located on the sulfur atom of the rhodamine units. Since the electron-rich sites of the vNTz-based compounds were geometrically close, this molecule takes on a twisted structure to decrease the Coulomb repulsion. The frontier orbital energy levels and distributions are also shown in Fig. 2. The distributions of the highest occupied molecular orbital (HOMO) and lowest unoccupied molecular orbital (LUMO) for both compounds were delocalized over the π-conjugated frameworks. The LUMO energy levels of the vNTz- and NTz-based compounds were estimated to be –3.41 and –3.49 eV, respectively, which indicate that these compounds can be employed as acceptors in OSCs when combined with P3HT as a donor.[23]

3.3. Properties

To investigate the electrochemical properties of the synthesized compounds, CV measurements were performed. Fig. 3 shows the voltammograms of **vNTz-T_{bo}R** and **NTz-T_{bo}R**, and the electrochemical data extracted from them are listed in Table 2. **NTz-T_{bo}R** showed one reversible reduction wave, but no additional reduction wave was observed when differential pulse voltammetry was employed in further negative sweep (data not shown). In contrast, three reversible reduction waves were observed for **vNTz-T_{bo}R**. The first half-wave reduction potentials ($E_{red}^{1/2}$) of **vNTz-T_{bo}R** and **NTz-T_{bo}R** were –1.22 and –1.21 V, respectively. Thus, the LUMO energy levels for **vNTz-T_{bo}R** (–3.58 eV) and **NTz-T_{bo}R** (–3.59 eV) showed similar values. This result indicates that the structural geometry of the NTz skeleton has little influence on the LUMO energy levels.

Chloroform solutions and thin films on quartz plates of the synthesized compounds were

Table 2. Properties of compounds.

compound	$E_{red}^{1/2}$ / V [a]	E_{LUMO} / eV [b]	λ_{abs} / nm [c]	ΔE_{opt} / nm [d]	ΔE_{opt} (film) / nm [e]	λ_{em} / nm [c]	I_p / eV [f]
vNTz-T_{eh}R	n.a.	n.a.	501	2.18	2.03	589	5.04
vNTz-T_{bo}R	–1.22, –1.39, –1.53	–3.58	501	2.18	2.03	590	5.19
NTz-T_{bo}R	–1.21	–3.59	557	1.96	1.76	626	5.06

[a] In CH_2Cl_2, 0.1 M $TBAPF_6$, V vs. Fc/Fc+. [b] Approximation that the Fc/Fc^+ level is –4.8 eV vs. vacuum. [c] In $CHCl_3$. [d] Determined by the onset of UV-vis absorption spectrum in $CHCl_3$. [e] Determined by the onset of UV-vis absorption spectrum in the film. [f] Estimated from PYS measurement in films.

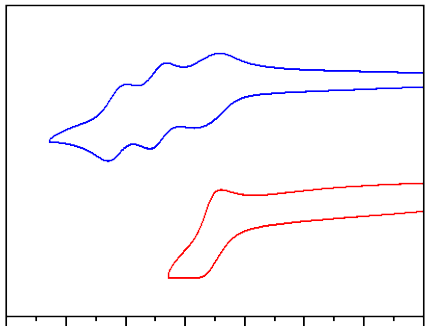

Fig. 3 Cyclic voltammograms of **vNTz-T$_{bo}$R** and **NTz-T$_{bo}$R**.

evaluated by UV-vis absorption spectroscopy (Fig. 4(a)). The corresponding spectroscopic data are summarized in Table 2. The UV-vis absorption spectra of **vNTz-T$_{bo}$R** and **vNTz-T$_{eh}$R**, *i.e.*, the compounds with the same π-conjugated structure, showed negligible differences when superimposed. This was true for both their solution and film states, indicating that the different alkyl groups do not significantly alter the photophysical properties of these vNTz-based compounds. The absorption maxima (λ_{abs}) of the vNTz-based compounds were blue-shifted by 56 nm relative to that of **NTz-T$_{bo}$R**. Additionally, the molar absorption coefficient of the vNTz-based compounds (7.4×10^4 L mol^{-1} cm^{-1}) was higher than that of **NTz-T$_{bo}$R**. Fluorescence measurements showed that the emission maximum (λ_{em}) of **NTz-T$_{bo}$R** was bathochromically shifted by 36 nm with respect to that of the vNTz-based compounds. Based on the λ_{abs} and λ_{em} values (Fig. 4(b)), the Stokes shifts were calculated as 3000 cm^{-1} for **vNTz-T$_{bo}$R** and 2000 cm^{-1} for **NTz-T$_{bo}$R**. The higher Stokes shift of **vNTz-T$_{bo}$R** is ascribed to its slightly twisted structure (Fig. 2).

Apparent red shifts were observed in the bands of the absorption and emission spectra of both compounds (**vNTz-T$_{bo}$R**: 47 nm, **NTz-T$_{bo}$R**: 78 nm) when they converted to the film state from the solution state. The relatively large red shift noted for **NTz-T$_{bo}$R** implies that the π–π stacking interactions of its film state are stronger than those of its solution state. solution state. The relatively large red shift noted for **NTz-T$_{bo}$R** implies that the π–π stacking interactions of its film state are stronger than those of its solution state.

The ionization potentials (I_p) of the compounds as thin-films were determined by PYS measurements (Fig. 5). Based on the onset, the I_p values of

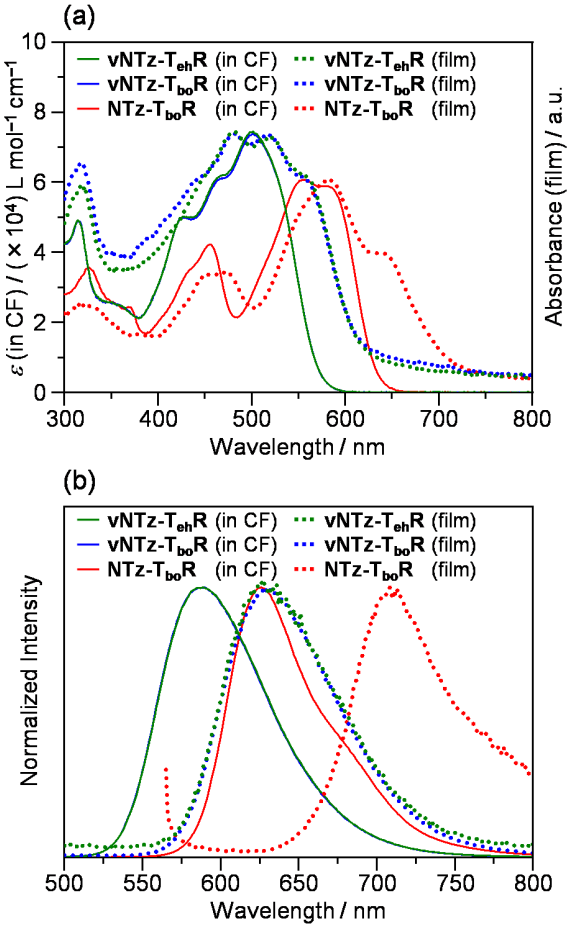

Fig. 4 (a) UV-vis absorption spectra and (b) emission spectra of compounds.

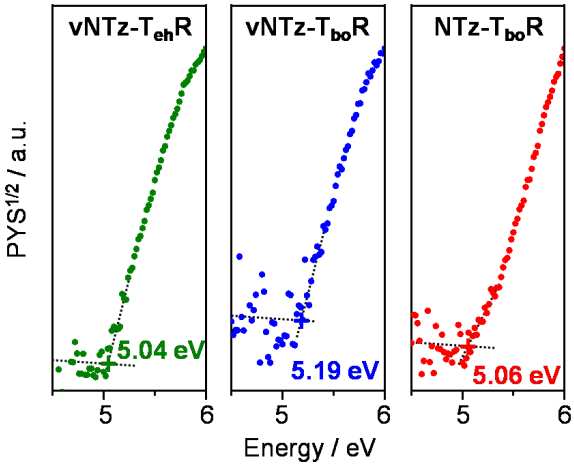

Fig. 5 PYS spectra of acceptors in thin films.

vNTz-T$_{eh}$R, **vNTz-T$_{bo}$R**, and **NTz-T$_{bo}$R** were determined to be 5.04, 5.19, and 5.06 eV, respectively. The I_p of **vNTz-T$_{bo}$R** was deeper than that of **NTz-T$_{bo}$R**, which is in good agreement with the DFT calculation (Fig. 2).

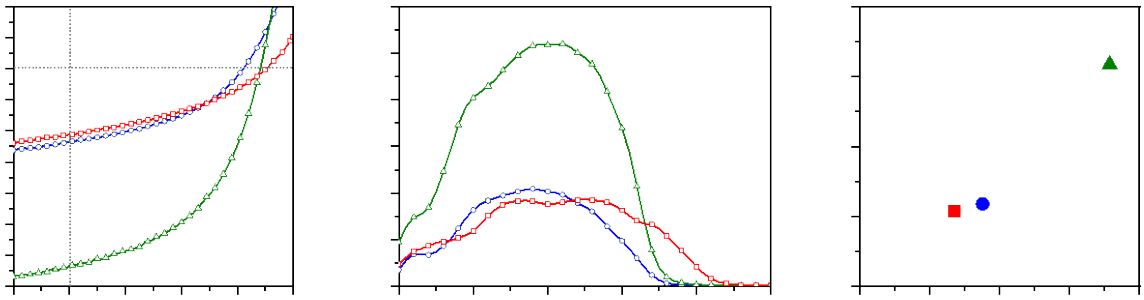

Fig. 6 (a) J-V characteristic and (b) external quantum efficiency spectra of OSC devices. (c) Plot of γ^d vs J_{SC} values for acceptor materials used in this study.

Table 3. OSC device data and surface free energies of acceptor films.

compounds	J_{SC} / mA cm^{-2}	V_{OC} / V	FF / %	PCE / %	γ^d / mJ cm^{-2}	γ^p / mJ cm^{-2}	SFE / mJ cm^{-2}
vNTz-T$_{eh}$R	6.34	0.68	48	2.06	17.9	7.2	25.0
vNTz-T$_{bo}$R	2.36	0.62	41	0.61	8.8	10.0	18.8
NTz-T$_{bo}$R	2.13	0.70	37	0.56	6.8	12.1	19.9

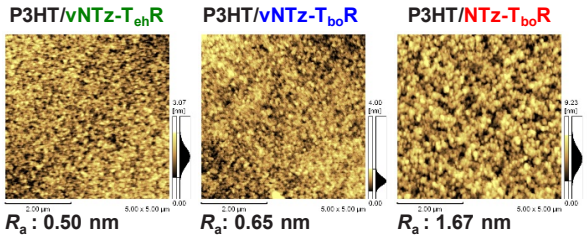

Fig. 7 AFM height images on active layers.

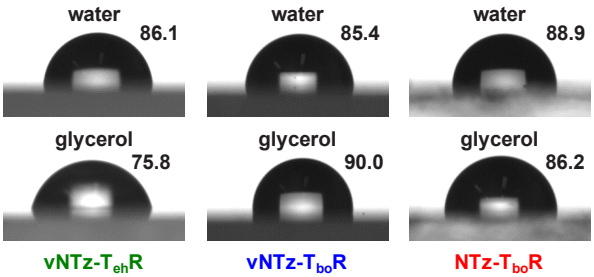

Fig. 8 Contact angles of thin films.

3.4 Photovoltaic Characteristics

The photovoltaic characteristics of our newly synthesized compounds when employed in OSCs were then investigated. In Fig. 6(a) and Table 3, the current-density–voltage (J–V) curves and the corresponding photovoltaic parameters of the devices are presented. Under the same fabrication conditions, **vNTz-T$_{bo}$R** and **NTz-T$_{bo}$R** showed comparable power conversion efficiencies (PCEs) of ~0.6%. However, a higher PCE of 2.06% was achieved by the **vNTz-T$_{eh}$R**-based OSC, which was mainly due to a significant increase in its short-circuit current density (J_{SC}). As indicated in Fig. 6(b), the external quantum efficiencies (EQEs) corresponded to the J_{SC} values of OSCs, and a maximum EQE of 52% was observed for the **vNTz-T$_{eh}$R**-based OSC.

To investigate the film morphologies of the active layers, AFM was performed. As shown in Fig. 7, all active layers had smooth surfaces suitable for OSCs; however, the **NTz-T$_{bo}$R**-based films were found to have slightly rougher surfaces. As long as the AFM measurements, no clear correlation was identified with respect to the morphological observations of these active layers.

We previously reported a correlation between the dispersion component (γ^d) of the surface free energy (SFE) for benzothiadiazole-based NFA films and the J_{SC} value of the OSCs they were employed in.[24] This correlation suggested that the donor–acceptor interfaces of the π-conjugated frameworks of acceptors with large γ^d values are more exposed than those of acceptors with small γ^d values, which is advantageous for charge separation. To obtain insight into the film properties of the acceptors synthesized in this work, their SFE, γ^d, and polar component (γ^p) values were determined from contact-angle measurements using water and glycerol as the probe liquids (Fig. 8 and Table 3). We then plotted the γ^d values of the acceptors against the J_{SC} values of the OSCs we employed them in (Fig. 6(c)). This plot showed a clear correlation between the two parameters, where the large γ^d component of **vNTz-T$_{eh}$R**

implies that the π-conjugated framework of this film is exposed. This trend is in good agreement with the photovoltaic results.

4. Conclusion

New, arch-shaped NFAs, **vNTz-T$_{eh}$R** and **vNTz-T$_{bo}$R**, were developed by introducing a vNTz unit into the central part of a π-conjugated backbone. Upon comparing **vNTz-T$_{bo}$R** to **NTz-T$_{bo}$R**, it was evident that the low-symmetry unit (vNTz) of the former material provided it with a higher solubility than that of the latter. Furthermore, electrochemical measurements indicated that **vNTz-T$_{bo}$R** and **NTz-T$_{bo}$R** showed almost identical LUMO energy levels. An OSC based on P3HT/**vNTz-T$_{eh}$R** showed a PCE of 2.06%, and the contact angle measurements implied that the **vNTz-T$_{eh}$R** film has a favorable surface for photo-carrier generation. Thus, this study demonstrated the potential applicability of arch-shaped NTz derivatives in organic electronics.

Acknowledgement

This work was supported by JSPS KAKENHI (20H02814, 20K21224, 20H05841, 20KK0123, 19K15505, 20H04639, and 20K15352), CREST (J205101030), and "Dynamic Alliance for Open Innovation Bridging Human, Environmental and Materials" from The Ministry of Education, Culture, Sports, Science and Technology, Japan. We are thankful to Nanotechnology Open Facilities, Osaka University (JPMXP09S21OS0010) and Mr. Asakawa for PYS measurements.

References

1. G. Li and Y. Yang, *Nat. Photon.*, **6** (2012) 1531.
2. O. Inganäs, *Adv. Mater.*, 30 (2018) 1800388.
3. G. Yu, J. Gao, J. C. Hummelen, F. Wudl, and A. J. Heeger, *Science*, **270** (1995) 1796.
4. Y. Li, *Acc. Chem. Res.*, **45** (2012) 723.
5. A. Wadsworth, Z. Hamid, M. Bidwell, R. S. Ashraf, J. I. Khan, D. H. Anjum, C. Cendra, J. Yan, E. Rezasoltani, A. A. Y. Guilbert, M. Azzouzi, N. Gasparini, J. H. Bannock, D. Baran, H. Wu, J. C. d. Mello, C. J. Brabec, A. Salleo, J. Nelson, F. Laquai, and I McCulloch, *Adv. Energy Mater.*, **8** (2018) 1801001.
6. C. Yan, S. Barlow, Z. Wang, H. Yan, A. K.-Y. Jen, S. R. Marder, and X. Zhan, *Nat. Rev. Mater.*, **3** (2018) 18003.
7. A. Wadsworth, M. Moser, A. Marks, M. S. Little, N. Gasparini, C. J. Brabec, D. Baran, and I. McCulloch, *Chem. Soc. Rev.*, **48** (2019) 1596.
8. C. Yang, S. Zhang, J. Ren, M. Gao, P. Bi, L. Ye, and J. Hou, *Energy Environ. Sci.*, **13** (2020) 2864.
9. Q. Liu, Y. Jiang, K. Jin, J. Qin, J. Xu, W. Li, J. Xiong, J. Liu, Z. Xiao, K. Sun, S. Yang, Z. Zhang, and L. Ding, *Sci. Bull.*, **65** (2020) 272.
10. W. hu, A. P. Spencer, S. Mukherjee, J. M. Alzola, V. K. Sangwan, S. H. Amsterdam, S. M. Swick, L. O. Jones, M. C. Heiber, A. A. Herzing, G. Li, C. L. Stern, D. M. DeLongchamp, K. L. Kohlstedt, M. C. Hersam, G. C. Schatz, M. R. Wasielewski, L. X. Chen, A. Facchetti, and T. J. Marks, *J. Am. Chem. Soc.*, **142** (2020) 14532.
11. C. Tang, D. Cai, and Q. Zheng, *J. Mater. Chem. A*, **7**, (2019) 9609.
12. R. Hou, M. Li, X. Ma, H. Huang, H. Lu, Q. Jia, Y. Liu, X. Xu, H.-B. Li, and Z. Bo, *ACS Appl. Mater. Interfaces*, **12** (2020) 46220.
13. Y. Ie, S. Sasada, M. Karakawa, and Y. Aso, *Org. Lett.*, **17** (2015) 4580.
14. S. Chatterjee, Y. Ie, M. Karakawa, and Y. Aso, *Adv. Funct. Mater.*, **26** (2016) 1161.
15. S. Chatterjee, Y. Ie, and Y. Aso, *ACS Omega*, **3** (2018) 5814.
16. S. Chatterjee, Y. Ie, T. Seo, T. Moriyama, G.-J. A. H. Wetzelaer, P. W. M. Blom, and Y. Aso, *NPG Asia Mater.*, **10** (2018) 1016.
17. S. Mataka, K. Takahashi, Y. Ikezaki, T. Hatta, A. Tori-i, and M. Tashiro, *Bull. Chem. Soc. Jpn.*, **64** (1991) 68.
18. S. Jinnai, Y. Ie, Y. Kashimoto, H. Yoshida, M. Karakawa, and Y. Aso, *J. Mater. Chem. A*, **5** (2017) 3932.
19. Suman and S. P. Singh, *J. Mater. Chem. A*, **7** (2019) 22701.
20. W. Zhao, S. Li, H. Yao, S. Zhang, Y. Zhang, B. Yang, and J. Hou, *J. Am. Chem. Soc.*, **139** (2017) 7148.
21. D. H. Kaelble, and K. C. Uy, *J. Adhesion*, **2** (1970) 50.
22. B. Fu, J. Baltzar, Z. Hu, A.-T. Chien, S. Kumar, C. L. Henderson, D. M. Collard, and E. Reichmanis, *Chem. Mater.*, **24** (2012) 4123.
23. M. C. Scharber, D. Mühlbacher, M. Koppe, P. Denk, C. Waldauf, A. J. Heeger, and C. J. Brabec, *Adv. Mater.*, **18** (2006) 789.
24. S. Jinnai, Y. Ie, M. Karakawa, T. Aernouts, Y. Nakajima, S. Mori, and Y. Aso, *Chem. Mater.*, **28** (2016) 1705.

Journal of Photopolymer Science and Technology
Volume 34, Number 3 (2021) 291−296 ©2021SPST

Improved Hole-Transporting Properties in Conjugated Polymers Mixed with Polystyrene as an Insulating Polymer

Yuya Horiuchi, Koshiro Midori, Hyung Do Kim*, and Hideo Ohkita*

Department of Polymer Chemistry, Graduate School of Engineering, Kyoto University, Katsura, Nishikyo, Kyoto 615-8510, Japan.
**hyungdokim@photo.polym.kyoto-u.ac.jp*
**ohkita@photo.polym.kyoto-u.ac.jp*

Herein, we study hole transport properties in various conjugated conducting polymers blended with polystyrene (PS) as an insulating polymer. By analyzing macroscopic current density–voltage characteristics, we found that the mobility is improved for the conjugated conducting polymers diluted in the PS matrix that exhibit a redshift in absorption spectra. This is probably ascribed to more ordered polymer chains caused by the addition of PS. We believe that such a dilution of polymer chains would be versatile strategies to enhancing charge transport properties, which will offer a breakthrough towards highly efficient wearable optoelectronic devices based on the conjugated polymers.

Keywords: Charge transport properties, Conjugated polymers, Insulating polymers, Blend films.

1. Introduction

Flexible and wearable optoelectronic devices, such as light-emitting diodes, photovoltaic devices, and photodetector devices, have recently attracted much attention owing to their potential applications in modern society.[1–3] Among all materials employed in these devices, conjugated conducting polymers are used as active layers in common and play a central role in transporting of charge carriers.[4–6] With the aim of their commercialization, one of most important issues in this community is, therefore, to achieve highly efficient charge transport in organic materials comparable to that in inorganic materials. For organic solar cells and organic photodetectors, in particular, it is more important to comprehend charge transport properties in blend films rather than in neat films since they are typically composed of an electron donor material (D) and an electron acceptor material (A).

Such blend films, however, are typically accompanied by changes in the degree of structure order and/or the packing orientation of polymer chains. This has a positive or negative impact on their charge transport properties depending on miscibility of polymers employed. For example, in the case of the polymer solar cells, it is found that a fill factor (FF), which is a criterion of charge transport in devices, is much lower in the ternary blend polymer solar cells based on D/D/A or D/A/A than that in D/A binary blend counterparts.[7,8] This degradation results from a decrease in carrier mobility μ due to the formation of more complicated transport paths incurred by the addition of third components. On the other hand, an opposite trend for charge transport has been recently reported by several groups including ours.[9–14] To be more specific, FF for the ternary blend solar cells was improved by the introduction of the third component as a donor or acceptor material in comparison with that for the binary blend devices. This is ascribed to more balanced μ between electrons and holes and/or enhanced μ as a result of more ordered structure of polymer chains in the ternary blend films. For such blend films, however, there would be some possible variations in the charge carrier density n caused by charge transfer (CT) complex at the D/A interfaces.[14] This makes it difficult for us to

Received April 1, 2021
Accepted April 14, 2021

disclose the origin of an improvement in charge transport properties in the blend films. On the other hand, we can focus on charge transport properties in the conjugated polymers blended with an insulating polymer without consideration of variations in n. Very recently, several groups including ours have reported that μ in the conjugated polymers diluted with insulating polymer matrix is higher compared to the conjugated polymer neat films.[15–20] This is attributed to a difference in molecular interactions and/or aggregation states between polymer chains, which are closely related to trap sites unfavorable for charge transport properties. However, little is known about universal criteria for effects of improvement in charge transport properties of the conjugated polymers induced by PS addition.

Herein, we have studied charge transport properties in a series of conjugated polymers blended with PS. More specifically, we employed poly[4,8-bis(5-(2-ethylhexyl)thiophen-2-yl)benzo[1,2-*b*:4,5-*b*′]dithiophene-*co*-3-fluorothieno[3,4-*b*]thiophene-2-carboxylate] (PTB7-Th), poly[2-methoxy-5-(3′,7′-dimethyloctyloxy)-1,4-phenylenevinylene] (MDMO-PPV), poly[2,5-bis(3′,7′-dimethyloctyloxy)-1,4-phenylenevinylene (DMO-PPV), and regiorandom poly(3-hexylthiophene) (RRa-P3HT) as conjugated polymers, and PS as an insulating polymer. Figure 1 shows chemical structures of these materials. For these blend films,

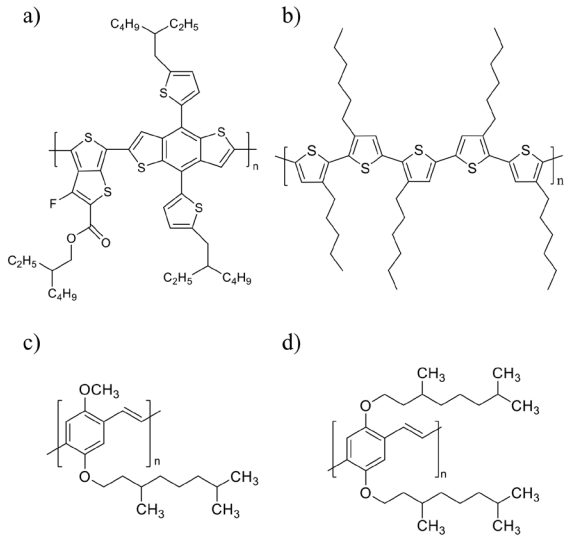

Fig. 1. Chemical structures of materials employed in this study: a) PTB7-Th, b) RRa-P3HT, c) MDMO-PPV, and d) DMO-PPV.

μ was evaluated from macroscopic current density–voltage (J–V) characteristics. As a result, we found that μ is higher in the blend films except for RRa-P3HT/PS blends rather than in the neat films. The origin of an increase in μ was discussed by measuring absorption spectra and conductive atomic force microscopy (C-AFM) images of these blend films.

2. Experimental

2.1 Materials

Four kinds of the conjugated polymers employed were PTB7-Th (1-Materials Inc., weight average molecular weight, M_w = 180,000), MDMO-PPV (Sigma–Aldrich), DMO-PPV (Sigma–Aldrich), and RRa-P3HT (Sigma–Aldrich). Polystyrenes with different molecular weights were purchased from Shodex (M_w = 3,250, 22,500, and 1,310,000). As a buffer layer, poly(3,4-ethylenedioxythiophene): poly(4-styrenesulfonate) (PEDOT:PSS, H.C. Starck Clevios PH500) was employed. All these materials employed were used without further purification.

2.2 Device fabrication

Hole only devises were fabricated as follows. Indium–tin-oxide (ITO)-coated glass (10 Ω per square) substrates were cleaned by ultrasonication with toluene, acetone, and then ethanol for 15 min each. The substrates were dried under nitrogen gas flow, and exposed to ozone under ultraviolet illumination for 30 min (Nippon Laser & Electronics, NL-UV253S). The solution of PEDOT:PSS was filtered with a PTFE syringe filter (pore size: 0.45 μm) and treated with ultrasonic crusher for 3 min. A layer of PEDOT:PSS was fabricated onto the ITO substrates by spin-coating at a spin rate of 400 rpm for 10 s and then 3000 rpm for 60 s, and subsequently dried on a hot plate at 140 °C for 10 min in air. The mixed solution was prepared by dissolving the conjugated polymer and PS with a different weight ratio of 10 : 0, 0.75 : 0.25, 0.4 : 0.6 and 0.2 : 0.8 in chlorobenzene or chloroform. The blend active layers were deposited atop ITO/PEDOT:PSS substrates by spin-coating at 1000 rpm for 60 s in the nitrogen atmosphere. The thickness of blend film was ~100 nm. Finally, Au (100 nm) or MoO_3/Al (10 nm/100 nm) electrode was thermally evaporated on top of the active layer. Consequently, the device layered structure was as follows: ITO/PEDOT:PSS/active layer/Electrode.

2.3 Measurement

J–V characteristics were measured with a direct-

current (DC) voltage and current source/monitor (Keithley, 2611B) in the dark. To evaluate μ, we analyzed space-charge-limited current (SCLC) of the blend films with the Mott–Gurney equation as follows.[21]

$$J = \frac{9}{8}\varepsilon_r\varepsilon_0\mu\frac{V^2}{L^3} \quad (1)$$

where ε_r is a relative dielectric constant of materials, ε_0 is the vacuum permittivity, and L is a thickness of the blend film. Here, ε_r is assumed to be 3, which is a typical value for most organic materials. Absorption spectra were measured with a spectrophotometer (Hitachi, U-4100). The film surface morphology and current image were measured simultaneously with an atomic force microscope (AFM, Shimadzu, SPM-9700) using an Au-coated silicon probe (NANO-SENSORS, PPP-CONTAu, tip radius of curvature < 10 nm, spring constant = 0.2 N m^{-1}) at a constant sample voltage of +5.0 V. The sample bias was applied to the ITO and the tip was grounded.

3. Results and discussion

Figure 2 shows μ of each donor/PS blend film with different weight ratios, which was evaluated by fitting the J–V characteristics in the SCLC region with a slope of two. For PTB7-Th/PS blends, μ was comparable to that of PTB7-Th neat films at 25 wt% PS, the largest at 60 wt% PS, and still larger than that of the neat films even at only 80 wt% PS. In other words, all the blend films exhibited μ comparable to or larger than PTB7-Th neat films. For MDMO-PPV/PS blends, μ increased with increasing PS fraction in the blends. Interestingly, the values of all μ were larger than that of MDMO-PPV neat films even though the fraction of the conductive polymers was smaller than that of the neat films. For DMO-PPV/PS blends, μ decreased with increasing PS fraction in the blends. However, the decreased μ was limited and much smaller than that expected from a decrease in the fraction of the conductive polymers. In other words, this finding rather suggests that an effective μ is improved with increasing PS fraction in the blends considering the volume fraction of the conjugated polymers. For RRa-P3HT/PS blends, on the other hand, μ significantly decreased by one order of magnitude even at 40 wt% of conductive polymers where other conjugated polymers exhibit the largest μ. In summary, μ was improved for PTB7-Th/PS, MDMO-PPV/PS, and DMO-PPV/PS blends while it decreased for RRa-P3HT/PS blends.

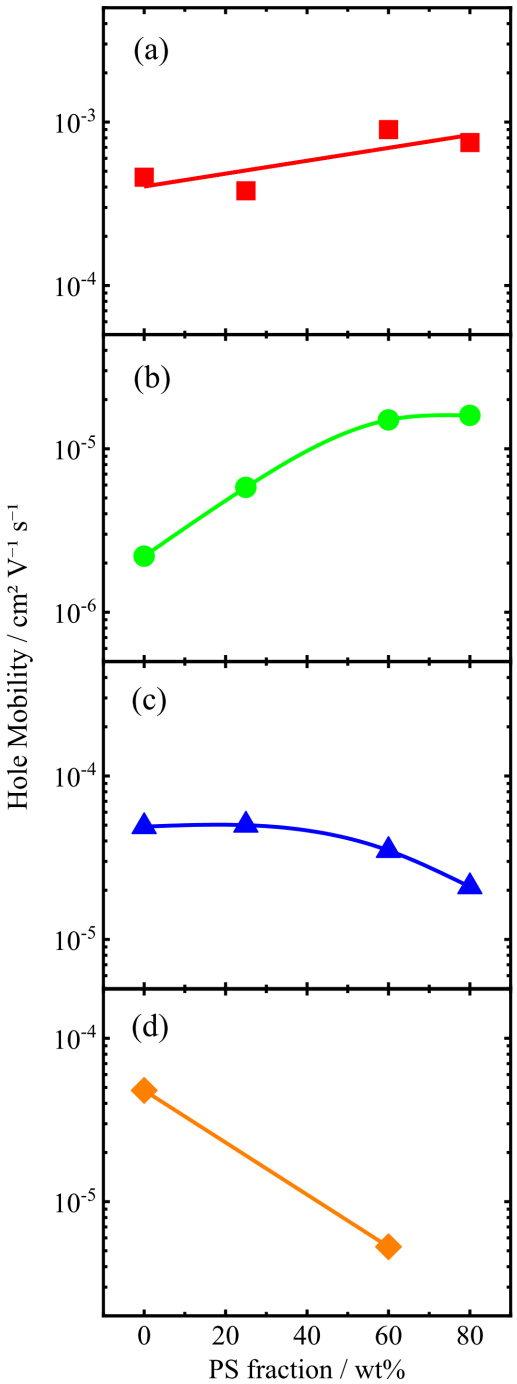

Fig. 2. Hole mobility of each donor/PS blend film with different weight ratio: a) PTB7-Th, b) MDMO-PPV, c) DMO-PPV, and d) RRa-P3HT.

In order to consider how molecular weights of PS matrix impact on charge transport properties, we evaluated μ for 40 wt% PTB7-Th in the PS matrix with different PS molecular weights. As a result, we found that μ decreases from 5.5 × 10^{-4} cm^2 V^{-1} s^{-1} for M_w = 22,000 to 2.9 × 10^{-4} cm^2 V^{-1} s^{-1} for M_w

= 131,000. Note that the μ for all the blends are comparable to or larger than that of PTB7-Th neat films. In other words, charge transport is improved for all the blends but is most effectively enhanced for the PS matrix with the smallest molecular weight (M_w = 3,250). Figure 3 shows AFM images of PTB7-Th/PS blends with different molecular weights of PS. For the largest molecular weight of PS matrix, sea and island domains were observed, suggesting large phase separation structures. For the smaller molecular weight of PS matrices, on the other hand, a well-mixed blend morphology was observed. This finding indicates that it would be beneficial for charge transport in the conjugated polymers blended with PS matrix.

To examine how such a blend morphology impacts on optoelectronic properties of the conjugated polymers mixed in PS matrix, we next measured the absorption spectra of these blend films.

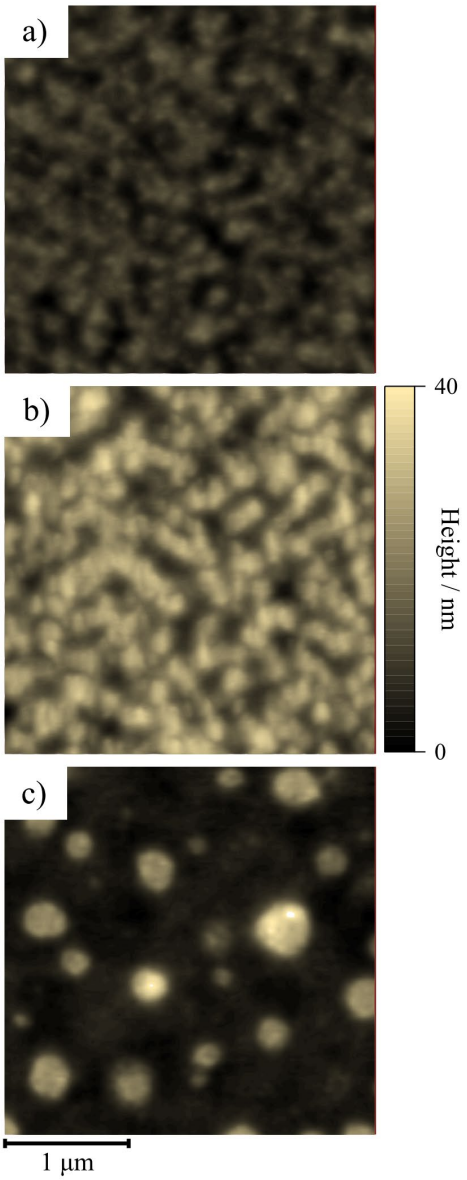

Fig. 3. AFM images of PTB7-Th/PS blend films with different molecular weights of PS: a) M_w = 3,250, b) M_w = 22,500, and c) M_w = 1,310,000.

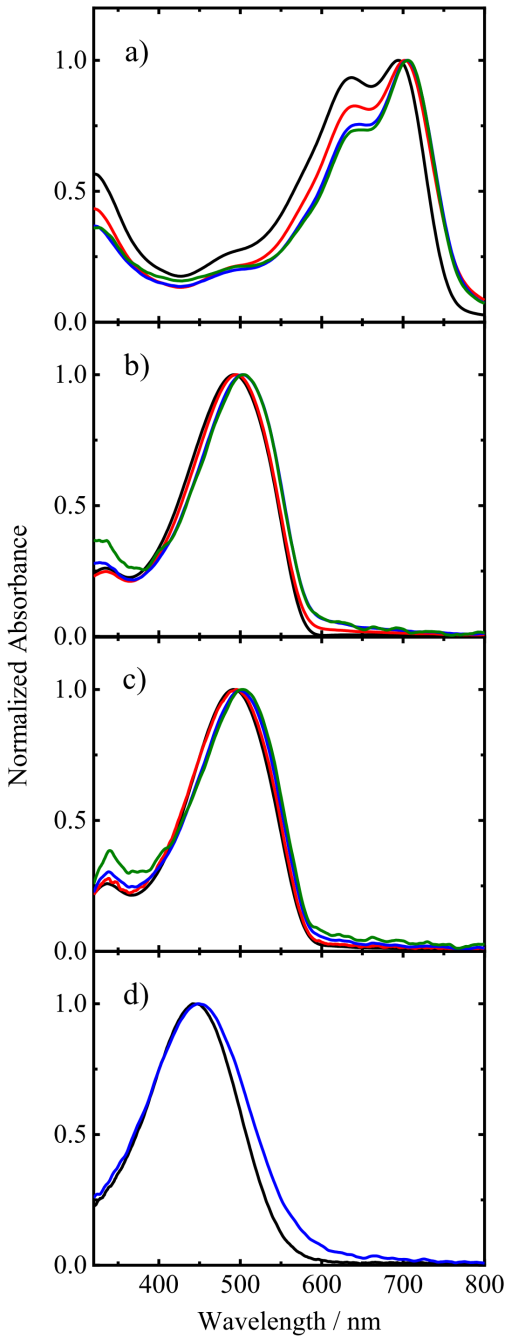

Fig. 4. Absorption spectra of a) PTB7-Th/PS, b) MDMO-PPV/PS, c) DMO-PPV/PS, and d) RRa-P3HT/PS blend films with different weight ratios: donor : PS = 1 : 0 (black lines), 0.75 : 0.25 (red lines), 0.4 : 0.6 (blue lines), and 0.2 : 0.8 (green lines).

For PTB7-Th/PS blends, as shown in Figure 4a, an absorption peak was red-shifted and a peak ratio of 0–0 to 0–1 vibronic bands increased in comparison with that of PTB7-Th neat films. The same trends were observed even for different molecular weights. This is consistent with our previous report for PTB7-Th, suggesting effectively enhanced backbone planarity.[14] For MDMO-PPV/PS and DMO-PPV/PS blend films, as shown in Figures 4b and 4c, absorption peaks were red-shifted in comparison with each neat film, implying improved an effective conjugation length of polymer chains. For RRa-P3HT/PS blends, on the other hand, no absorption shift was observed but instead absorption broadening was observed with a more distinct absorption tail as shown in Figure 4d. This finding suggests that inhomogeneities increased in RRa-P3HT/PS blends. In either case, there is a good correlation between charge transport properties and absorption spectra of polymer/PS blend films.

Finally, we studied local current properties on a scale of micrometers by C-AFM measurement. Here, we focus on C-AFM images of MDMO-PPV/PS films as an example. For MDMO-PPV neat films, as shown in Figures 5a and 5c, morphology and current map were homogeneous over the entire films. For MDMO-PPV/PS blend films, on the other hand, sea and island domains were observed in the topography image (Figure 5b). As shown in Figure 5d, several hot spots were observed in the current image: hot spots correspond to islands in the topography image. Thus, island domains can be ascribed to MDMO-PPV rich domains. The pixel ratio between the no current region and the current flow region does not match the blend ratio because of the lateral and/or vertical phase separation for 60 wt% of PS added blends. Interestingly, currents in hot spots are about 10 times larger than that in sea domains of the blend films or in the neat films. We therefore conclude that an improved charge transport in the polymer/PS blend films is due to the formation of such highly conductive hot spots. Further study is required to reveal polymer structures in hot spots.

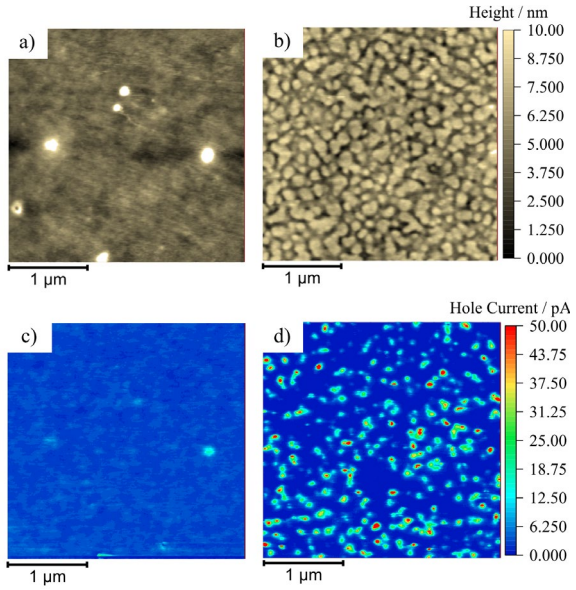

Fig. 5. Surface topographic images (top) and the corresponding hole current images (bottom) of MDMO-PPV/PS blend films with different weight fractions of PS: a) and c) PS 0 wt% and b) and d) PS 60 wt%.

4. Conclusion

We studied hole transport properties in a series of conjugated polymers blended in PS matrix. As a result, μ was improved for some polymer/PS blends. This improvement was dependent on molecular weights of PS matrix and more effective in PS matrix with small M_w, which gives a well-mixed blend morphology. Interestingly, we found a good correlation between hole transport properties and absorption spectra of the blend films based on a conjugated polymer and PS. More specifically, μ is improved for the polymer/PS blend films that exhibit red-shifted or enlarged ratio of 0–0 to 0–1 bands in absorption spectra: these are characteristic of an improvement in the effective conjugation length and the backbone planarity of the conjugated polymers. We also found such an improved charge transport is due to locally conductive hot spots in the polymer/PS blends on a scale of micrometers.

Acknowledgments

This study was supported by KAKENHI from Japan Society for the Promotion of Science (JSPS) (Grand Number 19K22217), a project commissioned by the New Energy and Industrial Technology Development Organization (NEDO), the Advanced Low Carbon Technology Research and Development Program (ALCA) of Japan Science and Technology Agency (JST) (Grant Number JPMJAL1404), and Research Grant by Hirose Foundation.

References

1. H. Ling, S. Liu, Z. Zheng, and F. Yan, *Small Methods*, **2** (2018) 1800070.
2. S. A. Hashemi, S. Ramakrishna and A. G. Aberle *Energy Environ. Sci*., **13** (2020) 685.

3. Y. Lee, H. Zhou, and T. W. Lee, *J. Mater. Chem. C*, **6** (2018) 3538.
4. C. Zhan, G. Yu, Y. Lu, L. Wang, E. Wujcik, and S. Wei, *J. Mater. Chem. C*, **5** (2017) 1569.
5. M. Ashizawa, Y. Zheng, H. Tran, Z. and Bao, *Prog. Polym. Sci.*, **100** (2020) 101181.
6. M. Chang, G. T. Lim, B. Park, and E. Reichmanis, *Polymers*, **9** (2017) 212.
7. H. Kim, M. Shin, and Y. Kim, *J. Phys. Chem. C*, **113** (2009) 1620.
8. P. Cheng, Y. Lia, and X. Zhan, *Energy Environ. Sci*., **7** (2014) 2005.
9. L. Nian, Y. Kan, H. Wang, K. Gao, B. Xu, Q. Rong, R. Wang, J. Wang, F. Liu, J. Chen, G. Zhou, T. P. Russell and A. K. -Y. Jen, *Energy Environ. Sci*., **11** (2018) 3392.
10. L. Lu, W. Chen, T. Xu, and L. Yu, *Nat. Commun.*, **6** (2015) 7327.
11. W. Zhao, S. Li, S. Zhang, X. Liu, and J. Hou, *Adv. Mater*., **29** (2017) 1604059.
12. K. Midori, T. Fukuhara, Y. Tamai, H. D. Kim, and H. Ohkita, *ChemPhysChem*., **20** (2019) 2683.
13. H. D. Kim, R. Shimizu, and H. Ohkita. *Chem. Lett.*, **47** (2018) 1059.
14. H. D. Kim, R. Iriguchi, T. Fukuhara, H. Benten, and H. Ohkita, *Chem. Asian J.*, **15** (2020) 796.
15. G. Lu, H. Tang, Y. Huan, S. Li, L. Li, Y. Wang, and X. Yang, *Adv. Funct. Mater.*, **20** (2010) 1714.
16. A. D. Scaccabarozzi and N. Stingelin, *J. Mater. Chem. A*, **2** (2014) 10818.
17. W. H. Lee and Y. D. Park, *Polymers*, **6** (2014) 1057.
18. B. Tan, H. Pan, H. Li, M. L. Minus. B. M. Budhlall, and M. J. Sobkowicz, *J. Phys. Chem. C*, **122** (2018) 2918.
19. S. M. Tuladhar, D. Poplavskyy, S. A. Choulis, J. R. Durrant, D. D. C. Bradley, and J. Nelson, *Adv. Funct. Mater*., **15** (2005) 1171.
20. D. Abbaszadeh, A. Kunz, G. A. H. Wetzelaer, J. J. Michels, N. I. Craciun, K. Koynov, I. Lieberwirth, and P. W. M. Blom, *Nat. Mater.*, **15** (2016) 628.
21. N. F. Mott and R. W. Gurney, "*Electronic processes in ionic crystals*", Oxford University Press, Oxford, 1940.

Journal of Photopolymer Science and Technology
Volume 34, Number 3 (2021) 297−305 ©2021SPST

Evaluation of Color Stability of Experimental Dental Composite Resins Prepared from Bis-EFMA, A Novel Monomer System

Ömer Hatipoğlu[1*], Emine Akyüz Turumtay[2], Ayşegül Göze Saygın[3], and Fatma Pertek Hatipoğlu[4]

[1] Department of Restorative Dentistry, Niğde Ömer Halisdemir University, Niğde, Turkey
[2] Department of Chemistry, Recep Tayyip Erdogan University, Rize, Turkey
[3] Department of Prosthodontics, Cumhuriyet University Faculty of Dentistry, Sivas, Turkey
[4] Special Dentistry, Niğde,, Turkey
**ohatipoglu@ohu.edu.tr*

Color stabilities of experimental composite resins based on Bis-EFMA (a novel bisphenol A [BPA]-free monomer system) with 3M ESPE FiltekTM Z250 (FZ) and experimental composite resins based on bisphenol A-glycidyl methacrylate (Bis-GMA) and urethane dimethacrylate (UDMA) were compared. Bis-EFMA was synthesized via the reaction between 9,9-bis[4-(2-hydroxyethoxy)phenyl]fluorene and 2-(methacryloyloxy)ethyl isocyanate. Experimental Bis-EFMA-, Bis-GMA-, and UMDA-based composites were prepared (20% of each of Bis-EFMA, Bis-GMA, UDMA, or triethylene glycol dimethacrylate (TEGDMA) and 60% glass filler). Eighty composite resin materials were produced (n=5). The initial color values of composites on the first day, first week, and after the first month after immersion into black tea, coffee, cola, and water solutions were measured using a spectrophotometer (VITA Easyshade® V; Zahnfabrik, Bad Säckingen, Germany) against a white background. UDMA- and Bis-EFMA-based composite resins exhibited significantly less ΔE and ΔL compared to Bis-GMA based composite resins ($p < 0.05$). No significant difference was found between FZ and other composites ($p > 0.05$). Tea and coffee caused significant changes in total color, light value, red–green, and blue–green coordinate values changes (ΔE, ΔL, Δa, and Δb, respectively) compared to water and cola ($p < 0.05$). At one month compared to one week and one day, ΔE, ΔL, Δa, and Δb were significantly different ($p < 0.05$). Bis-EFMA has the potential to be used in commercial dental composites as a substitute for Bis-GMA in terms of better color stability.

Keywords: Bisphenol A, Color Stability, Dental composite material, Resin matrix

1. Introduction

Bisphenol A glycidyl methacrylate (Bis-GMA) was introduced to the market as the first monomer used in resin-based composites (RBCs) in the early 1960s [1]. Bis-GMA is a product of the reaction between bisphenol A (BPA) and glycidyl methacrylate and is the most widely used monomer as an organic matrix in RBCs [2]. Bis-GMA has a high viscosity due to the strong hydrogen bonds between hydroxyl groups of monomer molecules. Bis-GMA also shows less polymerization shrinkage than other monomers due to its larger molecular weight. Today, Bis-GMA continues to be the most widely used monomer in RBCs; it constitutes approximately 20% of the standard resin composite content alone or in combination with urethane dimethacrylate (UDMA). Since Bis-GMA is highly viscous, it is diluted with different monomers with lower viscosity, such as ethylene glycol dimethacrylate (EGDMA), bisphenol A dimethacrylate (Bis-DMA), or triethylene glycol dimethacrylate (TEGDMA) to facilitate clinical

Received November 19, 2020
Accepted January 8, 2021

application and control viscosity [3]. Generally, among these monomers, TEGDMA is more preferred than other monomers for mixing due to its lower molecular weight. Dilutions of Bis-GMA and UDMA with TEGDMA reduce the viscosity of the RBC, facilitates its application, and increases the degree of polymerization conversion [4].

Monomers such as Bis-GMA and ethoxy bisphenol A dimethacrylate (Bis-EMA), are generally used in dental filling materials. Bis-DMA especially is used in fissure sealants as it is degraded via hydrolysis by salivary esterases and releases the BPA component into the gastrointestinal track. BPA is considered a potential health hazard because it affects and stimulates estrogenic receptors in tissue cultures [5]. R. Pulgar, M. F. Olea-Serrano, et al. [6] reported that a significant amount of BPA (1.8 μg/mg) is released from the Bis-GMA-based composite resins. At this level BPA causes toxic effects [7]. Low doses of BPA may trigger obesity, metabolic diseases, and insulin resistance by stimulating interleukin 6 (IL-6) and tumor necrosis factor α (TNFα) secretion and inhibiting adiponectin secretion [8]. Exposure to BPA is nowadays considered a risk factor for the development and progression of obesity and other metabolic diseases [9].

Due to these negative BPA-induced effects, research is being conducted on new RBCs that do not contain Bis-GMA. To prepare these new RBCs, new methacrylate monomers, such as urethane [10,11], cycloaliphatic [12,13], multi-branched [14,15], silicon-containing [16], and fluorinated methacrylates [17-19] have been considered as an alternative to Bis-GMA. Although some of these monomers exhibit great advantages compared to Bis-GMA, most of them exhibit lower mechanical properties compared to Bis-GMA. In addition to the novel methacrylate monomers, many new dental applications, such as oxiranes [20-22], thiol-enes [23-25], styrenic-methacrylate [26], thiol-Michael [27], and vinylcyclopropanes [28,29] have been proposed. However, although many novel methacrylate monomers or resin systems have been developed, an alternative system to Bis-GMA with sufficient mechanical properties has not yet been found. J. He and H. M. Kopperud [30] produced a novel monomer system called Bis-EFMA derived from 9,9-bis[4-(2-hydroxy-ethoxy)phenyl]fluorene (Bis-HEPF). In their study, they compared the mechanical and biological properties of Bis-EFMA- and Bis-GMA-based composites. Bis-EFMA-based composite resins showed low shrinkage, low water absorption, low cytotoxicity, and high flexural strength compared to Bis-GMA based ones. J. He and H. M. Kopperud [30] claimed that the Bis-EFMA monomer system is a powerful alternative to the Bis-GMA.

The purpose of this study was to compare the color stabilities of RBCs prepared with Bis-EFMA monomer system with a commercial and experimental composite resin based on Bis-GMA and UDMA monomers. The null hypotheses of this study consisted of three parts:

(1) The color stability of the experimental RBCs prepared with the Bis-EFMA monomer system is insufficient compared to the experimental based on Bis-GMA and UDMA and commercial RBCs.

(2) There is no significant difference among solutions concerning color stability.

(3) There is no significant difference among the exposure time periods in terms of color stability.

2. Experimental

2.1. Materials

Dibutyltin dilaurate (DBTL), camphorquinone (CQ), and Bis-HEPF were purchased from the Tokyo Chemical Industry (Tokyo, Japan). Bis-GMA, UDMA, TEGDMA, dimethyl aminoethyl methacrylate (DMAEMA), and 2-(methacryloyloxy)ethyl isocyanate (MEI) were purchased from the Sigma-Aldrich Co. (St. Louis, MO, USA). Silanized glass fillers (EEG102-07-S, d_{50} = 0.7 μm) were purchased from ESSCHEM Europe (Seaham, U.K.). 3M ESPE FiltekTM Z250 (FZ) as control material was purchased from 3M Co. (St. Paul, MN, USA).

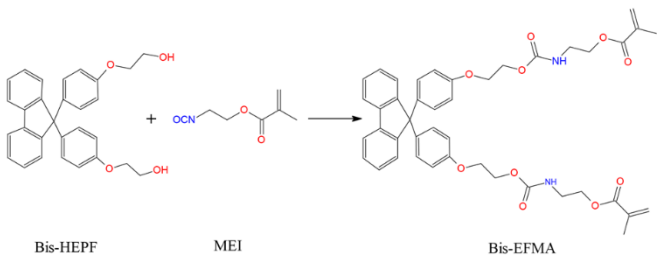

Fig. 1. Synthesis mechanism of Bis-EFMA.

2.2. Synthesis of Bis-EFMA

Bis-EFMA, derived from Bis-HEPF, was synthesized via the reaction between the −OH group in Bis-HEPF and −NCO group in MEI as shown in Fig. 1. For this synthesis, 1.37 g Bis-HEPF, 1 g MEI, and 25 mL of CH_2Cl_2 containing two drops of DBTL were mixed at room temperature. The reaction process was followed by FT-IR analysis of the sample taken from the reaction medium. The disappearance of the infrared absorbance peak of −NCO group at MEI observed at 2270 cm^{-1} indicated that the reaction finished (Fig. 2). After the reaction was complete, most of the CH_2Cl_2 was evaporated at 25 °C with a rotary evaporator. Large amounts of diethyl ether was poured into the remaining crude product to precipitate it. The resulting Bis-EFMA was dried in a rotary evaporator at 30 °C. Verification of the purity and structure of Bis-EFMA was examined using FT-IR and ^{1}H-NMR spectra. The structure of the resulting Bis-EFMA was investigated by FT-IR. IR (Bis-EFMA): ν (cm^{-1}) 3361, 2956, 1710, 1636, 1607, 1582, 1506, 1448, 1234, 1155, 1053. ^{1}H-NMR ($CDCl_3$, 400 Hz): 7.75-7.73, 7.36-7.31, 7.26-7.23, 7.11-7.09, 6.76-6.73 (16H, Ar-O), 6.09 (2H, trans, $2CH_2$=C(CH_3)CO), 5.56 (2H, cis, $2CH_2$=C(CH_3)CO), 5.08 (2H, 2-NH), 4.39-4.36, 4.22-4.19, 4.09-4.06 (12H, 2-$OCH_2CH_2OC(O)NHCH_2CH_2$), 3.48 (4H, 2-$OCH_2CH_2OC(O)NHCH_2CH_2$), 1.92 (6H,$2CH_2$=C(CH_3)CO). FT-IR and ^{1}H-NMR spectra are included in Figs. 2 and 3.

2.3. Preparation of dental resin matrix and experimental composites

The experimental resin matrix was prepared by

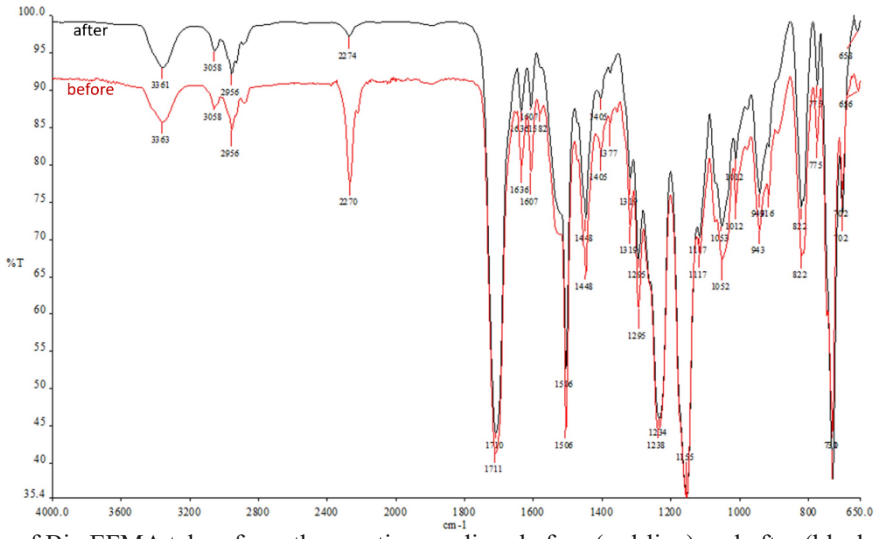

Fig. 2. FT-IR spectra of Bis-EFMA taken from the reaction medium before (red-line) and after (black-line) finalizing of the reaction.

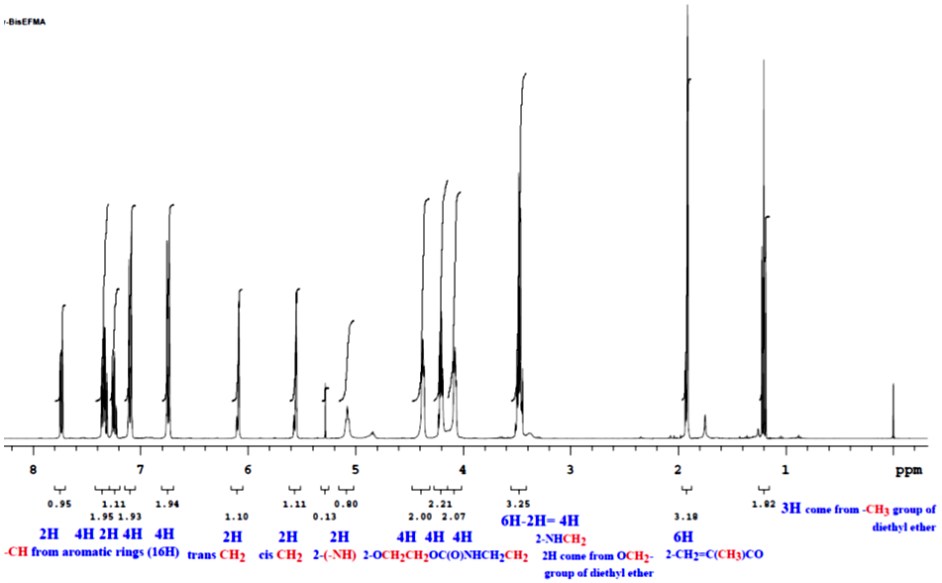

Fig. 3. ^{1}H-NMR spectrum of synthesized Bis-EFMA.

adding 50% by weight of Bis-EFMA (Bis-GMA and UDMA for control) and 50% by weight of TEGDMA and 0.7% by weight of CQ and 0.7% by weight of DMAEMA. The experimental composite resin was prepared by adding dental glass fillers to the resin matrices. The ratio of dental glass filler relative to the experimental composite was adjusted to 60% in a volume equivalent to the filler content of the FZ. The experimental resin was weighed in a mixing vessel, and fillers were added to the vessel in small portions. The composite was mixed using the Speedmixer device at 1400 rpm for 30 sec after the fillers were added. The properties of the experimental and commercial composite resins are shown in Table 1.

2.4. Preparation of solutions

Four different solutions (black tea, coffee, cola, and distilled water) were used for the study. Tea and coffee solutions were prepared according to the manufacturer's instructions. The black tea was prepared by immersing a black tea bag (Lipton yellow label tea bag tea, Turkey) in 150 mL of boiled water for 5 min. The coffee was prepared by mixing 15 g of coffee powder (Nescafé Classic; Nestlé, Vevey, Switzerland; pH 5.56) in 200 mL of hot water. No special preparation methods were applied to Coke (Coca Cola Co, Atlanta, GA; pH 2.52) and distilled water solutions. The temperature of all solutions was measured using a thermometer to correspond to the standard room temperature. The solutions were refreshed regularly every day.

2.5. Sample preparation

Each composite material was placed in metal molds to obtain cylindrical composite samples with a diameter of 8 mm and 2 mm thickness. The metal mold was pressed with a finger pressure between two microscopic glasses covered with mylar strips to remove excess material and eliminate voids from the composite material. The BisGMA/TEGDMA, UDMA/TEGDMA, and Bis-EFMA/TEGDMA experimental composite resins and FZ composite resin were placed into the molds in one step. After the excessive materials were removed, a total of 80 composite resin materials (n = 5) were polymerized for 20 sec with a light emitting diode (LED) light source (VALO Cordless, Ultradent, South Jordan, UT, USA; wavelength 390–490 nm; intensity 1000 mW/cm^2) according to the manufacturer's recommendations while the polymerizing LED light source was kept in contact with the glass.

2.6. Measuring color stability

The initial color values of RBCs and color values after one day, one week, and one month after immersion in the solution were measured using a spectrophotometer (VITA Easyshade® V; Zahnfabrik, Bad Säckingen, Germany) against a white background. Color measurements of each sample were repeated three times by an operator, and the average of the three values were recorded. Total color changes (ΔE) were calculated using the equation (1)

$$\Delta E = [(L0\text{-}L1)^2+(a0\text{-}a1)^2+(b0\text{-}b1)^2]^{1/2} \quad (1)$$

where $L0$, $L1$, $a0$, $a1$, $b0$, and $b1$ indicate that initial light value degree, degree of light value after immersion, initial red-green coordinate value, the red–green coordinate value after immersion, initial green–blue coordinate value, and the green–blue after immersion, respectively. Light value change (ΔL) and red–green and green–blue coordinate value changes (Δa and Δb, respectively) were calculated using the equations (2 to 4).

$$\Delta L=[(L0\text{-}L1)^2]^{1/2} \quad (2)$$

$$\Delta a=[(a0\text{-}a1)^2]^{1/2} \quad (3)$$

$$\Delta b=[(b0\text{-}b1)^2]^{1/2} \quad (4)$$

2.7. Statistical analysis

The Jamovi (Version 1.0.4) as accessed by https://www.jamovi.org, program was used for statistical analysis. Normality of data distribution was checked using the Shapiro–Wilk test. Due to normal distribution, an analysis of covariance (ANCOVA) was used for the color differences.

Table 1. The properties of the experimental and commercial composite resins used in the study.

Composite	Resin Matrix	Fillers		
		Type	Content (Vol%)	Size (μm)
FZ	Bis-GMA, TEGDMA, UDMA, and Bis-EMA	Zirconia/Silica	60	0.01–3.5
Bis-GMA/TEGDMA	Bis-GMA, TEGDMA	BaO/ SiO2/ B2O3	60	0.7
Bis-EFMA/TEGDMA	Bis-EFMA, TEGDMA	BaO/ SiO2/ B2O3	60	0.7
UDMA/TEGDMA	UDMA, TEGDMA	BaO/ SiO2/ B2O3	60	0.7

Significant differences were analysed with the Tukey's post hoc test ($a = 0.05$).

3. Results and discussion

UDMA- and Bis-EFMA-based composite resins exhibited significantly less ΔE and ΔL compared to Bis-GMA based composite resins ($p < 0.05$). No significant difference was found among other groups in terms of composite type ($p > 0.05$) as shown in Table 2. Tea and coffee exhibited significant differences in ΔE, ΔL, Δa, and Δb compared to water and cola ($p < 0.05$). Between tea and coffee, the only difference was found concerning Δa ($p < 0.001$). In terms of solution type, no significant difference was found among other groups ($p > 0.05$) (Table 3). The one month time period exhibited significant differences in ΔE, ΔL, Δa, and Δb compared to one week and one day ($p < 0.05$). In terms of time periods, no significant difference was found among other groups ($p > 0.05$) as shown in Table 4. Descriptive statistics of composite and solution types and time period groups regarding ΔE, ΔL, Δa, Δb values are presented in Table 5.

Dental resin matrix is one of the important parameters that can change many physical properties of RBCs. The monomer properties, such as viscosity, chemical structure of the polymer network, crosslink density, and molecular weight can affect the mechanical properties of the RBCs [31]. The presence of water in the resin, which causes oxidation of unreacted double bonds, paves the way for the pigments to penetrate the resin [32]. In this respect, there are differences among resins in terms of discoloration of composite materials. Bis-EFMA is a powerful alternative to traditional monomers in terms of improved mechanical property and lower cytotoxicity [30]. However, to our knowledge there are no reports addressing the color stability of Bis-EFMA monomer-based composite resin; therefore, in this study, the first evaluation of color stability of this candidate monomer was performed.

The three-dimensional (3D) color measurement formulas CIEL*a*b* and CIE2000 are recommended by the International Organization for Standardization (ISO) for calculating color differences. Statistically related results were obtained with two formulas in a previous study [33]. In the current study, CIEL*a*b* was preferred. Additionally, due to the challenge of providing an overall picture using ΔE values alone, all of the parameters (ΔL, Δa, Δb) were presented in the study with this preference. In a previous study, clinical perceptions and acceptable threshold values were reported as $\Delta E = 1$ and $\Delta E = 3.7$, respectively [34]. Based on these threshold values, during almost all time periods, ΔE was higher than the threshold of perceptibility ($\Delta E = 1$) and acceptability ($\Delta E = 3.7$) regardless of the composite or solution types except FZ (up to 1 week $\Delta E = 2.88–3.50$) and UDMA-based composites, which were immersed in water solutions (up to one month $\Delta E = 2.79–3.15$). These outcomes indicate that discoloration is a clinical problem in all RBCs, whether the composite is experimental or commercial.

The first null hypothesis was rejected, experimental RBCs prepared with the Bis-EFMA exhibited less discoloration compared to Bis-GMA based ones. Water absorption may soften the resin matrix and increase discoloration [35], and the color stability of the RBCs has been shown to correlate with water absorption and solubility [36,37]. UDMA- and Bis-EFMA-based materials contain carbamate linkages (-NHCOO-), which cause less water absorption, while Bis-GMA-based materials contain highly polar hydroxyl groups that cause high water sorption [30,38,39]. In line with the findings of the present study, Bis-GMA based composite resins, which have higher water absorption, have been shown to be more susceptible to staining than UDMA- and Bis-EFMA-based composite resins (in terms of ΔE and ΔL) [36]. Besides, it has been shown that there a correlation between the degree of conversion and both internal discoloration and water absorption exists, and as the degree of conversion increases, discoloration decreases [36,40]. The urethane groups in both monomers can increase the polymerization rate and provide advantages in terms of the degree of conversion compared to Bis-GMA [41]. Bis-GMA has hydrogen bonds between the hydroxyl groups, which cause disadvantages, such as very high viscosity. This structure manifests a low degree of conversion [41]. Already, in terms of both the degree of conversion and water absorption, UDMA and Bis-EFMA were shown to be superior to Bis-GMA [30,36].

TEGDMA was added to experimental composites to dilute monomers with higher viscosities. In this respect, it would not be a correct approach to evaluate the findings of Bis-GMA-, Bis-EFMA-, and UDMA-based experimental composites independently from TEGDMA. TEGDMA proportions may vary in composite contents, so we adjusted the TEGDMA proportion in experimental

composites to be 50% by weight of the resin content as J. He and H. M. Kopperud [30] did. TEGDMA, which has a low molecular weight (286 g/mol), led to an improvement in viscosity, reactivity, and final degree of conversion of the matrix phase. However, this monomer increases water sorption [42]. It has been shown in many studies that TEGDMA exhibits greater discoloration [43,44]. Bis-EMA has a higher molecular weight (540 g/mol), and it reduces viscosity and allows a high degree of conversion [36]. Bis-EMA, which has less hydrophilic structure, is superior to other monomers in terms of color stability [38,45]. FZ, which is a commercial composite, contains Bis-GMA, TEGDMA, UDMA, and Bis-EMA monomer composition in combination [46]. In this context, it is reasonable to expect FZ to be successful in terms of color stability. However, in this study, the FZ commercial product did not exhibit superior performance to the experimental composites in terms of color stability. Consistent with the study of J. He and H. M. Kopperud [30] in which it was determined that the water absorption of Bis-EFMA-based composites and FZ is close, in the current study, Bis-EFMA provided similar color stability values as FZ. Nevertheless, the differences between the experimental composites used in the study and the FZ is attributed to the type and size distribution of

Table 2. ANCOVA Post Hoc Comparisons - Composite type (Regardless of solution type and time periods).

Composite type	Composite type	Comparison (ΔE)			Comparison (ΔL)		
		MD	SE	p_{tukey}	MD	SE	p_{tukey}
Bis-GMA	UDMA	3.374	0.934	0.002*	2.985	0.726	< .001*
-	Bis-EFMA	2.47	0.934	0.044*	2.895	0.726	< .001*
-	FZ	1.075	0.934	0.658	1.53	0.726	0.154
UDMA	Bis-EFMA	-0.904	0.934	0.768	-0.09	0.726	0.999
-	FZ	-2.299	0.934	0.069	-1.455	0.726	0.19
Bis-EFMA	FZ	-1.395	0.934	0.443	-1.365	0.726	0.24
Composite type	Composite type	Comparison (Δa)			Comparison (Δb)		
		MD	SE	p_{tukey}	MD	SE	p_{tukey}
Bis-GMA	UDMA	0.61833	0.296	0.161	1.445	0.727	0.196
-	Bis-EFMA	-0.13667	0.296	0.967	0.753	0.727	0.728
-	FZ	-0.13	0.296	0.972	-0.35	0.727	0.963
UDMA	Bis-EFMA	-0.755	0.296	0.056	-0.692	0.727	0.777
-	FZ	-0.74833	0.296	0.059	-1.795	0.727	0.068
Bis-EFMA	FZ	0.00667	0.296	1	-1.103	0.727	0.429

* indicates the significance ($p < 0.05$), MD: Mean Differences.

Table 3. ANCOVA Post Hoc Comparisons – Solution type (Regardless of composite type and time periods).

Solution type	Solution type	Comparison (ΔE)			Comparison (ΔL)		
		MD	SE	p_{tukey}	MD	SE	p_{tukey}
Water	Cola	-0.506	0.934	0.949	0.693	0.726	0.775
-	Tea	-7.399	0.934	< .001*	-5.138	0.726	< .001*
-	Coffee	-7.649	0.934	< .001*	-4.985	0.726	< .001*
Cola	Tea	-6.892	0.934	< .001*	-5.832	0.726	< .001*
-	Coffee	-7.142	0.934	< .001*	-5.678	0.726	< .001*
Tea	Coffee	-0.25	0.934	0.993	0.153	0.726	0.997
Solution type	Solution type	Comparison (Δa)			Comparison (Δb)		
		MD	SE	p_{tukey}	MD	SE	p_{tukey}
Water	Cola	-0.377	0.296	0.582	-1.36	0.727	0.242
-	Tea	-3.182	0.296	< .001*	-3.86	0.727	< .001*
-	Coffee	-1.997	0.296	< .001*	-5.07	0.727	< .001*
Cola	Tea	-2.805	0.296	< .001*	-2.49	0.727	0.004*
-	Coffee	-1.62	0.296	< .001*	-3.7	0.727	< .001*
Tea	Coffee	1.185	0.296	< .001*	-1.21	0.727	0.347

* indicates the significance ($p < 0.05$), MD: Mean Differences.

Table 4. ANCOVA Post Hoc Comparisons – Time Periods (Regardless of composite and solution types).

Time Periods	Time Periods	Comparison (ΔE)			Comparison (ΔL)		
		MD	SE	p_{tukey}	MD	SE	p_{tukey}
1 day	1 week	-1.57	0.809	0.130	-1.26	0.628	0.115
-	1 month	-4.58	0.809	< .001*	-3.80	0.628	< .001*
1 week	1 month	-3.01	0.809	< .001*	-2.54	0.628	< .001*
Time Periods	Time Periods	Comparison (Δa)			Comparison (Δb)		
		MD	SE	p_{tukey}	MD	SE	p_{tukey}
1 day	1 week	-0.0375	0.257	0.988	-0.767	0.629	0.443
-	1 month	-0.8600	0.257	0.003*	-2.352	0.629	< .001*
1 week	1 month	-0.8225	0.257	0.004*	-1.585	0.629	0.034*

* indicates the significance ($p < 0.05$), MD: Mean Differences.

filler, and monomer composition.

Second null hypothesis was rejected, solution type exhibited significantly different discoloration. Many investigations reported that tea and coffee were the beverages that caused the most staining, a finding in agreement with those from current investigation [47-50]. The staining mechanisms of tea and coffee, which have yellow pigments, differ from each other. The discoloration produced by tea occurs via adsorption of high polar pigments to the surface. However, the situation is different for coffee because it changes the surface color by adsorption and absorption of lower polar pigments with smaller particle sizes [51]. In this study, the

Table 5. Descriptive statistics of composite type, solution, time period groups in regard to ΔE, ΔL, Δa, Δb values.

Composite type	Solution	Time Period	ΔE (mean±SD)	ΔL (mean±SD)	Δa (mean±SD)	Δb (mean±SD)
Bis-GMA/ TEGDMA	Water	1 day	4.94±1.27	3.66±1.04	0.060±0.0548	3.28±0.909
		1 week	5.56±3.18	4.84±3.34	0.660±0.472	1.96±1.62
		1 month	6.60±4.02	6.46±4.04	0.660±0.472	0.880±0.712
	Cola	1 day	3.76±1.10	2.06±1.39	1.96±0.288	2.20±0.866
		1 week	4.31±2.80	3.44±3.16	1.28±0.753	1.46±0.961
		1 month	8.27±4.94	7.08±4.04	1.54±1.75	3.40±3.21
	Tea	1 day	7.00±1.17	4.82±1.44	4.22±0.782	2.52±0.853
		1 week	10.0±9.21	5.14±8.91	2.46±0.888	4.94±7.69
		1 month	25.6±3.39	19.1±3.11	5.46±1.31	16.1±2.27
	Coffee	1 day	10.3±4.46	8.62±4.50	3.68±0.785	3.16±3.23
		1 week	10.6±2.84	8.46±2.97	2.34±1.26	4.86±3.47
		1 month	22.6±10.7	15.5±7.32	3.62±1.44	15.8±8.37
UDMA/ TEGDMA	Water	1 day	2.81±1.73	1.06±0.740	0.560±0.329	2.42±1.77
		1 week	2.79±2.16	1.68±2.18	0.240±0.261	1.72±1.52
		1 month	3.15±1.30	2.26±1.44	0.480±0.335	1.90±0.854
	Cola	1 day	6.42±5.68	1.94±0.723	1.22±0.829	5.54±6.14
		1 week	5.27±2.52	2.36±1.32	0.840±1.01	4.00±3.23
		1 month	4.51±3.67	1.72±0.722	1.26±1.19	3.54±3.96
	Tea	1 day	7.31±1.82	5.56±1.51	3.14±1.23	2.90±2.19
		1 week	11.5±2.97	9.96±1.90	3.36±1.30	4.36±2.64
		1 month	11.4±3.18	9.82±2.24	3.98±1.66	3.62±2.64
	Coffee	1 day	6.36±2.42	5.32±2.21	1.76±0.434	2.64±1.84
		1 week	8.31±4.83	5.88±2.24	1.74±0.627	4.54±5.61
		1 month	9.36±2.13	5.76±3.28	1.94±1.23	6.06±3.11
Bis-EFMA/ TEGDMA	Water	1 day	5.00±1.65	2.22±1.74	1.18±0.554	4.10±1.30
		1 week	5.22±2.16	4.50±2.50	0.580±0.396	2.12±0.983
		1 month	5.96±1.69	5.48±1.77	1.02±0.164	1.74±1.23
	Cola	1 day	3.35±0.785	1.62±1.16	0.900±0.731	2.48±0.864
		1 week	9.01±4.08	4.66±3.76	1.88±1.58	7.06±2.75
		1 month	4.26±4.25	1.56±1.13	1.44±0.783	3.50±4.23
	Tea	1 day	5.46±2.23	1.92±1.54	3.04±1.45	3.78±1.91
		1 week	6.70±1.13	2.22±1.31	4.70±0.992	3.60±2.17
		1 month	18.5±2.38	14.6±2.10	8.48±0.963	7.18±2.98
	Coffee	1 day	6.75±4.04	3.12±1.54	1.02±0.792	4.86±5.23
		1 week	9.46±3.39	5.28±2.74	1.76±0.623	6.62±4.68
		1 month	10.3±5.50	7.20±6.99	3.58±0.653	4.50±2.70
FZ	Water	1 day	2.88±1.47	6.78±10.9	1.34±1.35	1.14±0.893
		1 week	3.50±2.40	6.62±11.6	1.30±1.51	1.16±0.684
		1 month	3.81±1.79	6.10±8.07	2.14±1.69	1.76±1.16
	Cola	1 day	1.83±0.763	0.980±0.853	0.460±0.261	1.34±0.493
		1 week	4.08±3.04	2.42±2.15	0.840±0.321	3.12±2.23
		1 month	3.25±1.71	0.460±0.586	1.12±0.550	2.90±1.76
	Tea	1 day	11.0±11.0	9.30±9.79	3.64±3.26	4.10±4.42
		1 week	12.5±13.3	8.96±11.7	4.08±3.63	6.84±6.69
		1 month	13.9±5.93	8.88±3.52	1.84±0.902	10.5±4.95
	Coffee	1 day	13.9±12.2	8.16±5.84	2.88±2.42	10.3±11.1
		1 week	15.3±13.7	10.0±7.52	3.60±3.58	10.7±11.3
		1 month	20.8±5.36	15.1±6.15	6.26±6.56	11.0±0.52

SD: Standard deviation

lack of association between coffee and tea in terms of staining was consistent with findings from some previous studies [49]; however, some studies found that tea caused much more discoloration than coffee [47,52]. In this study, no difference was found between water and cola in terms of discoloration, a result that is consistent with the previous studies [49, 53].

Although cola, which has a low pH, can affect the surface integrity of the material, it caused less lack discoloration than tea and coffee possibly due to the lack of yellow pigments, such as tannins [51]. Consistent with this study, many previous studies conducted on water and cola found that these solutions showed the lowest mean ΔE values [45, 53-55]. Since water does not contain colorants, these color changes may be attributed to water absorption by the organic matrix.

The third null hypothesis was rejected, time periods exhibited significantly different discoloration. As the time period increased, ΔE values also increased. The analysis of immersion time alone revealed that the most noticeable discoloration occurred after 30 days. Irrespective of the type of solution used, findings revealed by previous studies, which showed that the longer staining periods increase discoloration, are consistent with the present study [45,56-59].

4. Conclusion

Bis-EFMA and UDMA monomers were found to be superior to Bis-GMA-based composites in terms of color stability. Besides, no significant difference was found between Bis-EFMA-based composite resins and FZ, which is used as a reference to evaluate whether a Bis-EFMA-based composite had the potential to be used as a commercial composite. Based on these findings, it was concluded that Bis-EFMA has the potential to be used in commercial dental composites as a substitute for Bis-GMA in terms of better color stability.

Acknowledgement

The authors would like to extend their appreciation to the Sutcu Imam University for funding the work (Project NO: 2019/1-24 M). Besides, they would like to thank Inci Dental Company who assists in the supply of experimental materials.

References

1. R. Z. Alshali, N. A. Salim, R. Sung, J. D. Satterthwaite, and N. Silikas, *Dent. Mater.*, **31** (2015) 711.
2. N. Garg and A. Garg, "*Textbook of operative dentistry*", Boydell & Brewer Ltd, New Delhi, 2010, p.300.
3. A. H. García, M. A. M. Lozano, J. C. Vila, A. B. Escribano, and P. F. Galve, *Med. Oral. Patol. Oral. Cir. Bucal.*, **11** (2006) 215.
4. R. Lagocka, K. Jakubowska, D. Chlubek, and J. Buczkowska-Radlinska, *Adv. Med. Sci.*, **60** (2015) 191.
5. N. Olea, R. Pulgar, P. Pérez, F. Olea-Serrano, A. Rivas, A. Novillo-Fertrell, V. Pedraza, A. M. Soto, and C. Sonnenschein, *Environ. Health. Perspect.*, **104** (1996) 298.
6. R. Pulgar, M. F. Olea-Serrano, A. Novillo-Fertrell, A. Rivas, P. Pazos, V. Pedraza, J. Navajas, and N. Olea, *Environ. Health. Perspect.*, **108** (2000) 21.
7. R. Steinmetz, N. G. Brown, D. L. Allen, R. M. Bigsby, and N. Ben-Jonathan, *Endocrinology*, **138** (1997) 1780.
8. E. R. Hugo, T. D. Brandebourg, J. G. Woo, J. Loftus, J. W. Alexander, and N. Ben-Jonathan, *Environ. Health. Perspect.*, **116** (2008) 1642.
9. P. Alonso-Magdalena, I. Quesada, and A. Nadal, *Nat. Rev. Endocrinol.*, **7** (2011) 346.
10. B. Yu, D. Liu, F. Liu, and J. He, *Adv. Polym. Technol.*, **33** (2014) 1.
11. M. Yin, F. Liu, and J. He, *J. Mech. Behav. Biomed. Mater.*, **57** (2016) 157.
12. S. Shi and J. Nie, *Dent. Mater.*, **24** (2008) 530.
13. T. K. Vaidyanathan and J. Vaidyanathan, *Acta. Biomater. Odontol. Scand.*, **1** (2015) 59.
14. B. Yu, F. Liu, and J. He, *J. Mech. Behav. Biomed. Mater.*, **35** (2014) 1.
15. B. Yu, F. Liu, J. He, Y. He, and Z. Lin, *Adv. Polym. Technol.*, **34** (2015) 1.
16. X. Liang, F. Liu, and J. He, *Dent. Mater.*, **30** (2014) 917.
17. M. Yin, S. Guo, F. Liu, and J. He, *J. Mech. Behav. Biomed. Mater.*, **51** (2015) 337.
18. S. Luo, W. Zhu, F. Liu, and J. He, *Int. J. Mol. Sci.*, **17** (2016) 1.
19. X. Liu, Z. Wang, C. Zhao, W. Bu, Y. Zhang, and H. Na, *J. Mech. Behav. Biomed. Mater.*, **77** (2018) 446.
20. J. Eick, E. Kostoryz, S. Rozzi, D. Jacobs, J. Oxman, C. Chappelow, A. Glaros, and D. Yourtee, *Dent. Mater.*, **18** (2002) 413.
21. J. D. Eick, R. E. Smith, C. S. Pinzino, and E. L. Kostoryz, *J. Dent.*, **34** (2006) 405.
22. C. C. Chappelow, C. S. Pinzino, S. S. Chen, L. Jeang, and J. D. Eick, *J. Appl. Polym. Sci.*, **103** (2007) 336.
23. N. B. Cramer, C. L. Couch, K. M. Schreck, J. E.

Boulden, R. Wydra, J. W. Stansbury, and C. N. Bowman, *Dent. Mater.*, **26** (2010) 799.
24. M. Podgórski, E. Becka, M. Claudino, A. Flores, P. K. Shah, J. W. Stansbury, and C. N. Bowman, *Dent. Mater.*, **31** (2015) 1255.
25. M. Podgórski, E. Becka, M. Claudino, A. Flores, P. K. Shah, J. W. Stansbury, and C. N. Bowman, *Dent Mater*, **31** (2015) 1263.
26. X. Wang, G. Huyang, S. V. Palagummi, X. Liu, D. Skrtic, C. Beauchamp, R. Bowen, and J. Sun, *Dent. Mater.*, **34** (2018) 228.
27. S. Huang, M. Podgorski, X. Zhang, J. Sinha, M. Claudino, J. W. Stansbury, and C. N. Bowman, *J. Dent. Res.,* **97** (2018) 530.
28. S. Tauscher, Y. Catel, P. Fässler, U. Fischer, and N. Moszner, *J. Appl. Polym. Sci.*, **134** (2017) 1.
29. Y. Catel, P. Fässler, U. Fischer, C. Gorsche, R. Liska, S. Schörpf, S. Tauscher, and N. Moszner, *Eur. Polym. J.*, **98** (2018) 439.
30. J. He and H. M. Kopperud, *Dent. Mater.*, **34** (2018) 1003.
31. N. Moszner and U. Salz, *Prog. Polym. Sci.*, **26** (2001) 535.
32. A. S. Sham, F. C. Chu, J. Chai, and T. W. Chow, *J. Prosthet. Dent.*, **91** (2004) 447.
33. L. Gregor, I. Krejci, E. Di Bella, A.J. Feilzer, S. Ardu, *Odontology*, **104** (2016) 305.
34. G. Khashayar, P. A. Bain, S. Salari, A. Dozic, C. J. Kleverlaan, and A. J. Feilzer, *J. Dent.*, **42** (2014) 637.
35. K. Söderholm, M. Zigan, M. Ragan, W. Fischlschweiger, and M. Bergman, *J. Dent. Res.*, **63** (1984) 1248.
36. A. S. Fonseca, A. D. Labruna Moreira, P. P. de Albuquerque, L. R. de Menezes, C. S. Pfeifer, and L. F. Schneider, *Dent. Mater.*, **33** (2017) 394.
37. F. M. EL-Sharkawy, N. M. Zaghloul, and A. M. Ell-kappaney, *Int. J. Compos. Mater.*, **2** (2012) 7.
38. I. Sideridou, V. Tserki, and G. Papanastasiou, *Biomaterials*, **24** (2003) 655.
39. S. Venz and B. Dickens, *J. Biomed. Mater. Res.*, **25** (1991) 1231.
40. S. Imazato, H. Tarumi, K. Kobayashi, H. Hiraguri, K. Oda, and Y. Tsuchitani, *Dent. Mater. J.*, **14** (1995) 23.
41. I. Sideridou, V. Tserki, and G. Papanastasiou, *Biomaterials*, **23** (2002) 1819.
42. I. Sideridou, V. Tserki, and G. Papanastasiou, *Biomaterials*, **24** (2003) 655.
43. N. Gonulol and F. Yilmaz, *J. Dent.*, **40,** Suppl, 2 (2012) 64.
44. A. U. Güler, E. Güler, A. Ç. Yücel, and E. J. Ertaş, *J. Appl. Oral. Sci.*, **17** (2009) 108.
45. N. Bahbishi, W. Mzain, B. Badeeb, H. M. Nassar, *Materials (Basel)*, **13** (2020) 1.
46. M. Karadas, O. Hatipoglu, H. Er, and E. Akyüz Turumtay, *J. Adhes. Sci. Technol.*, **38** (2018) 2631.
47. N. Tekce, S. Tuncer, M. Demirci, M. E. Serim, and C. Baydemir, *Restor. Dent. Endod.*, **40** (2015) 255.
48. S. Garoushi, L. Lassila, M. Hatem, M. Shembesh, L. Baady, Z. Salim, and P. Vallittu, *Acta. Odontol. Scand.*, **71** (2013) 144.
49. M. Karadas, *Scanning*, **38** (2016) 701.
50. I. Nasim, P. Neelakantan, R. Sujeer, and C. Subbarao, *J. Dent.*, **38** (2010) 137.
51. R. Bagheri, M. Burrow, and M. Tyas, *J. Dent.*, **33** (2005) 389.
52. M. R. Malekipour, A. Sharafi, S. Kazemi, S. Khazaei, and F. Shirani, *Dent. Res. J. (Isfahan)*, **9** (2012) 441.
53. A. A. Al Kheraif, S. S. Qasim, R. Ramakrishnaiah, and R. Ihteshamur, *Dent. Mater. J.*, **32** (2013) 326.
54. A. U. Guler, F. Yilmaz, T. Kulunk, E. Guler, and S. Kurt, *J. Prosthet. Dent.*, **94** (2005) 118.
55. E. Ertas, A. U. Güler, A. C. Yücel, H. Köprülü, and E. Güler, *Dent. Mater. J.*, **25** (2006) 371.
56. M. S. Kumar, R. Ajay, S. A. Miskeen Sahib, M. Chittrarasu, M. Navarasu, N. Ragavendran, and O. F. Burhanuddin Mohammed, *J. Pharm. Bioallied. Sci.*, **9** (2017) 161.
57. C. Barutcigil, K. Barutcigil, M. M. Ozarslan, A. Dundar, and B. Yilmaz, *J. Esthet. Restor. Dent.*, **30** (2018) 3.
58. A. K. Hasan, S. Sunarintyas, and D. Irnawati, *Dent. J. (Majalah Kedokteran Gigi)*, **42** (2009) 123.
59. S. Savas, O. Colgecen, B. Yasa, and E. Kucukyilmaz, *Niger. J. Clin. Pract.*, **22** (2019) 824.

Journal of Photopolymer Science and Technology
Volume 34, Number 3 (2021) 307−313 ©2021SPST

Synthesis and Structure-Activity Relationship of *N*-Substituted Carbazole Oxime Ester Photoinitiators

Huaqiao Lu and Zhiquan Li*

School of Chemical and Material Engineering, Jiangnan University, Wuxi, 214122, China
**lzq@jiangnan.edu.cn*

Four *N*-phenyl substituted carbazole oxime ester photoinitiators were synthesized and their structure-activity relationship were systematically investigated. These photoinitiators have a broad absorption in the range of 300-400 nm and the tail absorption extends above 400 nm. Under 405 nm LED light irradiation, the oxime esters undergo photodecarboxylation and generate active free radicals to induce polymerization of acrylates. The *tert*-butyl substituted aldehyde-oxime ester Ph-N-CZ-2 with terminal methyl group exhibit the best photoinitiation performance among the four *N*-substituted carbazole oxime esters.
Keywords: N-substituted carbazole, Oxime ester, Visible light

1. Introduction

Owing to its unique temporal and spatial controllability, photopolymerization has a wide range of applications in coating, 3D printing, photoresist, etc [1-9]. Compared to traditional thermal polymerization, photopolymerization is efficient, environmentally friendly and easy to operate [10,12]. As a key component of photopolymerization system, photoinitiators play a very important role; they not only determine the polymerization rate but also affect the quality of final products [13,14]. An oxime ester photoinitiator is a high-efficiency type I photoinitiator, which can undergo N-O bond decomposition under irradiation to generate imine free radicals and acyloxy free radicals. The latter decarboxylates to produce active species and initiates the polymerization of acrylate monomers [15,16].

Among various oxime ester photoinitiators, the ones containing carbazoles as chromophores are quite attractive because the azabenzo five-membered ring of carbazole with a rigid and planar conjugated structure can provide excellent photosensitivity. Also, multiple modifiable active sites of the carbazole facilitate further functionalization. The most famous example is the commercially available carbazole-based oxime ester OXE-02, which has become the predominantly used photoinitiator in color photoresist [17]. To extend the absorption region from UV to visible light, several mono- [18] and bifunctional [19] carbazole-based oxime esters containing carbon-carbon triple bonds as π bridges were synthesized. These A-π-D-π-A conjugated oxime esters not only exhibit excellent photosensitivity to 405 nm LED light, but also have excellent two-photon absorption capacity and can be used to prepare exquisite three-dimensional structures. In terms of quantum yield, the carbazole oxime ester initiators with a locked ring structure exhibit significantly improved quantum yield due to the increasing rigidity of the dye scaffolds which can suppress thermal inactivation [20]. However, the modification sites of the above-mentioned oxime esters mainly locate at the carbazole benzene ring, and until now there are much less reports on the *N*-substituted carbazole oxime ester initiators at the 9th position.

In this study, four N-substituted carbazole oxime ester initiators (Fig. 1) were prepared and their structure-activity relationship was systematically investigated. Ph-N-CZ-1 and Ph-N-CZ-2 were synthesized to study the effect of the substituents bonded to the aromatic rings. Ph-N-CZ-2 and Ph-N-CZ-3 were used to investigate the impact of the aldoxime ester and the ketooxime ester on initiator

Received January 22, 2021
Accepted March 1, 2021

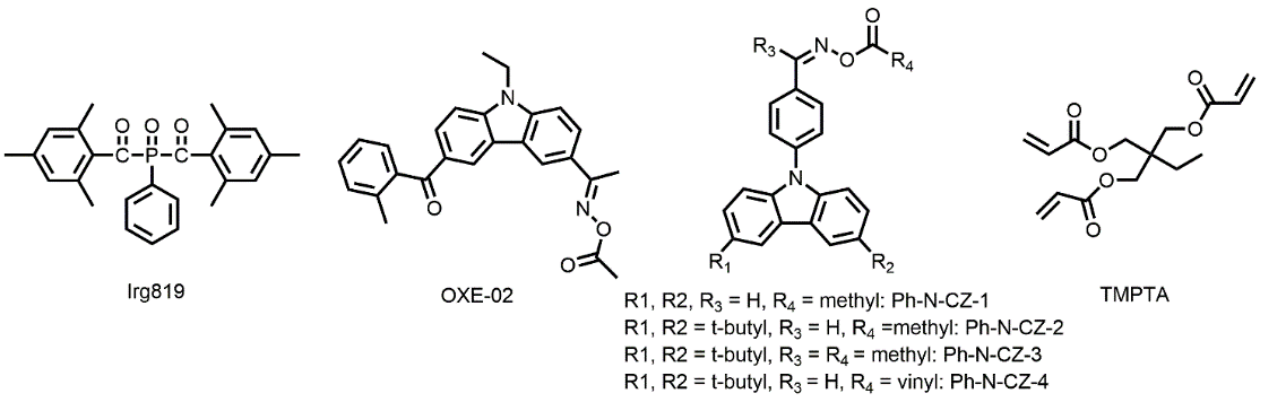

Fig. 1. Structure of the synthetic photoinitiators, the reference photoinitiators, and the monomer used in the formula.

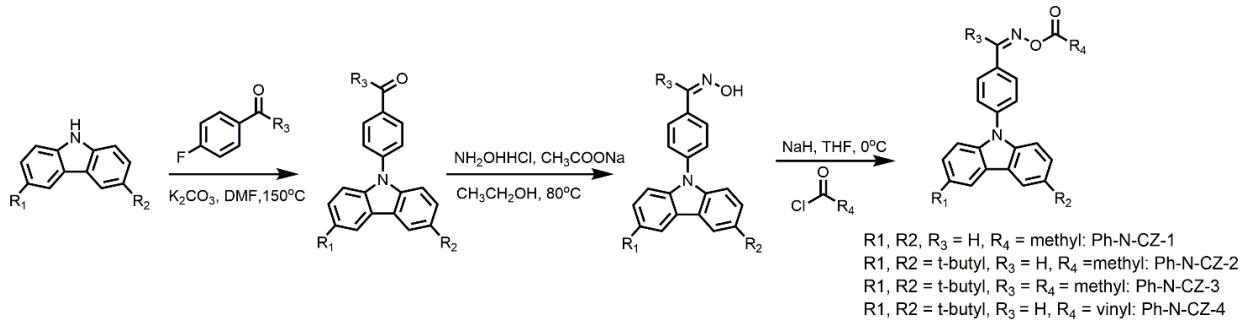

Scheme 1. Synthetic routes of N-substituted carbazolyl oxime ester initiators.

efficiency. In addition, Ph-N-CZ-4 was designed to compare the photoinitiation efficiency of the double-bond radical and the methyl radicals generated after photodecarboxylation (Scheme 1).

2. Experimental

Carbazole, 3,6-di-*tert*-butylcarbazole, 4-fluorobenzaldehyde, 4-fluoroacetophenone, potassium carbonate, hydroxylamine hydrochloride, anhydrous sodium acetate, acetyl chloride, acryloyl chloride, and anhydrous DMF were purchased from Adamas Reagent Co., Ltd. Potassium carbonate, hydroxylamine hydrochloride, anhydrous sodium acetate, acetyl chloride, enoyl chloride, ethanol, petroleum ether, and methylene chloride were obtained from Sinopharm Chemical Reagent Co., Ltd. Sodium hydride was purchased from Energy Chemical. Trimethylolpropane triacrylate (TMPTA) was supplied by Jiangsu Kailin Ruiyang Chemistry. Phenyl-*N*-*tert*-butylnitrone (PBN) was purchased from Tokyo Chemical Industry. All the reagents were of analytical grade and used as received without further purification. OXE-02 was synthesized in the laboratory [21].

Synthesis of 4-(9H-carbazol-9-yl)benzaldehyde *O*-acetyl oxime (Ph-N-CZ-1): Under ice bath conditions, 4-carbazolylbenzaldehyde oxime (0.1 g, 0.349 mmol) and sodium hydride (0.025 g, 1.047 mmol) were added to 10 mL tetrahydrofuran for 30 min. Then, acetyl chloride (0.095 g, 1.047 mmol) was added to the reaction mixture, and the reaction was continued for 30 min. After the completion of the reaction, the reaction was quenched with sodium bicarbonate solution, and the product was extracted with 3×20 mL of dichloromethane. The organic phase was collected and dried with anhydrous sodium sulfate, and the solvent was removed by rotary evaporation to obtain a crude product. After silica gel column chromatography (petroleum ether/dichloromethane = 5:2), 74 mg of yellow solid powder was obtained. Yield: 64.6%.^{1}H NMR (400 MHz, chloroform-d) δ 8.49 (s, 1H), 8.17 (d, J = 7.8 Hz, 2H), 8.03 – 7.99 (m, 2H), 7.70 (d, J = 8.3 Hz, 2H), 7.51 – 7.43 (m, 5H), 7.34 (ddd, J = 8.0, 6.5, 1.6 Hz, 2H), 2.31 (s, 3H). ^{13}C NMR (101 MHz, chloroform-d) δ 167.57, 153.89, 139.78, 139.22, 128.85, 127.71, 126.00, 125.13, 122.68, 119.45, 108.66, 18.6. Calcd. for $C_{21}H_{16}N_2O_2$ 328.1212, found, $[M+H]^+$=329.1295.

Synthesis of 1-(4-(3,6-di-*tert*-butyl-9*H*-carbazol-

9-yl)phenyl)ethan-1-one *O*-acetyl oxime (Ph-N-CZ-2) : Ph-N-CZ-2 was prepared via similar procedure described for Ph-N-CZ-1. Purification by column chromatography (petroleum ether/dichloromethane = 1:0.8) gave 0.238 g of the product as yellow solid powder. Yield: 86.4%. ^{1}H NMR (400 MHz, Chloroform-d) δ 8.17 (d, J = 1.9 Hz, 1H), 8.02 – 7.98 (m, 1H), 7.68 – 7.64 (m, 1H), 7.50 (dd, J = 8.7, 1.9 Hz, 1H), 7.41 (d, J = 8.6 Hz, 1H), 2.51 (s, 1H), 2.34 (s, 1H), 1.50 (s, 9H). ^{13}C NMR (101 MHz, chloroform-d) δ 167.61, 154.01, 142.48, 140.33, 137.54, 128.79, 127.10, 125.47, 122.79, 115.34, 108.16, 33.73, 30.94, 18.61. Calcd. for $C_{29}H_{32}N_2O_2$ 440.2464, found, $[M+H]^+$=441.2502.

Synthesis of 4-(3,6-di-*tert*-butyl-9*H*-carbazol-9-yl)benzaldehyde *O*-acetyl oxime (Ph-N-CZ-3): Ph-N-CZ-3 was prepared via similar procedure described for Ph-N-CZ-1. Purification by column chromatography (petroleum ether/dichloromethane = 10:3) gave 0.164 g of the product as yellow solid powder. Yield: 42.4%. ^{1}H NMR (400 MHz, chloroform-d) δ 8.48 (s, 1H), 8.16 (d, J = 1.9 Hz, 2H), 7.98 (d, J = 8.5 Hz, 2H), 7.69 (d, J = 8.4 Hz, 2H), 7.51 (dd, J = 8.7, 1.9 Hz, 2H), 7.43 (d, J = 8.6 Hz, 2H), 2.30 (s, 3H), 1.50 (s, 19H). ^{13}C NMR (101 MHz, chloroform-d) δ 167.77, 160.74, 142.25, 139.37, 137.71, 132.00, 127.48, 125.33, 122.73, 115.29, 108.12, 33.72, 30.95, 18.33, 13.40. Calcd. for $C_{30}H_{34}N_2O_2$ 454.2620, found, $[M+H]^+$=455.2674.

Synthesis of 4-(3,6-di-*tert*-butyl-9*H*-carbazol-9-yl)benzaldehyde *O*-acryloyl oxime (Ph-N-CZ-4): Ph-N-CZ-4 was prepared via similar procedure described for Ph-N-CZ-1. Purification by column chromatography (petroleum ether/dichloromethane = 1:0.8) gave 0.151 g of the product as yellow solid powder. Yield: 33.3%. ^{1}H NMR (400 MHz, chloroform-d) δ 8.55 (s, 1H), 8.17 (d, J = 1.8 Hz, 2H), 8.01 (d, J = 8.4 Hz, 2H), 7.70 (d, J = 8.4 Hz, 2H), 7.51 (dd, J = 8.7, 1.9 Hz, 2H), 7.44 (d, J = 8.7 Hz, 2H), 6.66 (dd, J = 17.4, 1.3 Hz, 1H), 6.33 (dd, J = 17.4, 10.5 Hz, 1H), 6.03 (dd, J = 10.5, 1.3 Hz, 1H), 1.50 (s, 19H). ^{13}C NMR (101 MHz, chloroform-d) δ 162.60, 154.61, 142.48, 140.39, 137.54, 131.50, 128.88, 127.09, 125.46, 125.14, 122.75, 115.33, 108.17, 33.73, 30.94. Calcd. for $C_{30}H_{34}N_2O_2$ 452.2464, found, $[M+H]^+$=453.2571.

Characterization: ^{1}H NMR and ^{13}C NMR spectra were obtained using a Bruker AVANCE III HD 400 MHz NMR spectrometer with $CDCl_3$ or DMSO-d_6 as the solvent. The high-resolution mass spectra were obtained using a Q-Tof-MS instrument from Bruker Daltonics.

Theoretical calculation: The molecular structures were optimized through m06-2x/def2svp, and the HOMO and LUMO of the photoinitiators were calculated at m06-2x/def2tzvp.

UV-visible spectroscopy: The UV-vis absorption spectra of PIs in acetonitrile were measured using a Beijing Purkinje TU-1901 UV-vis spectrophotometer. All sample solutions were examined in a quartz cuvette with 1 cm light path length and the PIs in acetonitrile with a concentration of 2×10^{-5} mol/L.

Steady-state photolysis: The photolysis studies of PIs were performed using a UV-vis spectrophotometer. Solutions of the PIs in acetonitrile with a concentration of 2×10^{-5} mol/L were examined upon 405 nm LED irradiation, and the light intensity was 100 mW/cm^2 at room temperature. Photolysis rates were calculated using Equation (1):

$$R_d = -\frac{d[PI]}{dt} = -\frac{1}{\varepsilon}\frac{d(A_t)}{dt} \quad (1)$$

Electron spin resonance (ESR) experiments: ESR spin-trapping experiments were carried out using an EMXplus-10/12 X-band spectrometer at 100 kHz magnetic field modulation. Ph-N-CZ-2 (0.05 mol/L) and PBN (0.1 mol/L) were dissolved in toluene and deoxygenated with nitrogen for 10 min before irradiation. The radicals generated when exposed to 405 nm LED irradiation (100 mW/cm^2) were trapped by PBN. The ESR spectra simulations were performed using Bruker Xenon software.

Photodecarboxylation experiment: In a glass sample bottle, a solution of Ph-N-CZ-1 in toluene with a concentration of 1.1 mol/L (left) and a solution of 1×10^{-4} mol/L sodium bicarbonate (right) containing phenolphthalein were prepared, and the two bottles were connected with a long needle as the airway. The airway is present on the liquid surface of the initiator-containing bottle and below the phenolphthalein liquid surface. The bottle containing initiator was irradiated using a 405 nm LED lamp with a light intensity of 100 mW/cm^2.

Photopolymerization kinetics: The light-sensitive resin system consists of a monomer (TMPTA) and PIs (1.5×10^{-5} mol/g resin), mixed evenly with a magnetic stir bar. Four synthesized *N*-substituted carbazole oxime esters were used as PIs, and Irg819 and Oxe-02 were used as reference (Fig. 1). Photopolymerization experiments were carried out by performing real-time Fourier transform infrared spectroscopy (500−4000 cm^{-1} wavelength range, acquisition rate 4 cm^{-1}), and a 405 nm LED lamp

(10 mW/cm^2) was used as the light source. TMPTA containing PIs were smeared on a KBr tablet, and another KBr was used to cover on the former for subsequent tests. The photopolymerization was evaluated by monitoring the change in double bonds, and the degree of conversion of double bond was calculated using Equation (2)

$$\text{Conversion}\ (\%) = [1 - \frac{A_t}{A_0}] \times 100\% \qquad (2)$$

where A_0 and A_t represent the area of double-bond absorption at 1652-1589 cm^{-1} at the time of 0 and t.

Thermal stability test: Thermogravimetric analysis (TGA) experiments were performed by using a Mettler Toledo TGA 1/1100SF instrument with about 4 mg of the sample under a nitrogen atmosphere. The temperature was increased from 30 °C to 800 °C at a rate of 30 °C min^{-1}.

3. Results and discussion

3.1. Theoretical calculations

The calculated frontier orbitals of the initiators are shown in Fig. 2. Good coplanarity between *N*-substituted phenyl groups and carbazole groups has been observed, indicating a large conjugation of the whole molecules. The electron cloud is mainly distributed on carbazole groups and *N*-substituted phenyl groups. The electron orbitals of the ester end groups and the *tert*-butyl electron orbitals have no significant effect on the electron cloud distribution of frontier molecular orbitals. The electron cloud distributed on the conjugated system before excitation shifts to the *N*-substituted phenyl group and oxime ester functional group after excitation, facilitating the breakage of N-O bond to generate active free radicals. According to the electron energy required for the electronic transition from HOMO to LUMO, after introducing a *tert*-butyl group at the positions 3 and 6 of carbazole, compared with Ph-N-CZ-1, the energy gap of Ph-N-CZ-2 and Ph-N-CZ-4 is reduced, but the transition energy of Ph-N-CZ-3, the ketoxime ester with *tert*-butyl substitution, has not been significantly reduced. This may cause the Ph-N-CZ-2 and Ph-N-CZ-4 to be more prone to N-O bond breakage than Ph-N-CZ-1 and Ph-N-CZ-3.

3.2. UV-Vis absorption and photolysis

The UV-vis absorption spectra of four *N*-substituted carbazole oxime ester photoinitiators and two reference initiators Irg819 and OXE-02 in acetonitrile at room temperature are shown in Fig. 3 (a). The *N*-substituted initiators have a broad absorption in the range of 300-400 nm, and the shapes of the absorption peaks are similar. This is caused by the similar chromophores of the four initiator molecules. Figure 3 (b) shows that the four initiators have a tail absorption above 400 nm, making them applicable to popularly used 405 nm LED lamps. When the *t*-butyl group is introduced at the 3rd and 6th positions of the carbazole, the maximum absorption peak of Ph-N-CZ-2 and Ph-N-CZ-4 red-shifted compared to that of Ph-N-CZ-1. However, the ketoxime ester Ph-N-CZ-3, which also has *t*-butyl substitution at positions 3 and 6, has a weaker tail absorption strength. The nearly identical absorption of Ph-N-CZ-2 and Ph-N-CZ-4 indicates that when the main structure of the initiator molecule is similar, the oxime ester terminal functional group slightly affects the light absorption behavior, which may cause a similar photolysis behavior.

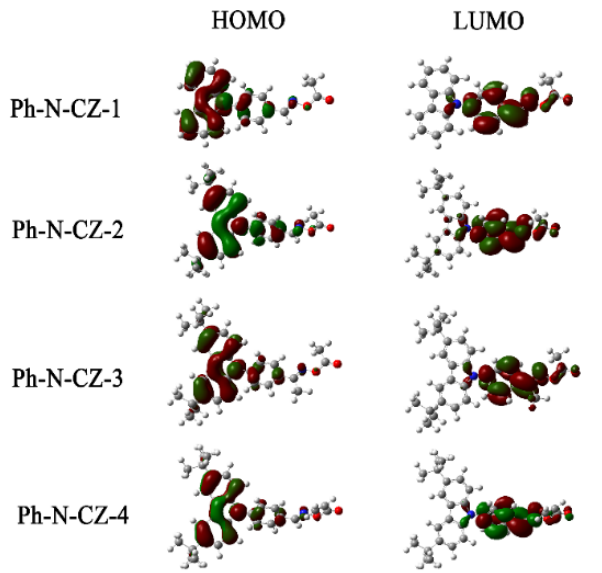

Fig. 2. Electron cloud distribution of frontier orbitals of the photoinitiators and the corresponding energy gaps.

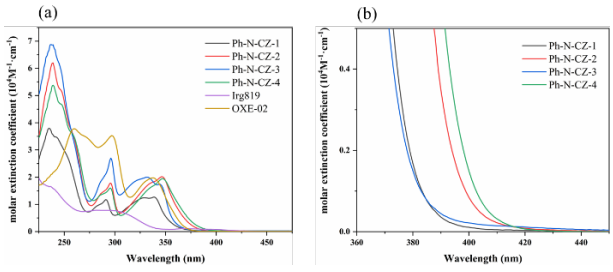

Fig. 3. (a) UV-vis absorption spectra of *N*-substituted carbazole oxime ester initiators (Ph-N-CZ-1, Ph-N-CZ-2, Ph-N-CZ-3, Ph-N-CZ-4) and reference initiators (Irg819, OXE-02) at room temperature in acetonitrile. (b)Tail absorption of *N*-substituted carbazole oxime ester initiators.

Steady-state photolysis tests were carried out in acetonitrile at room temperature with different irradiation times under 405 nm LED irradiation (Fig. 4). Photoinitiators Ph-N-CZ-1, Ph-N-CZ-2, and Ph-N-CZ-4 during light irradiation are blue-shifted, and the intensity of maximum absorption peaks decreases, indicating that the initiators are decomposed during the irradiation. The tail absorption of the three initiators all shifted to the short-wavelength direction. The photolysis rates of Ph-N-CZ-2 and Ph-N-CZ-4 are greater than that of Ph-N-CZ-1 (Fig. 4d). This is consistent with the conclusions obtained in Fig. 2; i.e., the introduction of electron-donating *t*-butyl group decreases the HOMO-LUMO transition energy gap, resulting in faster photodecomposition. For ketoxime ester photoinitiator Ph-N-CZ-3, the wavelength of maximum absorption peak of Ph-N-CZ-3 decreases with prolonging irradiation time but does not show a significant blue shift. Notably, the photolysis rate of Ph-N-CZ-2 was significantly higher than that of Ph-N-CZ-3, indicating that the photochemical activity of aldoxime ester initiator may be higher than that of ketoxime ester initiator.

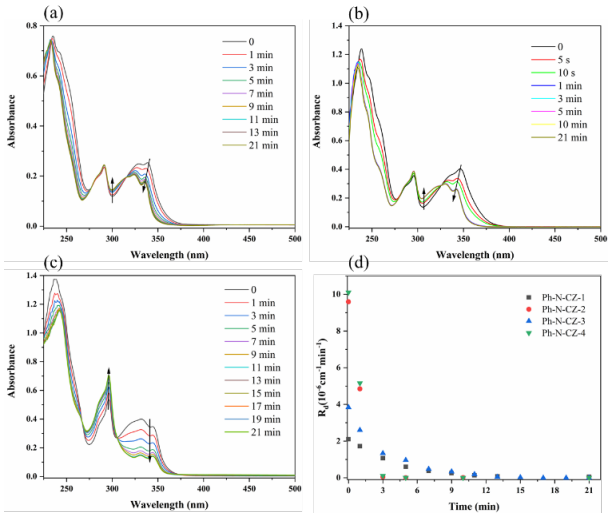

Fig. 4. Changes in UV-vis absorption spectra of *N*-substituted carbazole oxime esters (a) Ph-N-CZ-1, (b) Ph-N-CZ-2, and (c) Ph-N-CZ-3 in acetonitrile under irradiation of 405 nm LED light. (d) Photolysis rate of *N*-substituted carbazole oxime ester initiators with prolonging irradiation time.

Oxime esters has been proven to undergo photo-induced decarboxylation and then generate free radicals with high quantum yields. To confirm the occurrence of photoinduced decarboxylation, as shown in Figs. 5a and 5b, the toluene solution containing photoinitiator Ph-N-CZ-1 was irradiated with a 405 nm LED lamp. The fading color of sodium bicarbonate aqueous solution containing a pH indicator phenolphthalein indicates the generation of CO_2 after the photodecomposition of the photoinitiator.

Electron paramagnetic resonance (ESR) spectroscopy was employed to further confirm the formation of free radicals after photodecarboxylation. As shown in Fig. 5c, the generated free radicals trapped by PBN provide only one radical adduct with hyperfine coupling constants of αN=14.86 G, αH=3.54 G.

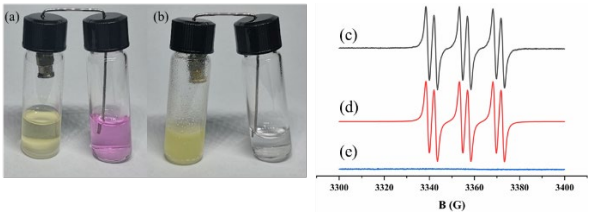

Fig. 5. Photodecarboxylation of photoinitiator Ph-N-CZ-1 (a) before and (b) after irradiation. ESR spectra of radicals trapped by PBN in benzene (c) experimental spectrum, (d) simulated spectrum, and (e) controlled experiment.

3.3. Photopolymerization kinetics

The photoinitiation efficiency of the photoinitiators were studied using real-time Fourier transform infrared spectroscopy. The curves of double-bond conversion with time for four *N*-substituted carbazole oxime ester initiators and two reference initiators under 405 nm LED light irradiation are shown in Fig. 6. All investigated PIs can initiate the polymerization of the acrylate monomer. After introducing *tert*-butyl at positions 3 and 6 of carbazole, the initiation activity of Ph-N-CZ-2 was significantly improved compared to Ph-N-CZ-1. According to the results of the steady-state photolysis experiments and theoretical calculations, the enhancement can be attributed to the reduced transition energy, red-shifted absorption wavelength and faster photolysis rate.

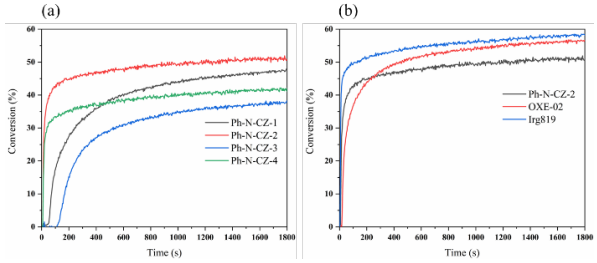

Fig. 6. Double-bond conversion of TMPTA in the presence of (a) the novel photoinitiators and (b) of the commercial photoinitiators under 405 nm LED illumination with a light intensity of 10 mW/cm^2.

Table 1. Photophysical properties and thermal decomposition temperature of Ph-N-CZs.

PIs	T_d (°C)	λ_{max} (nm)	ε_{max} ($M^{-1}cm^{-1}$)	$\varepsilon_{405\ nm}$($M^{-1}cm^{-1}$)
Ph-N-CZ-1	190 °C	339	12675	65
Ph-N-CZ-2	190 °C	346	20170	420
Ph-N-CZ-3	250 °C	344	17395	170
Ph-N-CZ-4	102 °C	347	19455	680

The initiation efficiency of Ph-N-CZ-2 containing terminal methyl group is superior to that of Ph-N-CZ-4 with terminal vinyl group. Considering that Ph-N-CZ-2 and Ph-N-CZ-4 display very similar absorption and photolysis behavior, the difference in photoinitiation performance should be derived from the generated active free radicals. The vinyl radicals formed by photolysis of Ph-N-CZ-4 are stabilized due to conjugation effect, leading to inferior activity of vinyl radicals towards to acrylate double bonds compared to methyl radicals from Ph-N-CZ-2. Moreover, the terminal vinyl group at the end of Ph-N-CZ-4 can participate in the polymerization reaction and the molecules will be introduced into the polymeric network, hindering the movement of active species, and further reducing the initiation activity.

The initiation activity of ketone-oxime ester initiator Ph-N-CZ-3 is significantly lower than that of aldehyde-oxime ester Ph-N-CZ-2, indicating that keto-based oxime ester initiators have a lower initiation activity than the corresponding aldehyde-based oxime ester initiators. This can be verified by steady-state photolysis experiments and theoretical calculations; i.e., Ph-N-CZ-3 has a larger transition energy and a slower photolysis rate. Moreover, ketone-oxime esters containing alkyl chains may have high molecular mobility, leading to additional oscillatory and rotational transition when excited, resulting in low quantum yields and therefore reduced initiation activity.

Overall, the *tert*-butyl substituted aldehyde-oxime ester Ph-N-CZ-2 with terminal methyl group exhibit the best photoinitiation performance among the four N-substituted carbazole oxime esters. As shown in Fig. 6 b, the initiator efficiency of Ph-N-CZ-2 is comparable to that of the reference initiator OXE-02, a highly efficient commercial oxime ester photoinitiator popularly used in photoresist. Higher conversion was observed for Irgacure 819 because the acylphosphine oxide can produce four free radicals after photocleavage and all these radicals are known to be efficient initiating radicals, while for the oxime ester photoinitiators, only one active species is generated after photodecarboxylation, due to the fact that the iminyl radical formed has only a poor initiation efficiency.

3.4. Thermal stability

Oxime ester photoinitiators are prone to bond-breaking reaction under heating condition due to the presence of a weak N-O bond, leading to the instability of resin photosensitive resin. A thermogravimetric analyzer (TGA) was used to study the thermal stability of the N-substituted carbazole oxime esters under heating conditions. Table 1 shows the thermal decomposition temperature of the four initiators; ketone-based oxime ester Ph-N-CZ-3 decomposes at 250 °C and has the best thermal stability among the four initiators. Among the three aldehyde-based oxime ester initiator molecules, Ph-N-CZ-1 and Ph-N-CZ-2 exhibit similar thermal stability, and Ph-N-CZ-4 has poor thermal stability and undergoes decomposition at 102 °C. The thermal decomposition temperatures of the four initiator molecules are all above 100 °C, indicating that the initiators will not undergo decomposition reactions under general room-temperature storage conditions and have good thermal stability.

Conclusion

Four N-phenyl substituted carbazole oxime ester photoinitiators were designed and synthesized. The novel photoinitiators have a broad absorption in the range of 300-400 nm and can effectively initiate free radical polymerization of acrylates under 405 nm LED light. The tert-butyl substituted aldehyde-oxime ester Ph-N-CZ-2. All the photoinitiators exhibits sufficient thermal stability for daily use.

Acknowledgement

The authors acknowledge the financial support by the Natural Science Foundation of Jiangsu Province (BK20191336).

References

1. Z. Q. Li, X, C. Zou, X, F. Shi, R. Liu, and Y. Yagci, *Nat. Commun.*, **10** (2019) 3560.
2. G. S. Liou, H. W. Chang, K. H. Lin, and Y. O. Su, *J. Polym. Sci., Part A: Polym. Chem.*, **47** (2009) 2118.
3. D. E. Fast, A. Lauer, J. P. Menzel, A-M. Kelterer, G. Gescheidt, and C. Barner-Kowollik, *Macromolecules*, **50** (2017) 1815.
4. J. J. Yang, C. Xu, Y. Xiong, X. L. Wang, Y. J. Xie, Z. Li, and H. D. Tang, *Macromol. Chem. Phys.*, **219** (2018) 1800256.
5. S. H. Wang, Y. J. Xiong, J. Lalevée, P. Xiao, J. Liu, and F. Y. Xing, *Toxicol. Vitro.*, **63** (2019) 104720.
6. S. Villotte, D. Gigmes, F. Dumur, and J. Lalevée, *Molecules*, **25** (2019) 149.
7. T. Jiao, Y. C. Lin, Y. Liu, J. Liu, and G. Lu, *Mater. Res. Express*, **7** (2020) 015334.
8. G. Y. Wu, and H. Deng, *J. Photopolym. Sci. Technol.*, **33** (2020) 537.
9. T . Amano, D. Hirata, Y. Hasegawa, and S. Takei, *J. Photopolym. Sci. Technol.*, **33** (2020) 445.
10. E. Hola, J. Ortyl, M. Jankowska, M. Pilch, M. Galek, F. Morlet-Savary, B. Graff, C. Dietlin, and J. Lalevée, *Polym. Chem.*, **11** (2020) 922.
11. E. Hola, M. Pilch, M. Galek, and J. Ortyl, *Polym. Chem.*, **11** (2020) 480.
12. W. W. Qiu, M. Q. Li, Y. N. Yang, Z. Q. Li, and K. Dietliker, *Polym. Chem.*, **11** (2020) 1356.
13. J. Zhang, J. Lalevée, N. S. Hill, J. Kiehl, D. Zhu, N. Cox, J. Langley, M. H. Stenzel, M. L. Coote, and P. Xiao, *Macromol. Rapid Commun.*, **41** (2020) 2000166.
14. F. Dumur, *Eur. Polym. J.*, **126** (2020) 109564.
15. Y. Miyake, H. Takahashi, N. Akai, K. Shibuya, and A. Kawai, *Chem. Lett.,* **43** (2014) 1275.
16. M. Griesser, A. Rosspeintner, C. Dworak, M. Hofer, G. Grabner, R. Liska, and G. Gescheidt, *Macromolecules*, **45** (2012) 8648.
17. X. Y. Ma, R. Q. Gu, L. J. Yu, W. X. Han, J. Li, X. Y. Li, and T. Wang, *Polym. Chem.*, **37** (2017) 6134.
18. J. Xu, G. P. Ma, K. M. Wang, J. M. Gu, S. Jiang, and J. Nie, *J. Appl. Polym.*, **123** (2011) 725.
19. P. Hu, W. W. Qiu, S. Naumov, T. Scherzer, Z. Y. Hu, Q. D. Chen, W. Knolle, and Z. Q. Li, *ChemPhotoChem*, **4** (2020) 224.
20. M. Makino, K. Uenishi, and T. Tsuchimura, *J. Photopolym. Sci. Technol.*, **31** (2018) 37.
21. L. Zhao, C. Qian, L. Gong, and X. Z. Chen, *Res. Chem. Intermed.*, **38** (2012) 105.

Journal of Photopolymer Science and Technology
Volume 34, Number 3 (2021) 315−320 ©2021SPST

Electrical and Optical Model of Reverse Mode Liquid Crystal Cells with Low Driving Voltage

Rumiko Yamaguchi* and Koichi Inoue

Cooperative Major in Life Cycle Design Engineering
Graduate School of Engineering Science, Akita University,
1-1 Tegata gakuenmachi, Akita 010-8502, Japan
** yrumiko@gipc.akita-u.ac.jp*

Electrical and optical properties in reverse mode polymer stabilized liquid crystal (LC) cells have been investigated. We have proposed a light scattering model between LC domains with different domain sizes to describe low driving voltage. The LC reorientation in large and small domains was numerically investigated by fitting to the measured relative permittivity of the cell as a function of applied voltage. Transmittance considering the light scattering between two size LC domains was estimated in addition to the scattering due to a refractive index mismatching between LC and the polymer matrix. By fitting the theoretical curve to the experimental data, we found that the light scattering between LC domains was dominant for the low driving voltage of the reverse mode LC cell.
Keywords: Nematic liquid crystal, Reverse mode, polymer network, light scattering, Relative permittivity, Refractive index

1. Introduction

A nematic liquid crystal (LC)/polymer composite system has been studied as a novel electro-optical material. A typical composite cell has been proposed as a polymer dispersed liquid crystals (PDLC) [1-4]. The volume fraction of the polymer is 40 - 60%. The PDLC can electrically switch the light scattering state to the transparent state, which is called a normal mode. A reverse mode cell, on the other hand, changes from the transparent state to the light scattering state. This system has distinct some advantages over the normal mode. Because, it can provide a high level of optical transparency (low haze) in the off-state and a fail-safe design for automotive applications.

Various methods have been reported for the preparation of reverse mode LC cells (see review of F. Ahmad *et al*. [5]). Polymer stabilized LC cells formed by of mesogenic polymer networks of 3 - 10% [6-14] have actively been studied. The reactive mesogen (RM) is photo-polymerized in the homogeneously, homeotropically or twisting oriented LC mixture [8-11]. The cell is very clear since optical axes of the polymer network and the LC are parallel to each other and the refractive index matching is obtained. When the voltage is applied to the cell, the LC reorients and the cell changes to the opaque state. However, the cell has a high driving voltage compared to a conventional LC display device. Therefore, a number of studies have been conducted to reduce the voltages.

We also have investigated reverse mode cells to improve cell characteristics by selecting composite materials and by controlling the cell fabrication process [11-14] and reported that the minimum transmittance was obtained, when LC molecules were not fully reoriented to the electric field yet. In order to explain these experimental results, we have assumed the light scattering between different size of LC domains [13]. Murai *et al*. have reported a similar relationship between transmittance and cell capacitance [15]. Wilderbeek *et al*. have reported that the further increase of the transmittance in the higher voltage was caused by the increase of domain size of the mobile LC fraction [16].

In this paper, we have proposed a simple model of the LC reorientation in large and small LC domains. By fitting theoretical curves to the

Received March 22, 2021
Accepted May 6, 2021

experimental data electrically and optically, it was clarified that the light scattering between large and small LC domains was dominant which causes the low driving voltage of the reverse mode LC cell.

2. Theoretical modeling

Figure 1(a) shows a scanning electron microscopy (SEM) image of the polymer network structure in the polymer stabilized LC cell after removing the LC. It is known that such a fibril or a rice grain-like polymer structure results in the low driving voltage compared to a smooth network strands [12, 17-19]. We have proposed the model of the polymer network structure which has large and small LC domains, as schematically shown in Fig.1(b). A similar model has been proposed in the LC droplet type normal mode PDLC by J. A. Ferrari *et al*. [20]. They have successfully enhanced the light scattering in the "pseudo-off-state".

2.1. Fitting to the Lichtenecker equation

Under the voltage application, LCs reorient with lower applied voltage in the larger LC domains (with higher voltage in smaller domains) [4,11,20,21]. The permittivity of the cell increases with the LC reorientation parallel to the electric field. According to Lichtenecker's logarithmic law [22], the effective permittivity of the composite material $\varepsilon_{\mathrm{eff}}$ can be expressed as

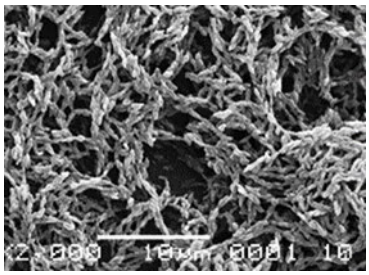

(a)

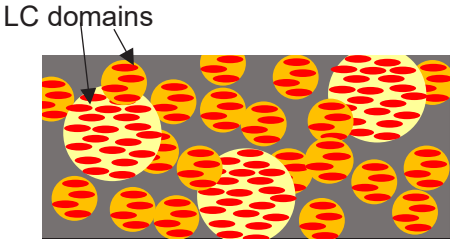

(b)

Fig. 1. (a) SEM photograph of the polymer network structure and (b) schematic model of large and small LC domains.

$$\ln(\varepsilon_{\mathrm{eff}}) = \sum \rho_i (\ln \varepsilon_i), \tag{1}$$

where ρ_i and ε_i are the volume fraction and the permittivity of material i, respectively. Based on our model, we have assumed four components, the polymer ρ_{p} and ε_{p}, the LC fixed on or inside the polymer network ($\rho_{\mathrm{LC}\perp}$ and $\varepsilon_{\mathrm{LC}\perp}$) [23-25], the LC in the large domain ($\rho_{\mathrm{LC\_L}}$ and $\varepsilon_{\mathrm{LC\_L}}$) and the LC in the small domain ($\rho_{\mathrm{LC\_S}}$ and $\varepsilon_{\mathrm{LC\_S}}$) in the reverse mode cell. Therefore, we theoretically obtain the cell permittivity as a function of applied voltage by rewriting the Eq. (1) in the following form

$$\begin{aligned} \ln\{\varepsilon(V)\} = {} & \rho_{\mathrm{p}} \ln(\varepsilon_{\mathrm{p}}) + \rho_{\mathrm{LC}\perp} \ln(\varepsilon_{\mathrm{LC}\perp}) \\ & + \rho_{\mathrm{LC\_L}} \ln\{\varepsilon_{\mathrm{LC\_L}}(V)\} \\ & + \rho_{\mathrm{LC\_S}} \ln\{\varepsilon_{\mathrm{LC_S}}(V)\}, \\ \rho_{\mathrm{p}} + \rho_{\mathrm{LC}\perp} + \rho_{\mathrm{LC\_L}} + \rho_{\mathrm{LC\_S}} = {} & 1 . \end{aligned} \tag{2}$$

2.2. Lambert-Beer equation

Next, we have numerically studied the transmittance by using the Lambert–Beer law which allows to estimate the transmittance of a narrow direct light beam passing through the PDLC as

$$T = T_0 \exp(-\tau d), \tag{3}$$

where T_0 is the incident light intensity, τ is a turbidity [21] and d is the cell thickness. The turbidity is proportional to a scattering cross section σ [19, 26-28]. Under the voltage application, $\sigma(V)$ of the PDLC in the anomalous diffraction approach [26] is written as

$$\sigma(V) = \sigma_0 \left[\frac{n_{\mathrm{LC}}(V)}{n_{\mathrm{p}}} - 1\right]^2, \tag{4}$$

where, σ_0 is a function that depends on the wavelength of the incident light and the domain size, $n_{\mathrm{LC}}(V)$ is a mean refractive index of LCs and n_{p} is a refractive index of the polymer. In order to describe two light scattering mismatches, one is that between the polymer matrix and mean refractive index of LCs and another is that between large and small LC domains, we rewrite the Ex. (3) in following form

$$\begin{aligned} T(V) = T_0 \exp\{ - \Bigg(& \alpha_0 \left[\frac{n_{\mathrm{LC}}(V)}{n_{\mathrm{p}}} - 1\right]^2 \\ & + \beta_0 \left[\frac{n_{\mathrm{LC\_L}}(V)}{n_{\mathrm{LC\_S}}(V)} - 1\right]^2 \Bigg) d \} , \end{aligned} \tag{5}$$

where effective refractive indices of the polymer and of the LC in large and small domains are respectively shown as n_{p}, $n_{\mathrm{LC\_L}}(V)$ and $n_{\mathrm{LC\_S}}(V)$. α_0 and β_0 are functions related to σ_0 and the LC domain density, which are fitting parameters in this study. $n_{\mathrm{LC}}(V)$ of the mean refractive index of the LC in both large and small domains is given by

$$n_{\mathrm{LC}}(V) = \frac{\rho_{\mathrm{LC\_L}} n_{\mathrm{LC\_L}}(V) + \rho_{\mathrm{LC\_S}} n_{\mathrm{LC\_S}}(V)}{\rho_{\mathrm{LC\_L}} + \rho_{\mathrm{LC\_S}}} \quad . \qquad (6)$$

3. Experimental

In the reverse mode polymer stabilized LC cell fabrication, the RM of ARLM-002 (Osaka organic chemical industry) and nematic LCs of MLC2136 and ZLI4792 from Merck were used. The RM of 5wt% was dissolved in MLC2136 and of 1wt% in ZLI-4792. The mixture was homogeneously oriented in the cell. The cell thickness was 10 μm. The cell was irradiated with UV light from a UV-LED (λ_{max}=365 nm) at room temperature. The UV intensity was 20 mW/cm^2 and irradiation time was 3000 s unless otherwise specified. A capacitance of the cell was measured using a HP 4284 LCR meter and a relative permittivity was estimated with the capacitance of the empty cell before introducing the mixture of LC and RM. The LC reorientation was evaluated as a relative permittivity as a function of applied voltage. The frequency of the applied voltage was 1 kHz. Electro-optical properties were measured using a polarized laser beam (640 nm) parallel to the LC director. A collection angle of scattered light was about 2°. 100% transmittance was defined as the light intensity detected without the cell.

4. Results and discussion

4.1. LC reorientation and relative permittivity

Figure 2 shows the relative permittivity of the pure LC and the reverse mode LC cell using MLC-2136. Symbols are measurement results and the solid line is theoretical fitting result. The permittivity of the pure LC perpendicular to the molecular axis ($\varepsilon_{\mathrm{LC}\perp}$) was 3.5. The permittivity parallel to the axis ($\varepsilon_{\mathrm{LC}//}$) was 10.2 which was obtained by linearly extrapolating the curve as a function of 1/V to infinite voltage $\varepsilon_{\mathrm{LC}}(\infty)$ [29]. We estimated the theoretical curve of the pure LC permittivity by numerically analyzing the free energy of the cell and the distribution of tilt angle θ in the homogeneous cell as a function of applied voltage [30]. Elastic constants of K_{11}=10 and K_{33}=20

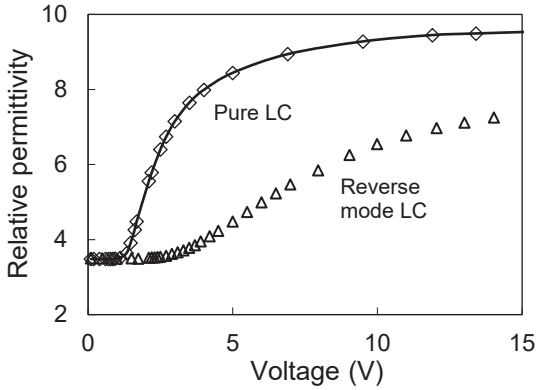

Fig. 2. Voltage vs. relative permittivity of the cell. Symbols: experimental data; solid line: theoretical fitting.

and dielectric anisotropy of $\Delta\varepsilon$ = 6.7 were used. The permittivity of the RM perpendicular to the molecular axis (ε_{p}) was 4.0. The measured permittivity of the reverse mode cell without the voltage was 3.5 which was almost the same as $\varepsilon_{\mathrm{LC}\perp}$ since the weight concentration ratio of the LC was 95wt%. Subsequently, we assumed that the polymer and LC volume fractions were the same as each weight concentration ratio. When the extremely large voltage was applied, the permittivity of the cell was estimated by linearly extrapolating the measured result as a function of 1/V. Then we obtained the value $\varepsilon(\infty)$ of 9.0. Here, if the LC was full reoriented to the electric field, $\varepsilon(\infty)$ would be 9.7. Then, Eq. (2) under the infinite voltage is rewritten as

$$\ln\{\varepsilon(\infty)\} = \rho_{\mathrm{p}} \ln(\varepsilon_{\mathrm{p}}) + \rho_{\mathrm{LC}\perp} \ln(\varepsilon_{\mathrm{LC}\perp}) + (1 - \rho_{\mathrm{p}} - \rho_{\mathrm{LC}\perp}) \ln(\varepsilon_{\mathrm{LC}//}), \qquad (7)$$

with considering the LC fixed on or inside the polymer network and we obtained $\rho_{\mathrm{LC}\perp}$ of 0.09. R.-Q. Ma and D.-K.Yang have reported that the volume fraction of RM network increased to 9% by trapped LCs inside the polymer with the monomer concentration of 5% [23]. Dessaud *et al*. have also reported that LC volume fraction attached to the RM is about 0.25 [24]. These values of the fixed LC volume fraction certainly depend on not only used materials and cell fabrication processes, but on the theoretical model to estimate the relative permittivity.

The threshold voltage V_{th} for the pure MLC-2136 and reveres mode cell were about 1.3 V and 2.9 V, respectively. It is well known that the V_{th} in the PDLC increases with decreasing the droplet diameter. Therefore, the V_{th} in the reverse mode cell also corresponds to the V_{th} in the large LC domain,

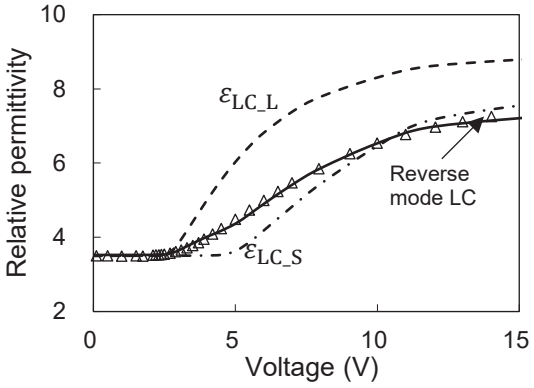

Fig. 3. Voltage vs. relative permittivity of the LC in large and small domains. Symbols: experimental data; solid line: theoretical fitting by Eq. (3).

which was 2.2 times of the V_{th} in the pure LC. Next, we fitted the theoretical curve to the measurement result by using fitting parameters of ρ_{LC_S} and V_{th} in the small LC domain. The actual LC domain form are shown in the SEM photograph of Fig. 1(a). Good agreement was obtained with ρ_{LC_S} of 0.50 (as a result ρ_{LC_L} was 0.36) and the V_{th} of 5.2 V, as shown in Fig. 3.

It is well known that the droplet size becomes larger with weaker UV intensity in the polymerization process of the PDLC. We verified the domain size effect in the reverse mode cell with the UV intensity of 2 mW/cm^2. We fitted the theoretical permittivity curve to the measurement result in the same procedure. Good agreement was also be obtained, as shown in Fig. 4. The volume fraction of the trapped LC $\rho_{LC\perp}$ was estimated to be 0.09, which was the same value as the cell with the UV intensity of 20 mW/cm^2. The V_{th} of the cell was reduced to 1.7 V due to large LC domains. The V_{th} in the large and small LC domains were respectively 1.3 and 2.0 times of that in the pure LC. ρ_{LC_L} and

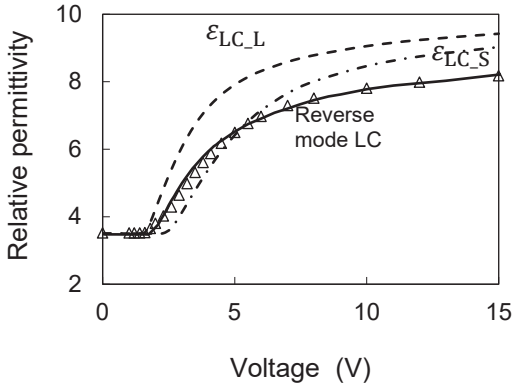

Fig. 4. Voltage vs. relative permittivity of the LC in large and small domains. Symbols: experimental data; solid line: theoretical fitting by Eq. (3).

ρ_{LC_S} were estimated to be 0.40 and 0.46, respectively.

4.2. Electro-optical property

Figure 5 shows the electro-optical property of reverse mode cells with UV intensities of 2 and 20 mW/cm^2 experimentally. The transmittance decreased by applying the exceeding the threshold voltage of permittivity properties. Transmittances became minimum at the applied voltage of 3.2 V and 6.6 V in the cell with UV intensities of 2 and 20 mW/cm^2, respectively. However, the permittivity at 3.2 V and 6.6 V was about 5.3 for both cells as shown in Figs. 3 and 4, which indicates that the average LC tilt angle was estimated about 30°. For pure MLC2136, refractive indices of n_e and n_o are 1.716 and 1.504, respectively and the mean LC index in the LC domain is estimated to be approximately 1.643 at these applied voltages. Since the n_p of the RM is about 1.700, such an index

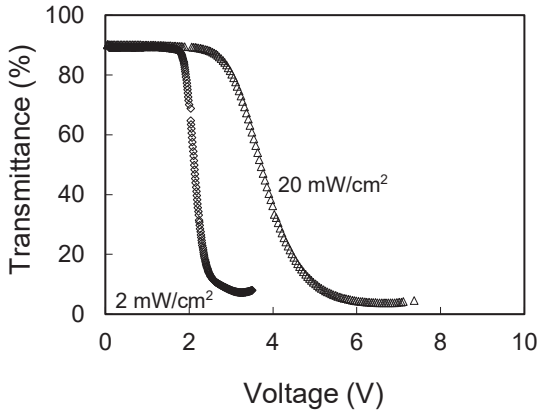

Fig. 5. Electro-optical properties in reverse mode cells.

mismatch between the polymer and LC is not enough to cause strong light scattering.

Therefore, the simulation model using Eq. (5) which includes the light scattering effect between large and small LC domains provided good agreement with the experimental data, as shown in Fig. 6. $n_{LC}(V)$, n_{LC_L} (V) and n_{LC_S} (V) were numerically obtained respectively through $\varepsilon_{LC}(V)$, ε_{LC_L} (V) and ε_{LC_S} (V) [30] shown in Fig. 3. Here, n_{p0} of 1.710 was obtained according to the equation considering with the trapped LC in the polymer,

$$n_{p0} = \frac{\rho_p n_p + \rho_{LC\perp} n_{LC\perp}}{\rho_p + \rho_{LC\perp}} . \quad (8)$$

The transmittance is normalized to 1 at 0 volt. The theoretical curve was obtained by using the fitting parameters of α_0=26 and β_0=75 μm^{-1}. Figure 6 also

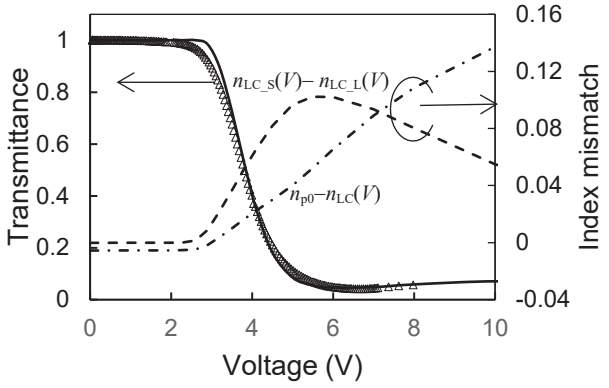

Fig. 6. Electro-optical property in the reverse mode cell in the cell with UV intensity of 20 mW/cm^2. Symbols: experimental data; solid line: theoretical fitting by Eq. (5).

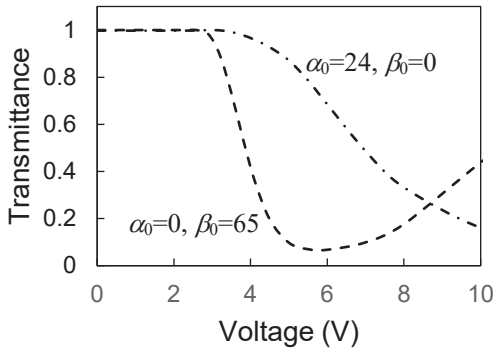

Fig. 7. Theoretical electro-optical curves with neglecting either factor α_0 or β_0.

shows calculated index differences between polymer and LC and that between large and small LC domains, as a function of applied voltage. The index difference between the polymer and LC increases with the applied voltage. On the other hand, the index difference between large and small LC domains peaks at about 5 V. Therefore, it indicates that the light scattering between LC domains is dominant around 5-6 V. In addition, we compare the theoretical curves with and without the light scattering between LC domains, as shown in Fig. 7 It indicates that the driving voltage more than 20 V is needed if without the effect of light scattering between LC domains.

Next, we verified the domain size effect for the optical simulation in the reverse mode cell with the weaker UV intensity of 2 mW/cm^2. Figure. 8 shows experimental and theoretical electro-optical properties. Fitting parameters used in this result were α_0 of 7 and β_0=110 μm^{-1}, which indicates that the light scattering between large and small LC domains is extremely dominant and contributes to lower driving voltage.

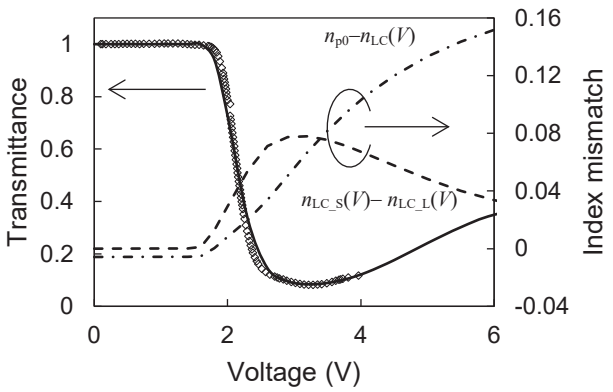

Fig. 8. Electro-optical property in the reverse mode cell with UV intensity of 2 mW/cm^2. Symbols: experimental data; solid line: theoretical fitting by Eq. (5).

Electrical and optical properties in the reverse mode LC cell was investigated using another LC material ZLI-4792 (K_{11}=13, K_{33}=17 and $\Delta\varepsilon$=5.1), as shown in Fig. 9. The SEM photograph of the RM morphology is also inserted Fig. 9. The RM concentration in the cell is only 1wt% and the SEM photograph, however, makes a prediction of higher volume fraction of the RM after the polymerization. Through the relative permittivity measurement and the theoretical fitting result, we obtained $\rho_{LC\perp}$ of 0.08. When the RM concentration increased to 5wt%, much LC was fixed to the polymer network and the driving voltage was higher than 50 V. Table 1 shows other fitting parameters for the measurement result shown in Fig. 9. Good agreement with the measurement data was obtained as shown in Fig. 9, which indicates that the simple light scattering model between large and small LC domain sizes can be applied to a variety of LC materials, PM concentrations and matrix morphologies.

Fitting parameters described so far were obtained by visually fitting to the measurement data. The

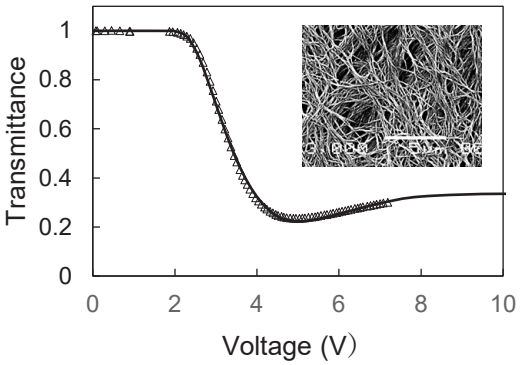

Fig. 9. Electro-optical property in the reverse mode cell using LC of ZLI-4792. Symbols: experimental data; solid line: theoretical fitting by Eq. (5).

theoretically fitting curve became significantly different from the measured one when the parameters were varied by ±10% and the relative error of parameters is about by ±5%.

Table 1. Fitting parameters for the reverse mode cell using LC of ZLI-4792.

ρ_{LC_L}	ρ_{LC_S}	V_{th_L} (V)	V_{th_S} (V)	α_0 (μm^{-1})	β_0 (μm^{-1})
0.55	0.36	2.2	4.8	30	74

5. Conclusion

We have proposed the simple large and small LC domain size model to describe the low driving electro-optical property in reverse mode LC cells. The experimental relative permittivity as a function of applied voltage of the cell was successfully fitted by using Lichtenecker's logarithmic law with four components of the polymerized RM, the LC fixed to the RM, LC in large domains and that in the small domains. The theoretical electro-optical property was also fitted to the experimental result by two light scattering mechanisms, one was that between polymer and reoriented LC and another was that between two-size LC domains. Finally, we found that the light scattering between LC domains was dominant for the low driving voltage. Our model indicates that an appropriate control of domain sizes and volume fractions of the LC allows for the coexistence of lower driving voltage and stronger light scattering.

Acknowledgments

This work was supported by Japan Society for the Promotion of Science (JSPS) KAKENHI grant number 18K04257.

References

1. J. L. Fergason, *SID Dig. Tech. Paper*, **16** (1985) 68.
2. P. S. Drzaic, *J. Appl. Phys.*, **60** (1986) 2142.
3. J. W. Doane, N. A. Vaz, B. G. Wu, and S. Zumer, *Appl. Phys. Lett.*, **48** (1986) 269.
4. N. A. Vaz, G. W. Smith, and G. P. Montgomery, Jr, *Mol. Cryst. Liq. Crys.*, **146** (1987) 1.
5. A. Farzana, M. Jamil, and Y. J. Jeon, *Electron. Mater. Lett.*, **10** (2014) 679.
6. R. A. M. Hikmet, *J. Appl. Phys*., **68**, (1990) 1.
7. R. A. M. Hikmet, *Liq. Cryst.*, **9** (1991) 405.
8. R. Yamaguchi, Y. Waki, and S. Sato, *Jpn. J. Appl. Phys.*, **36** (1997) 2771.
9. R. Yamaguchi, Y. Waki, and S. Sato, *J. Photopolym. Sci. Technol.*, **10** (1997) 19.
10. R. Yamaguchi and L. Xiong, L., *Jpn. J. Appl. Phys.*, **49** (2010) 06023.
11. R. Yamaguchi, K. Goto, and O. Yaroshchuk, *J. Photopolym. Sci. Technol.*, **25** (2012) 313.
12. R. Yamaguchi, K. Inoue, and R. Kurosawa, *J. Photopolym. Sci. Technol.*, **29** (2016) 289.
13. R. Yamaguchi, R. Sasaki, and K. Inoue, *J. Photopolym. Sci. Technol.*, **31** (2018) 301.
14. R. Yamaguchi, K. Sagawa, and S. Yanase, *J. Photopolym. Sci. Technol.*, **33** (2020) 307.
15. H. Murai, T. Gotoh, T. Nakata, and E. Hasegawa, *J. Appl. Phys.*, **81** (1997) 1962.
16. H. Wilderbeek, H. De Koning, J. Vorstenbosch, C. Chlon, K. Bastiaansen, and D. J. Broer, *Jpn. J. Appl. Phys.*, **41** (2002) 2128.
17. I. Dierking, L. L. Kosbar, A. Afzali-Ardakani, A. C. Lowe, and G. A. Held, *Appl. Phys. Lett*., **71** (1997) 2454.
18. I. Dierking, *Adv. Mater*., **12** (2000) 167.
19. R. Yamaguchi and S. Sakurai, *J. Photopolym. Sci. Technol.*, **27** (2014) 287.
20. J. A. Ferrari, E. A. Dalchiele, E. M. Frins, J. A. Gentilini, C. D. Perciante, and E. Scherschener, *J. Appl. Phys.*, **103** (2008) 084505.
21. P. S. Drzaic, *Mol. Cryst. Liq. Cryst.*, **261** (1995) 283.
22. K. Lichtenecker, *Physik. Zeitschr.,* **30** (1929) 805.
23 R.-Q. Ma and D.-K. Yang, *Phys. Rev. E*, **61** (2000) 1567.
24. N. Dessaud, P. Raynes, and P. Bonnett, *J. Appl. Phys*., **96** (2004) 4366.
25. D.-K. Yang, Y. Cui, H. Nemati, X.-C. Zhou, and A. Moheghi, *J. Appl. Phys.*, **114** (2013) 243515.
26. S. Žumer, *Phys. Rev. A*, **37** (1988) 4006.
27. D. Bosc, C. Trubert, B. Vioouze, and M. Gullbert, *Appl. Phys Lett.*, **68** (1996) 2489.
28. H. Dahsiung, Y. Chongxiu, and L. Byoungho, *Proc. SPIE*, **5636** (2005) 621.
29. A. A. M. G. Clark, E. P. Raynes, R. A. Smith, and R. J. A. Tough, *J. Phys. D: Appl. Phys.*, **13** (1980) 2151.
30. R. Yamaguchi, *IEICE Trans. Electron,* **E102-C** (2019) 810.

Journal of Photopolymer Science and Technology
Volume 34, Number 3 (2021) 321−327 ©2021SPST

Biocompatibility of Different Universal Adhesives During Short and Long Periods on Rat Model

Murat ÜNAL[1], Ayşegül SAYGIN[2], Tülay KOÇ[3], Merve CANDAN[1], İrem İPEK[1]

[1]Sivas Cumhuriyet University, Faculty of Dentistry, Department of Pediatric Dentistry
[2]Sivas Cumhuriyet University, Faculty of Dentistry, Department of Prosthodontics
[3]Sivas Cumhuriyet University, Faculty of Medicine, Department of Pathology
gmuratunal@hotmail.com

This in vivo research aimed to compare the biocompatibility of five different Universal adhesives (UAs) in short and long periods. 108 polyethylene tubes filled with five UAs [Group 1: All Bond Universal (ABU), Group 2: Prime Bond Elect Universal (PBU), Group 3: Single Bond Universal (SBU), Group 4: Clearfil Universal Bond Quick (CUB), Group 5: Futurabond U (FBU)] or Group 6: empty (control group)] were implanted into the dorsal connective tissue of 36 rats. Groups 1, 2 and 3 were implanted in 18 rats, the other groups Groups 4, 5 and 6 were implanted in 18 rats. Then, the rats were sacrificed after time intervals 7, 30 and 90 days (n=12). Biopsy samples were examined in terms of inflammatory reaction, necrosis, macrophage infiltrate, giant cell and fibrous capsule criteria. When the UAs groups and control group were compared on the 7th, 30th and 90th days, significant statistical differences were found only on the 7th day in terms of fibrous capsule and macrophage infiltrate ($p<0.05$). In addition, statistical significant differences were found upon within the control group in terms of inflammation, necrosis, giant cell, fibrous capsule and macrophage infiltrate criteria on the 7th, 30th and 90th days ($p<0.05$). The all UAs that we used in our study have showed good biocompatibility in the subcutaneous tissues of the rats, and we think that they could be used clinically with resin-based restorative materials in all restorative treatments including deep dentine caries restorations.

KEY WORDS: Universal Adhesives, Biocompatibiltity, Rat, Subcutaneous Tissue, Short-Long Period

1.Introduction

Biocompatibility is one of the essential features of any dental material (DM). It means that a material applied to living tissue could remain stable without causing any any deterioration in the surrounding tissues [1, 2]. DM' s biocompatibility are a complex issue that includes biological factors, patient risk factors, clinical experiences and engineering issues. It is likely for dentists, dentistry students, physician assistants, patients etc. to receive detriment in the process of applying dental materials [3]. One of the methods used to determine the biocompatibility of DMs is subcutaneous implantation test. Rats, pigs and hamsters are often used in these tests. Although it is a low-cost method, it provides researchers an easier analysis since it is not processed in hard tissues. In this method, while the formable materials are placed directly into the tissue, soft materials that can not be shaped are placed in the subcutaneous dermis area with a stick-shaped test material in tubes such as polyethylene [4, 5]. Universal adhesive (UA) systems are very popular new generation bonding systems, which could be used in 3 different methods as self-etch, total-etch, and selective-etch modes [6]. These adhesives could be attached to different types of biomaterials (ceramic, metal, zirconia, composite, etc.) and can be applied in different modes for any clinical situation [7]. Many of the dental adhesives contain specific carboxylate and/or phosphate monomers

Received March 25, 2021
Accepted May 3, 2021

that can ionically bond to calcium in hydroxyapatite [8]. UAs, also contain aromatic amines, photoinitiators and filler particles. These additional components may alter the biological behavior of the pulp-dentin complex if they are not included in the polymer network. Organic solvents that can be released after polymerization may reach pulp through dentin tubules and cause different degrees of irritation in the pulp [9]. HEMA is the hydrophilic monomer contained in UAs. It augments the infiltration of adhesive resin to dentin tubules, thereby providing a better bond strength to the tooth structures [10]. Camphorquinone (CQ), another component of UA systems is a photo-initiator released after polymerization [11, 12]. This is not a component of the polymer chain, so some of the components not involved in polymerization can cause oxidative stress, DNA damage and cytotoxicity [12]. During the polymerization process of the resin monomer, double carbon bonds (C = C) need to transform into a single carbon bond (C-C) to create polymer. If this chemical bond transformation is insufficient and incomplete transformation occurs, the material may cause cytotoxicity in the tissue. Resin based materials often may not polymerize completely when using light. As a result, it has been submitted that there is a significant relationship between leaking, non-polymerized monomers from resin based materials and their cytotoxic effects [13]. It is known that monomers released from adhesives can negatively affect the cellular function of fibroblasts and can cause direct biological reactions in the pulp tissue [14]. In addition, it is stated in some research that the monomers might cause odontogenic differentiation in stem - non stem pulp cells and delay in mineralization processes [15, 16]. While cytotoxic effects of dental adhesives have been shown in many in-vitro studies in the literature, the number of in-vivo studies is very limited. Also, when the literature reviewed, it would be seen that there is no in-vivo biocompatibility study related to UAs. As a result, this research is the first in-vivo study to histologically examine the biocompatibilities of different UAs, fibrous capsule, inflammation, necrosis, giant cell formations and macrophage infilrate on the rat model.

The null hypothesis in our study was that 5 different UA systems would differ significantly in terms of biocompatibility at different time intervals.

2. Experimental

2.1. Materials

This research was approved by the Ethics Commission of Sivas Cumhuriyet University Animal Experiments (2019/217).

A total of 36 Wistar male albino rats, weighing 200-220 gr, were used in the study. All experiments were conducted in compliance with the National Institute of Health' s Guidelines for the Care, Use of Laboratory Animals, in accordance with the 1964 Helsinki declaration and its later amendments or comparable ethical standards. The subjects were kept in standard test cages at 22-24°C, 55-70% humidity, 1 atm pressure for 12 hours in a light/dark room and their health status was checked regularly. In present study, five different UAs that would determine each group were used and their contents are shown in Table 1. 5 mm length, 1.5 mm inner diameter polyurethane [Nontoxic Scalp Vein 19G] tubes(PTs) were disinfected with 96 % alcohol solution before experiment. UAs were placed in PTs prepared in standard sizes under sterile conditions with the help of a bonding brush. A total of 6 PTs for each UA group were polymerized with a LED light device (Elipar™ S 10, 3M ESPE™, St. Paul, MN, USA) for 10 seconds from all surfaces. 108 PTs were obtained, filled with 5 different UA and without UA (control) [(Group 1: All-Bond Universal® (AB) (Bisco Inc., USA); Group 2: Prime&Bond Universal Elect (PB) (Dentsply Caulk, USA); Group 3: Single Bond Universal Adhesive (SB) (3M ESPE, USA); Group 4: Clearfill Universal Bond Quik (CB) (Kuraray NoritakeDental Inc., Japan); Group 5: Futurabond® U (FB) (Voco GmbH, Germany) and Group 6 (control)]. Groups 1, 2 and 3 were implanted in 18 rats, the other groups Groups 4, 5 and 6 were implanted in 18 rats.

2.2. Method

The animals have been anesthetized with ketamine HCL (25 mg/kg) and xylazine (10 mg/kg). After shaving the animals dorsal area and cleaning these surface, the regions where the samples would be placed were determined. Areas were created by making totally 3 incisions in the dorsal part of each animal to the skin and subcutaneous region in the determined operation areas which 2 in the shoulder and 1 being in waist regions. The incisions were adjusted to be on either side of the midline and at least 2 cm apart from each other. After then, subcutaneous pockets of 1 cm depth were created by blunt dissection in the incision areas, using

dissecting scissors. PT containing a different UA material was placed in each subcutaneous pocket under aseptic conditions. Subsequently, the incision lines were sutured by silk 3.0 sutures.

After waiting time intervals of 7, 30 and 90 days, 12 rats were euthanized after anesthesia on each time periods. The regions under the skin where PTs placed were detected. The biopsy specimens, together with the PT and sufficient normal surrounding connective tissue, were removed.

All biopsied specimens were kept in sterile storage containers for 24-48 hours in 10% buffered formalin solution and fixation process were performed. Xylene was used for deparaffinization of undyed sections and for lamination after staining. Paraffin was used to hardening the tissues. This situation enabled histological examination and obtaining sections from biopsy materials. Microtome device (Thermo 36 Scientific Shandon Finesse 325, China) was used to obtain 5µm thick sections from the paraffinized tissues.

Hematoxylin & Eosin was used to dye deparaffinized samples. Light microscope (Nikon Eclipse E200, Japan) was used for histological examination of tissue preparations. Light microscope (Nikon Eclipse E400, Japan) with digital camera attachment (Nikon DS-Ri1, Japan) was used to photograph histological images. After the prepared slides were examined under 40, 100 and 200 X magnifications with a light microscope, they were photographed under the light microscope with digital camera attachment. The tissue samples were quantitatively evaluated by a pathologist (T.K) using the scoring shown in Table 2 for the criteria of inflammation, fibrous capsule, necrosis, giant cell and macrophage infiltrate.

Table 1. Five different UAs and their composition

Materials/Lot number	pH	Manufacturer	Composition
Clearfil Universal Bond Quick (000010)	2.3	Kuraray, Okayama, Japan	10-MDP, Bis-GMA, HEMA, Hydrophilic amide monomer, Colloidal silica, Ethanol, dl-Camphorquinone, Accelerators, Water, Sodium fluoride
Single Bond Universal (70818C)	2.7	3M ESPE St. Paul, MN USA	10-MDP phosphate monomer, Vitrebond copolymer, HEMA, dimethacrylate resins, filler, silane, initiators, ethanol, water
All Bond Universal (1700005470)	3.2	Bisco, Schaumburg, IL USA	10-MDP phosphate monomer, Bis-GMA, HEMA, water, ethanol, photoinitiator
Prime Bond Elect Universal (1703000839)	2.5	Dentsply, Caulk, USA	Mono-, di- and trimethacrylate resins, PENTA, diketone, stabilisersorganic phosphine oxide, cetylaminehydrofluoride, acetone, water, self-cure activator
Futura bond U (18077614)	2.3	Voco, Germany	2 HEMA Bis-GMA HEMA, acidic adhesive monomer, urethane dimethacrylate, catalyst, silica, nanoparticles, ethanol

Table 2. Histological criteria and scores

Criteria	Scores			
	0	1	2	3
İnflammation	No detected inflammatory cells	Less than 25 cells (mild)	Between 25 and 125 cells (moderate)	125 or more cells (severe)
Fibrous Capsule	Absent	Thin , ≤150 µm	Thick , ≥150 µm	
Macrophage Infiltrate	<10 cells	≥10 to 20 cells	≥20 to 30 cells	>30 cells
Necrosis	Absent	Present		
Giant Cells	Absent	Present		

2.3. Statistical Analysis

The data obtained in present study were analyzed in the SPSS 22.0 software. Kruskal-Wallis test was used in the evaluation of the data, in which the datas obtained from more than two independent groups were compared, as the parametric test assumptions were not met. In addition, Mann-Whitney U test was used to find groups that made a difference. Friedman test was used to compare the datas obtained at different times and Wilcoxon test was used to find the difference between the groups. $P < 0.05$ value was accepted as statistically significant.

3. Results and discussion

All statistical results of this study are shown in the Table 3. Analysis of data from UAs and the control groups in terms of inflammation, fibrous capsule, necrosis, giant cell and macrophage infiltrate criteria on the 7th, 30th and 90th days has indicated the following results (Figure 1): When the 7th day inflammation scores of the UA groups were compared, the difference between the groups was found to be significant ($p <0.05$). When the values for the groups were compared in pairs, the difference between the single bond-control and prime bond-control was found to be significant ($p <0.05$), while the difference between the other groups was found to be insignificant ($p> 0.05$). When the 30th day inflammation scores of the UA groups were compared, the difference between the groups was found to be significant ($p <0.05$). When the values for the groups were compared in pairs, the difference between the single bond-control was found to be significant ($p <0.05$), while the difference between the other groups was found to be insignificant ($p> 0.05$). When the 90th day inflammation scores of the UA groups were compared, the difference between the groups was found to be significant ($p <0.05$). When the values for the groups were compared in pairs, the difference between the single bond-clearfill bond, single bond-control, clearfill bond-prime bond, clearfill bond-futura bond, prime bond-control and futura bond-control was found to be significant ($p <0.05$), while the difference between the other groups was found to be insignificant ($p > 0.05$). When the 90th day inflammation scores of the UA groups were compared, the difference between the groups was found to be significant ($p <0.05$). When the values for the groups were compared in pairs, the difference between the single bond-clearfill bond, single bond-control, clearfill bond-prime bond, clearfill bond-futura bond, prime bond-control and futura bond-control was found to be significant ($p <0.05$), while the difference between the other groups was found to be insignificant ($p > 0.05$). There were significant differences in *AB*'s giant cell and macrophage infiltrate criteria ($p <0.05$), while there was no significant difference in terms of fibrous capsule, giant cell and necrosis ($p> 0.05$). There were significant differences in giant cell, macrophage infiltrate and inflammation criteria ($p <0.05$) in *PB, CB and FB* groups, while the difference was not significant in terms of fibrous capsule and necrosis ($p> 0.05$). There were significant differences in giant cell, macrophage infiltrate, fibrous capsule and inflammation criteria ($p <0.05$) in the *SB* group, while the difference was not significant in terms of necrosis ($p> 0.05$). There were significant differences ($p<0.05$) in the all five histological evaluation criteria in *control* group. ** Between group comparisons in terms of criteria and time have yield these results: The intergroup difference was significant on the 7th day ($p <0.05$) in terms of macrophage infiltrate and fibrous capsule criteria, while there was no significant difference on the 30th and 90th days ($p> 0.05$). The intergroup difference was insignificant on the 7th, 30th and 90th days ($p> 0.05$) in terms of giant cell, inflammation and necrosis criteria. According to the results of our study, it has been observed that the biocompatibility of 5 different universal adhesives changes over time. Therefore, the null hypothesis was accepted. Although several studies have been carried out to evaluate the biological properties of many materials used in dentistry, the number of studies on universal adhesives are quite limited in the literature [5, 9, 11, 15, 16]. Under the light of this fact, we clinically analyzed the biocompatibility of UAs that facilitate application in three different ways. Experimental animals are frequently used in biocompatibility research to evaluate the tissue response of the DMs and provide crucial information about the biocompatibility of materials. In dentistry, animal studies are carried out to develop surgical techniques or identify the effects of DMs on the living tissues and these researches play a very important role in determining their effectiveness and reliability of these materials. It has been stated that local inflammation and toxicities could be determined through the implantation of DMs into the subcutaneous connective tissue in experimental animals. Since the resulting inflammatory tissue response is similar to that of exposed pulp and connective tissue, subcutaneous implantation tests are considered as a reliable

method for assessing the biocompatibility of DMs [17]. It is known that subcutaneous implantation tests generally consider day 7, 30 and 90 as experimental periods.

Fig. 1. Histopathological section samples belonging to all groups.

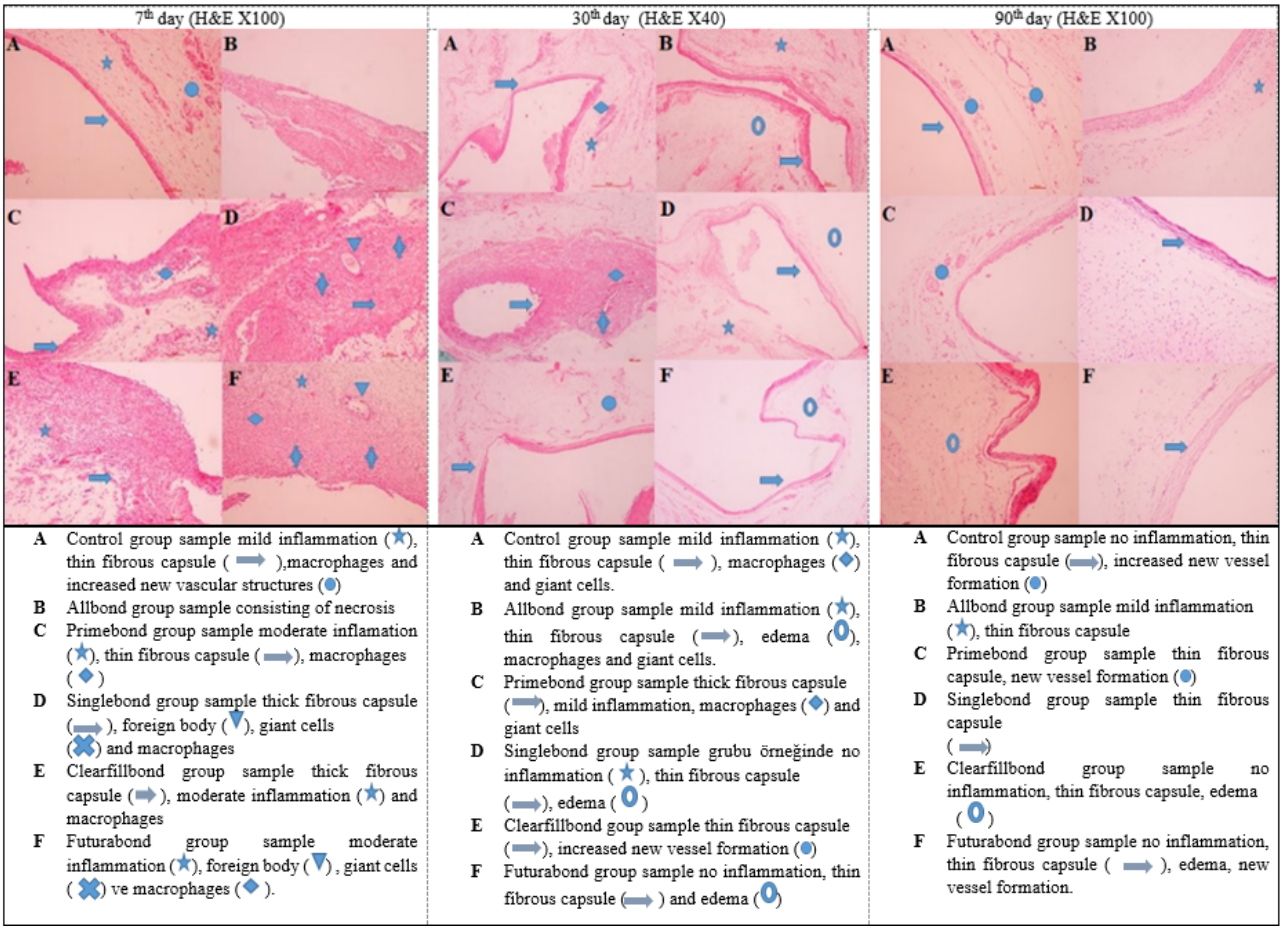

Following these periods, the test material excised with some intact tissue around it is examined histologically. In the examination, the duration and severity of the inflammatory response is the basis [18, 19]. In line with these thoughts, as time intervals in our study; we examined histological changes in tissues at 7, 30 and 90 days parameters. In biocompatibility studies, the tissue' s response to the material is evaluated between the 2nd and 12th weeks. In both processes, if there is no reaction or it is moderate, the material is confirmed to pass the test. If the reaction started at week 2 decreases at week 12, the material is still confirmed to pass the test. However, the samples showing moderate reactions in both periods are considered to fail the test. Although there is no reaction or moderate reaction at week 2, it is considered that the material fails the test if it is moderate or severe at the end of week 12 [17]. Based on these criteria, it can be said that all the universal adhesives have passed the biocompatibility test when the results of our study are examined. Costa et al. [20] evaluated the biocompatibility of two different dental adhesives and calcium hydroxide in the subcutaneous tissues of the rats on the 7th, 30th and 60th days. At the end of the 7th day, a moderate inflammatory response detected in both adhesives. At the end of the 30th day, fibrous capsules surrounding the tubes were observed. After 60 days, they found a continuous inflammatory reaction mediated by macrophage and giant cells in most of the samples, as well as connective tissue healing. In present research, the inflammation was high on the 7th day and decreased in 30 days.

The inflammation continued to decrease towards the 90th day. In addition, due to the decrease in inflammation over time, the thickness of the fibrous capsule, macrophage infiltrate and giant cell decreased. Santos et al. [21] evaluated the biocompatibility of 4 different orthodontic adhesives in rat subcutaneous tissue, argued that the severe inflammation that occurred on the 7th day was not caused by the applied material but by the trauma caused by the surgical procedure. In addition, all orthodontic adhesives were found to have good biocompatibility at the end of the 30th day. Teixeira et al. [22] evaluated the biocompatibility of three different adhesives and calcium hydroxide on the 15th, 30th and 60th days, a moderate-intensive. inflammatory reaction was observed at the end of the 15th day. It was reported that the inflammatory response decreased over time and there was no inflammatory response to calcium hydroxide at the end of the 30th day, and a thin capsule formation. At the end of the 60th day, it determined that an ongoing inflammatory reaction to the dental adhesives developed. In our study, a moderate inflammatory reaction was observed on the 7th day and a low inflammatory reaction at the end of the 30th day in all the UA's. On the 90th day, the low inflammation continued.

In addition, fibrous capsule thickness, macrophage infiltration and giant cell decreased from 7th day to 90th day. In addition to in-vivo studies mentioned above, in vitro cytotoxicity studies, which included some universal adhesive systems, are described below. In an in-vitro study by Yıldırım et al. [23] the cytotoxicity of 5 different adhesives was compared at the 24th, 48th and 72nd hours in the cell culture medium. It is stated that the cytotoxic effect of all adhesives increases depending on the dose and varied over time. In our study, the inflammation of all UAs used changed and decreased over time Necrosis is defined as the uncontrolled death of the cell and is associated with the increase of the resulting lifeless cells and the release of increased inflammatory cytokines. It was seen only in one sample on the 7th day in the Allbond, Single bond and Clearfil groups, which are among the universal adhesives in our study. No necrosis was observed in any group on the 30th and 90th days Futura universal adhesive used in our study contains UDMA, unlike the other 4 universal adhesive materials. In their study, Szep et al [24], suggested that materials containing the BisGMA + UDMA + HEMA will be more toxic than materials containing BisGMA + HEMA. When the results of our study are examined, it is seen that they are similar to the results of the study by Szep et al.

Table 3. Evaluation results for all UAs groups, on day 7th, 30th and 90th

		All bond		Prime bond		Single bond		Clearfill bond		Futura bond		Control		
Parameters	Time	Mean	Min-Max (med)	Mean	Min-Max (med)	Mean	Min-Max (med)	Mean	Min-Max (med)	Mean	Min-Max (med)	Mean	Min-Max (med)	p-value
Inflammation	7^{th} day	$2,00^{a,b}$	1-3(2)	$2,33^{A}$	1-3(2)	$2,5^{B,a}$	1-3(3)	$2,00^{a}$	1-3(2)	$1,67^{a}$	1-2(2)	$1,00^{A,B}$	1-1(1)	0,021*
	30th day	$1,33^{a,c}$	1-2(1)	$1,00^{a}$	0-2(1)	$1,67^{A}$	1-2(2)	$1,33^{b}$	1-2(1)	$1,00^{b}$	1-1(1)	$0,50^{A,a}$	0-1(0,5)	0,020*
	90th day	$0,67^{b,c}$	0-1(1)	$0,83^{A,B,a}$	0-1(1)	$0,83^{C,D,a}$	0-1(1)	$0,17^{B,C,E,a,b}$	0-1(0)	$0,83^{E,F,a,b}$	0-1(1)	$0,17^{A,D,F,a}$	0-1(0)	0,023*
	p-value	0,011*		0,015*		0,011*		0,004*		0,015*		0,022*		
Fibrous capsule	7th day	1,5	1-2(1,5)	1,33	1-2(1)	$1,83^{A,a}$	1-2(2)	$1,83^{B}$	1-2(2)	1,5	1-2(1,5)	$1^{A,B}$	1-1(1)	0,040*
	30th day	1,33	1-2(1)	1,16	1-2(1)	1,16	1-2(1)	1,5	1-2(1,5)	1,16	1-2(1)	$1,6^{a,}$	1-2(2)	0,323
	90th day	0,83	0-1(1)	1,16	1-2(1)	1^{a}	0-2(1)	1,16	1-2(1)	1	1-1(1)	$0,66^{a}$	0-1(1)	0,332
	p-value	0,074		0,717		0,023*		0,135		0,097		0,015*		
Necrosis	7th day	0,16	0-1(0)	0,33	0-1(0)	0,16	0-1(0)	0,16	0-1(0)	0	0-0(0)	$0,66^{a,b}$	0-1(1)	0,145
	30th day	0	0-0(0)	0	0-0(0)	0	0-0(0)	0	0-0(0)	0	0-0(0)	0^{a}	0-0(0)	
	90th day	0	0-0(0)	0	0-0(0)	0	0-0(0)	0	0-0(0)	0	0-0(0)	0^{b}	0-0(0)	
	p-value	0,368		0,135		0,368		0,368				0,018*		
Giant cell	7th day	$0,83^{a}$	0-1(1)	$1^{a,b}$	1-1(1)	$0,83^{a,b}$	0-1(1)	$0,83^{a}$	0-1(1)	1^{a}	1-1(1)	$0,83^{a}$	0-1(1)	0,821
	30th day	0,5	0-1(0,5)	$0,33^{a}$	0-1(0)	0^{a}	0-0(0)	0,5	0-1(0,5)	0,5	0-1(0,5)	0,5	0-1(0,5)	0,416
	90th day	$0,16^{a}$	0-1(0)	$0,33^{b}$	0-1(0)	0^{b}	0-0(0)	0^{a}	0-0(0)	$0,16^{a}$	0-1(0)	0^{a}	0-0(0)	0,361
	p-value	0,047*		0,041*		0,007*		0,022*		0,004*		0,042*		
Macrophage Infiltrate	7th day	$1,5^{a,b}$	0-3(1,5)	$1,83^{A,B,a,b}$	1-3(2)	$2,16^{a,b}$	1-3(2,5)	$1,16^{a,b}$	0-3(2)	$2,83^{A,C,a,b}$	2-3(3)	$0,83^{B,C,a}$	0-1(1)	0,048*
	30th day	$0,5^{a}$	0-1(0,5)	$0,16^{a}$	0-1(0)	0^{a}	0-0(0)	$0,16^{a}$	0-1(0)	$0,5^{a}$	0-1(0,5)	0,33	0-1(0)	0,314
	90th day	0^{b}	0-0(0)	0^{b}	0-0(0)	0^{b}	0-0(0)	0^{b}	0-0(0)	0^{b}	0-0(0)	0^{a}	0-0(0)	
	p-value	0,030*		0,003*		0,002*		0,023*		0,011*		0,042*		

*The same lowercase letters in vertical column Show statistically significance and the same capital letters in the horizontal column show statistically significance ($p < 0,05$)

4. Conclusions

With in the limitation of this animal designed study, different UA systems was not differ significantly in terms of biocompatibility at different time intervals. While the tissue response they formed in the tissue is observed in the short term (7th day), in the long term (90th day) it is almost negligible. As a result, UAs could be applied safely in dentistry applications.

Acknowledgment

We would like to thank Dr. Ziynet Çınar for supporting in the evaluation of the statistical data and to the Serkan Çelikgün for the histology staining. Authors declare that they have no direct or indirect financial interests related to this study.

References

1. C. A. de Souza Costa, J. Hebling, D. L. Scheffel, D. G. Soares, F. G. Basso, and A. P. D. Ribeiro, *Dental Materials*, **30** (2014) 769.
2. P. E. Murray, C. G. Godoy, and F. G. Godoy, *Medicina Oral, Patología Oral y Cirugía Bucal (Internet)*, **12** (2007) 258.
3. B. Habib, J. A. Von Fraunhofer, and CF. Driscoll, *Journal of Prosthodontics: Implant, Esthetic and Reconstructive Dentistry*, **14** (2005) 164.
4. M. Goldberg, *Clinical oral investigations*, **12** (2008) 1.
5. H. Schweikl, G. Spagnuolo, and G. Schmalz, *Journal of Dental Research*, **85** (2006) 870.
6. T. Cengiz, M. Unal, *Microscopy and Research Technique*, **82** (2019) 1032.
7. G. Marchesi, A. Frassetto, A. Mazzoni, F. Apolonio, M. Diolosa, M. Cadenaro, R. Di Lenarda, D. H. Pashley, F. Tay, and L. Breschi, *Journal of Dentistry*, **42** (2014) 603.
8. K. Yoshihara, Y. Yoshida, N. Nagaoka, S. Hayakawa, T. Okihara, J. De Munck, Y. Maruo, G. Nishigawa, S. Minagi, and A. Osaka, *Dental Materials*, **29** (2013) 888.
9. S. T. Elias, A. Fd. Santos, F. C. Garcia, P. N. Pereira, L. A. Hilgert, Y. M. Fonseca-Bazzo, E. N. Guerra, and A. P. D. Ribeiro, *Brazilian Dental Journal*, **26** (2015) 160.
10. J. Perdigão, M. A. Muñoz, A. Sezinando, I. V. Luque-Martinez, R. Staichak, A. Reis, and A. D. Loguercio, *Operative Dentistry*, **39** (2014) 489.
11. N. J. Lin, L. O. Bailey, M. L. Becker, N. R. Washburn, and L. A. Henderson, *Acta Biomaterialia*, **3** (2007) 163.
12. J. Volk, C. Ziemann, G. Leyhausen, and W. Geurtsen, *Dental Materials*, **25** (2009) 1556.
13. R. Şişman, A. Aksoy, M. Yalçın, and E. Karaöz, *Journal of Oral Science*, **58** (2016) 299.
14. P. Murray, A. Smith, F. G. Godoy, and P. Lumley, *International Endodontic Journal*, **41** (2008) 389.
15. A. Bakopoulou, G. Leyhausen, J. Volk, P. Koidis, and W. Geurtsen, *Dental Materials*, **28** (2012) 327.
16. A. Bakopoulou, G. Leyhausen, J. Volk, A. Tsiftsoglou, P. Garefis, P. Koidis, and W. Geurtsen, *Dental Materials*, **27** (2011) 608.
17. N. S. Sönmez, E. Sönmez, and C. Akçaboy, *Indian Journal of Dental Research*, **21** (2010) 537.
18. V. Janke, N. Von Neuhoff, B. Schlegelberger, G. Leyhausen, and W. Geurtsen, *Journal of Dental Research*, **82** (2003) 814.
19. S. Tanchev, P. Georgiev, S. Georgieva, and S. Dimitrov, *Bulgarian Journal of Veterinary Medicine*, **7** (2004) 77.
20. C. A. de Souza Costa, H. M.Teixeira, A. B. L. do Nascimento, and J. Hebling, *Journal of Endodontics*, **26** (2000) 512.
21. R. L. d. Santos, M. M. Pithon, A. B. N. Fernandes, M. G. Cabral, and A. C. d. O. Ruellas, *Journal of Applied Oral Science*, **18** (2010) 498.
22. H. Teixeira, A. Do Nascimento, J. Hebling, and C. De Souza Costa, *Journal of Oral Rehabilitation*, **33** (2006) 542.
23. Z. S. Yıldırım, Ş. Bakır, E. Bakır and E. Foto, *Oral Health & Preventive Dentistry*, **16** (2018) 525.
24. S. Szep, A. Kunkel, K. Ronge, and D. Heidemann, *Journal of Biomedical Materials Research: An Official Journal of The Society for Biomaterials, The Japanese Society for Biomaterials, and The Australian Society for Biomaterials and the Korean Society for Biomaterials*, **63** (2002) 53.

JOURNAL OF PHOTOPOLYMER SCIENCE AND TECHNOLOGY
Volume 34, Number 3, 2021